

# NATIONAL BUREAU OF STANDARDS REPORT

6313

PROPERTY OF  
SOUTHWEST RESEARCH INSTITUTE LIBRARY  
SAN ANTONIO, TEXAS

## ATTENUATION COEFFICIENTS OF HIGH ENERGY X-RAYS

FINAL REPORT

1 May 1959

by

H. W. Koch and J. M. Wyckoff  
High Energy Radiation Section  
Atomic and Radiation Physics Division

to

Nuclear Physics Division  
Air Force Office of Scientific Research, ARDC

Washington 25, D. C.  
CONTRACT NO. CSO-680-57-2

FILE NO. 3-1-10



U. S. DEPARTMENT OF COMMERCE  
NATIONAL BUREAU OF STANDARDS

## THE NATIONAL BUREAU OF STANDARDS

### Functions and Activities

The functions of the National Bureau of Standards are set forth in the Act of Congress, March 3, 1901, as amended by Congress in Public Law 619, 1950. These include the development and maintenance of the national standards of measurement and the provision of means and methods for making measurements consistent with these standards; the determination of physical constants and properties of materials; the development of methods and instruments for testing materials, devices, and structures; advisory services to Government Agencies on scientific and technical problems; invention and development of devices to serve special needs of the Government; and the development of standard practices, codes, and specifications. The work includes basic and applied research, development, engineering, instrumentation, testing, evaluation, calibration services, and various consultation and information services. A major portion of the Bureau's work is performed for other Government Agencies, particularly the Department of Defense and the Atomic Energy Commission. The scope of activities is suggested by the listing of divisions and sections on the inside of the back cover.

### Reports and Publications

The results of the Bureau's work take the form of either actual equipment and devices or published papers and reports. Reports are issued to the sponsoring agency of a particular project or program. Published papers appear either in the Bureau's own series of publications or in the journals of professional and scientific societies. The Bureau itself publishes three monthly periodicals, available from the Government Printing Office: The Journal of Research, which presents complete papers reporting technical investigations; the Technical News Bulletin, which presents summary and preliminary reports on work in progress; and Basic Radio Propagation Predictions, which provides data for determining the best frequencies to use for radio communications throughout the world. There are also five series of nonperiodical publications: The Applied Mathematics Series, Circulars, Handbooks, Building Materials and Structures Reports, and Miscellaneous Publications.

Information on the Bureau's publications can be found in NBS Circular 460, Publications of the National Bureau of Standards (\$1.25) and its Supplement (\$0.75), available from the Superintendent of Documents, Government Printing Office, Washington 25, D. C.

Inquiries regarding the Bureau's reports should be addressed to the Office of Technical Information, National Bureau of Standards, Washington 25, D. C.

# NATIONAL BUREAU OF STANDARDS REPORT

NBS PROJECT

NBS REPORT

0411-11-3150

1 May 1959

6313

## ATTENUATION COEFFICIENTS OF HIGH ENERGY X-RAYS

by

H. W. Koch and J. M. Wyckoff  
High Energy Radiation Section  
Atomic and Radiation Physics Division

to

Nuclear Physics Division  
Air Force Office of Scientific Research, ARDC  
Washington 25, D. C.

CONTRACT NO. CSO-680-57-2  
FILE NO. 3-1-10

### IMPORTANT NOTICE

NATIONAL BUREAU OF STANDARDS REPORTS are intended for use within the laboratory. For additional evaluation and listing of this Report, either the Office of the Director, National Bureau of Standards, or the Office of the Director, National Institute of Standards and Technology, however, by the Government to reproduce additional copies.

Approved for public release by the Director of the National Institute of Standards and Technology (NIST) on October 9, 2015.

progress accounting documents formally published it is subjected to reproduction, or open-literature permission is obtained in writing from the agency. Such permission is not needed, prepared if that agency wishes.



U. S. DEPARTMENT OF COMMERCE  
NATIONAL BUREAU OF STANDARDS



# ATTENUATION COEFFICIENTS OF HIGH ENERGY X-RAYS

by

H. W. Koch and J. M. Wyckoff

## Introduction

This report is a final report issued at the termination of an Air Force Office of Scientific Research Project entitled "Attenuation Coefficients of High Energy X-rays". The project is continuing under the direct support of the National Bureau of Standards as project number 0466.

The objective of the program initiated with Air Force support was the direct measurement of the total attenuation coefficients for X-rays in the energy range from 5 to 180 Mev. The research to date has resulted in detailed attenuation coefficients in hydrogen, carbon, water and aluminum, which demonstrate specific areas requiring further theoretical and experimental investigations. For example, the NBS experiments have shown that the attenuation coefficients listed in the standard reference, NBS Circular 583 entitled "X-ray Attenuation Coefficients from 10 kev to 100 Mev", <sup>1/a/</sup> are incorrect by about 4% at 60 Mev for low atomic number materials. The source of the discrepancy is not understood, although the pair production cross section is suspect. A complete understanding will result from further experimental and theoretical estimates of phenomena such as the radiative corrections to the Compton and pair cross sections, and the limited accuracy of pair production predictions.

During the course of the present experiments <sup>2/3/</sup> it was necessary to investigate such related areas as high-energy X-ray spectra <sup>4/5/6/7/</sup>, development and operation of large scintillation spectrometers <sup>8/9/10/11/12/</sup>,

<sup>a/</sup> The references identified by superscripts in the introduction and background sections are listed at the end of the background section.

pulse height analyzers<sup>13/</sup> (four separate analyzers were investigated for this project), and the principles of absorption and scattering experiments.<sup>14/15/</sup> Most of these investigations were made possible because of the AFOSR support of this project. In order to illustrate these investigations, this final report includes additional background material (attachment A), a copy of a paper in the Review of Scientific Instruments (attachment B) that provided the basis of the present work, and two papers (attachments C and D) that have been prepared for publication. The papers are:

- B) R. S. Foote and H. W. Koch, Scintillation Spectrometers for Measuring the Total Energy of X-ray Photons, Rev. Sci. Instr., 25, 746 (1954)<sup>8/</sup>
- C) J. M. Wyckoff and H. W. Koch, X-ray Attenuation Coefficients from 15 to 80 Mev for Hydrogen, Carbon, Water, and Aluminum, Phys. Rev., (To be submitted for publication)<sup>3/</sup>
- D) H. W. Koch and J. W. Motz, Bremsstrahlung Formulas and Experimental Data, Rev. Mod. Phys., (To be submitted for publication)<sup>7/</sup>.

Additional Background Material

The experiment described in Attachment C used the bremsstrahlung spectrum of X-rays from a 180 Mev synchrotron. The X-rays were transmitted through long attenuators to measure the attenuation coefficients versus X-ray energy. The X-ray detector was a large scintillation spectrometer consisting of a sodium-iodide crystal arrangement whose dimensions were 5" diameter by 9" long<sup>8/</sup>. The spectrometer was developed on this project and is described in detail in attachment B.

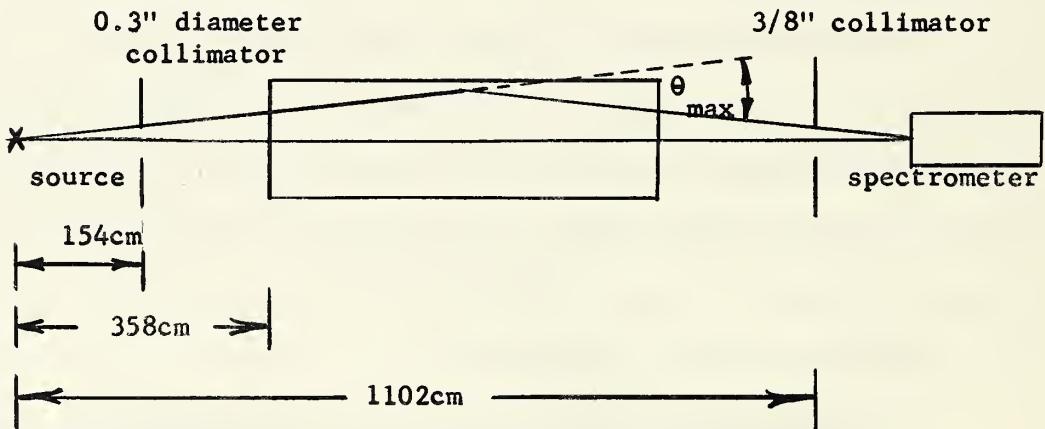
Although the detailed results of the project are given in attachment C, it was not possible in that description to emphasize the various experimental and theoretical conditions that were important to the attenuation experiment. The following is an enumeration and an amplification of those conditions.

The important requirements were:

1. A high energy X-ray source that was continuously distributed in energy with X-rays in the energy range from 10 to 90 Mev. This energy range permitted an accurate evaluation of the total attenuation coefficient from 30 to 80 Mev where the electronic processes predominate. The range also permitted a determination of the coefficients from 15 to 30 Mev where the nuclear absorptions are also important for low atomic number materials. The shape of the distribution of X-ray intensity (photon number times photon energy) was derived by Hisdal<sup>16/</sup> for the case of a small-solid-angle detector

located on the axis of the X-ray beam. The geometrical conditions assumed by Hisdal were very well satisfied in the present experiment. Hisdal's shape has further been changed to account for the coulomb corrections of Davies, Bethe, and Maximon<sup>7/,17/</sup>.

2. A good attenuation geometry that was necessary to insure a measurement of the primary interaction probability without appreciable secondary inscattering corrections. The corrections<sup>1/</sup> can be understood from the schematic arrangement of the geometries:



$\theta_{max}$  is the maximum scattering angle of photons that can get into the spectrometer and is  $4.2 \times 10^{-3}$  radians. The ratio of the scattered intensity, S, to the direct intensity, D, is given<sup>1/</sup> by:

$$\frac{S}{D} = N \pi r_o^2 \frac{Z}{A} t_o \theta_{max}^2 \left[ 1 - \frac{\theta_{max}^2}{12} (9\alpha + 4) \right] \quad (1)$$

where  $N \pi r_o^2 \frac{Z}{A} = 0.150 \frac{Z}{A} \text{ cm}^2/\text{g}$

$t_{o max} = 700 \text{ g/cm}^2$  for carbon,  $428 \text{ g/cm}^2$  for aluminum, and  $461 \text{ g/cm}^2$  for water.

$\alpha = \text{photon energy in } m_o c^2 \text{ units.}$

Thus  $\frac{S}{D} = 0.075 \text{ cm}^2/\text{g} \times 700 \text{ g./cm}^2 \times (4.2 \times 10^{-3})^2$  for carbon<sup>3/</sup>.  
 $= 0.9 \times 10^{-3}$  or 0.1%, which is negligible.

3. A high intensity X-ray source. The intensity of the synchrotron operating at 90 Mev was  $30 \text{ mw/cm}^2$  at 1 meter from the target which is large compared to most other high energy X-ray sources. This energy flux density permitted the use of the long attenuators with the scintillation spectrometer.
4. An X-ray spectrometer whose detection efficiency was almost 100% and whose energy resolution was about 12%. This resolution was tolerable for the attenuation coefficients versus energy measured in the present experiment. The determination of the response functions for the spectrometer was the subject of a separate investigation<sup>12/</sup>.
5. Recording of all photon energies simultaneously. The spectrometer characteristic of continuous recording of all photon energies in conjunction with a 256 channel pulse height analyzer made possible the good precision of one photon energy relative to another that was possible in the attenuation coefficient measurements in this experiment.
6. The ability to use long attenuators. Long attenuators are desirable in order to amplify the sensitivity of an X-ray intensity change to an attenuation coefficient change. The amplification can be understood from the differential attenuation relation:

$$\frac{dI}{I} = \tau \rho x \left( \frac{d\tau}{\tau} \right) \quad (3)$$

where  $d\bar{\tau}$  is the change in the total attenuation coefficient,  $\bar{\tau}$ , that produces the intensity change,  $\frac{dI}{I}$ , in transmission of X-rays through an absorber length of  $\bar{\tau} \rho x$  mean free paths. In the present experiment attenuators of 10 mean free paths ( $\bar{\tau} \rho x = 10$ ) of carbon, water, and aluminum were used. Thus, since a 2% intensity change was easily measurable, a measurement of an attenuation coefficient to 0.2% was in principle possible. It is also obvious from Table 1 that the total nuclear cross sections are sufficiently large compared to the electronic cross sections that a large dip will be produced in a high-energy X-ray spectrum by an attenuator whose length is 10 mean free paths.

TABLE 1

Material	Energy	Total Nuclear	Total Nuclear Plus Electronic	Expected $\frac{dI}{I}$ for $\bar{\tau} \rho x = 10$
Carbon	22.4 Mev	0.0012cm <sup>2</sup> /g	0.0164cm <sup>2</sup> /g	73%
Water	22.5 Mev	0.00075cm <sup>2</sup> /g	0.01855cm <sup>2</sup> /g	40%
Aluminum	20.5 Mev	0.0012cm <sup>2</sup> /g	0.0228cm <sup>2</sup> /g	53%

7. The attenuators are of such a length that the data may be interpreted easily. It is shown below that for relatively broad nuclear levels and short attenuators the attenuation dip in the X-ray spectrum will be a direct function of length and integrated nuclear cross section. For either a very sharp resonance or very long attenuators, the attenuation will be a function of the square root of length and integrated cross section. The results of the experiment reported in attachment C have been analyzed by assuming that the nuclear cross section shape could be resolved by the spectrometer and that the nuclear attenuation was exponential (linear for short lengths). These analyses have resulted in experimental nuclear cross

sections that are fairly close to, and somewhat larger than, cross sections synthesized from data obtained by very different methods. If resonances as sharply defined as the 15.1 Mev carbon resonance (an extreme example) made up the giant resonance region, the experimental nuclear cross sections would have been much smaller (and not larger) than the synthesized cross sections. These results suggest that the nuclear cross sections for carbon, water, and aluminum have very little fine structure in the giant resonance region.

The above comments can be understood from a calculation of the quantity measured experimentally - the number of photons removed by nuclear absorption from the spectrum,  $I_0 \Gamma_{\text{eff}}$ . For the case where the doppler width may be neglected, this quantity can be evaluated from the expression:

$$\Gamma_{\text{eff}} = \int_{-\infty}^{+\infty} [1 - e^{-\sigma_{\alpha}(E) N x}] d(E - E_0) \quad (4)$$

$$\text{where } \sigma_{\alpha}(E) = \frac{\pi}{2} \chi^2 \left( \frac{2J+1}{2I+1} \right) \frac{\Gamma \Gamma_{\gamma}}{(E-E_0)^2 + \frac{\Gamma^2}{4}} \text{ cm}^2$$

$\Gamma$  = total width for a nuclear level in e.v.

$\Gamma_{\gamma}$  = radiation width for a nuclear level in e.v.

$$\chi = \frac{1.95 \times 10^{-11}}{E(\text{Mev})} \text{ cm}$$

$N$  = atoms/cc

$E$  = photon energy

$E_0$  = resonance energy

$$\text{and } \int \sigma_{\alpha} dE = \frac{\pi}{\Gamma} \left[ \pi \chi^2 \left( \frac{2J+1}{2I+1} \right) \Gamma \Gamma_{\gamma} \right] \text{ e.v.} \cdot \text{cm}^2$$

The integral (4) can be solved explicitly in Bessel functions as done by Dardel and Persson<sup>18/</sup> or can be solved for two special cases in series expansions<sup>19/</sup> in the variable,  $t$ , where

$$t = 2\pi \chi^2 \left( \frac{2J+1}{2I+1} \right) \frac{\Gamma_\gamma}{\Gamma} xN .$$

When  $t \ll 1$ ,  $\Gamma_{\text{eff}} = \frac{\Gamma}{2} \pi \left[ t - \frac{1}{2} \frac{t^2}{2!} + \frac{3t^3}{8 \cdot 3!} + \dots \right]$

or, to a first approximation,  $\Gamma_{\text{eff}} = (\Gamma \pi t/2)$  (5)

When  $t \gg 1$ ,  $\Gamma_{\text{eff}} = \frac{\Gamma}{2} \pi \left[ 2 \sqrt{\frac{t}{\pi}} - \frac{1}{2} \frac{1}{\sqrt{\pi t}} - \frac{3}{16 \sqrt{\pi t^3}} + \dots \right]$

or, to a first approximation,  $\Gamma_{\text{eff}} = (\Gamma \sqrt{\pi t})$  (6)

Since  $t = \frac{2xN}{\pi \Gamma} \int \sigma_a(E) dE$ , (7)

equation (5) becomes

$$\Gamma_{\text{eff}} = xN \int \sigma_a(E) dE \quad \text{for } t \ll 1 \quad (8)$$

and equation (6) becomes

$$\Gamma_{\text{eff}} = \sqrt{2xN \Gamma} \int \sigma_a(E) dE \quad \text{for } t \gg 1 \quad (9)$$

For purposes of illustration, let us apply these expressions to the extreme example of the 15.1 Mev level in carbon whose characteristics have been reported<sup>20/</sup> as

$$\frac{\Gamma_\gamma}{\Gamma} = 0.77 \pm 0.08, \Gamma = 74 \pm 11 \text{ ev}$$

$$\int \sigma_a dE = \frac{\Gamma}{\Gamma_\gamma} \int \sigma_s dE = \frac{2.1 \pm 0.2 \text{ Mev mb}}{.77} = 2.7 \times 10^{-21} \text{ ev} \cdot \text{cm}^2$$

The value of  $t$  obtained from equation (7) is 996. This value makes appropriate the use of equation (9) from which is obtained  $\Gamma_{\text{eff}} = 4.2$  kev for a 500cm carbon attenuator.

If the integrated cross section of the 15 Mev level had been in a broad resonance, the  $\Gamma_{\text{eff}}$  from equation (8) would have been 116 kev and the number of photons removed from the spectrum for a 500cm carbon rod would have been 27 times larger. The experimental effect, therefore, is considerably suppressed by very sharp resonances. As stated previously, the approximate agreement of the giant resonance, differential and integrated cross sections from the present experiment with other data suggests that sharp resonances do not play a large role in the giant resonance absorption for carbon, oxygen, or aluminum.

References for the Introduction and Background Sections

1. G. W. Grodstein, X-ray Attenuation Coefficients from 10 kev to 100 Mev, NBS Circular No. 583, (U. S. Government Printing Office, Washington, D. C., 1957).
2. J. M. Wyckoff and H. W. Koch, Mass-absorption Coefficients for 40 to 80 Mev X-rays in Carbon, Water and Aluminum, Bull. Am. Phys. Soc. Ser. II, 3, 174 (1958).
3. J. M. Wyckoff and H. W. Koch, X-ray Attenuation Coefficients from 15 to 80 Mev for Hydrogen, Carbon, Water and Aluminum., Phys. Rev. (To be submitted for publication)
4. N. Starfelt and H. W. Koch, Differential Cross Section Measurements of Thin-Target Bremsstrahlung Produced by 2.7 to 9.7 Mev Electrons, Phys. Rev., 102, 1598 (1956).
5. E. G. Fuller, E. Hayward, and H. W. Koch, Shape of the High-Energy End of the Electron-Bremsstrahlung Spectrum, Phys. Rev., 109, 630 (1958).
6. U. Fano, H. W. Koch, and J. W. Motz, Evaluation of Bremsstrahlung Cross Sections at the High-Frequency Limit, Phys. Rev., 112, 1679 (1958).
7. H. W. Koch and J. W. Motz, Bremsstrahlung Formulas and Experimental Data, NBS Report No. 6104 (1958); a revised version of this report is included in this final report.
8. R. S. Foote and H. W. Koch, Scintillation Spectrometers for Measuring the Total Energy of X-ray Photons, Rev. Sci. Instr., 25, 746 (1954).

9. H. W. Koch and J. M. Wyckoff, Response of a Sodium-Iodide Scintillation Spectrometer to 10- to 20-Million-Electron-Volt Electrons and X-rays, J. Research Natl. Bur. Standards 56, 319 (1956).
10. H. W. Koch, J. E. Leiss, and J. S. Pruitt, Crystal Spectrometer Calibration of a High Energy X-ray Intensity Monitor, Bull. Am. Phys. Soc. II, 1, 199 (1956)A; this work has been extended in a report entitled "Crystal Spectrometer Calibration of High Energy X-ray Intensity Monitors", J. E. Leiss, J. S. Pruitt, R. A. Schrack, NBS Report 6149 (1958).
11. J. E. Leiss and J. M. Wyckoff, Angular Distribution of the 15-Mev Gamma-Rays Scattered from  $C^{12}$ , Bull. Am. Phys. Soc. II, 1, A(1956).
12. H. W. Koch and J. M. Wyckoff, Response Functions of Total-Absorption Spectrometers, IRE Trans. on Nuclear Science, NS-5, No. 3, 127 (1958).
13. H. W. Koch and R. W. Johnston, Editors, Multichannel Pulse Height Analyzers, NAS-NRC Publication 467, (1957).
14. H. W. Koch and R. S. Foote, Total-Absorption X-ray Spectrometry: Application to Betatron Experiments, Nucleonics 12, No. 3, 51, (1954)
15. H. W. Koch, Direct Observation of Nuclear Absorption and Elastic Scattering of X-rays, Proceedings of the 1954 Glasgow Conference on Nuclear and Meson Physics, Edited by E. H. Bellamy and R. G. Moorhouse (Pergamon Press, New York, 1955).
16. E. Hisdal, Bremsstrahlung Spectra Corrected for Multiple Scattering in the Target, Phys. Rev. 105, 1821 (1957).

17. H. Davies, H. A. Bethe, L. C. Maximon, Theory of Bremsstrahlung and Pair Production, II. Integral Cross Section for Pair Production, Phys. Rev. 93, 788 (1954)
18. G. V. Dardel and R. Persson, Determination of Neutron Resonance Parameters from Measurements of the Absorption Integral, Nature 170, 1117 (1952)
19. M. Abramowitz, Private Communication.
20. E. Hayward and E. G. Fuller, Photon Self-Absorption and Scattering by the 15.1-Mev Level in  $C^{12}$ , Phys. Rev. 106, 991 (1957), and Private Communication.

## Scintillation Spectrometers for Measuring the Total Energy of X-Ray Photons

R. S. FOOTE AND H. W. KOCH  
*Radiation Physics Laboratory, National Bureau of Standards,\* Washington, D. C.*

(Received October 7, 1953)

X-ray spectrometers are described that operate on the principle of totally absorbing the energy of an individual x-ray photon in a scintillator. Experiments with scintillators of xylene containing terphenyl, and of sodium iodide activated by thallium, show that detection efficiencies better than 80 percent and energy resolutions better than 10 percent are attainable in the x-ray energy range from  $\frac{1}{2}$  to 50 Mev. Monte Carlo calculations and crude scaling laws that simplify extrapolations to other size scintillators are discussed.

### INTRODUCTION

THE determination of the energy of an individual x-ray photon is usually accomplished by the analysis of a single interaction of the photon with matter. The interaction processes that have permitted accuracies of better than 5 percent in the energy measurement are coherent scattering, photoelectric absorption, Compton scattering, and pair production.<sup>1</sup> Although good energy resolution<sup>2</sup> is obtainable by these techniques, their main disadvantage is low detection efficiencies, which are characteristically of the order of  $10^{-3}$  percent.

The combination of a detection efficiency close to 100 percent and a good energy resolution is attainable by the application of scintillation spectrometers in which x-ray photons interact multiple times and are totally absorbed. The total absorption of an x-ray photon in a large volume of scintillation material will produce a light pulse amplitude that is proportional to the x-ray energy. Preliminary results<sup>3</sup> have been reported on a spectrometer that employed a tank of xylene liquid and terphenyl plus photomultiplier light detectors. The following report will describe the details of the xylene spectrometer and two sodium iodide spectrometers that are intended for research with pulsed<sup>4</sup> accelerators in the x-ray energy range from  $\frac{1}{2}$  to 50 Mev.

Several physicists at other laboratories have made independent suggestions, experiments, and calculations on the general principle of "total absorption" spectrometers.

\* Supported in part by the U. S. Office of Scientific Research of the Air Research and Development Command.

<sup>1</sup> J. W. M. DuMond, *Rev. Sci. Instr.* **18**, 626 (1947); Motz, Müller, Wyckoff, Kim, and Gibson, *Rev. Sci. Instr.* (in press); R. Hofstadter and J. A. McIntyre, *Nucleonics* **7**, No. 3, 32 (1950); R. L. Walker and B. D. McDaniel, *Phys. Rev.* **74**, 315 (1948).

<sup>2</sup> Energy resolution of the pulse-height distribution produced by monoenergetic x-rays will be defined as the width at half of the maximum intensity divided by the pulse height at this maximum. The width defined here is the total width of the distribution and includes the width of the photoelectric peak which forms the basis of a more common and less stringent definition of resolution.

<sup>3</sup> M. Cleland and H. W. Koch, *Phys. Rev.* **86**, 588A (1952).

<sup>4</sup> The word "pulsed" refers to the short burst of x-rays that is repeated at the repetition rate or operating frequency of the accelerator.

R. Sternheimer<sup>5</sup> has made shower calculations in order to estimate the energy resolution obtainable with a 4 in. diameter and 10 in. long sodium iodide crystal spectrometer that was proposed for the measurement of the energy of 2-Bev x-ray photons. He also investigated a combination of lead glass and organic liquid scintillator for the same measurement.

The recent work of Kantz and Hofstadter<sup>6</sup> has permitted useful predictions on the performance of sodium-iodide, total-absorption spectrometers for 100 to 160 Mev electrons and x-rays. In their experiments they measured the distribution of energy loss in copper produced by 110 and 157 Mev electron beams.

The results in references 3, 5, and 6 show that total absorption spectrometers can provide good energy resolution with high detection efficiencies for x-rays. A third desirable and concomitant characteristic of this type of spectrometer is the possibility of supplying the x-ray energy information from a single voltage pulse instead of the requirement of a coincident counting of two particles as in a pair spectrometer.

The importance of high detection efficiencies and the disadvantage of two-particle coincident counting in work with pulsed accelerators were demonstrated by J. L. Lawson.<sup>7</sup> He analyzed the length of experimental time required to measure a spectrum of betatron x-rays with a pair spectrometer. Low x-ray intensities were required with the betatron in order to minimize the possible confusion of the positron from one pair with the electron from another. As a result, the experimental time for many low-energy, pulsed-accelerator experiments using a pair spectrometer is of the order of weeks<sup>7</sup> or longer, and is intolerably long.

In contrast, the time for similar experiments with a total absorption spectrometer is of the order of hours.<sup>8</sup> Therefore, many experiments with pulsed accelerators should become feasible by the proper application of these spectrometers.

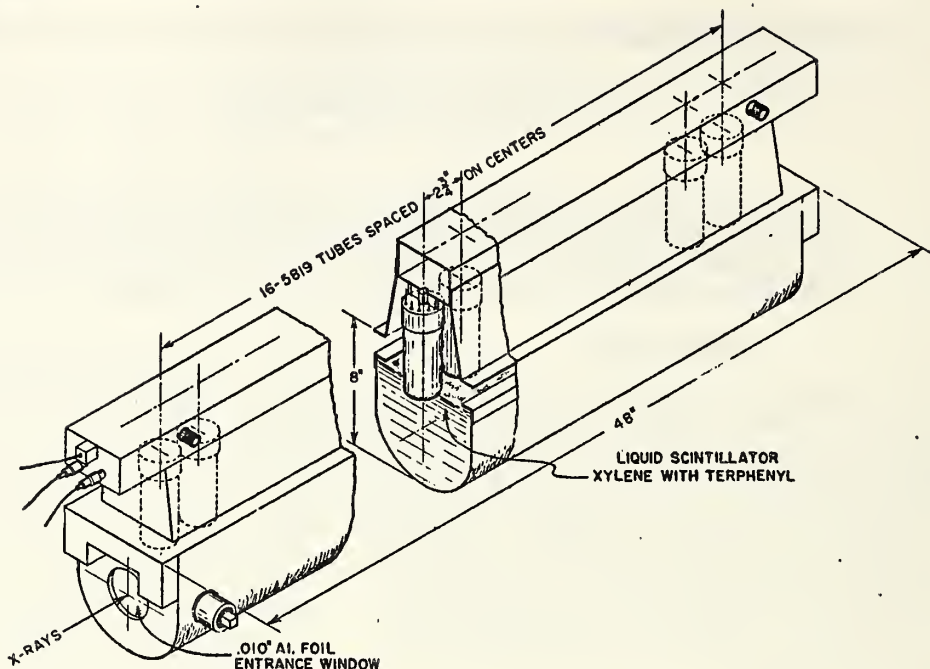
<sup>5</sup> R. Sternheimer, Brookhaven National Laboratory No. RS-5 (Oct. 11, 1951).

<sup>6</sup> A. Kantz and R. Hofstadter, *Phys. Rev.* **89**, 607 (1953).

<sup>7</sup> J. L. Lawson *et al.*, Quarterly Progress Report No. 6, General Electric Research Laboratory, Contract N7onr-332 (Sept. 1, 1948).

<sup>8</sup> Following the arguments of reference 7, one can show that 46 minutes is the required experimental time to obtain 10 000 real counts with a single count device, such as a total absorption spectrometer.

FIG. 1. A xylene (terphenyl) total absorption x-ray spectrometer. The xylene container is  $7\frac{1}{8}$  in. inside diameter by 48 in. long.



The discussion of spectrometers that follows deals with the Monte Carlo calculations, the construction details, and the experimental applications for the three models that have been built at the National Bureau of Standards. The general characteristics of these devices are:

1. Scintillator: Xylene liquid with 2 g/liter of terphenyl. Size:  $7\frac{1}{8}$  in. diameter by 48 in. long. Light detectors: sixteen 2-in. diameter photomultipliers.

2. Scintillator: Thallium activated sodium iodide crystals. (a) Size: 2 in. by 2 in. by 5 in. in three separate units. Light detectors: three 2-in. diameter photomultipliers. (b) Size: 5 in. diameter by 8 in. long in two separate units. Light detectors: eight 2-in. diameter photomultipliers.

#### XYLENE SPECTROMETER

A liquid scintillation spectrometer was the first model constructed because of its ease of fabrication and relatively small cost. The scintillator consisted of a  $7\frac{1}{8}$  in. diameter by 48 in. long tank of xylene liquid in which was dissolved terphenyl crystal to a concentration of 2 grams per liter. Single x-ray photons, whose energies were to be measured by the spectrometer, were directed down the central axis of the effective scintillator volume. The light resulting from the absorption of radiation energy in the liquid was detected by sixteen RCA 5819 photomultipliers. A schematic picture of the spectrometer is shown in Fig. 1.

The photomultiplier output pulses can supply the data from which the energy can be obtained with good

energy resolution, for the individual x-rays producing those pulses, if three conditions are satisfied.

First, most of the cascading interactions by which the original x-ray photon dissipates its energy must be confined to the spectrometer scintillator.

Second, the light resulting from energy loss in the scintillator must be collected uniformly.

Third, the number of light photons detected by the photomultiplier tubes for each absorbed x-ray must be large enough to minimize the effect of statistical fluctuations. This is particularly a problem for the xylene (terphenyl) scintillator because of its large size and poor geometry, and because the number of photons liberated for a given electron energy loss is small.<sup>9</sup>

Most of the time during the development of the spectrometer of Fig. 1 was spent in insuring uniform and efficient light collection to satisfy conditions 2 and 3. However, because of the recent availability of self-absorption data<sup>10</sup> for light in scintillators and of large-area photomultipliers, the present xylene-spectrometer design can be considerably improved and will not be described in detail. Therefore, only the results of calculations will be given, since they should prove to be a useful guide to satisfying condition 1 in any future design of a spectrometer employing an organic scintillator.

<sup>9</sup> *Experimental Nuclear Physics* (John Wiley and Sons, New York, 1952), Vol. 1, p. 52; and J. I. Hopkins, *Rev. Sci. Instr.* **22**, 29 (1951).

<sup>10</sup> Princeton University results on xylene and toluene in private communication from A. Meyer.

## MONTE CARLO CALCULATIONS FOR XYLENE

The Monte Carlo sampling technique<sup>11</sup> was used to provide quantitative evaluation of the performance of a specific scintillator in a total absorption spectrometer. The calculations for xylene were done for the five x-ray photon energies of 1, 5, 15, 25 and 35 Mev, and for a tank that was 6.5 in. in diameter and 48 in. long. A larger diameter of  $7\frac{1}{8}$  in. was used in practice. For each Monte Carlo history an individual x-ray photon was followed in to the xylene until the x-ray energy was degraded to a value that was 0.2 percent of the initial energy. The energy that was retained in the xylene was divided by the primary x-ray energy to obtain a fractional pulse height. The calculations were performed for 78 cases of 1-Mev primary photons, 71 cases of 5 Mev, 128 cases of 15 Mev, 201 cases of 25 Mev, and 267 cases of 35 Mev.

The distributions of fractional pulse heights are plotted in Fig. 2. The ordinate scale is the frequency of events on a logarithmic scale. The pulse height distribution for 1 Mev x-rays shows an extremely poor energy resolution, since almost all pulse heights up to the maximum are equally probable. At 5 Mev, the energy resolution is about 10 percent and is improving with energy. At energies of 15, 25, and 35 Mev the energy resolution is better than 7 percent.

These energy resolutions would have been those found in practice if the energy resolution had been determined solely by the electronic energy retained in the scintillator. However, experiments with betatron x-ray

spectra and arguments on light collection efficiencies indicated that energy resolutions poorer than those predicted were obtained.

## SODIUM IODIDE SPECTROMETER

The attractiveness of sodium iodide as the total absorption scintillator comes from the large density, high atomic number, large light emission per Mev of electron energy loss, and good optical properties. Other advantages will become obvious from the discussion on the x-ray measurements at energies from 87 kev to 17.6 Mev. In this range, the xylene spectrometer, as it was built, would have been completely unsuitable because the energy resolution was poor and the cosmic-ray background was large.

Rough scaling laws were applied in order to determine the size requirements of the sodium iodide from the experiences with the xylene. On this basis the two sizes, 2 in. by 2 in. by 10 in. and 3 in. by 3 in. by 10 in., of sodium iodide were selected for the Monte Carlo calculations. The x-ray photons were directed along the long dimension, and were centered on the square cross section.

## (a) Theory

## (1) Monte Carlo Calculations

The detail with which Monte Carlo calculations<sup>†</sup> had to be performed for sodium iodide was greater than that for xylene. This arises from the high atomic number of sodium iodide which makes necessary the additional detailed examination of the photoelectric, pair production, bremsstrahlung, and annihilation processes. The calculations were performed for 166 cases of primary photons of 4.45 Mev, 66 cases of 16 Mev and 18 cases of 40 Mev.

The most significant results of the calculations were the predictions of the pulse height distributions to be expected from a 2-in. by 2-in. by 10-in. and a 3-in. by 3-in. by 10-in. sodium iodide, total-absorption spectrometer. These results are shown in Fig. 3. Each curve has been averaged from histograms that were based admittedly on poor statistics. Therefore, not too much significance should be placed on the detailed shape of each curve. However, the trends among the three x-ray energies, and from the smaller crystal to the larger crystal, are thought to be significant. Note that the 4.5-Mev pulse height distribution shows evidence of subpeaks due to the escape of one and two annihilation quanta. Note also that the energy resolution obtainable with the 3-in. by 3-in. by 10-in. spectrometer is almost energy independent and is approximately 10 percent.

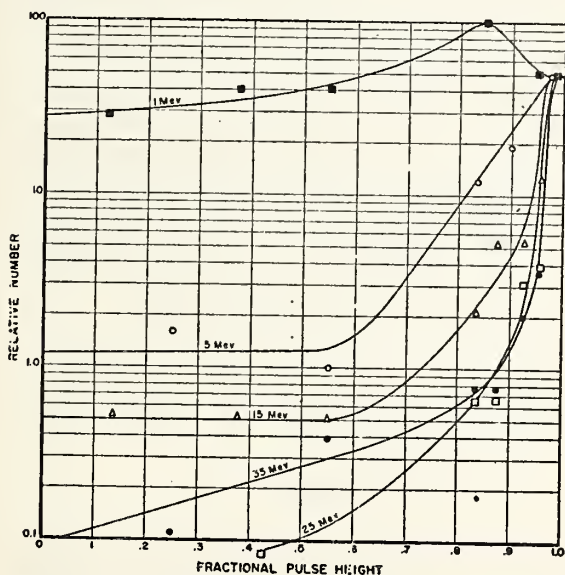


FIG. 2. Monte Carlo predictions for a xylene (terphenyl) spectrometer. The fractional pulse height distributions are predicted to result from the absorption of monoenergetic x-rays of the energies labeled above each curve.

<sup>11</sup> G. Goertzel, AEC-D 2808 (February 1950); Natl. Bur. Standards, Publication AMS-12 (1951); H. Kahn, *Nucleonics* 6, 27, 60 (1950).

<sup>†</sup> Note added in proof.—A recent paper by J. G. Campbell and A. J. F. Boyle [*Australian J. Phys.* 6, 171 (1953)] contains the details of a Monte Carlo calculation for sodium iodide which differs slightly from the procedure used in the present work.

(2) *Extrapolation to Other Sizes*

Predictions and experiments with a small-sized crystal in a total absorption spectrometer can be used as the basis for understanding the results obtainable with larger-sized crystals. Since Monte Carlo calculations for a variety of crystal sizes are tedious, and since large crystals are expensive, the description of the crude extrapolation procedure used by the authors is given here. This method was intended only for x-ray photons with energies greater than 10 Mev.

The main features of the pulse height distribution produced by monoenergetic x-rays are the percentage energy resolution and the relative pulse height position of the most probable pulse height. If the most probable pulse height is located at the fractional pulse height of 1 and if the energy resolution is 0 percent, then all of the pulses will be located at one pulse height and the spectrometer is said to operate perfectly. As the most probable pulse height decreases from 1, the percent energy resolution increases approximately in proportion to the decrease in the most probable height. This proportion results from the nature of the cascade process by which an x-ray loses energy. Therefore, in the following it is assumed that the most probable pulse height is displaced from 1 by an amount determined by the average loss,  $\Delta E_T$ , of the initial photon energy,  $E_0$ , from the crystal. Likewise, it is assumed that the energy resolution is given by

$$\frac{2\Delta E_T}{(E_0 - \Delta E_T)}$$

The question of extrapolating between different sized crystals resolves itself into a prediction of the average energy loss of photons from the various crystals.

To the assumptions on the pulse height distributions was added the assumption that the average energy losses produced by finite radii  $(\Delta E)_r$  and lengths  $(\Delta E)_l$  are independent. Therefore, the combined average energy loss will be

$$(\Delta E)_r^2 = [(\Delta E)_l]^2 + [(\Delta E)_r]^2 \quad (1)$$

(a) *Effect of radius.*—The Monte Carlo calculations for the 3-in. by 3-in. by 10-in. sodium iodide crystal showed that an energy resolution of 10 percent or a  $(\Delta E)_r$  of  $0.05 E_0$  is obtainable. This imperfect resolution can be assumed to be due entirely to the small size of the crystal in the lateral dimension. The radiation that propagates sideways is composed of annihilation radiation, low energy Compton scattered secondaries, and low energy bremsstrahlung. This energy will be attenuated with an absorption coefficient of approximately 1 Mev radiation, which is  $0.544 \text{ in.}^{-1}$ . Therefore, the average energy loss produced by a finite radius,  $r$ , can be derived by setting the integral of the exponential, constant  $x e^{-0.544r}$ , from 1.8 to infinity, equal to  $0.05 E_0$ . Thus it can

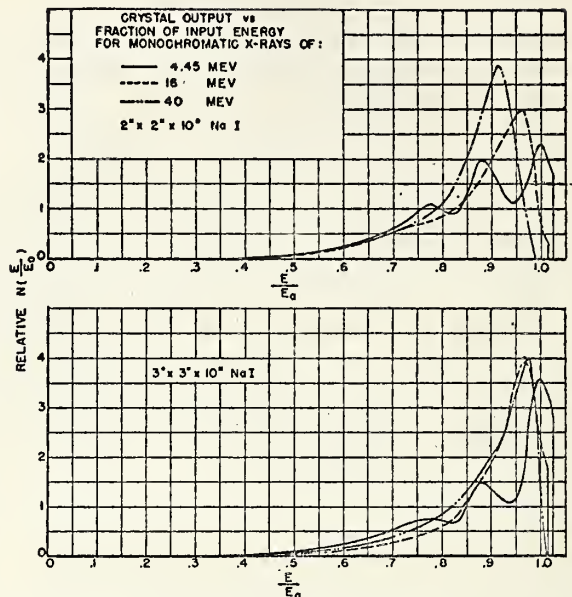


FIG. 3. Monte Carlo predictions for a 2-in. by 2-in. by 10-in., and a 3-in. by 3-in. by 10-in., NaI(Tl) spectrometer.

be shown that

$$(\Delta E)_r = 0.136 E_0 e^{-0.544r} \quad (2)$$

where  $r$  is greater than 1.8 in.

The results of this calculation are given in Table I. It will be noted from the values of (% energy resolution), that a crystal with a 5 in. diameter cross section will provide an energy resolution that is approximately a factor of 2 better than that obtainable with a 2-in. by 2-in. by 10-in. crystal.

(b) *Effect of length.*—The absorption coefficient of the x-ray energy that determines the shape of the energy absorption *versus* depth curve in the material governs the length of the spectrometer. Kantz and Hofstadter<sup>6</sup> have shown experimentally that the slope of the semilog plot of energy *versus* depth in copper is somewhat smaller than that obtained from the absorption coefficient,  $\mu_m$ , of the most penetrating photons.<sup>12</sup>

The minimum absorption coefficient,  $\mu_m$ , for sodium iodide is  $0.32 \text{ in.}^{-1}$  and occurs at 5 Mev. Therefore, in a manner similar to extrapolations described for the radial direction, the average energy loss resulting from a crystal that is  $l$  in. long is

$$(\Delta E)_l = 2.47 R E_0 e^{-0.32l} \quad (3)$$

where  $l$  is greater than 5 in., and  $R$  is the energy resolution obtained experimentally for a 5 in. long, and infinitely wide crystal. An approximation to  $R$  can be found from the measurements with a 2-in. by 2-in. by 5-in. crystal. These results as drawn in Fig. 8 show that  $R$  is approximately 15 percent. The results in

<sup>12</sup> U. Fano, *Nucleonics* 11, (Sept. 1953) has shown theoretically that the energy *versus* depth relationship is expected to be  $\exp -\mu_m x \cdot \exp H \cdot [(\mu_m x)^{\frac{1}{2}}] \cdot x^{-5/6}$  at extremely great depths.  $H$  is a constant for each material and has values around 2 to 3.

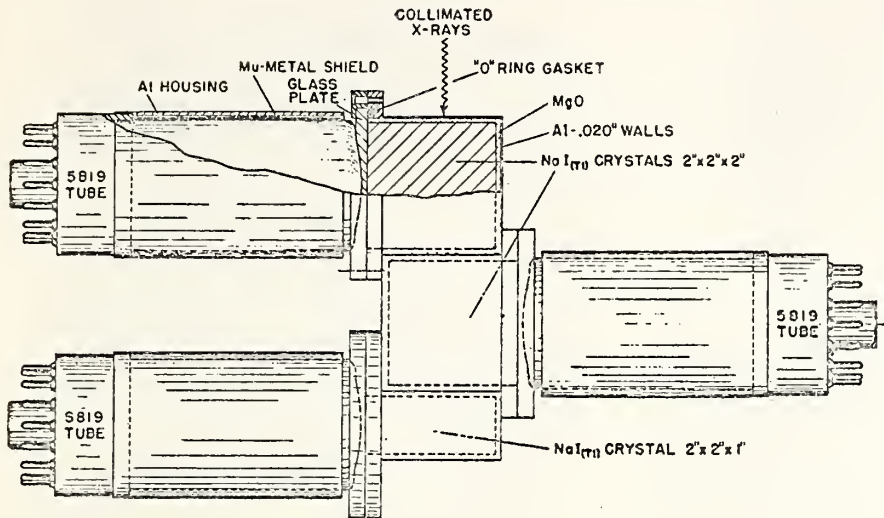


FIG. 4. A 2-in. by 2-in. by 5-in. NaI(Tl) total absorption x-ray spectrometer using three separate crystals.

Table II were obtained with this value of  $R$  substituted in Eq. (3).

(c) Experiment

(1) 2-In. by 2-In. by 5-In. NaI(Tl) Spectrometer

The Monte Carlo calculations were partially verified by determinations of pulse height frequency distributions produced by monoenergetic x-rays in a 2-in. by 2-in. by 5-in. sodium iodide spectrometer.

The 2-in. by 2-in. by 5-in. scintillator, which was available from another experiment,<sup>13</sup> was composed of

three single crystals. One selected RCA 5819 photomultiplier monitored the light from each crystal as shown schematically in Fig. 4. Also shown in this figure are the details of the crystal containers.

The photomultipliers were operated at voltages of the order of 600 volts and were adjusted to provide over-all gains that were the same. This adjustment was accomplished by observing the cathode follower outputs of each multiplier when the x-rays from Cs<sup>137</sup> were producing light pulses in the NaI crystals.

The voltage outputs were then added in the voltage

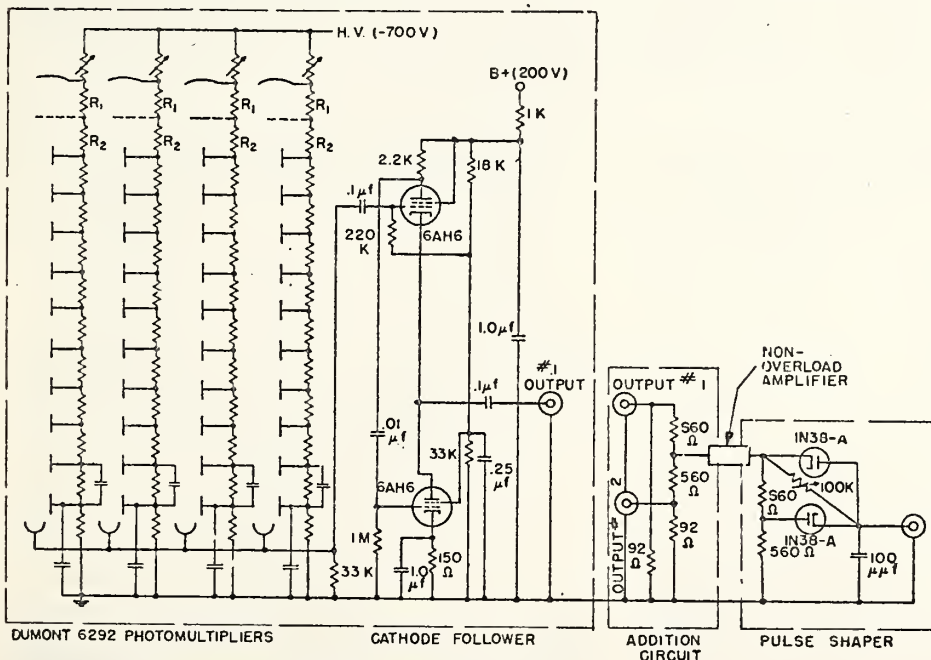


FIG. 5. Circuit diagram for a total absorption spectrometer. Four dynode resistor networks are shown. A similar group of four networks plus a cathode follower output were used with a spectrometer composed of two separate crystals, each being viewed by four photomultipliers per crystal.  $R_1 = 680K$ ;  $R_2 = 100K$ ; all other dynode resistors =  $220K$ ; dynode by-pass condensers =  $0.01 \mu f$ .

<sup>13</sup> R. S. Foote and G. Kamm, Phys. Rev. 87, 193A (1952).

TABLE I. Effect of width on average energy loss.

Radius $r$ (in.)	$(\Delta E)_r/E_0$	(% energy resolution) $_r$
2	0.046	9.6
2.25	0.040	8.3
2.5	0.035	7.3
2.75	0.031	6.4
3.0	0.027	5.6
4.0	0.015	3.1
5.0	0.009	1.8

addition circuit<sup>14</sup> of Fig. 5, in order that the single voltage pulse from the addition circuit was proportional to the total light output from the three crystals. This voltage pulse was amplified by a nonoverloading amplifier<sup>15</sup> and flattened by the simple circuit<sup>16</sup> shown in Fig. 5. The final pulse, which was flat for 0.3 microsecond, was analyzed either by a single channel pulse height analyzer,<sup>17</sup> or by photographing the dots obtained from pulse heights on an oscilloscope face.

The gamma rays that were used to test the response of the 2-in. by 2-in. by 5-in. spectrometer to monoenergetic lines were those from  $\text{Cs}^{137}$  (0.669 Mev),  $\text{Co}^{60}$  (1.17 and 1.33 Mev), and  $\text{B}^{11}(\beta, \gamma)\text{C}^{12}$  (4.45, 11.6, and 16 Mev). The incident photons were defined by a  $\frac{1}{2}$ -in. hole in an eight-inch lead wall.<sup>18</sup> The  $\frac{1}{2}$ -in. beam was incident on the 2-in. by 2-in. face of the combination crystal.

Figures 6-8 give the pulse height frequency distributions resulting from the gamma ray experiments. The  $\text{B}^{11}(\beta, \gamma)\text{C}^{12}$  distributions can be compared directly with the Monte Carlo results of Fig. 3. However, as shown by Table II, the 5-in. length of the experimental crystal would be expected to make the energy resolution considerably<sup>19</sup> worse than expected for the 10-in. length of the calculations.

TABLE II. Effect of length on average energy loss.

Length $l$ (in.)	$(\Delta E)_l/E_0$	(% energy resolution) $_l$
5	0.075	16.0
6	0.055	11.6
7	0.040	8.3
8	0.027	5.6
9	0.020	4.1
10	0.015	3.2

<sup>14</sup> *Electron Tube Circuits* (McGraw-Hill Book Company, Inc., New York, 1950), p. 148.

<sup>15</sup> R. L. Chase and W. A. Higinbotham, *Rev. Sci. Instr.* **23**, 34 (1952).

<sup>16</sup> Private communication furnished by L. G. Mann.

<sup>17</sup> The single channel discriminator that was used was an Atomic Instrument Company Model Number 510 discriminator.

<sup>18</sup> Considerable shielding is required in the use of a total absorption spectrometer because of the nondirectional sensitivity to all background radiations. The whole inside area of the enclosure provides background counts, while a small area provides the primary radiation under examination.

<sup>19</sup> The small 2-in. by 2-in. cross section probably will affect the energy resolution to the same degree as the small 5-in. length.

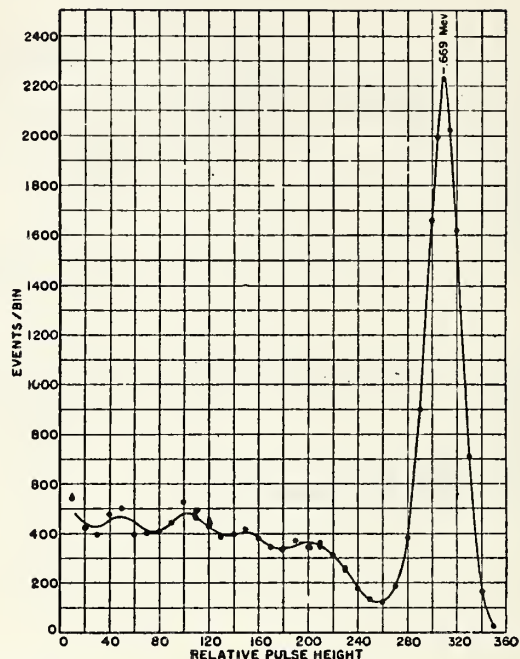


FIG. 6. The pulse height distribution produced by the gamma rays from  $\text{Cs}^{137}$ , using a 2-in. by 2-in. by 2-in. NaI(Tl) spectrometer. The beam aperture was a  $\frac{1}{2}$ -in. hole in an 8-in. thick wall.

The real usefulness of total absorption spectrometers for betatron research can be illustrated by the pulse height distribution of Fig. 9. This distribution was produced by 30-Mev betatron x-rays that were transmitted by 30 cm of copper. The spectrometer, betatron target and absorber were set up in a good geometry experiment<sup>20</sup> so that most absorption or scattering events would remove the x-rays from those detected by the spectrometer.

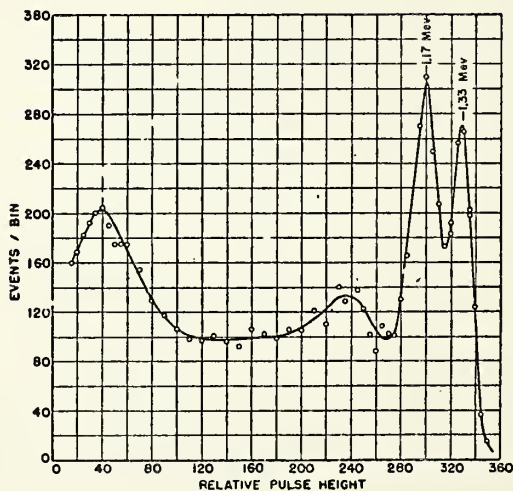


FIG. 7. The pulse height distribution produced by the gamma rays from  $\text{Co}^{60}$ , using a 2-in. by 2-in. by 2-in. NaI(Tl) spectrometer. The beam aperture was a  $\frac{1}{2}$ -in. hole in an 8-in. thick lead wall.

<sup>20</sup> H. W. Koch and R. S. Foote, *Phys. Rev.* **91**, 455A (1953).

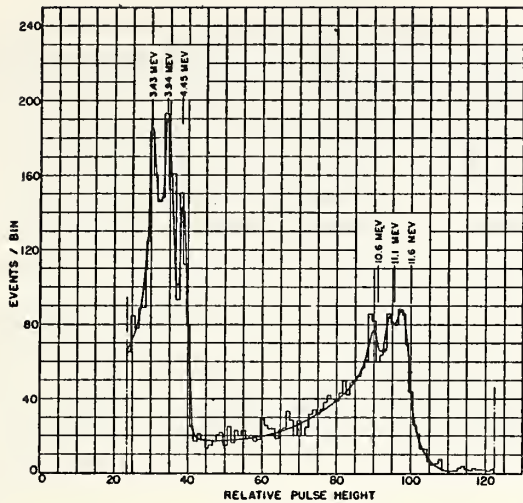


FIG. 8. The pulse height distribution produced by the gamma rays from  $B^{11}(p,\gamma)C^{12}$  using a NaI(Tl) spectrometer 2 in. by 2 in. by 5 in. The data were obtained on film over a period of three hours by bombarding  $B^{11}$  with 180 kev protons. The beam aperture was a  $\frac{1}{2}$ -in. hole in a 9-in. lead floor.

The copper length represents 8.9 electronic mean free paths of absorption or an attenuation of approximately 100 000. Thus, the high detection efficiency of the spectrometer made it possible to tolerate the large x-ray attenuation.

Large attenuations were desirable in order to make evident the intensity dip at a pulse height of 43 (Fig. 9) caused by the nuclear absorption of x-rays. The dip occurs because the nuclear absorption band is narrow and is superimposed on a smoothly varying electronic absorption function.

Relatively short times were involved in measuring the x-ray spectrum from a betatron. The data in Fig. 9 represent 30 000 counts that were recorded at a rate of 11 000 counts per hour. This low counting rate provided one detected photon every 60 betatron bursts and prevented more than 1 percent pileup of two photons in any one burst.

#### (2) 5-In. Diameter by 8-In. Long NaI(Tl) Spectrometer

On the basis of the results obtained from the above experiments and calculations, a larger NaI(Tl) spectrometer was designed. The scintillator, which was effectively a 5-in. diameter and 8-in. long crystal, was chosen as a compromise between crystal availability and the energy resolution, possible at high x-ray energies. Two crystals were used to obtain the 8-in. length, each crystal being 5 in. in diameter and 4 in. long.<sup>21</sup>

These crystals were potted in individual containers and placed back-to-back as seen in Fig. 10. Figure 11 shows the details of the crystal container assembly.

<sup>21</sup> The crystals were obtained from the Harshaw Chemical Company, Cleveland, Ohio.

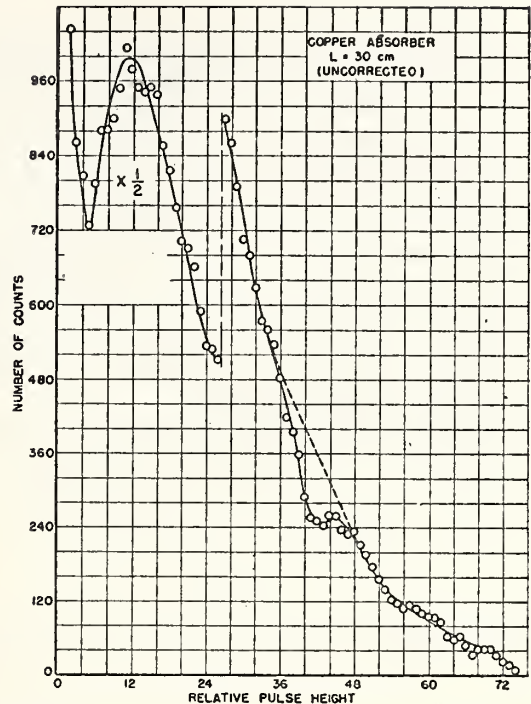


FIG. 9. The pulse height distribution produced by 30-Mev betatron x-rays transmitted through 30 cm of copper. The data were obtained by dot photography of the voltage pulse heights from the 2-in. by 2-in. by 5-in. NaI(Tl) spectrometer shown in Fig. 4. The dip at 42 divisions is due to nuclear absorption of x-rays at 18.1 Mev.

Care must be taken to obtain material that is free from natural radioactivity, especially in the glass, which is apt to contain large amounts of  $K^{40}$  in its potassium oxide content.

Before the crystals were potted, they were sanded on all sides except the surface adjacent to the glass window. The sanding was performed in a dry box and finished with 4/0 garnet paper. The polishing was done by the gentle application of a solvent, methyl alcohol, on soft tissue paper; care was taken not to wet the crystal and cause thermal shock. The crystal-to-glass optical contact was made by Dow-Corning 200 000 centistoke silicone fluid. Bonding agent, R-313, was procured from the Carl H. Biggs Company, Los Angeles, California.<sup>22</sup> The crystal container was evacuated in order to cause the aluminum end plate to push against the crystal and provide a positive crystal-to-glass contact.

Four DuMont 6292 two-in. flat end window photomultiplier tubes were faced into each of the two crystals as seen in Fig. 10. A polished aluminum reflector covered the glass except where photomultiplier-to-glass optical contact was made. The attempt was to receive as many of the light photons as possible. Single photomultiplier operation on each crystal gave 19 percent

<sup>22</sup> U. S. Atomic Energy Commission Report NYO-1577.

resolution of  $\text{Cs}^{137}$  gamma rays, whereas four tubes gathering light from the same crystal gave 10 percent resolution. Later use of the DuMont five-inch photomultiplier, K-1198, also gave a resolution of 10 percent.

The pulse height distributions produced by 0.67 Mev and 2.6 Mev gamma rays were investigated as a function of their position in the crystal. The results for the 0.67 Mev  $\text{Cs}^{137}$  gamma ray are shown in Figs. 12 and 13. Figure 12 shows the longitudinal dependence of the light created by the gammas passing through a  $\frac{3}{8}$ -in. diameter collimator hole as a function of position in the crystal. The radial dependence (i.e., across a diameter on the aluminum end plate) of pulse height and resolution is shown in Fig. 13.

One of the major concerns with large crystals was the magnitude of the background counting rate. In

order to study the background, the spectrometer was shielded with 4 in. of lead on all sides and the differential pulse height spectrum of Fig. 14 was obtained. The peak at 1.45 Mev<sup>23</sup> was found to be due to the  $\text{K}^{40}$  in the glass plate that was used in sealing the crystal into the can. For almost all of the radioactive source experiments, the magnitude of the background was tolerable. For betatron experiments, the background is completely negligible because of the time gating that is used.

Figures 15-25 show the pulse height distributions that were obtained by the use of  $\text{Cd}^{109}$ ,  $\text{Hg}^{203}$ ,  $\text{Ba}^{132}$ ,  $\text{Cs}^{137}$ ,  $\text{Zn}^{66}$ ,  $\text{Co}^{60}$ , a uranium ore sample, a Th-Ra sample,  $\text{Po}-\alpha\text{-Be}$ ,  $\text{B}^{11}(p,\gamma)\text{C}^{12}$ , and  $\text{Li}^7(p,\gamma)\text{Be}^8$ . These distributions display the operating characteristics of the large-crystal, sodium-iodide spectrometer in the

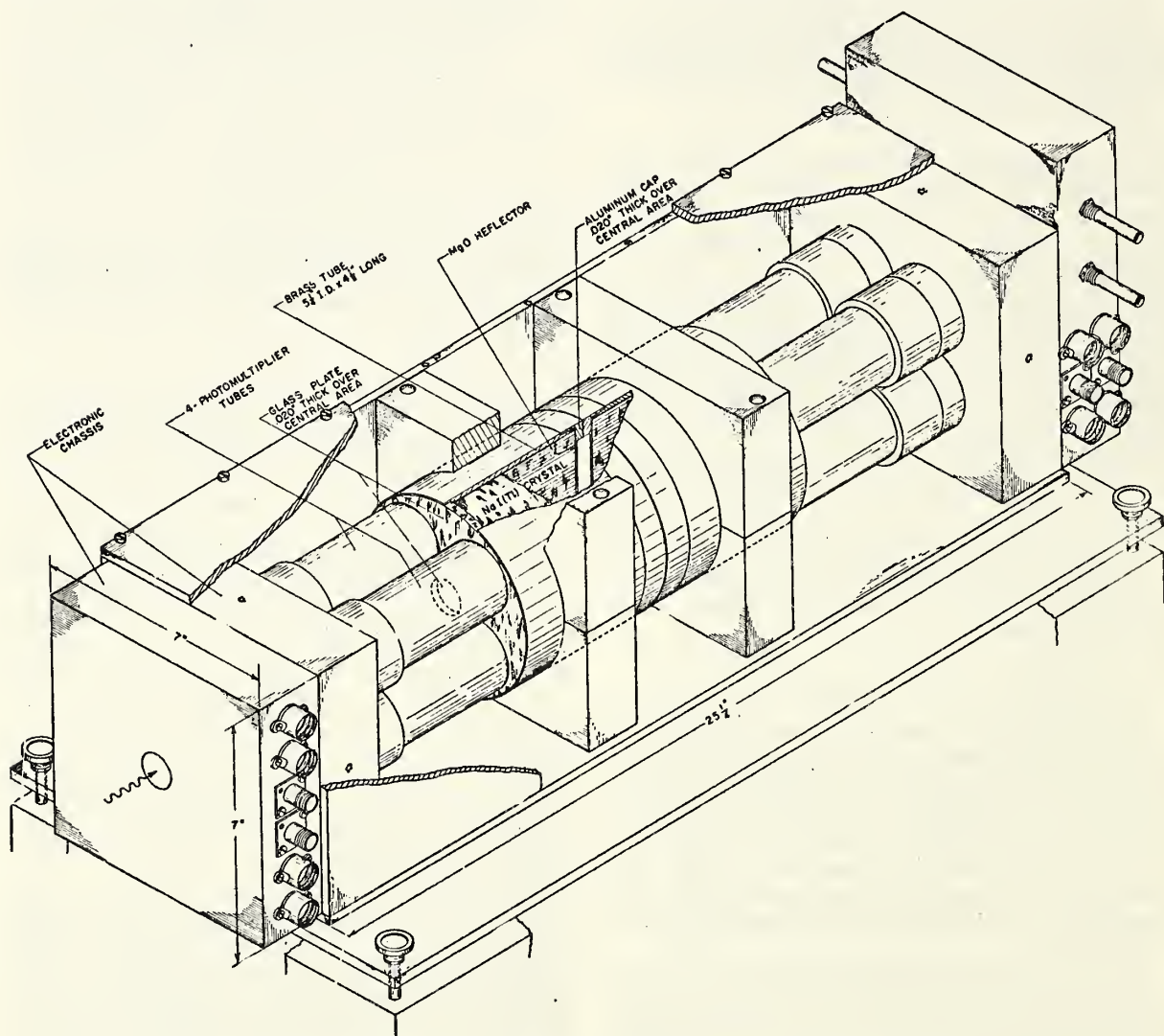


FIG. 10. A 5-in. diameter by 8-in. long NaI(Tl) total absorption x-ray spectrometer.

<sup>23</sup> K. Way et al., *Nuclear Data Table* (National Bureau of Standards, Washington, D. C., 1950), circular 499.

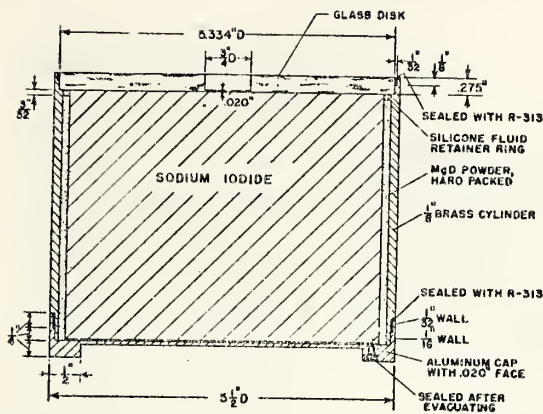


Fig. 11. A 5-in. diameter by 4-in. long NaI(Tl) crystal container. The glass disk was thinned to 0.020 in. to reduce x-ray absorption.

energy range from 87 kev to 17.6 Mev. The most obvious qualitative characteristics of the distributions of Figs. 15-25 are the predominant peaks and the small numbers of pulses at low pulse height. These characteristics are to be contrasted with the results obtainable with small crystals, where separate peaks due to the Compton, pair, and photoelectric effects result from one monoenergetic gamma line.

For the x-ray energies below 2.6 Mev, the data were obtained with a 5 in. diameter by 4 in. long NaI(Tl) spectrometer. Exactly similar data would be obtainable with a 5 in. diameter by 8 in. long crystal, since the pulse height distribution and energy resolution at these energies are determined almost entirely by statistical fluctuations as will be shown later.

The first indication that the energy resolution at low energies was limited primarily by statistical fluctuations was obtained from the linearity of a plot

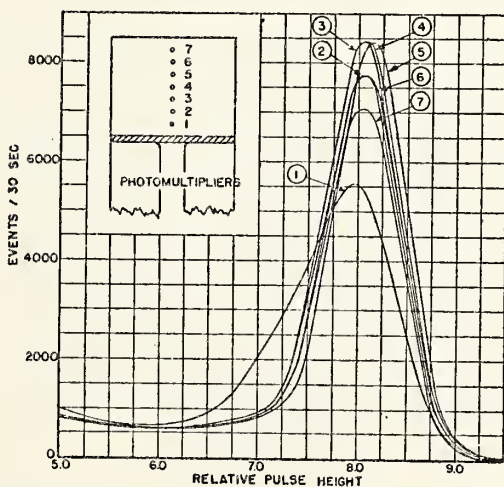


Fig. 12. The longitudinal dependence of pulse height versus source position along the wall of the 5-in. diameter by 4-in. long NaI(Tl) crystal using the gamma rays from Cs<sup>137</sup>. The beam aperture was a 3/8-in. hole in an 8-in. thick lead wall.

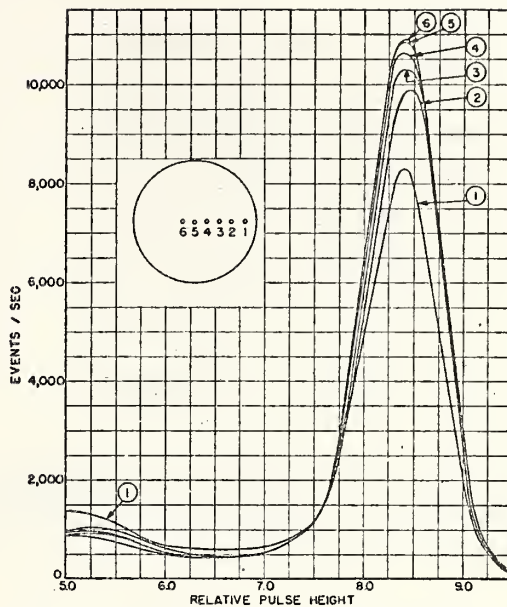


Fig. 13. The radial dependence of pulse height versus position across the end cap of the 5-in. diameter by 4-in. long NaI(Tl) crystal using Cs<sup>137</sup> gamma rays. The beam aperture was a 3/8-in. hole in an 8-in. thick lead wall.

of the position of the most probable pulse height versus gamma ray energy. After corrections for window width of the single channel pulse height discriminator, the position was shown to be a linear function of the energy by the plot of Fig. 26.

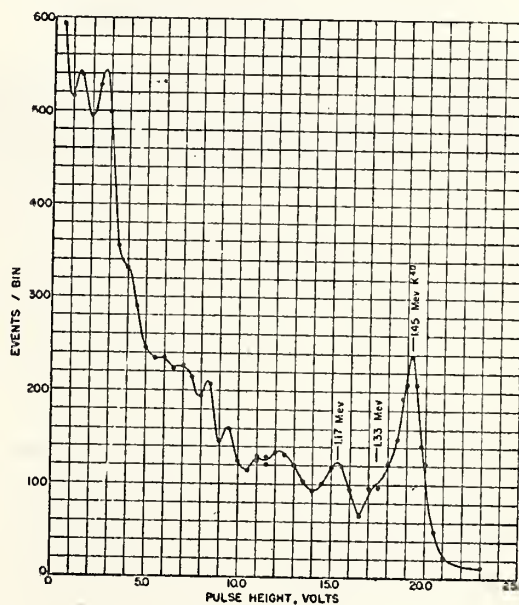


Fig. 14. The pulse height distribution produced by background in a 5-in. diameter by 4-in. long NaI(Tl) crystal, surrounded by a 4-in. wall of lead. The bin width was 0.30 volt as set by the single-channel analyzer. The counting time was 4 min per bin. The K<sup>40</sup> contamination was found to be in the glass disk. Integral counts above 0.5 volt were approximately 19 000 events in 4 min.

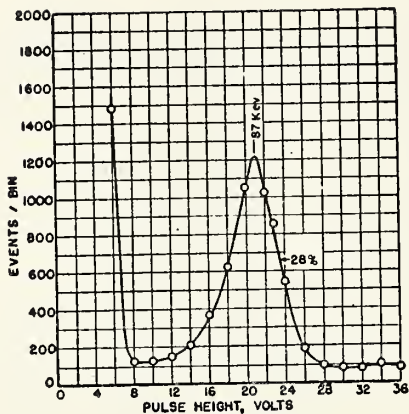


FIG. 15. The pulse height distribution produced by gamma rays from  $\text{Cd}^{109}$  using a 5-in. diameter by 4-in. long NaI(Tl) spectrometer. The bin width as set by the single channel analyzer was 0.30 volt. Counting time per bin was 30 seconds. The beam aperture was a  $\frac{1}{2}$ -in. hole in a 1-in. lead wall.

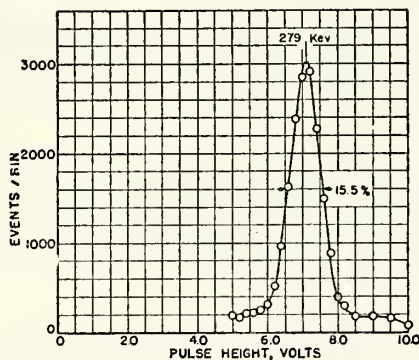


FIG. 16. The pulse height distribution produced by the gamma rays from  $\text{Hg}^{203}$  using a 5-in. diameter by 4-in. long NaI(Tl) spectrometer. The bin width as set by the single channel analyzer was 0.30 volt. The counting time per bin was 30 seconds. The beam aperture was a  $\frac{3}{8}$ -in. hole in an 8-in. lead wall.

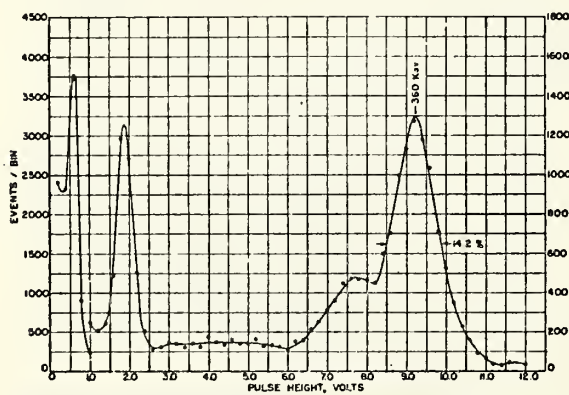


FIG. 17. The pulse height distribution produced by the gamma rays from  $\text{Ba}^{133}$  using a 5-in. diameter by 4-in. long NaI(Tl) spectrometer. The bin width as set by the single channel analyzer was 0.30 volt. The counting time per bin was 30 seconds. The beam aperture was a  $\frac{3}{8}$ -in. hole in a 1-in. lead wall.

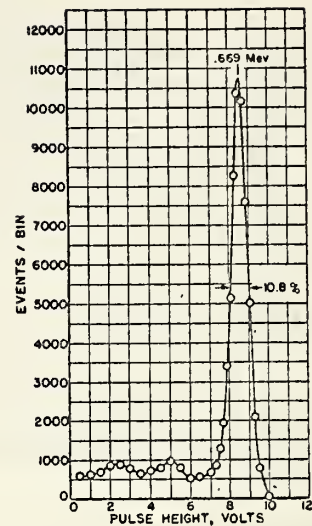


FIG. 18. The pulse height distribution produced by the gamma rays from  $\text{Cs}^{137}$  using a 5-in. diameter by 4-in. long NaI(Tl) spectrometer. The bin width as set by the single channel analyzer was 0.30 volt. The counting time per bin was 30 seconds. The beam aperture was a  $\frac{3}{8}$ -in. hole in an 8-in. thick lead wall.

The experimental data for x-ray energies above 2.6 Mev were obtained with monoenergetic lines that were

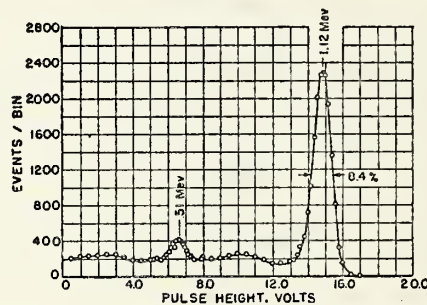


FIG. 19. The pulse height distribution produced by the gamma rays from  $\text{Zn}^{65}$  using a 5-in. diameter by 4-in. long NaI(Tl) spectrometer. The bin width set by the single channel analyzer was 0.30 volt. The counting time per bin was 30 seconds. The beam aperture was a  $\frac{3}{8}$ -in. hole in an 8-in. lead wall.

available only with low intensities. Consequently, poor geometries were used in order to obtain practical

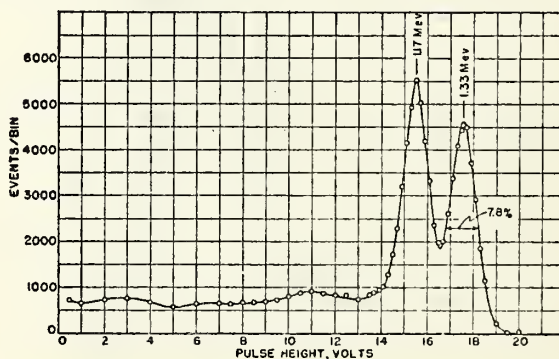


FIG. 20. The pulse height distribution produced by the gamma rays from  $\text{Co}^{60}$  using a 5-in. diameter by 4-in. long NaI(Tl) spectrometer. The bin width as determined by the single channel analyzer was 0.30 volt. The counting time per bin was 30 seconds. The beam aperture was a  $\frac{3}{8}$ -in. hole in an 8-in. thick lead wall.

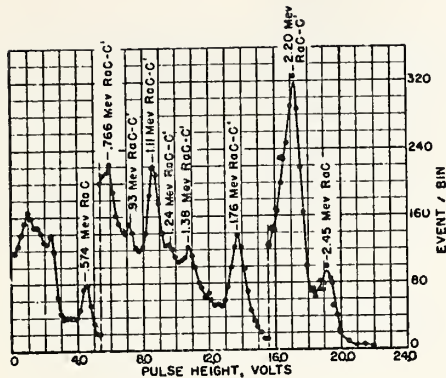


FIG. 21. The pulse height distribution produced by the gamma rays from a uranium ore sample using a 5-in. diameter by 4-in. long NaI(Tl) spectrometer. The bin width was set by the single channel analyzer with a window width of 0.30 volt. Counting time per bin was 30 seconds. The source was positioned on the aluminum end cap of the spectrometer crystal.

counting rates. The poor geometry resulted in the irradiation of a cylinder of a large diameter on the axis of the spectrometer crystal. In order to compare the 4.45-Mev to 17.6-Mev data with the low energy data, corrections must be applied to the high energy data to an idealized irradiation of the central axis of the crystal.

For example, the 4.45-Mev pulse height spectrum of Fig. 23B was obtained with a 15-curie Po- $\alpha$ -Be neutron source whose x-ray intensity was small. As a result, a large lead aperture was used in the shielding wall which permitted the irradiation of a 1.5-in. diameter circle at a 2-in. depth in the spectrometer crystal. If the x-rays were limited to a fine pencil on the axis of the crystal, the first annihilation subpeak would be reduced, and the width of the major peak would be reduced from an energy resolution of 8.6 percent to 6.8 percent. The reduction factor was

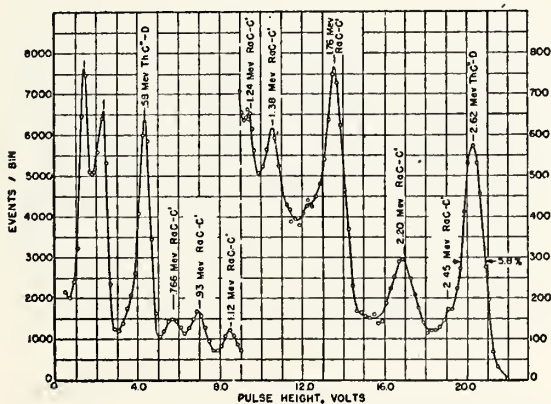


FIG. 22. The pulse height distribution produced by the gamma rays from a sample of thorium-radium using a 5-in. diameter by 4-in. long NaI(Tl) spectrometer. The bin width was set by the single channel analyzer with a window width of 0.30 volt. Counting time per bin was 30 seconds. The beam aperture was a 3/8-in. hole in an 8-in. lead wall.

obtained from an application of the factors in Table I, which supply the effect of the crystal diameter on the energy resolution.

A similar correction resulting from poor geometries must be applied to the B<sup>11</sup>(*p*, $\gamma$ ) and the Li<sup>7</sup>(*p*, $\gamma$ ) data. Both of these experiments were made with a geometry, which resulted in the irradiation of a 1-in. diameter circle at a 2-in. depth in the crystal. With a better geometry, the 11.3 percent resolution at 11.6 Mev (Fig. 24B) would become 8.7 percent, while the 10.4 percent resolution at 17.6 Mev (Fig. 25B) would become 7.8 percent.

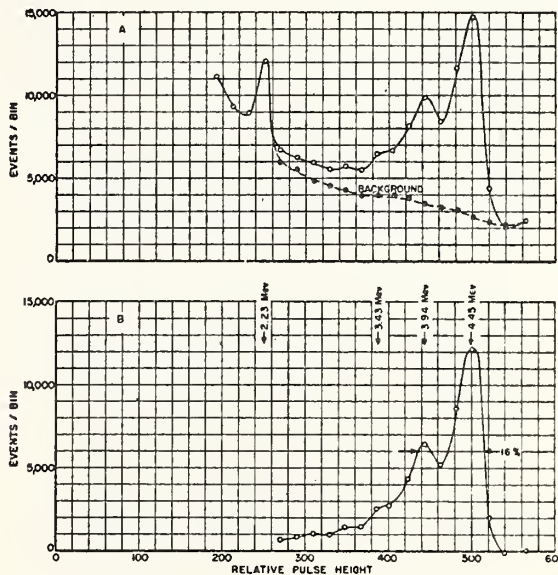


FIG. 23. The pulse height distribution produced by the gamma rays from a 15-curie Po-Be source using a 5-in. diameter by 8-in. long NaI(Tl) spectrometer. The source was imbedded at the center of a cylinder of water with a radius of 11 in. The beam aperture was 1-in. hole in an 8-in. lead wall. The maximum at 3.94 Mev represents those photon cascades from which one annihilation quantum of 0.51 Mev has escaped from the crystal. The smaller peak at 3.43 Mev resulted from the escape of two annihilation quanta and is less pronounced than the 3.94-Mev peak because of the smaller probability that two oppositely directed photons will escape. The 2.23-Mev line resulted from neutron capture by the hydrogen in the water shield. The bin width was 20 scale divisions. The data were obtained with a 20-channel differential analyzer in a counting time of 4 min. A similar time was used to measure the background.

The corrected energy resolutions for the high energy lines are summarized with the low energy values in Fig. 27. The values at 16 and 40 Mev were obtained by correcting the Monte Carlo results of Fig. 3 by the use of the factors in Table I. Estimated uncertainties are given on the points which apply to energies below 2.6 Mev. Similar uncertainties were not estimated for the high energy points.

The energy resolution for the x-ray energies below 2.6 Mev is limited largely by the statistical fluctuations in the light photons from the crystal that are detected by the photomultipliers. This is illustrated by curve

A (Fig. 27), which is a plot of the statistical fluctuation function,  $1/(E)^{1/2}$  normalized at the 87-kev point.

The energy resolution contribution caused by energy loss from the crystal, curve B, can be derived from the energy resolution determined experimentally. It was assumed that the statistical contribution and the energy loss contribution are independent. Therefore, the experimental resolution will be the square root of the sum of the squares of the two percent contributions.

Below 200 kev, curve B is zero, since the x-rays are absorbed entirely by the photoelectric effect. Between 200 kev and 2 Mev, the energy loss results primarily from the backscattering of a Compton photon out of the front face of the crystal spectrometer. Little

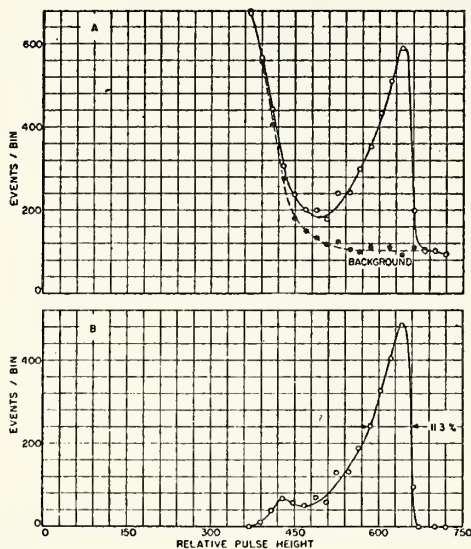


FIG. 24. Curve A. The pulse height distribution produced by the 11.6-Mev gamma rays from  $B^{11}(\beta, \gamma)C^{12}$  plus background using a 5-in. diameter by 8-in. long NaI(Tl) spectrometer. The data were obtained with a 20-channel differential analyzer whose bin width was 20 scale divisions. The counting time was one hour and 16 min for each of the curves. The beam aperture was a  $\frac{3}{8}$ -in. hole in an 8-in. lead wall. The source to lead-wall distance was 5 in. Curve B. The data of curve A with background subtracted. Some evidence for a subpeak at 615 divisions caused by the escape of one annihilation quantum was found in measurements made by dot photography of voltage pulses on an oscilloscope face.

radiation leaks out of the sides of the crystal because in this energy range the lateral radiation will be absorbed quickly with an absorption coefficient of approximately 400 kev radiation. At energies above 2 Mev, the lateral radiation is composed of annihilation radiation and x-ray energies with a mean value about 1 Mev. The increased penetrability of these radiations accounts primarily for the sharp rise of curve B above 2 Mev.

Curves A and B of Fig. 27 suggest possible improvements that could be made in the total absorption spectrometer used in the present experiments. Improved light collection and conversion efficiencies could reduce

the magnitude of the statistical fluctuations, of curve A, by no more than a factor of 2. This specific factor is based on experiences of this and other laboratories with small sodium iodide crystals.

In the energy range from 200 kev to 2 Mev, the energy resolution could be improved by the use of a radiation trap on the crystal face in order to prevent

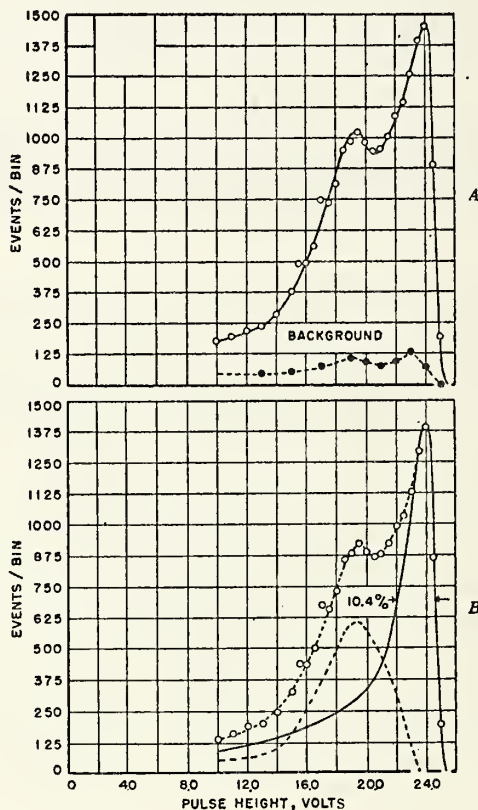


FIG. 25. Curve A. The pulse height distribution produced by the 14.8-Mev and 17.6-Mev gamma rays from  $Li^7(\beta, \gamma)Be^8$  plus background using a 5-in. diameter by 8-in. long NaI(Tl) spectrometer. The protons were accelerated to 915 kev at a beam current of 20 microamperes. The lithium target was thick and was viewed at  $90^\circ$  to the proton beam. Under these conditions, the ratio of the intensities of the narrow 17.6-Mev line to the broad 14.8-Mev line should be 1.6 [M. B. Stearns and B. D. McDaniel, Phys. Rev. 82, 450 (1951)]. The data were obtained with a single-channel discriminator whose bin width was 0.3 volt. The counting time per bin was 2 min. The beam aperture was a  $\frac{3}{8}$ -in. hole in an 8-in. lead wall. Curve B. The data of curve A with background subtracted. The shape of the pulse height distribution produced by the 17.6-Mev gamma rays (solid curve) was obtained by adjusting the ratio of the areas produced by the two lines to equal a value of 1.6.

the escape of backscattered Compton x-rays from the front face of the crystal.

Loss of energy out of the sides and end of the spectrometer crystal determine the energy resolution above 2 Mev. This contribution could be reduced by increasing the crystal size according to the guide provided by the data of Tables I and II. Also, improvement in the

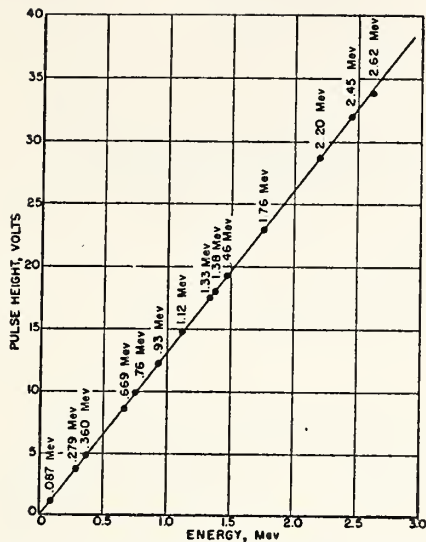


FIG. 26. Linearity of pulse height in volts *versus* the gamma ray energy in Mev as determined from Figs. 15 through 22.

energy resolution and a reduction in the number of pulses that appear below the main peak of a pulse height distribution should be obtainable by setting the subcrystals along the spectrometer length in coincidence.

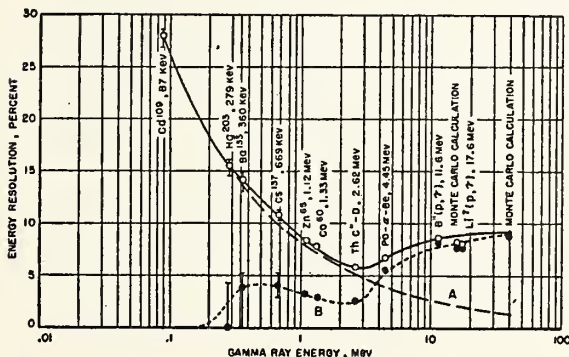


FIG. 27. The percent energy resolution (solid curve) as a function of the gamma ray energy as obtainable with a 5-in. diameter by 8-in. long NaI(Tl) spectrometer. These resolutions were determined from the data of Figs. 15-25. The resolution was analyzed into the percent contribution due to statistical fluctuations (curve A) and the percent contribution due to energy loss from the crystal (curve B).

## DISCUSSION

The discussion of spectrometers in this report has stressed the experiments and general usefulness of the large sodium iodide crystal spectrometer. This spectrometer with the aid of simple electronic circuitry such as photomultipliers, one high voltage power supply, and one linear amplifier provides voltage pulses that are approximately proportional to the absorbed x-ray energy in the range from 100 keV to 50 MeV. The availability of good quality, large crystals made this work possible.

The description of the xylene work has not been emphasized because the spectrometer as shown in Fig. 1 was a preliminary design on which many improvements are possible. The unit as built should have energy resolutions of the order of 10 percent at energies above 15 MeV, and might prove useful. However, the energy resolution below 15 MeV is poor, and is limited by the statistical fluctuations in the light photons detected by the photomultipliers and by the energy leakage out of the sides of the xylene bath.

The principal advantage of the xylene spectrometer would be in the fast time constant of  $2 \times 10^{-9}$  sec of the xylene compared to that for sodium iodide of 0.25 microsecond. For some applications, the danger of discoloring the solid crystal by radiation damage might also be regarded as an advantage of the xylene since it would not be discolored locally.

## ACKNOWLEDGMENT

We wish to acknowledge our indebtedness for the many important contributions to this investigation. M. L. Cleland helped in the initial stages of the work in the experiments with the xylene spectrometer. C. MacCallum, a summer student in our laboratory, performed the Monte Carlo calculations for NaI that were described in Fig. 3. L. B. Mortara was invaluable in obtaining the data for many of the figures.

The data with the  $\text{Li}^7(p,\gamma)$  rays were obtained with an accelerator at the Department of Terrestrial Magnetism, which was kindly made available by N. P. Heydenburg. The 20-channel differential analyzer, the  $\text{Bi}^{214}(p,\gamma)$  and  $\text{Po}-\alpha$ -Be sources were facilities of the Naval Research Laboratory, which were used through the courtesy of C. V. Strain, W. R. Faust, and J. O. Elliott.



## Abstract

X-Ray Attenuation Coefficients from 15 to 80 Mev  
for Hydrogen, Carbon, Water and Aluminum

by

J.M. Wyckoff and H.W. Koch  
National Bureau of Standards

The X-ray attenuation coefficients for hydrogen, carbon, water, and aluminum have been measured in the energy range from 15 to 80 Mev. Varying lengths of the attenuators were placed in a 90 Mev bremsstrahlung beam in a good geometry experiment using a large sodium-iodide total-absorption spectrometer as the detector. In the hydrogen case, a difference method employing cyclohexane ( $C_6H_{12}$ ) and graphite was used. The theoretical attenuation coefficients, due to electronic processes, were calculated using selected Compton and triplet cross sections in addition to the small quasi-deuteron cross sections. A pair cross section increase of 2.25% was required for carbon, water and aluminum to bring the total calculated coefficients into agreement with the measured coefficients in the 60 Mev region. The difference between these calculated cross sections and the measured cross sections in the 15 to 50 Mev region has been ascribed to the giant resonance nuclear absorption. A larger high energy tail to this absorption than predicted by  $(\gamma, p)$  and  $(\gamma, n)$  experiments is indicated.

X-Ray Attenuation Coefficients from 15 to 80 Mev  
for Hydrogen, Carbon, Water and Aluminum

by

J.M. Wyckoff and H.W. Koch  
National Bureau of Standards

Introduction

The paper by G. W. Grodstein<sup>1/</sup> summarized the theoretical and experimental situation on high energy and narrow beam attenuation coefficients up to 1957. The theoretical coefficients in the 2 to 100 Mev X-ray range were adjusted to fit the experimental data, in order to account for the inaccuracies<sup>2/</sup> of the Born-approximation pair coefficients for elements with high atomic numbers (Z). However, the Grodstein summary listed a prediction of the total coefficients for low Z elements which were lower than the pair spectrometer measurements of Lawson<sup>3/</sup> at 88 Mev by 4% for copper and aluminum. The recent measurements of Moffatt et al<sup>4,5/</sup> agree with the Lawson results and used the tip of a bremsstrahlung spectrum for total attenuation measurements at 94, 68, and 42 Mev.

In the present experiment<sup>6/</sup>, the entire 90 Mev bremsstrahlung spectrum from a synchrotron was measured with a sodium-iodide spectrometer in a good-geometry experiment for photon energies from 15 to 80 Mev. The use of this spectrometer combined with the high intensity synchrotron beam made it possible to attenuate the primary X-rays by a factor of over 10,000 with a resulting enhancement of the effect of small changes in the attenuation coefficient. Consequently, the coefficients should be accurate to  $\pm 0.9\%$  in the region of 30 to 80 Mev with somewhat greater uncertainties in the 15 to 30 Mev region for carbon, water and aluminum.

In principle, the broad energy range from 15 to 80 Mev allowed separate evaluation of the electronic and nuclear attenuation processes in those regions where they were important. The particular choice of low-Z absorbers was made in order to emphasize the nuclear absorption as well as make possible an accurate measurement of the electronic attenuation in the 30 to 80 Mev region where it was changing only slowly with energy. The results are shown to be in good quantitative agreement with those of Moffatt et al. Comparisons are also made with theoretical predictions and with measurements of the aluminum nuclear attenuation by techniques similar to the present one made by Ziegler<sup>7/</sup>, Kochum and Starfelt<sup>8/</sup>, and Mihailovic et al<sup>9/</sup>.

## II. Experimental Arrangement

Fig. 1 shows the geometry as well as the measuring equipment used. The source of the X-rays was a 180 Mev synchrotron that was operated at 90 Mev for most of the experiments giving good attenuation measurements up to 80 Mev. A few experiments at 35 Mev gave pulse height distributions that were very sensitive to the nuclear absorption cross sections in the giant resonance region.

A primary collimator 0.30" in diameter was located such that a beam 0.70" in diameter impinged on the attenuator. The attenuator characteristics are listed in Table 1. A secondary collimator following the attenuator was 0.59" in diameter and was located to restrict the beam striking the 5" diameter by 9" long sodium-iodide, spectrometer<sup>10/</sup> to 0.88" in diameter.

The beam was monitored by a multiplate, thin-walled, transmission ionization chamber. Temperature regulation of the chamber batteries minimized drifts in the vibrating reed electrometer used to measure the collected charge though small corrections were required for experiments with very low X-ray intensities.

The signal from the photo-multiplier was fed via a cathode follower to a core memory type, 256 channel, pulse height analyzer. The stability of this device against drift in channel width and base line was tested daily and proved to be very good. The circuit of the analyzer and the 200 microsecond long synchrotron burst prevented pile-up of spectrometer pulses so that the distortion in the experimental pulse height distributions obtained from the spectrometer was negligible at the running rates of about two counts per synchrotron X-ray burst. A separate fast discriminator and scaler were used with a relatively small and known deadtime to determine the normalization constant of counts per charge. The spectrometer signal was gated to reduce the background of pulses that occurred at times between the synchrotron X-ray bursts.

A series of separate experiments made it possible to calculate and correct for the response functions of the spectrometer as discussed by Koch and Wyckoff<sup>11/</sup>. These results were used to construct a 56 element by 56 element matrix describing the response functions that was encoded for use on an electronic computer. The application of this matrix will be discussed in the next section.

### III. Data and Results

Fig. 2 gives the pulse height distributions as plotted by the pen recorder on the output of the analyzer for three different lengths of carbon. The first step in analyzing these data was to correct for unequal analyzer channel width (a maximum of 9%) and for background. The data were then normalized to a given ionization charge collected on the plates of the monitor chamber. The results are given in Fig. 3. An uncorrected attenuation coefficient may be calculated for each analyzer channel with these data. These coefficients reflect a weighted average of the attenuation coefficients in a broad energy band, since a family of energies, as shown in Fig. 4, contribute to the counts in any given analyzer channel due to the shape of the spectrometer response functions. The correction for this detector response was small at most energies but required a fairly detailed evaluation.

The definition and the determination of the correction factor can be understood from the definition of the attenuation coefficient,  $\tilde{\tau}$ , in  $\text{cm}^2/\text{g}$  by the equation:

$$\tilde{\tau}_I = \ln(I_{\text{in}}/I_{\text{out}}) / \rho x, \quad (1)$$

where  $I$  is the number of photons,  $\rho$  the density in  $\text{gm}/\text{cc}$ , and  $x$  is the length of the attenuator in centimeters. The correction factor,  $A$ , to obtain this attenuation coefficient from the uncorrected attenuation coefficient,  $\tilde{\tau}_c$ , is defined by:

$$A = \frac{\tilde{\tau}_I}{\tilde{\tau}_c} = \frac{\tilde{\tau}_I}{\ln(C_{\text{in}}/C_{\text{out}}) / \rho x} \quad (2)$$

where the denominator contains a ratio of counts,  $C_{\text{in}}/C_{\text{out}}$ , in place of the ratio of photons in Equation (1).  $A$  was calculated from an estimated attenuation coefficient,  $\tilde{\tau}_I$ , and from the ratio of counts obtained from predicted pulse height distributions. The predicted distributions for a given attenuator were computed from an assumed bremsstrahlung spectrum, the  $\tilde{\tau}_I$ , and the response function matrix. The correction factor for carbon as well as the other attenuators is shown in Fig. 5. It is seen that the correction factors do reflect the assumed nuclear cross sections. Fortunately, the factors are small ratios even at the giant resonance energies, and, therefore, are relatively insensitive to the assumptions on spectra, attenuation coefficients, and response-function shapes. The application of the factors for carbon to the uncorrected attenuation coefficients obtained from Fig. 3 results in the fully corrected attenuation coefficients for carbon shown in Fig. 6.

As shown in Table 1, the experimental effort emphasized carbon for which seven different lengths were used. A least-squares fit to the logarithm of the resulting experimental counts versus carbon length gave uncorrected ratios of counts per channel that were well determined.

The experiments with other attenuators were referred to the pulse height distributions obtained with one specific length of carbon in order to improve the accuracy. The data obtained with the reference length of carbon was used to determine the zero-attenuator distributions by means of the detailed carbon experiments. This procedure made it unnecessary to measure the pulse height distribution for an unfiltered X-ray beam in terms of an absolute monitor current. The drift corrections to this monitor current would have been large and would have made the measurements difficult. Consideration of this method will show that the attenuation coefficients of water and aluminum are almost independent of the carbon uncertainties in density, lengths, or assumed attenuation coefficients.

The procedure for hydrogen was slightly different than that for the other materials. The hydrogen attenuation coefficient was obtained from a ratio of the photons transmitted by carbon and cyclohexane ( $C_6H_{12}$ ) attenuators containing the same number of carbon atoms. The difference in the attenuators was  $82.7 \text{ g/cm}^2$  of hydrogen. Although this length was equivalent to 11.8 meters of liquid hydrogen, it was much less in  $\text{g/cm}^2$  than the length of the other attenuators used. The probable accuracy of the hydrogen results is less than that for the other attenuators because of the small length of hydrogen, the poorer statistical accuracy in a subtraction method involving two large quantities, and the relatively rapid change in the attenuation coefficient with energy.

The fully corrected experimental coefficients for hydrogen, carbon, water, and aluminum are tabulated in Table II and shown in Fig. 7(a), (b), (c), and (d). A predicted coefficient that will be discussed in the next section is also drawn on these figures.

An additional method of determining the coefficient was the detailed prediction of the shapes of pulse height distributions produced by X-rays transmitted by one particular length of absorber. The predictions allowed a sensitive test of the magnitude and a test of the shape, within limitations imposed by the resolutions of the spectrometer, of the giant resonance nuclear cross sections around 20 Mev. For these tests, the synchrotron was operated at about 35 Mev to produce pulse height distributions of very excellent counting statistics. The results without

an attenuator are shown in Fig. 8 and are compared with a predicted curve. Experiments were performed with this same 35 Mev bremsstrahlung spectrum with an absorber of  $351.5 \text{ g/cm}^2$  of carbon and the results are plotted in Fig. 9. The comparisons in Figs. 8 and 9 with the predicted spectrum are good and justify the assumptions to be discussed in section VI-D.

#### IV. Estimate of Errors in the Experimental Attenuation Coefficients.

Examples of the magnitudes of the major sources of error are given in Table III for hydrogen and carbon. The statistical errors in standard deviations have been multiplied by 3 to convert them to maximum errors in order to combine the errors by quadrature with the systematic errors. The systematic errors are inherently maximum error estimates.

As can be seen from the table, the density correction has introduced a large uncertainty. The nonuniformities in the graphite attenuator rods were investigated for us by C. T. Collett of the NBS Density group who had one sample rod cut into six sections longitudinally. Three of these sections were turned down from 2" diameter to 1.25" and then to 3/4" diameter. The longitudinal variations in density of less than 0.6% did not affect the measured attenuation. However, the central zone through which the X-rays passed had a mean density of 1.6637 compared to 1.6640 for the 1.25" sample and 1.6809 for the full 2" sample. Thus a 1.0% correction was applied to the gross density measurements of the graphite rods with an uncertainty of  $\pm 0.2\%$  estimated to account for nonuniformity from rod to rod. The density determination for the aluminum attenuator had an assigned uncertainty of  $\pm 0.002\%$ . Due to the "difference method" used for the measurements of the hydrogen coefficient, the uncertainty due to the carbon density had a large effect on this particular coefficient.

The uncertainties in the attenuation coefficient due to uncertainties in the response-function correction factor were taken to be 1/5 of the percentage correction factor with a minimum of 0.2%. Even though a separate calculation is given for the energies below 30 Mev, it should be cautioned that the uncertainties in the giant resonance region are difficult to estimate. For these energies, the uncertainties due to the energy assignments and the effects of fine structure in the cross section values could be particularly large.

The small sources of error of recombination in the monitor chamber and inscattering effects for the present geometry are grouped as one item. Uncertainties introduced by electrometer drift, channel width changes, electrometer condenser measurement, liquid temperature corrections and attenuator material impurities were negligible.

#### V. Predictions of the Total Attenuation Coefficients.

The predictions of Tables IV(a) and (b) that are shown in Figures 7(a), (b), (c) and (d) will be described in detail in this section. The major attenuation processes from 30 to 80 Mev - pair production, triplet production, Compton scattering and nuclear absorption by the quasi-deuteron process - are discussed in part A. At these energies, other nuclear processes should be unimportant. The nuclear processes that are important in the giant resonance region around 20 Mev will be discussed in part B.

##### A. Electronic and Quasi-deuteron Contributions

###### 1. Pair Production

The major contribution to the total cross section for carbon, water and aluminum is pair production. Calculations of this cross section for non-screened atoms were made by using Bethe-Ashkin's<sup>12/</sup> Formula 110, originally derived by Bethe-Heitler<sup>13/</sup>. This formula gives cross sections for carbon in millibarns that are 76.28 (10 Mev), 110.08 (15 Mev), 117.14 (20 Mev), 141.48 (30 Mev), 161.13 (40 Mev), 174.96 (50 Mev), 186.23 (60 Mev), 204.41 (80 Mev), and 218.74 (100 Mev). Other materials go as the ratio of their  $Z^2$  values. These values should be more accurate and at 60 Mev are about 1% below those that are evaluated by removing the Thomas-Fermi screening from the simpler expression, Bethe-Ashkin's<sup>12/</sup> Formula 114.

The pair cross section listed for hydrogen was calculated using Formula 114. A comparison of the 60 Mev result with a more accurate Formula 110 calculation with a screening correction showed the results listed here to be about 1% low. As the pair contribution to the hydrogen cross section was small this was considered acceptable. No correction was made for effects on the hydrogen coefficient of the cyclohexane molecular binding since the correction is negligible. These effects will reduce the screening correction which is only 1% at 60 Mev.

Two corrections to the non-screened cross sections for other attenuators must be considered. The Coulomb correction of Davies, Bethe, and Maximon<sup>2/</sup> has been applied and is everywhere below 0.4%. The screening correction was based on the form factor obtained from the Hartree self-consistent-field model<sup>14/,15/</sup>. This correction makes the pair cross section at 60 Mev for carbon larger by 0.5% than that obtained from a Thomas-Fermi screening correction.

As is noted in Table IV(a), the corrected pair cross sections for carbon, oxygen and aluminum were multiplied by a constant  $K = 1.0225$ . This constant was justified by comparing the experimental counts per charge for lengths of carbon and aluminum containing equal numbers of electrons. The ratio of the transmitted X-ray intensities should depend only on the difference of the pair cross sections of these materials, since the Z-dependent cross sections for the Compton, triplet and quasi-deuteron processes and their corrections should drop out. A correction for the detector response function was required to convert the ratio of the counts to the ratio of the photons measured. It was found that at 60 Mev an increase of more than 2% to both the carbon and aluminum theoretical pair cross sections was required in order to predict the experimental ratio of photons. This experiment suggested that the pair cross section is the major one to be modified in order to provide a consistent check with the experimental total attenuation coefficients.

## 2. Triplet Production

Pair production in the field of the atomic electrons (triplets) has a cross section that is only about  $1/Z$  times the nuclear pair cross section. However, the differences between the various theoretical predictions of this process, as shown in Fig. 10, are of the order of 30%. Therefore, the uncertainties in predicting the total attenuation cross sections for hydrogen, carbon, water, and aluminum are large. Joseph and Rohrlich<sup>16/</sup> summarize the status of the theory and suggest that the true cross section for free electrons should be between the

Borsellino triplet estimate<sup>17/</sup> as an upper limit and the Votruba calculation<sup>18/</sup> as a lower limit. Experiments by Malamud<sup>19/</sup> and calculation by Suh and Bethe<sup>20/</sup> indicate a closer agreement with the Borsellino values at high energies. Although the experiment of Moffatt and Weeks<sup>5/</sup> gave somewhat lower results, the recent diffusion cloud chamber experiment of E. L. Hart et al<sup>21/</sup> yields results that are consistent with the Borsellino or Wheeler and Lamb<sup>22/</sup> triplet cross sections at energies of 10 to 100 Mev in hydrogen. The triplet cross sections of Borsellino were used in the present report in obtaining a predicted total cross section.

### 3. Compton Scattering

The cross section included for this process was calculated by the Klein-Nishina formula for free electrons as tabulated in NBS Circular 583<sup>1/</sup>.

### 4. Photoelectric and Other Electronic Attenuation Processes

No electronic processes other than those discussed above were included in the theoretical prediction. Most of the additional effects are either small or could not be included properly. For example, (a) the photoelectric cross section is  $2.4 \times 10^{-31} \text{ cm}^2$  per atom for carbon at 15 Mev which is negligibly small; and (b) the Delbruck scattering cross section is about  $10^{-31} \text{ cm}^2$  per atom for aluminum at 60 Mev. Other effects, such as (c) atomic binding effects in the Compton process, and (d) Rayleigh scattering by the atomic electrons are also expected to be small.

The main effects that have not been included adequately are (e) the radiative corrections to the pair and Compton processes including the double Compton process<sup>23/,24/</sup>. These corrections to the differential cross sections in experiments with good energy resolution (of the order of 100 kev) and good geometry will be large. For example, Brown and Feynman<sup>24/</sup> estimate the Compton cross section correction at zero degrees (where the double Compton cross-section is zero) will decrease the cross section by 3.8% at a photon energy of 50 Mev and 5.3% at 150 Mev. Also, Bjorken, Drell, and Frautschi<sup>25/</sup> show that the large-angle pair cross section will have a radiative correction less than 5%. However, in the present experiment, the corrections of interest are those that change the integrated cross-section for removal of photons from the detector.

The present detector arrangement has the characteristics of good geometry but relatively poor energy resolution. For this case, the radiative corrections to the component of the total attenuation cross sections will have a small, but not negligible, influence on the total attenuation cross section.

In spite of the possible importance of the radiative corrections, the predicted attenuation coefficients were calculated without the radiative corrections and without the other electronic processes (a) to (d).

#### 5. Quasi-deuteron Production.

Levinger<sup>26/</sup> has proposed that the quasi-deuteron cross section may be calculated by the formula  $\sigma_{pd} = (6.4 NZ\sigma_d)/A$  for high energies. Barton and Smith<sup>27/</sup> found that this expression was in agreement with their measurements on helium and lithium with 280 Mev bremsstrahlung. Danos<sup>28/</sup> has calculated an approximate quenching factor that reduces this cross section to 40% of this value for carbon at 50 Mev and 30% for aluminum at this energy. Based on Whalin et al<sup>29/</sup> deuteron cross section measurements the quasi-deuteron cross section listed in Table IV-a were calculated using this quenching factor. The relatively small values of this component as well as the variation with Z similar to the triplet cross section makes it difficult to evaluate the correctness of this calculation from this experiment.

#### B. Nuclear Attenuation Processes in the Giant Resonance Region.

The only important nuclear processes<sup>30/</sup> in the energy range from 15 to 40 Mev are those leading to neutron and proton production. Unfortunately, the only complete data on these processes are for carbon. Table V gives the references for this and other materials for which the nuclear cross section has been synthesized. For carbon-12 the photo-proton cross sections used up to 24 Mev which presumably correspond only to ground state transitions in the boron-11, are those given by Cohen, et al<sup>31/</sup>. At energies above 21 Mev it is necessary to include the excited state transitions as measured by Penner and Leiss<sup>32/</sup>. The photo-neutron cross sections measured by Barber, George, and Reagan<sup>33/</sup> by a study of the 20 minute carbon-11 radioactivity automatically include both the ground and excited state transitions. However, the  $(\gamma, 2n)$  cross section with a threshold of 32 Mev would not be included.

The oxygen ( $\gamma$ , p) and ( $\gamma$ , n) data of Cohen et al<sup>31/</sup> and Katz et al<sup>34/</sup> respectively were used in the synthesis of a total nuclear cross section up to 23 Mev. Above 23 Mev the total ( $\gamma$ , p) cross section shape found by Penner and Leiss was normalized to the lower energy data to provide the total nuclear cross section. A similar procedure was followed for aluminum with a normalization at 22.5 Mev. The resulting predictions are marked "synthesis" in Fig. 7 and Fig. 11.

The experimental, nuclear absorption curves shown on these figures result from the shape of the synthesized cross sections below the giant resonance peak. Above this peak, the curves result from a subtraction of the predicted electronic component from the experimental total attenuation coefficient. In addition, the accurate prediction of pulse height distributions, as demonstrated in Fig. 9, was used to define in more detail the shape and magnitude of the total attenuation coefficient in the giant resonance region. For this reason the solid curve drawn as the experimental result in the top of Fig. 7(a), (b), (c), and (d) do not always pass exactly through the experimental points.

## VI. Discussion of Results.

### A. Total Cross Sections in the Energy Range from 30 to 80 Mev.

The most accurate results from this experiment are the total cross sections in the energy range from 30 to 80 Mev where the cross section varies slowly with energy and the spectrometer resolution corrections are small. When a comparison of the experimental points in Fig. 7(a), (b), (c), and (d) are made with the predictions of G. Grodstein<sup>1/</sup> the experimental results are consistently higher. The Grodstein values were obtained with a slightly inaccurate pair cross section, Votruba triplet cross section, and a Klein-Nishina Compton cross section. Each cross section choice will receive comment.

An increase of the pair cross section values, as described in Section VA1, can be justified for three separate reasons. First, the experiment performed with equal lengths of electrons in a carbon and aluminum attenuator required about a 2% increase in the pair cross section values at 60 Mev. Second, the triplet cross section is not a large enough fraction of the total cross section in carbon and aluminum attenuators at 60 Mev to be able to explain the discrepancy between the Grodstein value and the experiment. Therefore the pair cross section is suspect. Third, the high-energy experimental results (60-300 Mev) on total attenuation cross sections summarized by Malamud<sup>19/</sup> are almost all larger by 1 to 3% than the theoretical predictions for high atomic number attenuators where the pair cross sections predominate.

Unfortunately, no theoretical reason is available to explain the 2.25% increase in pair cross section that was used in the present interpretations. Therefore, it was assumed that the increase was independent of energy and it was applied to the pair coefficients for carbon, water, and aluminum. No increase in pair cross section was assumed in the case of hydrogen.

If the increase in the pair cross section is accepted and the validity of the uncorrected Klein-Nishina Compton cross section is assumed, then the remainder cross section may be evaluated as a triplet cross section. This type of comparison has been made in Table VI at 60 Mev for hydrogen, carbon, water, and aluminum. Also listed are each of the calculated triplet cross sections illustrated for carbon in Fig. 10. The conclusion to be drawn from this comparison is that the Votruba triplet cross section is too small and outside the limits of the present interpretations. On the other hand the Borsellino triplet predictions permit a good comparison with the experiment.

The assumption that the Compton cross section is given by the Klein-Nishina formula might be incorrect because of the radiative corrections calculated by Brown and Feynman<sup>24/</sup>. For carbon, water, and aluminum at 60 Mev the Compton cross sections are a relatively small part of the total cross sections. However, the total cross section in hydrogen is predominantly affected by the Compton cross section.

In this case (Fig. 7a), the experimental results are, within the experimental uncertainties, the same as the predicted cross sections obtained with the Klein-Nishina Compton, the Bethe-Heitler pair, and the Borsellino triplet cross sections. Therefore, this result suggests that corrections to the integrated Compton cross section are small.

#### B. Total Cross Sections in the Energy Range of 13 to 18 Mev.

Though the experimental results are about 1% higher than the predictions in this region the large uncertainties, arising from the response function correction factors and energy assignments, make the agreement within the experimental uncertainties. The biggest disagreement is with the recent nuclear detector data of Bergsteinsson et al<sup>37/</sup> who found experimental values at 14 to 20 Mev that were lower than the present experiment; this difference is not presently understood.

#### C. Pulse Height Predictions.

The close agreement between the predicted and measured pulse height distribution in the case where no attenuator is placed before the detector, Fig. 8, is a sensitive test of the combined effects of the assumed Davies, Bethe, Maximon<sup>2/</sup>, bremsstrahlung shape with Hisdal's<sup>38/</sup> target thickness correction and the response function matrix. If the input spectrum and the matrix are proper, then Fig. 9 shows a test of the assumed attenuation coefficients only. Small trial deviations from the experimental nuclear absorption coefficients as plotted on Fig. 7, led to rather large departures from the experimental curve of Fig. 9.

#### D. Nuclear Cross Sections.

The least accurate results from this experiment are the total nuclear attenuation cross sections, since they result from the subtraction of an uncertain electronic contribution from the total attenuation cross section. In addition, the response function of the spectrometer, which has a full width at half maximum of 15% at 22 Mev, cannot be expected to resolve fine structure or rapid variations in the nuclear cross section. However, it is believed significant comments can be made about the differential and integrated cross sections.

The differential nuclear cross sections are given by the curves of Fig. 11 for carbon, oxygen, and aluminum and are labeled "experiment". These cross sections are uncertain by  $\pm 6\%$  and should be systematically in error as a function of the atomic number of the attenuator. For example, the electronic contribution was removed by subtracting the sum of the Compton, triplet, and an increased pair cross section. The factor of increase for the pair cross section was 1.0225. If this factor at 22 Mev should have been smaller then all of the nuclear cross sections would be larger. Therefore, the fact that the carbon cross sections (synthesis and this experiment) at the peak of the giant resonance agree, and that carbon has been examined in great detail by previous experiments, suggests that the discrepancy for oxygen is real. In addition, the increase in the oxygen total nuclear cross section above the synthesized value is consistent with the oxygen scattering results of Garwin and Penfold<sup>39/</sup>.

The differential nuclear cross section for aluminum has been measured at three other laboratories and is shown for comparison with the aluminum results of this experiment in Fig. 12. Mihailović et al<sup>9/</sup> used a Compton spectrometer to measure the spectrum of X-rays transmitted by aluminum attenuators, while Ziegler<sup>7/</sup> used a pair spectrometer. Kochum and Starfelt<sup>8/</sup> used a technique very similar to that used in this experiment. The large differences in cross sections derived at the different laboratories is not understood.

The integrated cross sections obtained from the areas under the cross sections of Fig. 11 can be compared with the predictions of various sum rules. The two theoretical sum rules available are the dipole sum rule of Levinger and Bethe<sup>40/</sup> and the sum rule of Gell-Mann, Goldberger, and Thirring<sup>41/</sup>.

The Levinger-Bethe sum rule is

$$\int_0^{\infty} \sigma \, dk = (0.06 NZ/A) [1 + 0.8x] \text{ Mev-barns} \quad (3)$$

where  $x =$  the fraction of attractive exchange force. This rule is intended to cover only the dipole contributions and the non-mesonic or low energy interactions.

The Gell-Mann, Goldberger, Thirring<sup>41/</sup> sum rule is

$$\int_0^{\infty} \sigma \, dk = (0.06 \text{ NZ/A}) \left[ 1 + (0.1 \text{ A}^2/\text{NZ}) \right] \text{ Mev-barns} \quad (4)$$

and is intended to cover all multipole contributions up to the photomeson threshold to a first-order approximation.

Both sum rules are approximate and give the same predictions for  $x = 0.5$  for carbon, oxygen and aluminum. Table VII compares the predictions with the integrations of the present giant resonance cross sections plus an estimate of the quasi-deuteron contributions up to the meson threshold. The table also shows that a change in the pair correction factor from 1.0225 to 1.03 decreases the integrated carbon cross section by 13%. The assigned uncertainty to the experimental integrated cross section is  $\pm 15\%$ . Therefore, the oxygen and aluminum integrated cross sections may be considered to agree with the theoretical sum rules while the carbon value is somewhat higher than expected.

## VII. Conclusions

The principle on which the present experiment was based was the simultaneous recording of all X-ray energies in a spectrum transmitted by very long absorbers. The simultaneous recording permitted all X-ray energies to be examined at once and reduced the stability requirements on the equipment. The requirements are much less severe, for example, than the requirements with a Compton or pair spectrometer in which one or a few channels are examined at a time. The recording of a whole spectrum has permitted the search for small and unexpected nuclear absorption processes. Thus it is possible to conclude that for carbon, water, and aluminum there are no appreciable unexpected nuclear absorption processes in the 30 to 80 Mev energy range.

The long absorbers that could be used because of the high sensitivity of the sodium iodide spectrometers permitted the accurate determination of attenuation coefficients, particularly when the coefficients varied little with photon energy. The correction factors required due to the response function of the detector though significant were relatively small and thus introduced little error in the calculations.

The greatest uncertainties in the interpretations resulted from the inadequate theoretical information available on the corrections to the Compton, pair and triplet cross sections. These inadequacies prevented a detailed and accurate interpretation of the attenuation coefficients measured in the present experiment. When these inadequacies have been rectified, more reliable data on the total nuclear absorption shapes may be obtained from the present results.

Table I  
Summary of Attenuation Coefficient Experiments

Carbon				
Symbol	Length	Dimensions	Synchrotron energy	Time
	g/cm <sup>2</sup>	inches	Mev	minutes
0	0		90	30
1L Carbon	107.13	2.0 Dia.	90	128
2L Carbon	215.92	2.0	90	133
3L Carbon	306.15	2.0	90	149
4L Carbon	396.82	2.0	90	136
5L Carbon	496.43	2.0	90	114
6L Carbon	604.81	2.0	90	160
7L Carbon	698.86	2.0	90	142
BG Carbon	698.86	2.0	90	14
+ 4"Pb	0		34.2	129
Carbon	351.5	2.0	34.2	654
Aluminum				
Aluminum	427.71	1.5 x 1.625	90	187
Carbon	527.42	2.0 Dia	90	207
Water				
Water	461.50	2.0625 I.D.	90	184
Carbon	527.42	2.0 Dia	90	207
Hydrogen				
Cyclohexane	579.07	2.0625 I.D.	90	236
Carbon	496.43	2.0 Dia	90	114

Liquids were in aluminum tubes; Carbon was in the form of graphite rods; Aluminum was in the form of extruded bars.

Table II

Experimental Attenuation Coefficients in cm<sup>2</sup>/g

Energy, Mev	$\tau_c$	$\tau_{Al}$	$\tau_{H_2O}$	$\tau_H$
13.3	.01795	.02213	.02026	.02521
17.5	.01648	.02219	.01883	.02239
21.5	.01626	.02268	.01846	.02018
25.9	.01566	.02193	.01766	.01822
30.3	.01507	.02208	.01721	.01702
34.3	.01482	.02231	.01701	.01622
38.3	.01465	.02259	.01693	.01546
42.3	.01453	.02279	.01684	.01472
46.3	.01446	.02300	.01677	.01409
50.3	.01440	.02322	.01675	.01375
54.3	.01440	.02351	.01676	.01347
58.3	.01440	.02367	.01681	.01310
62.3	.01442	.02392	.01685	.01293
66.2	.01442	.02409	.01685	.01258
70.2	.01442	.02429	.01687	.01233
74.2	.01445	.02454	.01696	.01203
78.2	.01445	.02472	.01699	.01155
82.2	.01447	.02500	.01711	.01116

Table III

Sources of Error and Estimates of Uncertainties in Percent

	Hydrogen		Carbon	
	Below 30 Mev	Above 30 Mev	Below 30 Mev	Above 30 Mev
Statistics	2.4	2.4	.84	.84
Recombination and In-Scattering	.0	.0	.05	.05
Density	1.4	1.4	.2	.2
Response Function C.F.	2.8 max.	.2 min.	.8	.2
Total, $\sqrt{\epsilon^2}$	4.0	2.8	1.2	.89

Table IVa  
Calculated Attenuation Coefficients

Energy Mev	Compton Pair		Triplet	Nuclear Giant res.	Quasi-deuteron	Total with nuclear		Total without nuclear	
	barns	barns	barns	barns	barns	barns	cm <sup>2</sup> /g	barns	cm <sup>2</sup> /g
Hydrogen						R = .5997			
10	.0510	.0021	.0011			.0542	.03250		
15	.0377	.0027	.0018			.0422	.02531		
20	.0302	.0032	.0023			.0357	.02141		
30	.0220	.0039	.0031			.0290	.01739		
40	.01746	.0044	.0037			.0256	.01535		
50	.01456	.0048	.0041			.0235	.01409		
60	.01254	.0051	.0045			.0221	.01325		
80	.00988	.0056	.0051			.0206	.01235		
100	.00820	.0060	.0056			.0198	.01187		
Carbon						R = .05016			
10	.3060	.0775	.0070			.3905	.01959		
15	.2260	.1013	.0110	.0		.3383	.01697	same	
20	.1814	.1181	.0140	.0080		.3215	.01613	.3135	.01573
30	.1319	.1415	.0190	.0090	.0000	.3014	.01512	.2924	.01467
40	.1048	.1590	.0220	.0048	.0004	.2910	.01460	.2862	.01436
50	.0874	.1727	.0250	.0016	.0012	.2879	.01444	.2863	.01436
60	.0752	.1828	.0270	.0010	.0015	.2875	.01442	.2865	.01437
80	.0593	.1987	.0300	.0	.0016	.2896	.01453	same	
100	.0492	.2107	.0333		.0014	.2946	.01478		
Oxygen						R = .03765			
10	.4080	.1369	.0093			.5542	.02087		
15	.3020	.1791	.0150	.0		.4961	.01868	same	
20	.2420	.2097	.0190	.0045		.4752	.01789	.4707	.01772
30	.1759	.2507	.0250	.0057	.0000	.4573	.01722	.4516	.01700
40	.1397	.2813	.0290	.0030	.0005	.4535	.01707	.4505	.01696
50	.1165	.3051	.0330	.0010	.0015	.4561	.01718	.4561	.01717
60	.1003	.3219	.0360	.0	.0020	.4602	.01733	same	
80	.0790	.3501	.0400		.0021	.4712	.01774		
100	.0656	.3711	.0440		.0018	.4825	.01817		
Aluminum						R = .02233			
10	.6630	.3611	.0150	.0		1.0391	.02320	same	
15	.4900	.4707	.0230	.0013		.9850	.02200	.9837	.02197
20	.3930	.5489	.0300	.0466		1.0185	.02274	.9719	.02170
30	.2860	.6542	.0400	.0072	.0000	.9874	.02205	.9802	.02189
40	.2270	.7339	.0480	.0049	.0003	1.0133	.02263	1.0092	.02254
50	.1893	.7962	.0530	.0009	.0019	1.0413	.02325	1.0404	.02323
60	.1630	.8409	.0580	.0	.0032	1.0651	.02378	same	
80	.1284	.9106	.0660		.0036	1.1086	.02476		
100	.1065	.9639	.0720		.0031	1.1455	.02558		

Compton - Klein-Nishina

Pair (Unscreened Bethe and Heitler - Hartree screening - Coulomb Corrections)

This was multiplied by 1.0225 for C, O and Al

Triplet - Borsellino

Nuclear - experimental (see text)

Quasi-deuteron - Levinger with Danos quenching from Whalin exp.

Conversion factor -  $R = (\text{cm}^2/\text{g}) / (\text{barns}/\text{atom})$

Table IVb  
Calculated Attenuation Coefficients for Water

Energy Mev	Hydrogen barns	2x barns	Oxygen barns	barns		cm <sup>2</sup> /g R=.03344	Without Nuclear		
				H <sub>2</sub> O Molecule	Oxygen		H <sub>2</sub> O	H <sub>2</sub> O	
									cm <sup>2</sup> /g
10	.0542	.1084	.5542	.6626	.02216	.5542	.6626	.02216	
15	.0422	.0844	.4961	.5805	.01941	.4961	.5805	.01941	
20	.0357	.0714	.4752	.5466	.01828	.4707	.5421	.01813	
30	.0290	.0580	.4573	.5153	.01723	.4516	.5096	.01704	
40	.0256	.0512	.4535	.5047	.01688	.4505	.5017	.01678	
50	.0235	.0470	.4561	.5031	.01682	.4561	.5031	.01682	
60	.0221	.0441	.4602	.5043	.01686	.4602	.5043	.01686	
80	.0206	.0412	.4712	.5124	.01713	.4712	.5123	.01713	
100	.0198	.0396	.4825	.5221	.01746	.4825	.5221	.01746	

Table V  
Photo Nuclear Cross Section Data

Isotope	Reaction	Energy Range	Cross Section	Reference	
C <sup>12</sup>	(γ,n)	19 -38 Mev	Absolute	Barber et al	33
	(γ,p)g.s.	16.5-24 Mev	Absolute	Cohen et al	31
	(γ,p)g.s.	24 -50 Mev	Absolute	Penner and Leiss	32
	(γ,p*) excited s.	24 -50 Mev	Absolute	Penner and Leiss	
O <sup>16</sup>	(γ,n)	16 -22.5 Mev	Absolute plus extrapolation to 23 Mev	Katz et al	34
	(γ,p)	18 -25 Mev	Absolute	Cohen et al	31
	(γ,p)	23 -45 Mev	Shape normalized to total absolute σ at 23 Mev	Penner and Leiss	32
Al <sup>27</sup>	(γ,n)	16 -22 Mev	Absolute	Montabelli et al	35
	(γ,p)	15 -24 Mev	Absolute	Halpern and Mann	36
	(γ,p)	22.5-40 Mev	Shape normalized to total absolute σ at 22.5 Mev	Penner and Leiss	

Table VI

Triplet Calculation at 60 Mev in Millibarns

	Hydrogen	Carbon	Water	Aluminum
Exp. total*	21.71±.21	287.28±.60	502.39±1.7	1064.5±2.4
Compton	12.54	75.2	125.4	163.0
Corrected Pair	5.1	182.8	332.1	840.9
Remainder "Triplet"	4.07±.21	29.20±.60	45. ±1.7	60.6±2.4
Votruba Triplet	3.3	20	29	42
Borsellino Triplet	4.5	27	45	58
(1/Z)xPair	5.1	30.5	41.5	64.7
Wheeler and Lamb	5.2	31	52	68
W-L with Exchange	3.5 <sup>2,3</sup>	21	35	45

\* Only statistical errors have been indicated in this table.

Table VII

Integrated Cross Sections in Mev-barns, Sum Rule Comparisons

	K = 1.0225			K = 1.03
	Carbon	Oxygen	Aluminum	Carbon
Nuclear	.267	.191	.373	.219
Quenched quasi-deuteron	.110	.141	.233	.110
Total	.377	.332	.606	.329
G-G-T Sum Rule*	.252	.341	.567	.252
Ratio: $\frac{\text{Total exp.}}{\text{Sum Rule}}$	1.50	.974	1.069	1.31

$$* \int_0^{\mu} \sigma_T dE = .06 \frac{NZ}{A} \left[ 1 + 0.1 \frac{A}{NZ} \right]^2 \text{ Mev-barns}$$

References

1. G. White Grodstein, X-ray Attenuation Coefficients from 10 kev to 100 Mev, National Bureau of Standards Circular No. 583, (U. S. Government Printing Office, Washington, D. C., 1957).  
An earlier unpublished NBS Report (1952) also by G. White Grodstein has been widely duplicated in the literature.  
C. M. Davisson and R. D. Evans, Revs. Mod. Phys. 24, 102 (1952);  
R. H. Morgan, Handbook of Radiology, (The Year-Book Publishers, Inc., Chicago, 1955) p. 99-117;  
K. Siegbahn, Beta- and Gamma-Ray Spectroscopy, (Interscience Publishers, Inc. New York, 1955) p. 857-874.  
The basic difference between these two reports is in the triplet cross sections used. The 1952 report used the Borsellino cross sections, while NBS Circular 583 used the Votruba results. To illustrate the differences, the present experiment at 60 Mev yields a carbon attenuation coefficient of  $.01441 \pm 1\% \text{ cm}^2/\text{g}$  to be compared with  $.0142 \text{ cm}^2/\text{g}$  in the 1952 NBS Report and  $.0138 \text{ cm}^2/\text{g}$  in NBS Circular 583.
2. H. Davies, H. A. Bethe, and L. C. Maximon, Phys. Rev. 93, 788 (1954).
3. J. L. Lawson, Phys. Rev. 75, 433 (1949).
4. Moffatt, Thresher, Weeks and Wilson, Proc. Roy. Soc. A, 244, 245 (1958).
5. J. Moffatt and G. C. Weeks, Proc. Phys. Soc. (London) 73, 114 (1959).
6. J. M. Wyckoff and H. W. Koch, Bull. Am. Phys. Soc. Ser. II 3, 174 (1958).
7. B. Ziegler, Zeit. für Physik, Bd. 152, S. 566 (1958).
8. J. Kockum and N. Starfelt, Nuclear Physics, (to be published).
9. M. V. Mihailović, G. Pregl, G. Kernel and M. Kregar, Phys. Rev. Letters, (to be published).
0. R. S. Foote and H. W. Koch, Rev. Sci. Instr. 25, 746 (1954).
1. H. W. Koch and J. M. Wyckoff, Proc. Sixth Scintillation Counter Symposium, IRE Transactions on Nuclear Science, NS-5-No. 3, 127 (1958).

12. E. Segre, Editor, Experimental Nuclear Physics, Vol. I, (John Wiley & Sons, Inc., New York, 1953) first edition, Section by H. A. Bethe and J. Ashkin, pp. 326, 327. These formulas were evaluated with the help of R. A. Schrack to whom we are indebted.
13. H. A. Bethe and W. Heitler, Proc. Roy. Soc. A, 146 (1934).
14. A. T. Nelms and I. Oppenheim, J. Res. NBS 55, 53 (1955).
15. We are indebted to R. T. McGinnies for performing this calculation at 60 Mev for carbon and aluminum. The correction was subsequently applied to the Thomas-Fermi correction at all energies.
16. J. Joseph and F. Rohrlich, Rev. Mod. Phys. 30, 354 (1958).
17. A. Borsellino, Helv. Phys. Acta 20, 136 (1947); Nuovo Cimento 4, 112 (1947).
18. V. Votruba, Phys. Rev. 73, 1468 (1948); Bul. intern. acad. tchèque sci., Prague 49, 19 (1948).
19. E. Malamud, Phys. Rev., (to be published).
20. Kiu S. Suh and H. A. Bethe, Bull. Am. Phys. Soc. Ser. II 4, 13 (1959) and Phys. Rev. (to be published).
21. E. L. Hart, G. Cocconi, V. T. Cocconi and J. M. Sellen, Phys. Rev. (to be published).
22. J. A. Wheeler and W. E. Lamb Jr., Phys. Rev. 55, 858 (1939).
23. W. Heitler, The Quantum Theory of Radiation, 3rd edition, (Oxford at the Clarendon Press, London, 1954) p. 227.
24. L. M. Brown and R. P. Feynman, Phys. Rev. 85, 231 (1952).
25. J. D. Bjorken, S. D. Drell and S. C. Frautschi, Phys. Rev. 112, 1409 (1958).
26. J. S. Levinger, Phys. Rev. 84, 43 (1951).
27. M. Q. Barton and J. H. Smith, Phys. Rev. 110, 1143 (1958).
28. M. Danos, Bull. Am. Phys. Soc. Ser. II 4, 102 (1959); and private communication.
29. E. A. Whalin, B. D. Schriever and A. O. Hanson, Phys. Rev. 101, 377 (1956).

30. The photo alpha production process is reported by F. K. Goward and J. J. Wilkins, Cross Sections for the Photo-Disintegrations  $^{12}\text{C}$  ( $\gamma, 3\alpha$ ) and  $^{16}\text{O}(\gamma, 4\alpha)$  A. E. R. E. Memorandum G/M127 (Ministry of Supply, Harwell, Berks, U. K., 1952); It has a maximum of 0.4 millibarns and was not included in these calculations. Similarly the ( $\gamma, \gamma$ ) process with a 0.1 millibarn maximum was neglected.
31. L. Cohen, A. K. Mann, B. J. Patton, K. Reibel, W. E. Stephens, and E. J. Winhold, Phys. Rev. 104, 108 (1956).
32. S. Penner and J. E. Leiss, Phys. Rev. (to be published); private communication.
33. W. C. Barber, W. D. George and D. D. Reagan, Phys. Rev. 98, 73 (1955).
34. L. Katz, R. N. H. Haslam, R. J. Horsley, A. G. W. Cameron and R. Montalbetti, Phys. Rev. 95, 464 (1954).
35. R. Montalbetti, L. Katz and J. Goldemberg, Phys. Rev. 91, 659 (1953).
36. J. Halpern and A. K. Mann, Phys. Rev. 83, 370 (1951).
37. J. L. Bergsteinsson, L. B. Robinson, A. K. M. Siddiq, R. J. Horsley, and R. N. H. Haslam, Can.J. Phys. 36, 140 (1958).
38. E. Hisdal, Phys. Rev. 105, 1821 (1957).
39. E. L. Garwin and A. S. Penfold, Bull. Am. Phys. Soc., Ser. II 4, 288 (1959).
40. J. S. Levinger and H. A. Bethe, Phys. Rev. 78, 115 (1950).
41. M. Gell-Mann, M. L. Goldberger and W. E. Thirring, Phys. Rev. 95, 1612 (1954).

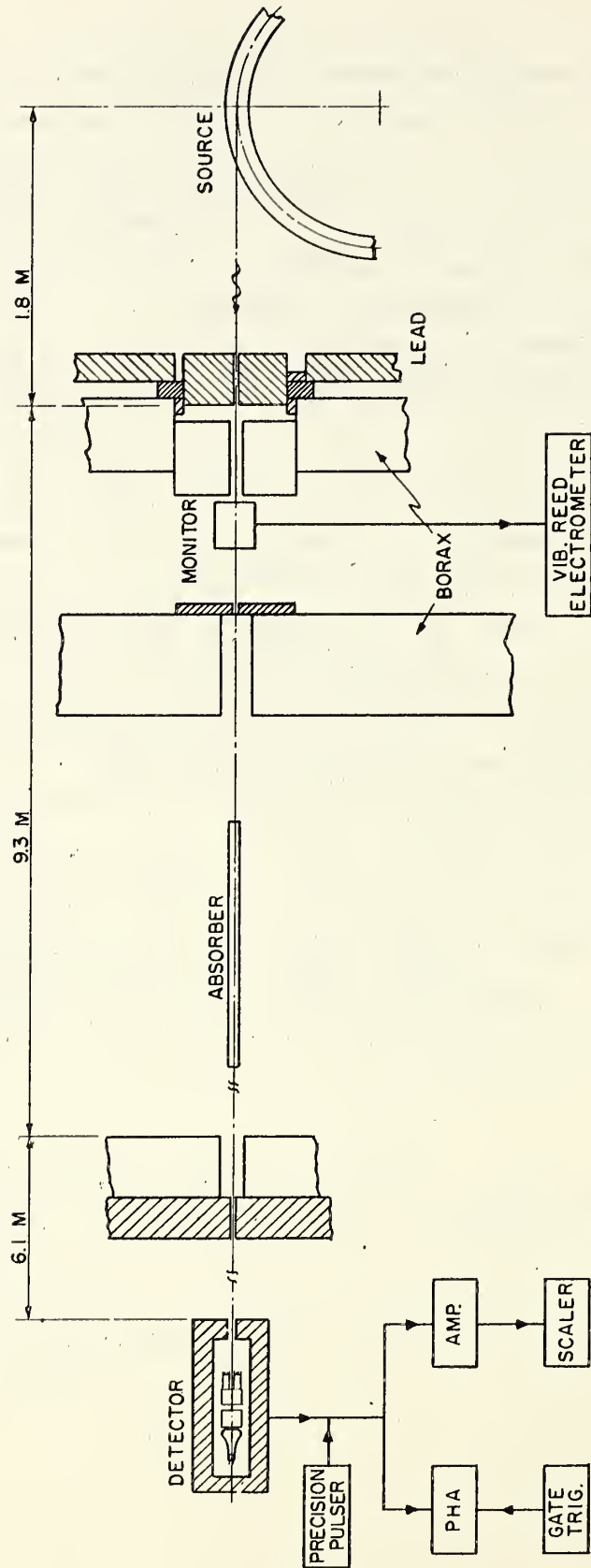


Fig. 1. Experimental geometry and block diagram.

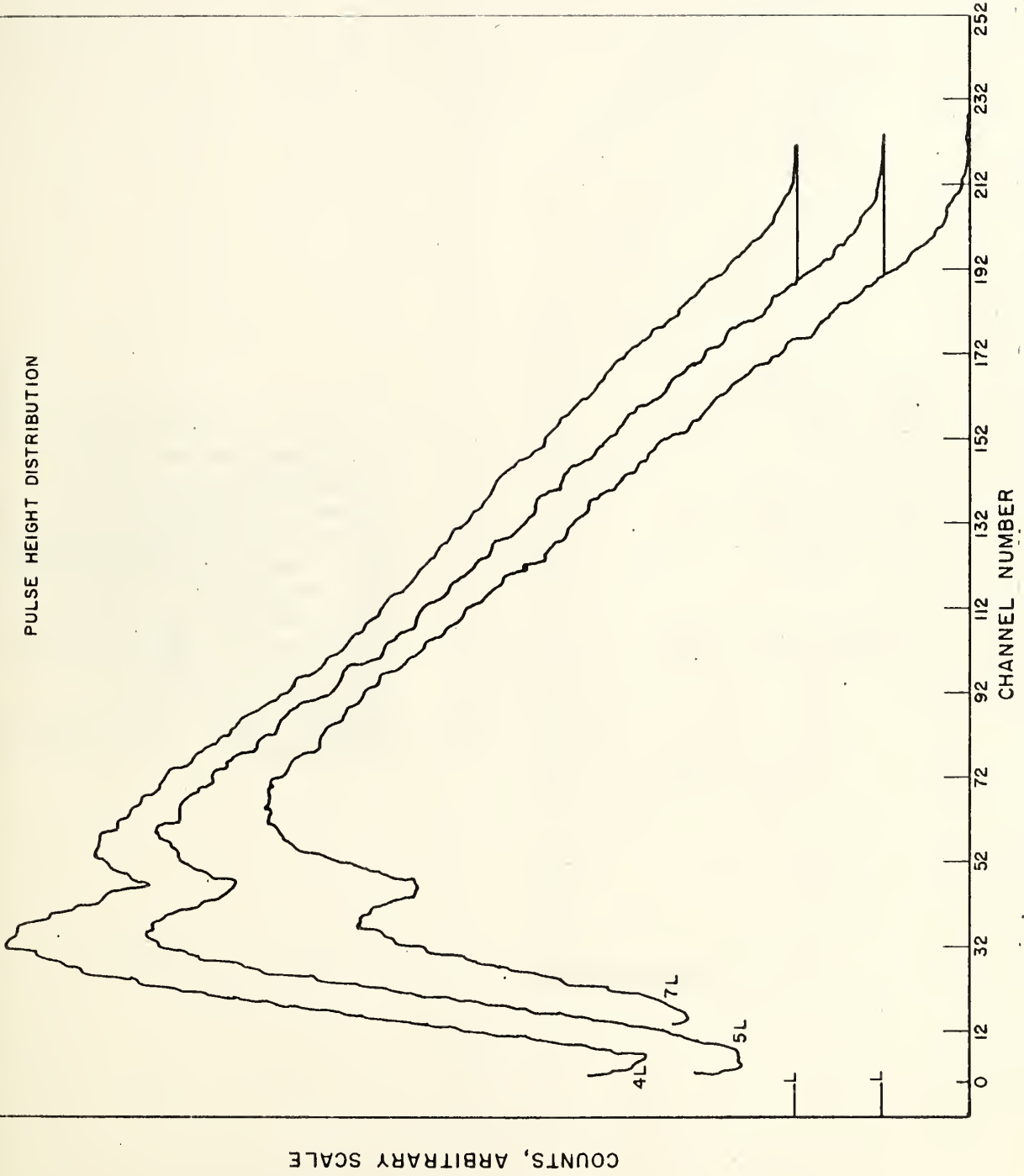


Fig. 2. Raw pulse height distributions for the X-rays passing through 396.82 (4L), 496.43 (5L) and 698.86 (7L) g/cm<sup>2</sup> of carbon. These data have been taken directly from the pulse height analyzer output with no background or channel width corrections.

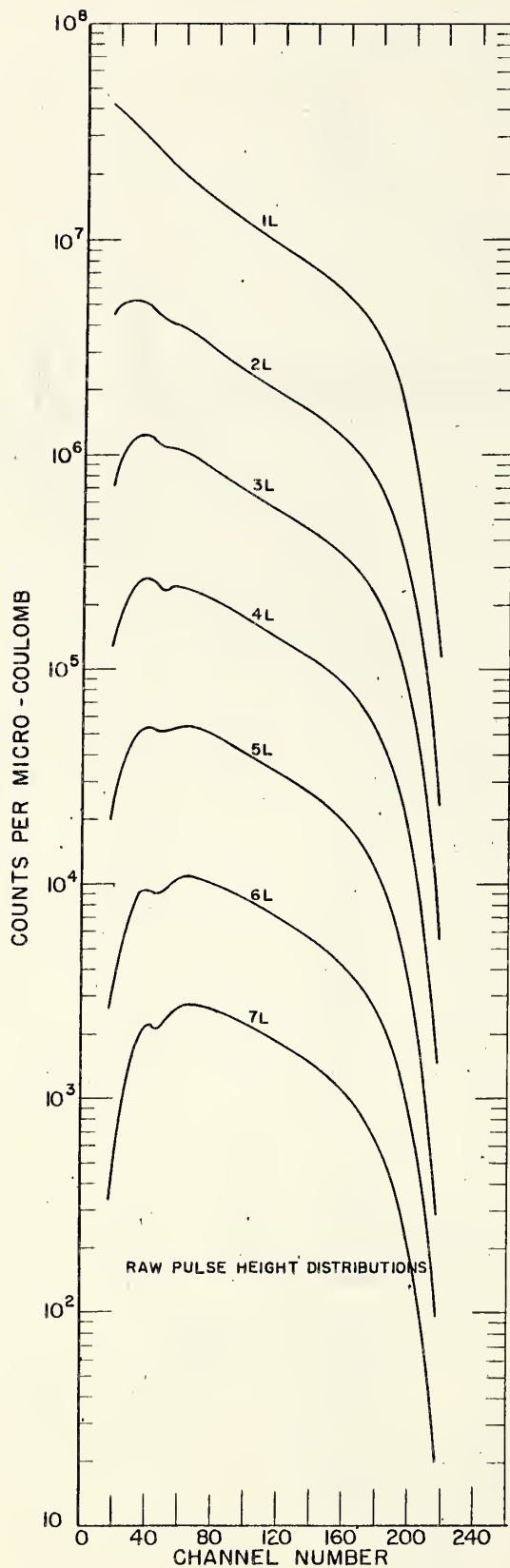


Fig. 3. Pulse height distributions for 90 Mev bremsstrahlung that have passed through seven different lengths of graphite. The absorber characteristics are tabulated in Table 1. These curves have been corrected for channel width and background and have been normalized to a common input as measured by the monitor.

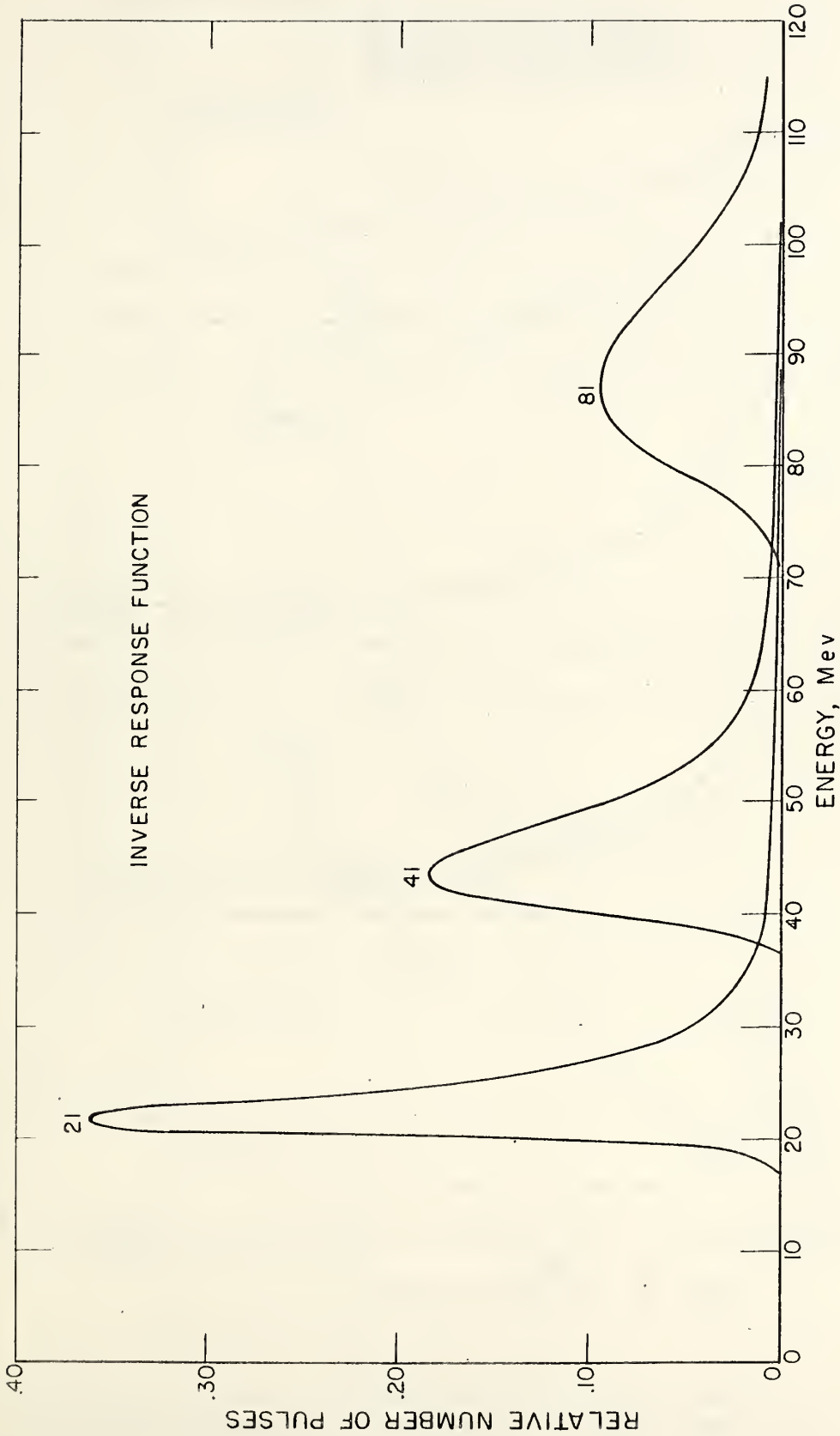


Fig. 4. Three inverse response function curves. These show the photon energies that contribute to the particular pulse height of 21, 41 and 81 Mev for the 5" diameter by 9" long NaI(Tl) spectrometer. The data for each curve is taken from one row of the response function matrix.

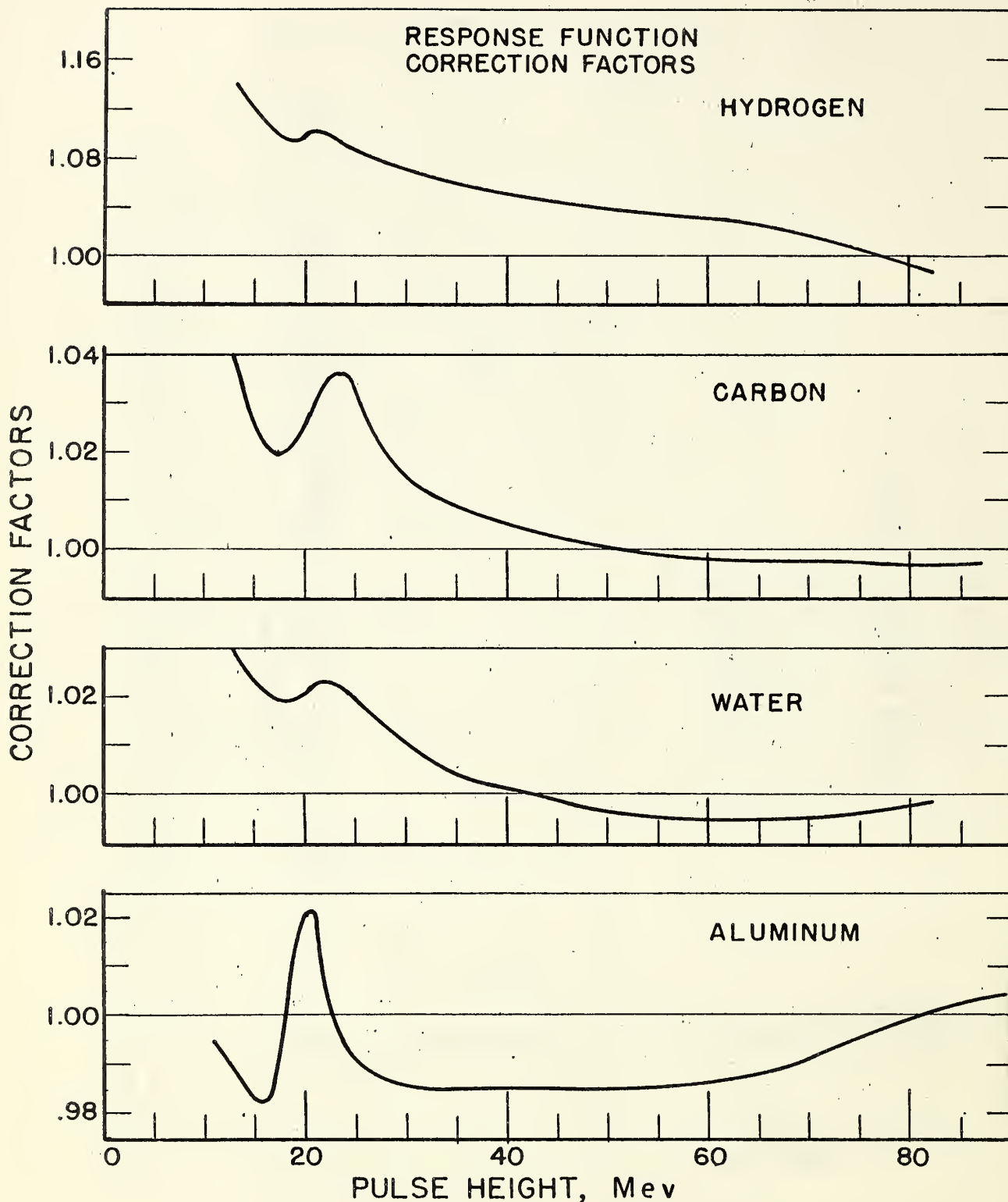


Fig. 5. Response function correction factors for the attenuation coefficients obtained from the pulse height distributions for hydrogen, carbon, water, and aluminum. These factors have been calculated using assumed coefficients and the response function matrix to predict the pulse height distributions.

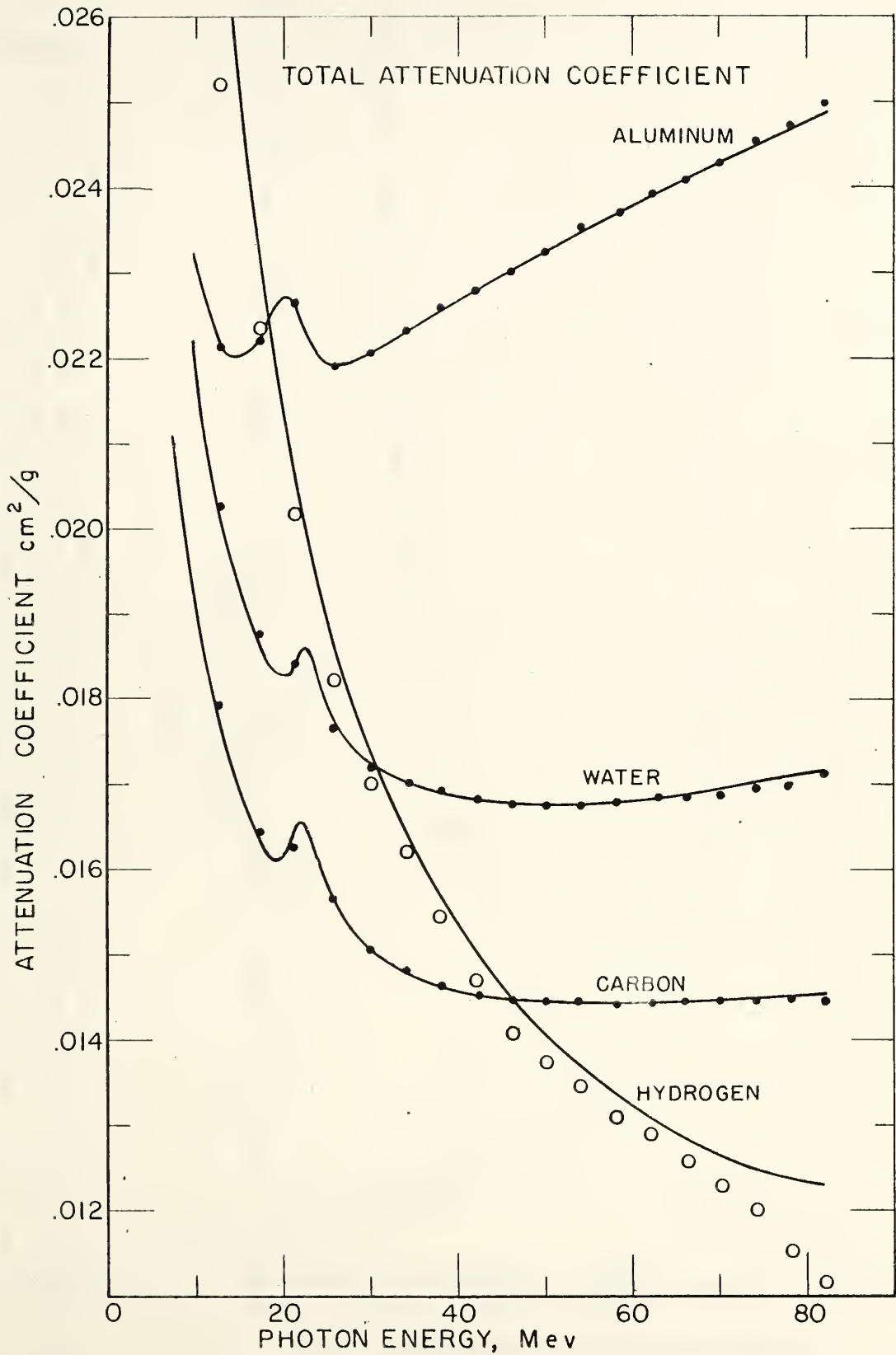


Fig. 6. Predicted attenuation coefficients (solid lines) (see text) and experimental points for hydrogen, carbon, water, and aluminum.

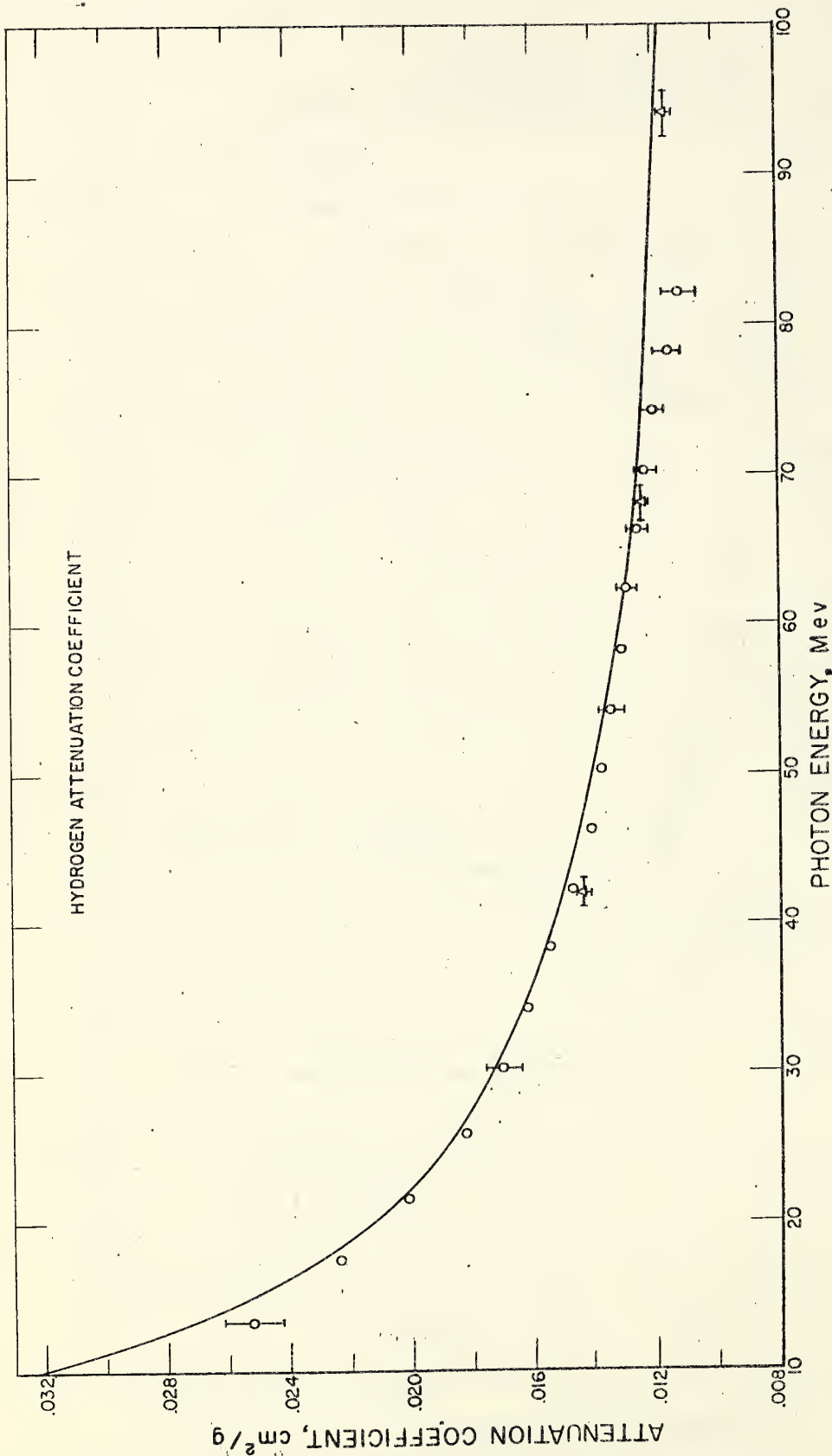


Fig. 7a.

Fig. 7. Detailed plot of attenuation coefficients for (a) hydrogen, (b) carbon, (c) water, and (d) aluminum showing the predicted solid lines (see text) and the experimental points. The maximum error is indicated on (a) while only the statistical accuracy is indicated on (b), (c) and (d). The results of the Circular 583 carbon calculation are shown. The carbon curve has been plotted for a pair correction factor of 1.000 and 1.0300 in addition to the value 1.0225 used for water and aluminum curves. The synthesis of a nuclear cross section is shown for carbon, water and aluminum as well as the experimental nuclear cross section obtained by subtracting the predicted curve for the electronic processes only from the experimental points. Experimental points of Lawson<sup>3/</sup> at 88 Mev and Moffatt et al<sup>4,5/</sup> at 94, 68 and 42 Mev are shown by triangles with some of the lower energy results tabulated in reference 1.

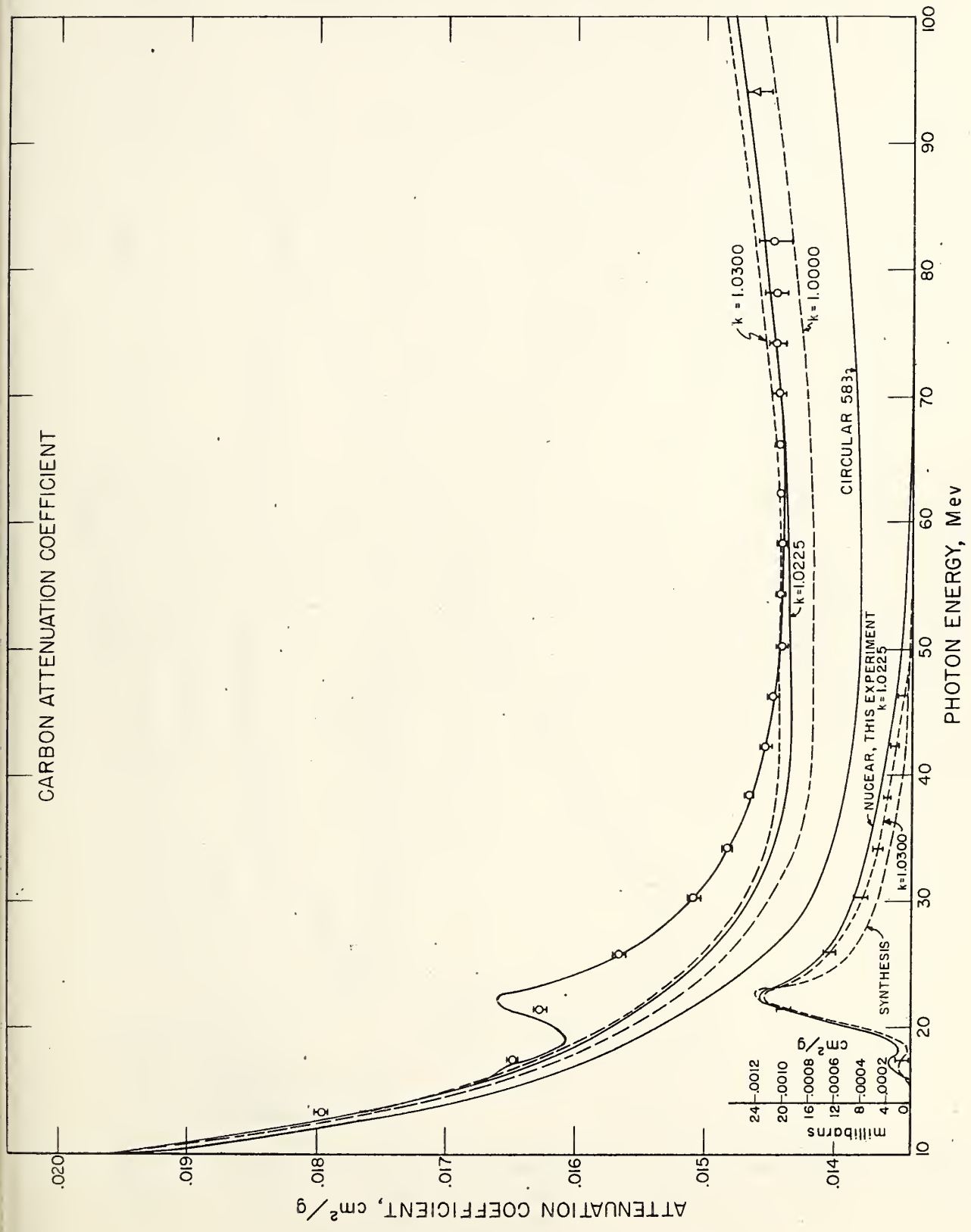


Fig. 7b.

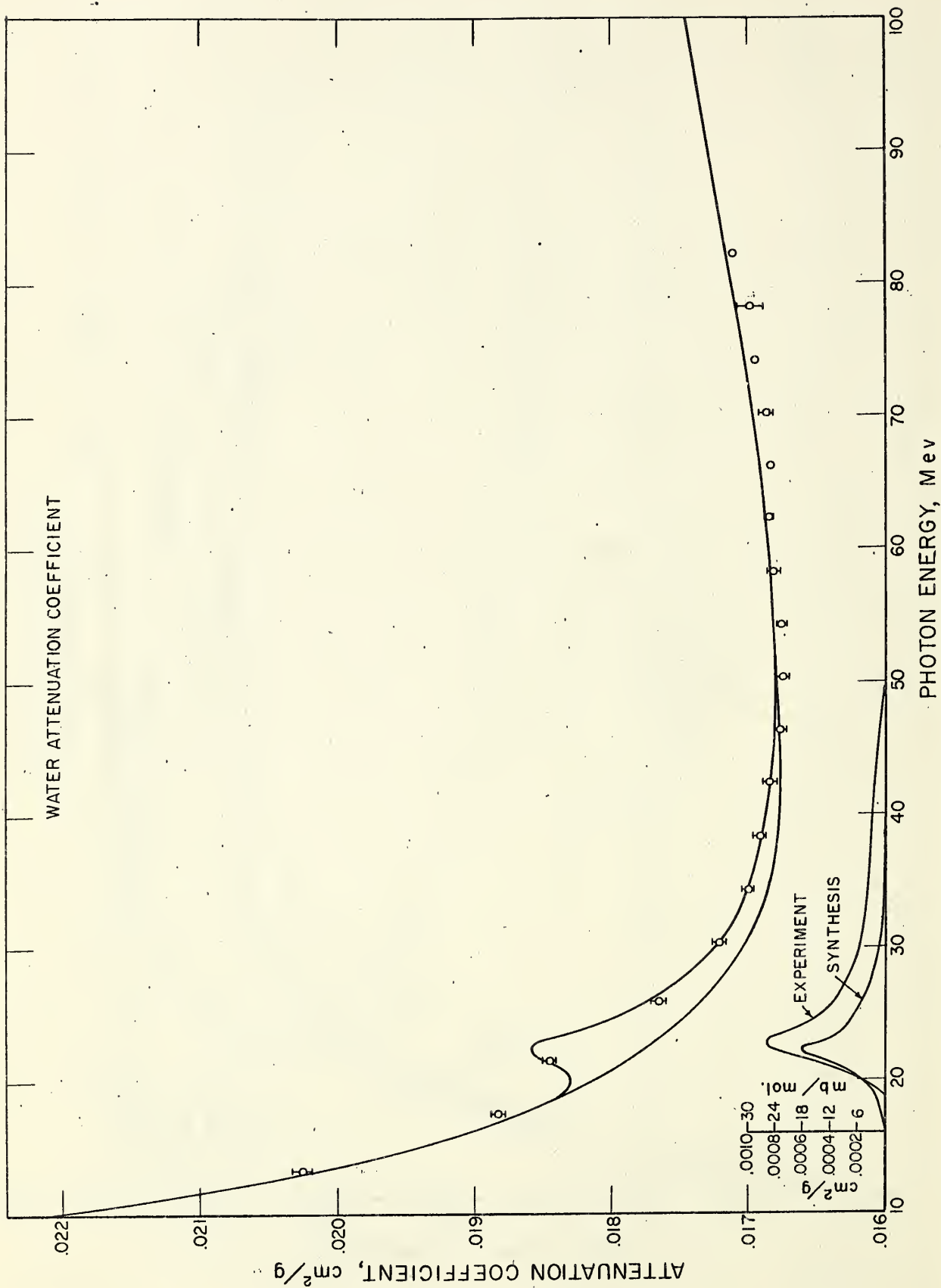


Fig. 7c.

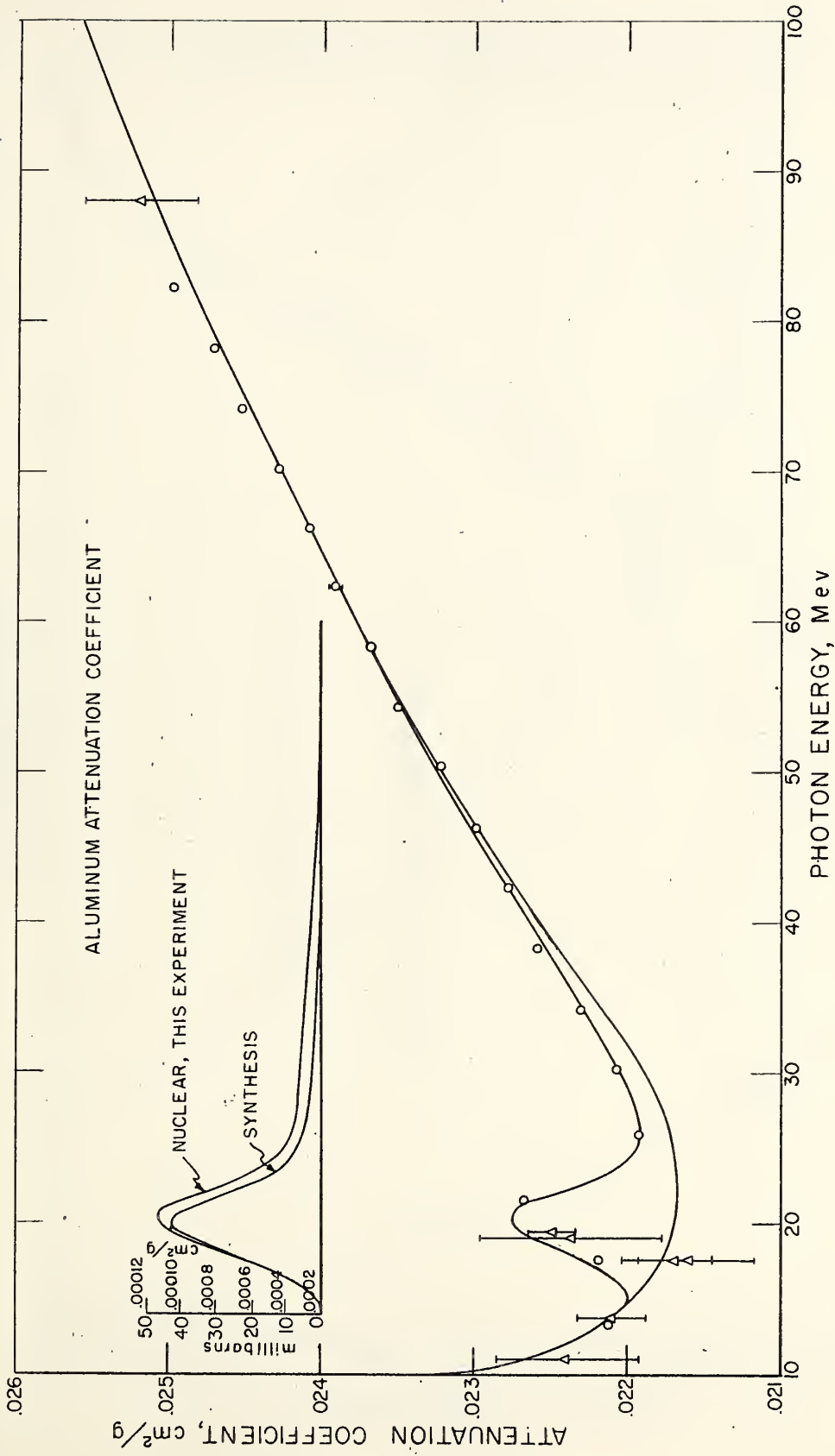


Fig. 7d.

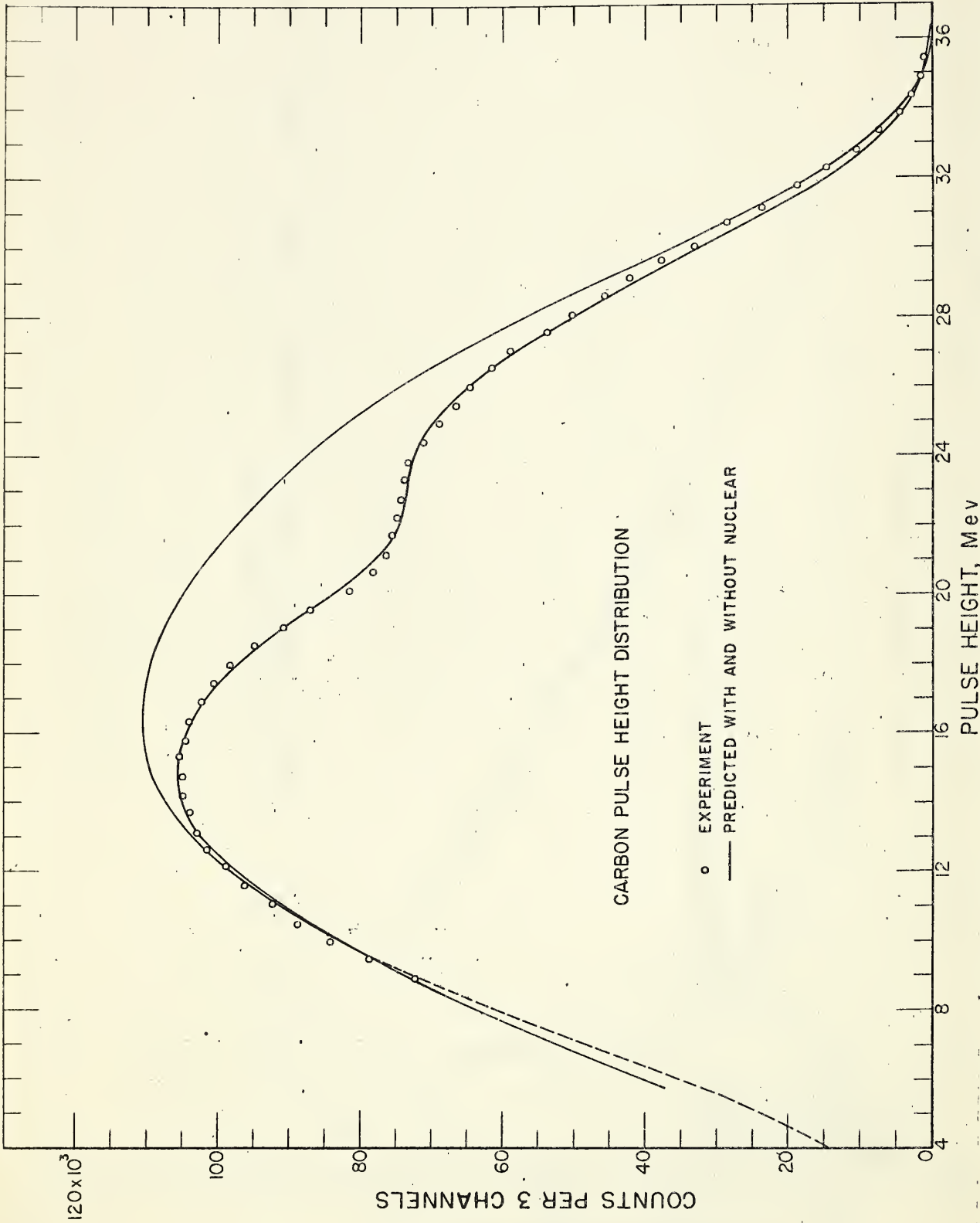


Fig. 8. The pulse height distribution (solid line) predicted for a 34.2 Mev bremsstrahlung spectrum that has passed through 351.5 g/cm<sup>2</sup> of carbon to enter a 5" diameter by 9" long NaI(Tl) total absorption spectrometer. The electronic attenuation processes only yield the top curve; the inclusion of the "experimental" nuclear cross section yields the lower curve. Plotted experimental points have been corrected for channel width and background (dotted line). The vertical normalization of the predicted curves is arbitrary.

PULSE HEIGHT DISTRIBUTION

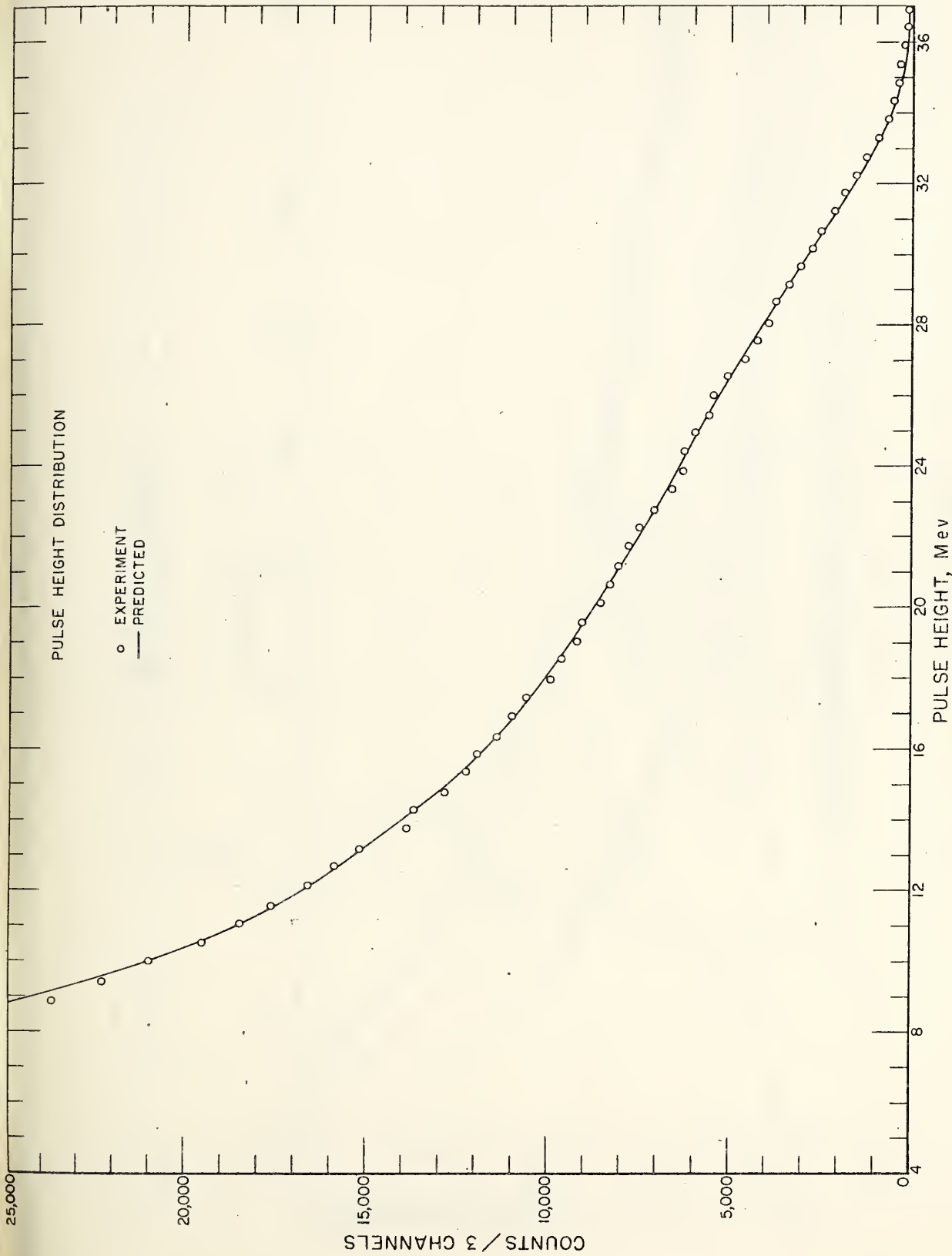


Fig. 9. The predicted pulse height distribution (solid line) for a 35.3 Mev bremsstrahlung spectrum passing through the donut wall and monitor ionization chamber to strike a 5" diameter by 9" long NaI(Tl) total absorption spectrometer. An initial Davies-Bethe-Maximon<sup>2</sup>/ spectrum using Hisdal's<sup>37</sup> target correction was used. The plotted experimental points have been corrected for channel width, and background was negligible. The predicted curve has an arbitrary vertical normalization.

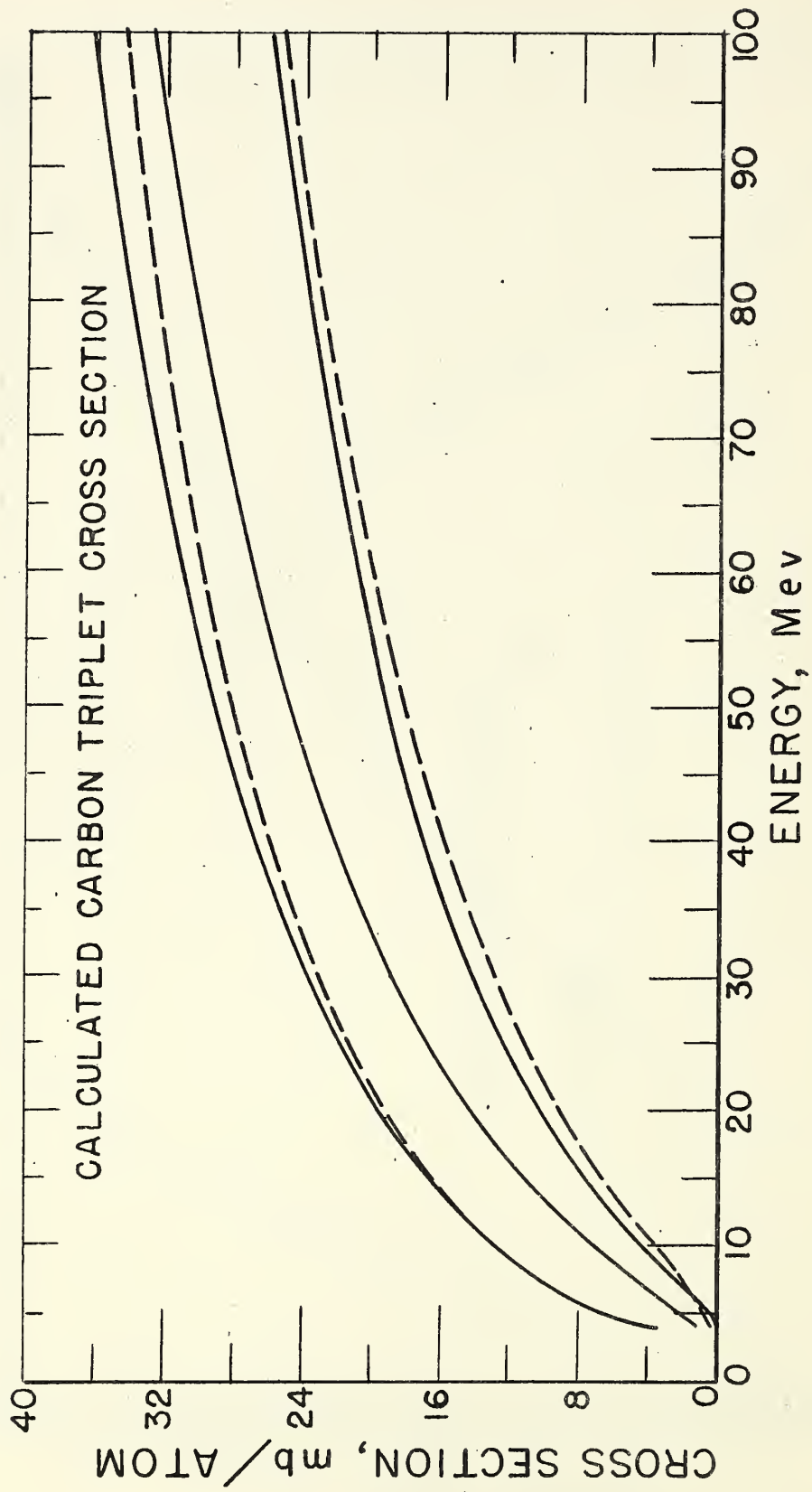


Fig. 10. Five different carbon triplet cross section predictions. From top to bottom they are (a) Wheeler and Lamb<sup>22/</sup>, (b) (1/Z) times the corrected pair cross section, (c) Borsellino<sup>17/</sup>, (d) Wheeler and Lamb with an exchange correction suggested by Joseph and Rohrlisch<sup>16/</sup>, and (e) Votruba<sup>18/</sup>

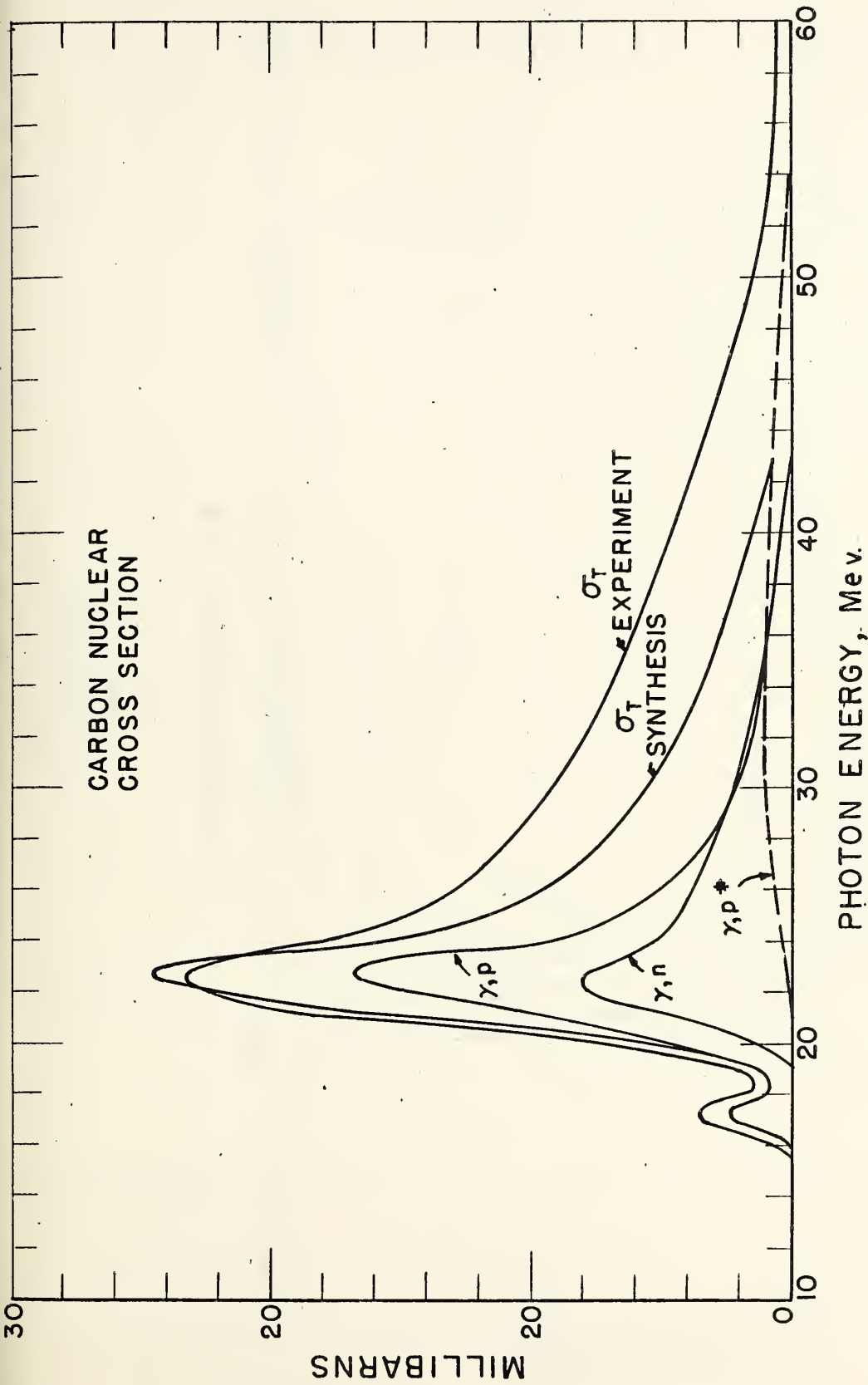


Fig. 11a.

Fig. 11. The  $(\gamma, n)$ ,  $(\gamma, p)$  and  $(\gamma, p^*)$  components of the total nuclear cross sections. The sum of these is labeled "synthesis" and the experimental cross sections (see text) are shown for (a) carbon, (b) oxygen (water), and (c) aluminum. The references for these data are listed in Table IV.

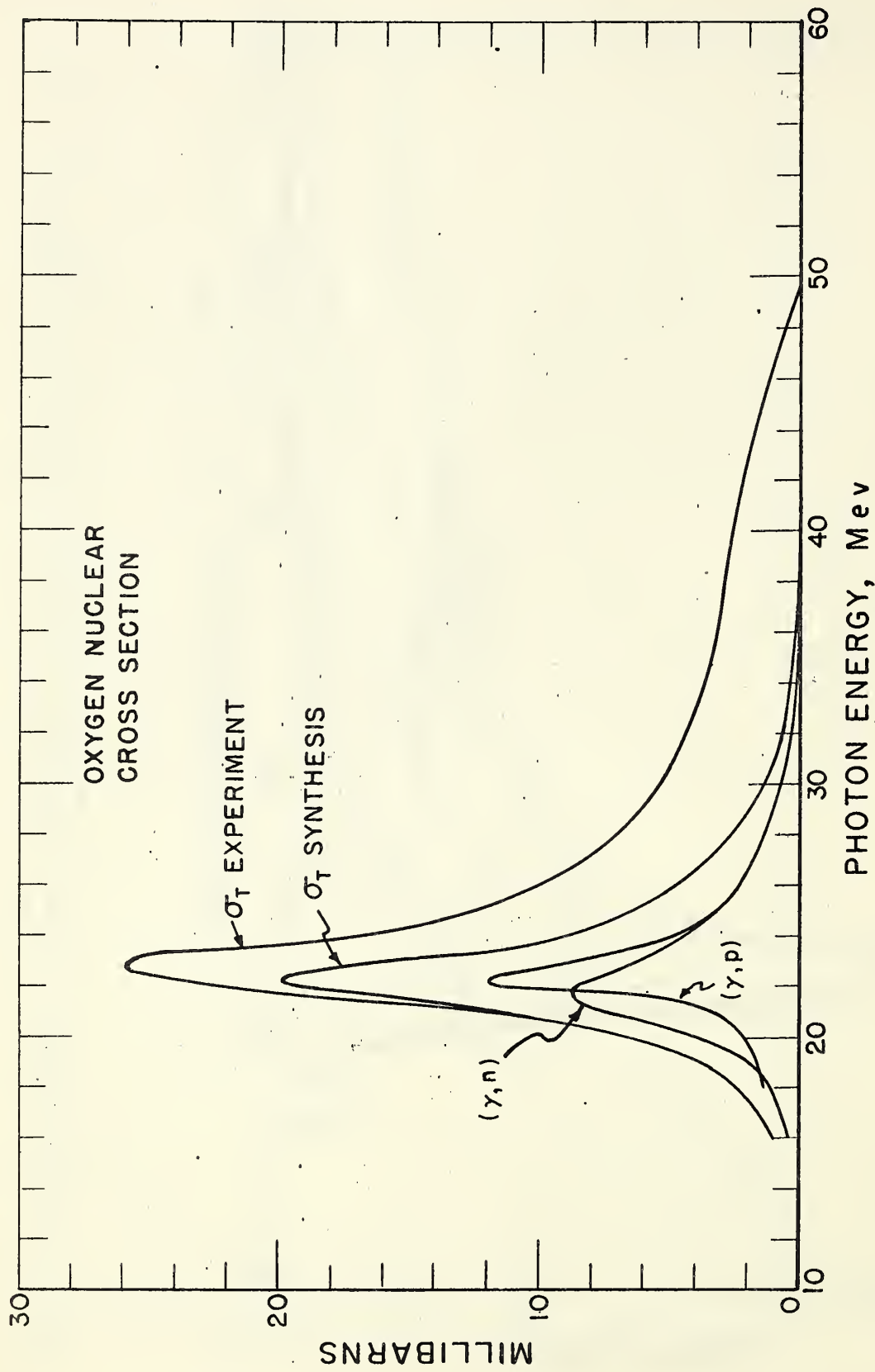


Fig. 11b.

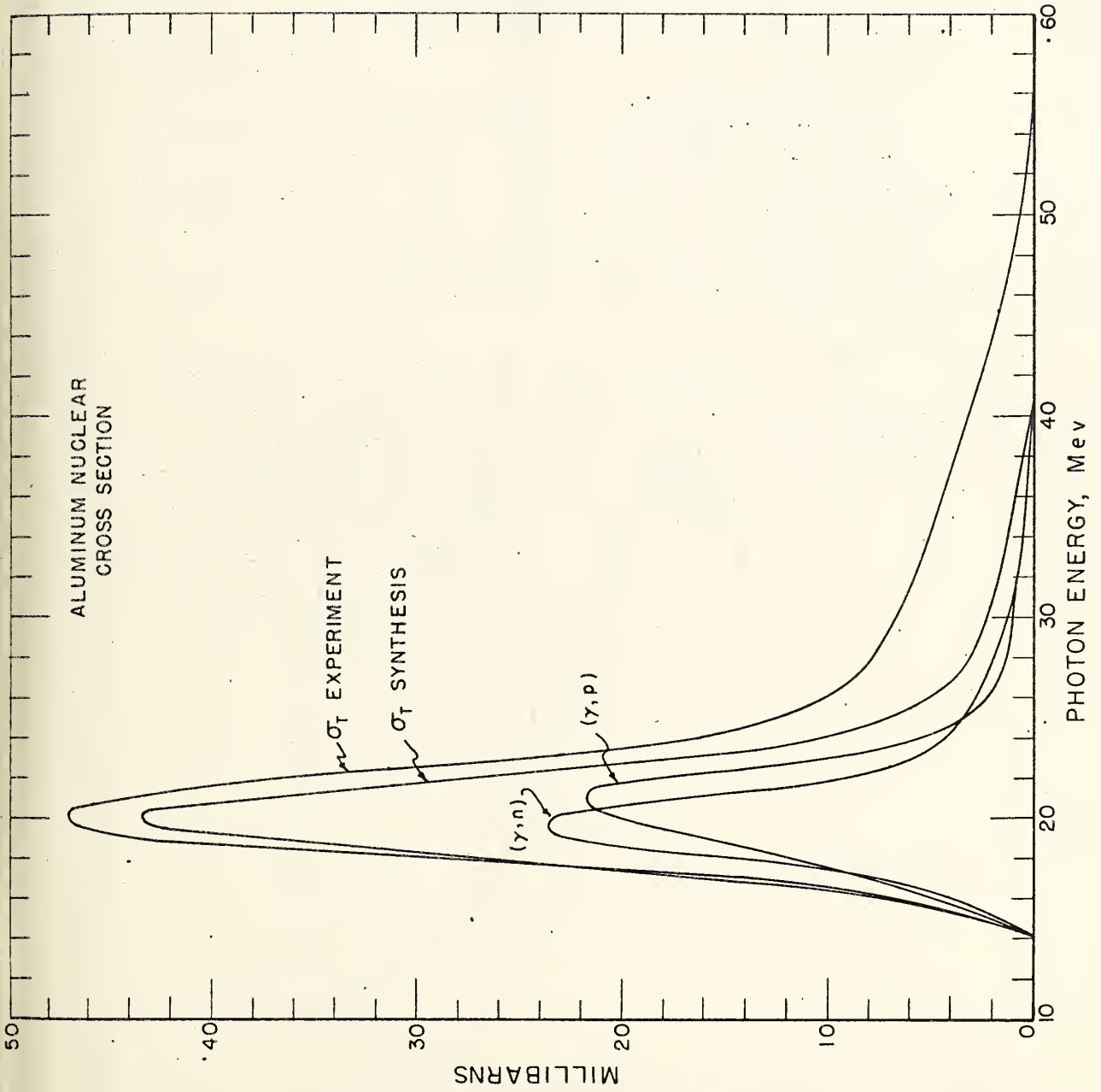


Fig. 11c.

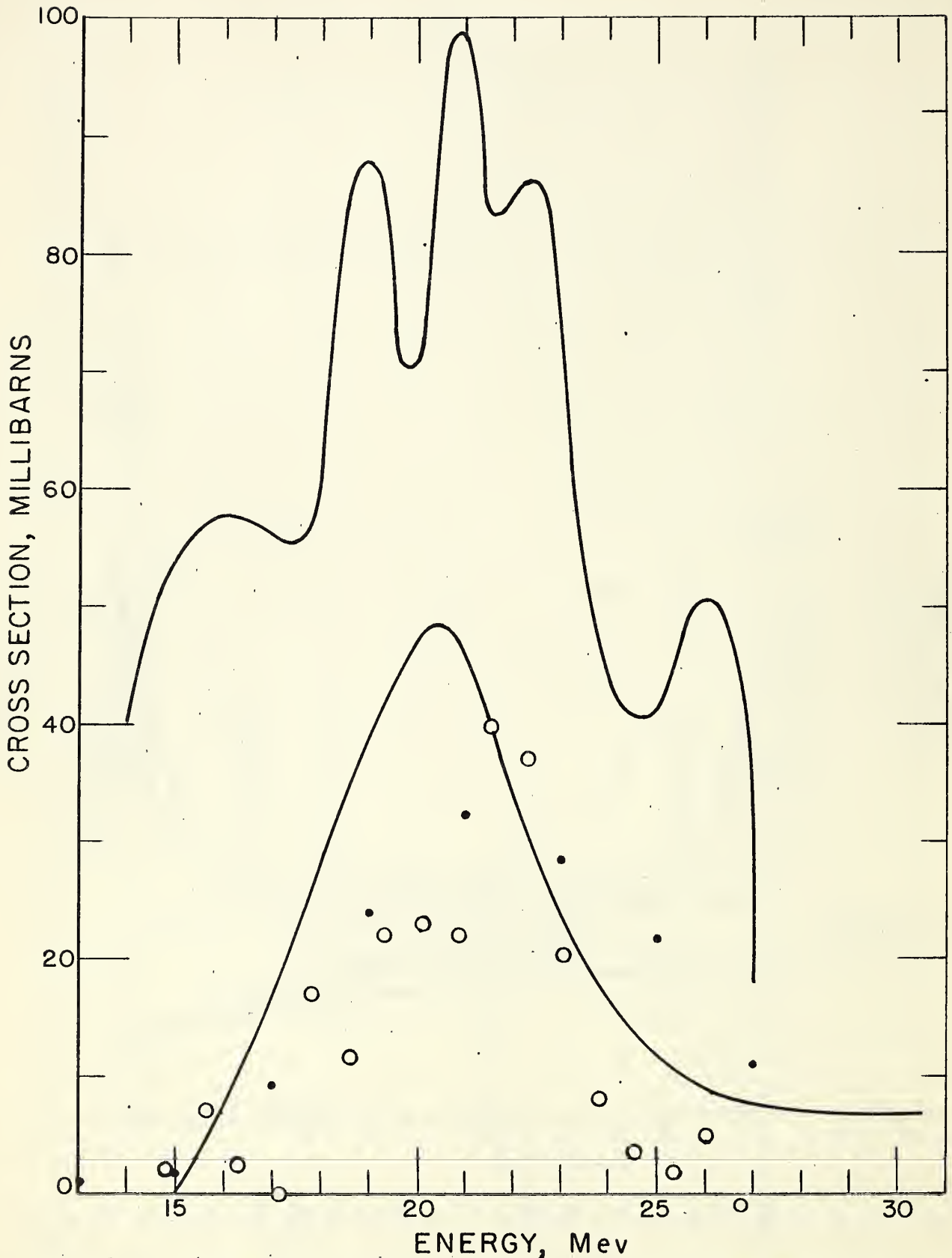


Fig. 12. Comparison of the total aluminum attenuation cross section obtained at different laboratories. The top curve is from the Compton spectrometer work of Mihailović et al<sup>9/</sup>; the bottom curve is the experimental result of this experiment; the open circles are the results of Ziegler<sup>7/</sup> obtained with a pair spectrometer and the closed circles are the NaI(Tl) results of Kochum and Starfelt<sup>8/</sup>.

## BREMSSTRAHLUNG CROSS SECTION FORMULAS AND RELATED DATA\*

H. W. Koch and J. W. Motz

National Bureau of Standards, Washington, D. C.

## TABLE OF CONTENTS

- I. Introduction
- II. Bremsstrahlung Cross Sections
  - A. Symbols, Constants, and Energy-Momentum Relations
  - B. Types of Cross Section Calculations
  - C. Bremsstrahlung Cross Section Formulas and Classification Diagrams
    - (1) Born-Approximation Cross Section Formulas
    - (2) Extreme-Relativistic Cross Section Formulas with Coulomb Correction
  - D. Graphical Representation of the Formulas
    - (1) Dependence of the Bremsstrahlung Spectrum on Electron Energy
    - (2) Dependence of the Bremsstrahlung Spectrum on Photon Angle
    - (3) Screening Effects and Coulomb Corrections
  - E. Corrections for the Cross Section Formulas
    - (1) Coulomb Corrections
      - a. Non-Relativistic Energies
      - b. Intermediate Energies
      - c. Relativistic Energies
    - (2) High-Frequency-Limit Corrections
    - (3) Screening Corrections
  - F. Comparison of Theory and Experiment
    - (1) Cross Section Differential in Photon Energy and Angle
    - (2) Cross Section Differential in Photon Energy
    - (3) Total Cross Section
  - G. Summary

\* The research reported here was supported jointly by the U. S. Atomic Energy Commission, and by the U. S. Air Force, through the Office of Scientific Research of the Air Research and Development Command.

### III. Electron-Electron Bremsstrahlung

A. Maximum Photon Energy

B. Cross Section Formulas for Free Electrons

(1) Non-Relativistic Energies

(2) Extreme-Relativistic Energies

C. Cross Section Formulas with Binding Corrections

### IV. Thick-Target Bremsstrahlung Production

A. Thick-Target Bremsstrahlung Angular Distributions

(1) Non-Relativistic and Intermediate Energies

(2) Relativistic Energies

B. Thick-Target Bremsstrahlung Spectra

(1) Non-Relativistic and Intermediate Energies

(2) Relativistic Energies

C. Efficiency for Bremsstrahlung Production

(1) Non-Relativistic and Intermediate Energies

(2) Relativistic Energies

### V. Acknowledgments

## I. Introduction

Considerable information about the bremsstrahlung process has accumulated during the past several years. This information includes various cross section calculations and measurements, which have helped to provide a more accurate description of the process. Unfortunately this material has never been assembled and integrated in an easily referenced form, although some general reviews<sup>1/</sup> on the subject are available. The present paper is intended to provide a coherent summary of the bremsstrahlung cross section formulas and related data. The theoretical formulas and their specific limitations are presented in a form that is most convenient for practical calculations. In addition, estimates of the accuracy of these formulas are given for cases where comparisons can be made with experimental results. Correction factors that are available are indicated in either numerical or analytical form. A brief summary of other data pertaining to electron-electron and to thick target bremsstrahlung is also included. No results are presented for electron and photon polarization effects.

In the organization of this paper, Section IIB briefly discusses the problem of making exact cross section calculations and indicates the general types of calculations that have been completed. A summary of the various cross section formulas is given in Section IIC. Section IID gives useful graphical information derived from the various formulas in IIC. Section IIE lists corrections that can be applied to the above formulas. In Section IIF, experimental bremsstrahlung cross sections are compared with the theoretical results contained in Section IIC and D. Conclusions with regard to the accuracy of the theory are presented in Section IIG. Section III summarizes the very sparse material that is available on electron-electron bremsstrahlung. Finally, Section IV gives a brief treatment of thick target bremsstrahlung with information on the bremsstrahlung angular distributions (IVA), the spectra (IVB), and the production efficiencies (IVC).

## II. Bremsstrahlung Cross Sections

The cross sections discussed in this section apply to the bremsstrahlung process<sup>2/</sup> in which an electron is decelerated in the field of an atomic nucleus. These cross sections give direct estimates of the properties of the radiation emitted when electrons are incident on thin<sup>3/</sup> targets, and provide basic data for analyzing the thick target bremsstrahlung considered in Section IV.

### A. Symbols, Constants, and Energy-momentum Relations

$E_0, E$  = Initial and final total energy of the electron in a collision, in  $m_0 c^2$  units.\*

$p_0, p$  = Initial and final momentum of the electron in a collision, in  $m_0 c$  units.

$T_0, T$  = Initial and final kinetic energy of the electron in a collision, in  $m_0 c^2$  units.\*

$k, k$  = Energy and momentum of the emitted photon, in  $m_0 c^2$  and  $m_0 c$  units.\*

$\mathcal{E}_0$  = Total energy of an electron incident on a thick target, in  $m_0 c^2$  units.\*

$\mathcal{T}_0$  = Kinetic energy of an electron incident on a thick target, in  $m_0 c^2$  units.\*

$\theta_0, \theta$  = Angles of  $p_0$  and  $p$  with respect to  $k$ .

---

\*This system of units for the symbols is used consistently throughout this paper. For cases in which the data are given in Mev units, these symbols have the multiplicative factor 0.51; for example, the kinetic energy in Mev units is represented by the quantity  $0.51 T_0$ .

- $\emptyset$  = Angle between the planes  $(\underline{p}_0, \underline{k})$  and  $(\underline{p}, \underline{k})$ .
- $d\Omega_k$  = Element of solid angle in the direction of  $\underline{k} = \sin\theta_0 d\theta_0 d\emptyset$ .
- $d\Omega_p$  = Element of solid angle in the direction of  $\underline{p} = \sin\theta d\theta d\emptyset$ .
- $\underline{q}$  = Momentum transferred to the nucleus, in  $m_0 c$  units.
- $= \underline{p}_0 - \underline{p} - \underline{k}$ ;  $q^2 = p_0^2 + p^2 + k^2 - 2p_0 k \cos\theta_0 + 2pk \cos\theta - 2p_0 p (\cos\theta \cos\theta_0 + \sin\theta \sin\theta_0 \cos\emptyset)$ .
- $\beta_0, \beta$  = Ratio of the initial and final electron velocity in a collision to the velocity of light.
- $Z$  = Atomic number of target material.
- $d\sigma_j$  = Bremsstrahlung cross section, differential with respect to the parameter  $j$ , in units of  $\text{cm}^2$  per atom per incident electron.
- $d\tau$  = Volume element.
- $\underline{r}$  = Radius vector from a center, in units of the Compton wave length,  $\lambda_0$ .
- $\alpha$  = Angle of  $\underline{k}$  with respect to the direction of the electron beam incident on a thick target.
- $N_0$  =  $6.03 \times 10^{23}$  atoms (or molecules) per mole.
- $c$  =  $3.00 \times 10^{10}$  cm per sec.
- $e$  =  $4.80 \times 10^{-10}$  esu =  $1.60 \times 10^{-19}$  Coulombs.
- $e^2$  =  $1.44 \times 10^{-13}$  Mev cm.
- $\hbar$  =  $h/2\pi = 6.58 \times 10^{-22}$  Mev sec =  $1.05 \times 10^{-27}$  erg sec.
- $hc$  = 12.4 Kev-Angstroms.
- $\hbar c$  =  $1.97 \times 10^{-11}$  Mev cm.
- $\hbar c/e^2$  = 137.
- $m_0$  =  $9.11 \times 10^{-28}$  gm (electron mass).

$$m_0 c^2 = 0.511 \text{ Mev.}$$

$$\lambda_0 = \hbar/m_0 c = 3.86 \times 10^{-11} \text{ cm (Compton wave length).}$$

$$r_0 = e^2/m_0 c^2 = \lambda_0/137 = 2.82 \times 10^{-13} \text{ cm (Classical electron radius).}$$

$$\phi = Z^2 r_0^2/137 = Z^2 5.78 \times 10^{-28} \text{ cm}^2.$$

$$a_0 = \hbar^2/m_0 e^2 = 0.530 \times 10^{-8} \text{ cm (radius of hydrogen atom).}$$

$$= 137 \lambda_0 = (137)^2 r_0$$

$$\phi_0 = 8\pi r_0^2/3 \text{ (Thomson formula)} = 6.64 \times 10^{-25} \text{ cm}^2.$$

$$e^2/a_0 = 2 I_0 = 27.2 \text{ ev.}$$

$$I_0 = \text{Ionization energy of hydrogen atom} = 1/2(137)^2 \text{ in } m_0 c^2 \text{ units.}$$

$$Z^2 I_0 = \text{Ionization energy of K-electron (if } \ll 1).$$

$$1 \text{ Mev} = 1.60 \times 10^{-6} \text{ erg.}$$

$$E_0^2 = p_0^2 + 1, E^2 = p^2 + 1.$$

$$E_0 = T_0 + 1, E = T + 1.$$

$$E_0 = \frac{1}{\sqrt{1 - \beta_0^2}}, E = \frac{1}{\sqrt{1 - \beta^2}}$$

$$E_0 = k + E.$$

$$p_0 = \sqrt{T_0(T_0 + 2)}, p = \sqrt{T(T + 2)}$$

$$p_0 = \frac{\beta_0}{\sqrt{1 - \beta_0^2}}, p = \frac{\beta}{\sqrt{1 - \beta^2}}$$

$$\beta_0 = \frac{p_0}{E_0}, \beta = \frac{p}{E}.$$

### B. Types of Cross Section Calculations

The bremsstrahlung cross section,  $d\sigma$ , for single photon emission in a large cubic box of side  $L$ , is given by the transition probability per atom per electron. This cross section can be expressed in dimensions of  $\text{cm}^2$  as

$$d\sigma = \frac{w}{\left(\frac{p_o c}{E_o}\right)} \left(\frac{\hbar}{m_o c}\right)^3 L^3 \quad (\text{II-1})$$

where

$$w = \frac{2\pi}{\hbar} \rho_f |H_{if}|^2 \quad (\text{II-2})$$

The term  $\rho_f$  is the density of final states and can be written as

$$\rho_f = \frac{pEk^2 dk d\Omega_k d\Omega_p L^6}{(2\pi)^6 m_o c^2} \quad (\text{II-3})$$

The term  $H_{if}$  is the matrix element for the transition of the system from an initial state before the emission of the photon to a final state after the emission. The quantity  $|H_{if}|^2$  in Formula (II-2) can be written as

$$|H_{if}|^2 = \left(\frac{2\pi}{k} \frac{e^2}{\hbar c}\right) (m_o c^2)^2 \left| \int \psi_f^* (\underline{\lambda} \cdot \underline{\alpha}) e^{-i\underline{k} \cdot \underline{r}} \psi_i d\tau \right|^2 L^{-9} \quad (\text{II-4})$$

In the above,  $\underline{\lambda}$  is the unit polarization vector of the photon,  $\underline{\alpha}$  is the Dirac matrix, and  $\psi_i$  and  $\psi_f$  are the Dirac wave functions for the initial and final electrons, respectively. Therefore the cross section in  $\text{cm}^2$  can be written as

$$d\sigma = \frac{137r_o^2}{(2\pi)^4} \frac{pE_o E}{p_o} \left| \int \psi_f^* (\underline{\lambda} \cdot \underline{\alpha}) e^{-i\underline{k} \cdot \underline{r}} \psi_i d\tau \right|^2 k dk d\Omega_k d\Omega_p \quad (\text{II-5})$$

It is evident that the important quantity to be evaluated is the matrix element,  $H_{if}$ , defined in Formula (II-4).

The problem of evaluating an "exact" expression for the cross section involves, therefore, the use in the matrix element of "exact" wave functions, which describe an electron in a screened, nuclear Coulomb field. It is not possible to solve the Dirac wave equation in closed form for an electron in a Coulomb field, primarily because the wave function must be represented as an infinite series<sup>4/</sup>. Therefore, various approximate wave functions and procedures have been used.

The cross section calculations that have been made may be classified either as non-relativistic or relativistic depending on whether the Schrödinger or Dirac form of the Hamiltonian is used for the electron and field system. The calculations have been carried out with (a) non-relativistic Coulomb wave functions (Sommerfeld), (b) relativistic Coulomb wave functions (Sommerfeld-Maue) valid to first order in  $\left(\frac{Z}{137}\right)^{2/l}$ , where  $l$  is the angular momentum quantum number that is the summation index in the expansion of the wave function, and (c) free-particle wave functions perturbed to first order in  $Z$  (Born-approximation procedure).

The non-relativistic cross section formulas derived in the dipole approximation by Sommerfeld<sup>5/</sup> with Coulomb wave functions have a complicated form with hypergeometric functions and are difficult to evaluate. Some numerical estimates<sup>6/</sup> of the Sommerfeld cross sections have been made for selected values of the electron energy, the target atomic number, and the photon energy. However, the theory is only valid when  $\beta_0$  is small compared to unity, and it can be expected to break down for initial electron energies greater than a few kilovolts. In addition, the theory disregards screening effects which are important for very low energies and for targets with high atomic numbers. Because of these limitations, the results of the Sommerfeld theory are not presented in this report.

Cross section calculations with relativistic Coulomb wave functions (Sommerfeld-Maue) including screening corrections have been made by Olsen, Maximon, and Wergeland<sup>7/</sup> and by Olsen and Maximon<sup>8/</sup>. Their formulas are valid only in the extreme-relativistic region (above 50 Mev). Their results have the form of an additive correction factor to the Born-approximation formulas.

The cross section formulas calculated by the Born-approximation procedure with free-particle wave functions are available in a relatively simple analytical form for non-relativistic and relativistic energies, with or without screening. In general, the Born approximation theory becomes less reliable as (a) the atomic number of the target increases, (b) the initial electron energy decreases, and (c) the photon energy approaches the high frequency limit. However, in spite of their limited validity, the Born-approximation formulas have been surprisingly successful in predicting the properties of the bremsstrahlung radiation. Even where there is a breakdown of the Born approximation, the accuracy of the cross section formulas is still reasonably good, and in the worst cases (except at the high frequency limit), they can be expected to give at least the correct order of magnitude. Therefore, this paper emphasizes the Born-approximation cross section formulas and includes various theoretical and empirical corrections to these formulas. Detailed references to the many papers in which these formulas are derived are given in Table 3.

### C. Bremsstrahlung Cross Section Formulas and Classification Diagrams

A general classification of the various differential forms of the bremsstrahlung cross section is presented in Chart 1 for the Born-approximation formulas and in Chart 2 for the extreme-relativistic formulas that contain the Coulomb correction. The formulas represented in these charts are summed over the directions of the electron spin and the photon polarization vectors, and do not include all of the possible differential forms of the cross section. The primary formula gives the cross section that is differential in photon energy and in photon and electron emission angles. The remaining formulas that branch out from this starting point are divided into two main groups that are designated as screened or non-screened. Further subdivisions are made; these depend on the type of screening approximation, and on whether non-relativistic, extreme-relativistic, small-angle, or large-angle approximations are used. For most of the cases, the charts include the names of the principal authors associated with a particular formula.

The formulas are identified as follows: (a) the number applied to a particular differential form of the cross section, (b) the first letter indicates either B for Born approximation (Chart 1) or C for Coulomb correction (Chart 2), (c) the second letter indicates either S for screening or N for no screening, and (d) the last letter a, b, or c indicates further subdivisions for specific approximations. The following notation has been adopted in this report. The differential forms of the bremsstrahlung cross section are designated by the symbol,  $d\sigma_{\alpha,\beta,\dots}$ . This symbol is the bremsstrahlung cross section that is differential only with respect to the parameters given by the subscripts  $\alpha, \beta, \dots$ , and is explicitly defined by  $d\sigma_{\alpha,\beta,\dots} = \frac{d^n \sigma}{d\alpha d\beta \dots} d\alpha d\beta \dots$ . The unit of the cross section,  $d\sigma_{\alpha,\beta,\dots}$ , is  $\text{cm}^2$  per atom per incident electron.

The symbols and definitions for the specific cross sections are as follows:

(a)  $d\sigma_{k,\theta_0,\theta,\emptyset}$  is the bremsstrahlung cross section that is differential with respect to the photon energy,  $k$ , and to the photon and electron emission angles,  $\theta_0, \theta$ , and  $\emptyset$ . This formula contains the parameters  $E_0, Z, k, \theta_0, \theta$ , and  $\emptyset$ .

(b)  $d\sigma_{k,\theta_0,\emptyset}$  is the bremsstrahlung cross section that is differential with respect to the photon energy,  $k$ , and the emission angles  $\theta_0$  and  $\emptyset$ . It can be obtained by integrating the differential cross section in (a) over the direction of the outgoing electron. This formula contains the parameters  $E_0, Z, k$ , and  $\theta_0$ .

(c)  $d\sigma_k$  is the bremsstrahlung cross section that is differential with respect to the photon energy,  $k$ . It can be obtained by integrating the differential cross section in (a) over the emission directions of the photon and the electron. This formula contains the parameters  $E_0, Z$ , and  $k$ .

(d)  $\emptyset_{\text{rad}}$  is the only cross section symbol used in this report that does not represent a differential form of the bremsstrahlung cross section.

It is equal to the quantity,  $\frac{1}{E_0} \int_0^{T_0} k d\sigma_k$ . This form of a total bremsstrahlung

cross section integrated over photon energy and photon and electron emission angles was introduced by Heitler<sup>9/</sup>, who has defined it as the cross section for the energy lost by radiation. This formula contains the parameters  $E_0$  and  $Z$ .

The Born-approximation formulas that apply to Chart 1 are presented in Table 1, and the extreme-relativistic formulas with the Coulomb correction that apply to Chart 2 are presented in Table 2. The important references and approximations for the formulas in Tables 1 and 2 are listed in Table 3. The explicit expressions for the formulas in Tables 1 and 2 are not necessarily the same as the formulas in the original references because the attempt is made to use consistent units and symbols, with energies and momenta expressed in  $m_0 c^2$  and  $m_0 c$  units respectively.

CHART 1

Born Approximation Cross Section Formulas

$d\sigma_{k,\theta,\phi}$   
(Differential in Photon Energy and in Photon and Electron Emission Angles.)

$d\sigma_{k,\theta,\phi}$   
(Differential in Photon Energy and Angle.)

$d\sigma_k$   
(Differential in Photon Energy.)

$\sigma_{rad}$   
(Total Radiation Cross Section.)

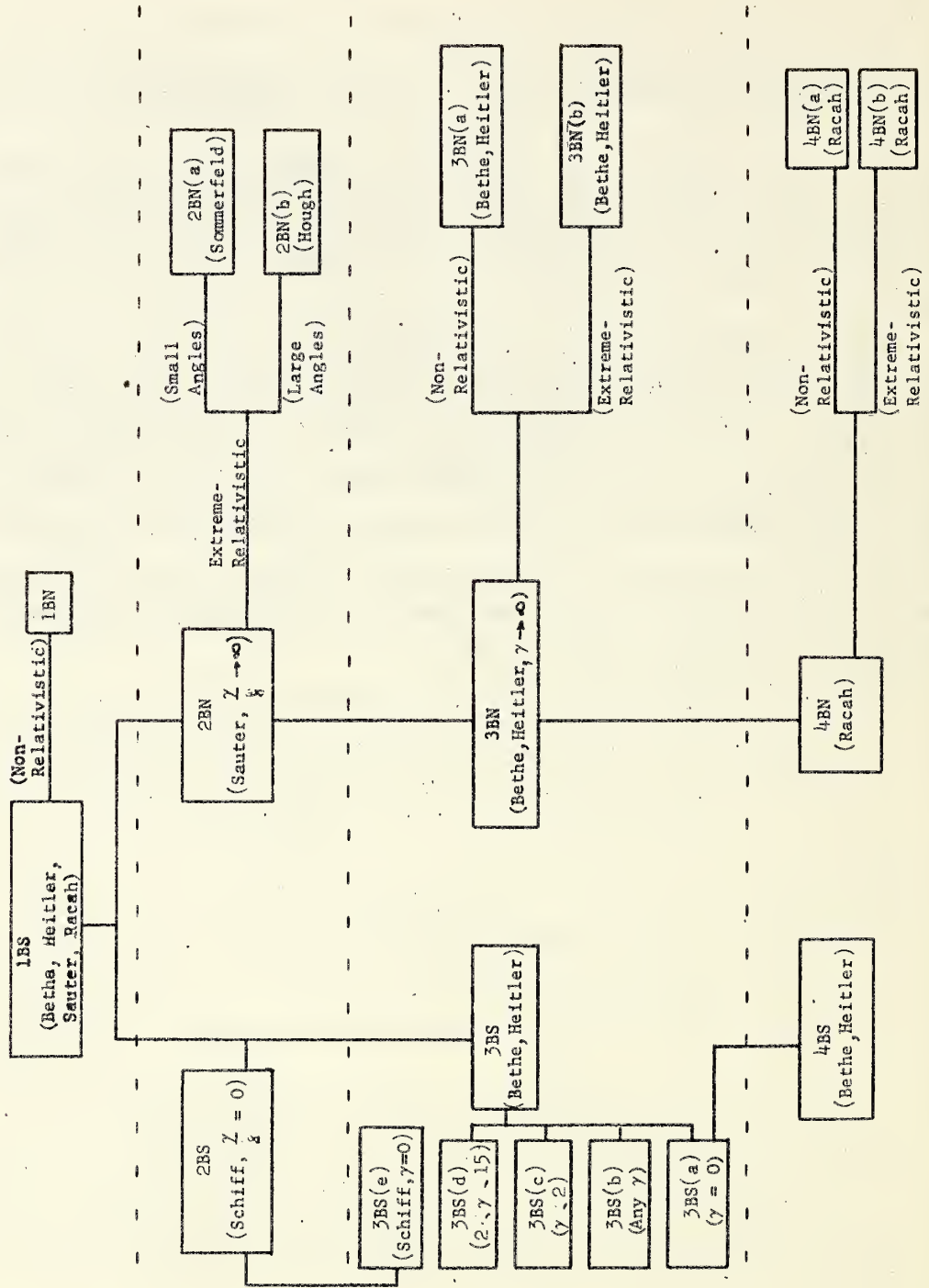


CHART 2

Extreme-Relativistic Cross Section Formulas with Coulomb Correction

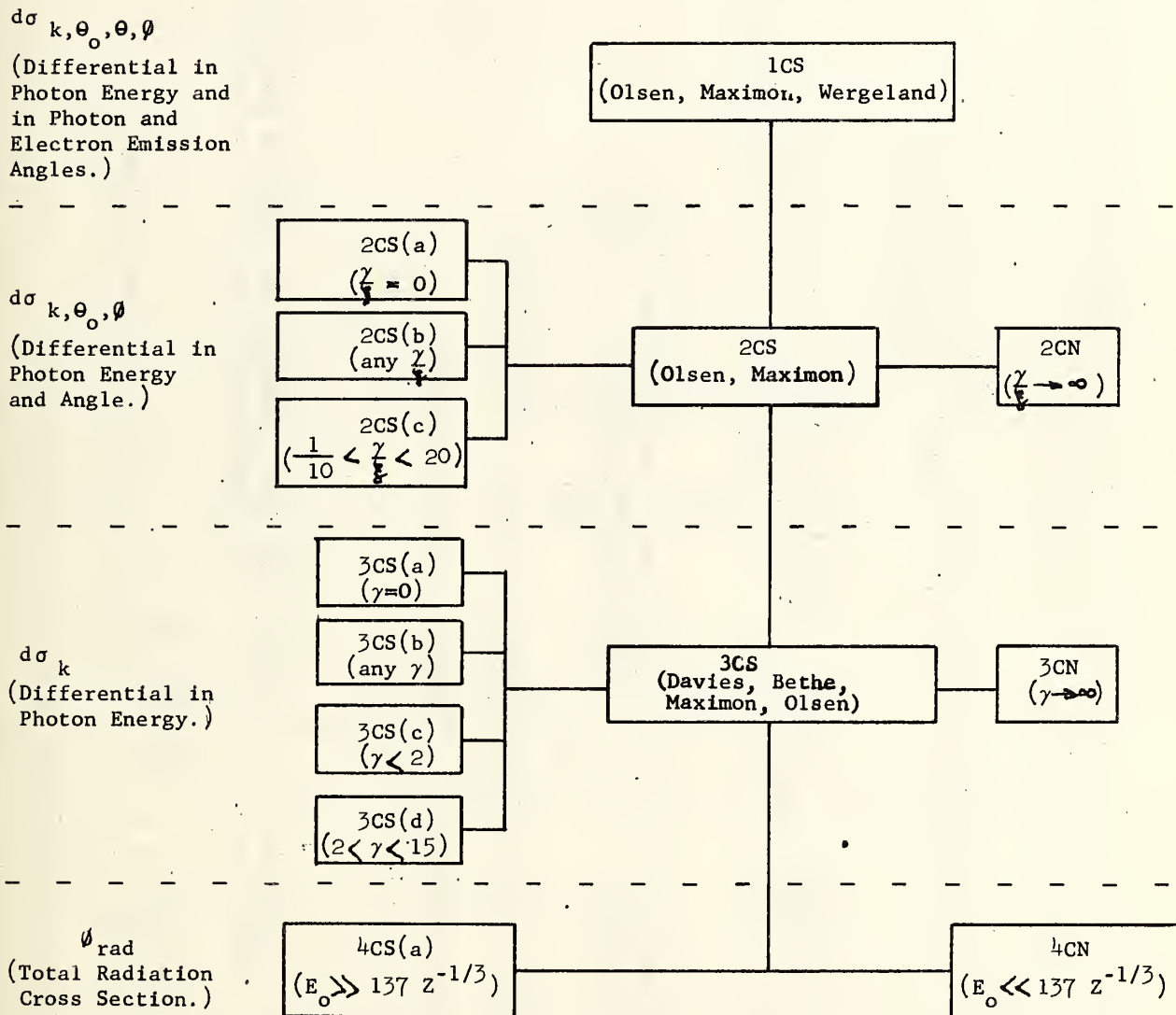


TABLE 1

Born-Approximation Cross Section Formulas

Formula 1BS - Differential in photon energy and in photon and electron emission angles. Approximation (H). Reference Formulas: 13 in ref. (a), 2 in ref. (b), 13 in ref. (c), 29 in ref. (e).

$$d\sigma_{k,\theta,\theta_0,\phi} = \frac{Z^2}{137} \left( \frac{r_0}{2\pi} \right)^2 [1 - F(q, Z)]^2 \frac{dk}{k} \frac{p}{p_0} \frac{d\Omega}{q^4} \left\{ \frac{p \sin^2 \theta}{(E - p \cos \theta)^2} + \frac{p^2 \sin^2 \theta_0}{(E_0 - p_0 \cos \theta_0)^2} + \frac{p^2 \sin^2 \theta}{(4E_0^2 - q^2)} \right\} (4E_0^2 - q^2)$$

$$2pp_0 \sin \theta \sin \theta_0 \cos \phi (4E_0^2 - q^2) + \frac{2k^2 (p^2 \sin^2 \theta + p_0^2 \sin^2 \theta_0 - 2pp_0 \sin \theta \sin \theta_0 \cos \phi)}{(E - p \cos \theta)(E_0 - p_0 \cos \theta_0)}$$

where  $q^2 = p^2 + p_0^2 + k^2 - 2p_0 k \cos \theta + 2pk \cos \theta - 2p_0 p (\cos \theta \cos \theta_0 + \sin \theta \sin \theta_0 \cos \phi)$

and  $F(q, z)$  = Atomic Form factor discussed in Section IIE (3)

Formula 1BN - Differential in photon energy and in photon and electron emission angles. Approximations (H), (B), (I). Reference Formula 17 in ref. (c).

$$d\sigma_{k,\theta,\theta_0,\phi} = \frac{Z^2}{137} \left( \frac{r_0}{\pi} \right)^2 \frac{dk}{k} \frac{p}{p_0} \frac{d\Omega}{q^4} \left\{ \frac{p \sin^2 \theta + p_0^2 \sin^2 \theta_0 - 2pp_0 \sin \theta \sin \theta_0 \cos \phi}{q} \right\}$$

where  $q^2 = p^2 + p_0^2 - 2pp_0 (\cos \theta \cos \theta_0 + \sin \theta \sin \theta_0 \cos \phi)$

TABLE 1 (Continued)

Formula 2BS - Differential in photon energy and angle.

Approximations (H), (G), (M), (J), (K). Reference Formula 1 in ref. (h).

$$d\sigma_{k,\theta_0} = \frac{4Z^2 r_0^2}{137} \frac{dk}{k} y dy \left\{ \frac{16y^2 E_0}{(y^2+1)^4 E_0} - \frac{(E_0+E)^2}{(y^2+1)^2 E_0^2} \left[ \frac{E_0^2+E^2}{(y^2+1)^2 E_0^2} - \frac{4y^2 E}{(y^2+1)^4 E_0} \right] \ln(y) \right\}$$

where  $y = E_0 \theta_0$ ,  $\frac{1}{M(y)} = \left( \frac{k}{2E_0 E} \right)^2 + \left( \frac{Z^{1/3}}{111(y^2+1)} \right)^2$

Comment: This formula becomes Formula 2BN(a) when  $Z = 0$  in  $M(y)$ .

Formula 2BN - Differential in photon energy and angle.

Approximations (H), (B). Reference Formulas: 11 in ref. (d), 4.1 in ref. (f).

$$d\sigma_{k,\theta_0,\theta} = \frac{Z^2 r_0^2}{8\pi 137} \frac{dk}{k} \frac{p}{p_0} d\Omega_k \left\{ \frac{8 \sin^2 \theta_0^2 (2E_0^2+1)}{p_0^2 \Delta_0^4} - \frac{2(5E_0^2+2EE_0+3)}{p_0^2 \Delta_0^2} - \frac{2(p_0^2-k^2)}{Q^2 \Delta_0^2} + \frac{4E}{p_0^2 \Delta_0} + \frac{L}{pp_0} \left[ \frac{4E_0 \sin^2 \theta_0 (3k-p_0^2 E)}{p_0^2 \Delta_0^4} + \frac{4E_0^2 (E_0^2+E^2)}{p_0^2 \Delta_0^2} \right] \right. \\ \left. + \frac{2-2(7E_0^2-3EE_0+E^2)}{p_0^2 \Delta_0^2} + \frac{2k(E_0^2+EE_0-1)}{p_0^2 \Delta_0} \right\} - \left( \frac{4\epsilon}{p\Delta_0} \right) + \left( \frac{\epsilon^Q}{pQ} \right) \left[ \frac{4}{\Delta_0^2} - \frac{6k}{\Delta_0} - \frac{2k(p_0^2-k^2)}{Q^2 \Delta_0} \right]$$

where  $L = \ln \left[ \frac{EE_0-1+pp_0}{EE_0-1-pp_0} \right]$ ;  $\Delta_0 = E_0 - p_0 \cos \theta_0$ ;  $\epsilon = \ln \left[ \frac{E+p}{E-p} \right]$ ;  $\epsilon^Q = \ln \left[ \frac{Q+p}{Q-p} \right]$

$$Q^2 = p_0^2 + k^2 - 2p_0 k \cos \theta_0$$

Formula 2BN(a) - Differential in photon energy and angle.

Approximations (H), (B), (J), (K).

$$d\sigma_{k,\theta_0,\theta} = \frac{2Z^2 r_0^2}{\pi 137} \frac{E}{E_0} \frac{dk}{k} d\Omega_k \left\{ \frac{16(\theta_0 E_0)^2 E_0^2}{(1+\theta_0^2 E_0^2)^4} - \frac{(E_0+E)^2 E_0}{E(1+\theta_0^2 E_0^2)^2} + 2\ln \left( \frac{EE_0}{k} \right) \left[ \frac{(E^2+E_0^2) E_0}{E(1+\theta_0^2 E_0^2)^2} - \frac{4\theta_0^2 E_0^4}{(1+\theta_0^2 E_0^2)^4} \right] \right\}$$

Comment: This formula was obtained from Formula 2BN by making the high energy and small angle approximations. The same result is obtainable from Formula 2BS by setting  $Z=0$  in  $M(y)$ .

Formula 2BN(b) - Differential in photon energy and angle.

Approximations (H), (B), (J), (L). Reference Formula 8 in ref. (i).

$$d\sigma_{k,\theta_0,\theta} = \frac{Z^2 r_0^2}{4\pi 137} \frac{E}{E_0^3} \frac{dk}{k} \frac{d\Omega_k}{(1-\cos \theta_0)^2} \left\{ \left( \frac{E_0^2+E^2}{EE_0} \right) \sin^2 \theta_0 \ln \frac{2E_0 E}{k} - \frac{(5E_0+2E)}{E_0} + \frac{2[E^2-2E^2 \ln \frac{k}{E_0}]}{E_0 E} [1-\cos \theta_0] - \frac{E [Q^2+E(k-E_0 \cos \theta_0)]}{E_0 Q^2 (1-\cos \theta_0)} \right. \\ \left. - \frac{E k (1-\cos \theta_0)}{EQ^3} [3Q^2+E(E_0+k)] \ln \left( \frac{E+E}{Q-E} \right) \right\}$$

where  $Q^2 = E^2 + 2kE_0(1-\cos \theta_0)$

TABLE 1 (Continued)

Formula 3BS - Differential in photon energy.

Approximations (H), (J). Reference Formulas: 31,34,35 in ref. (a); 62 in ref. (b);  
21, 26 in ref. (c); 56-58b in ref. (j).

$$d\sigma_k = \frac{4Z^2 r_o^2}{137} \frac{dk}{k} \left\{ \left( 1 + \left( \frac{E}{E_o} \right)^2 \right) \left[ \frac{\phi_1(\gamma)}{4} - \frac{1}{3} \ln Z \right] - \frac{2 \cdot E}{3 E_o} \left[ \frac{\phi_2(\gamma)}{4} - \frac{1}{3} \ln Z \right] \right\}$$

Formula 3BS(a) - Complete screening ( $\gamma=0$  or  $\phi_1(\gamma=0) = 4 \ln 183$ ;  $\phi_2(\gamma=0) = \phi_1(\gamma=0) - \frac{2}{3}$ )

Formula 3BS with  $\gamma=0$ :

$$d\sigma_k = \frac{4Z^2 r_o^2}{137} \frac{dk}{k} \left\{ \left[ 1 + \left( \frac{E}{E_o} \right)^2 - \frac{2}{3} \frac{E}{E_o} \right] \ln(183Z^{-1/3}) + \frac{1}{9} \frac{E}{E_o} \right\}$$

Formula 3BS(b) - Arbitrary screening

$$d\sigma_k = \frac{4Z^2 r_o^2}{137} \frac{dk}{k} \left\{ \left( 1 + \left( \frac{E}{E_o} \right)^2 \right) \left[ \int_0^1 (q-\delta)^2 (1-F(q))^2 \frac{dq}{q^3} + 1 \right] - \frac{2}{3} \frac{E}{E_o} \left[ \int_0^1 (q^3 - 6\delta^2 q \ln \frac{q}{\delta} + 3\delta^2 q - 4\delta^3) \right. \right. \\ \left. \left. \times \left( 1-F(q) \right)^2 \frac{dq}{q} + \frac{5}{6} \right] \right\}$$

$$\text{where } \delta = \frac{k}{2E_o E}$$

Formula 3BS(c) - Intermediate screening I ( $\gamma < 2$ )

Formula 3BS with  $\phi_1(\gamma)$  and  $\phi_2(\gamma)$  given in Figure 1.

Formula 3BS(d) - Intermediate screening II ( $2 < \gamma < 15$ )

Formula 3BS with  $\phi_1(\gamma) = \phi_2(\gamma) = 19.19 - 4 \ln \gamma - 4c(\gamma)$  with  $c(\gamma)$  given in Figure 2:

$$d\sigma_k = \frac{4Z^2 r_o^2}{137} \frac{dk}{k} \left[ 1 + \left( \frac{E}{E_o} \right)^2 - \frac{2}{3} \frac{E}{E_o} \right] \left[ \ln \frac{2E_o E}{k} - \frac{1}{2} - c(\gamma) \right]$$

Formula 3BS(e) - Differential in photon energy.

Approximations (H), (G), (M), (J). Reference Formula 3 in ref. (h).

$$d\sigma_k = \frac{2Z^2 r_o^2}{137} \frac{dk}{k} \left\{ \left( 1 + \left( \frac{E}{E_o} \right)^2 - \frac{2}{3} \frac{E}{E_o} \right) \left( \ln M(0) + 1 - \frac{2}{b} \tan^{-1} \frac{E}{b} \right) \frac{E}{E_o} \left[ \frac{2}{b^2} \ln(1+b^2) + \frac{4(2-b^2)}{3b^3} \tan^{-1} b - \frac{8}{3b^2} + \frac{2}{9} \right] \right\}$$

$$\text{where } b = \left( \frac{2E_o E Z^{1/3}}{111k} \right); \frac{1}{M(0)} = \left( \frac{k}{2E_o E} \right)^2 + \left( \frac{Z^{1/3}}{111} \right)^2$$

Comments: This formula is obtained from Formula 50 of ref. (b).

TABLE 1 (Continued)

Formula 3BN - Differential in photon energy.

Approximations (H), (B).

Reference Formulas: 15 in ref. (a), 16 in ref. (c), 17 in ref. (d), 37 in ref. (e).

$$d\sigma_k = \frac{Z^2 r_o^2}{137} \frac{dk}{k} \frac{p}{p_o} \left[ \frac{4}{3} - \frac{2E_o E}{k p_o} + \left( \frac{E_o E}{3 p_o} + \frac{E E_o}{p_o p} - \frac{E E_o}{p_o} \right) \left[ \frac{8E_o E}{3 p_o p} + L \frac{E E_o}{p_o p} \right] + \frac{k^2 (E_o^2 + p_o^2)^2}{3^3 p_o p} + \frac{k}{2 p_o p} \left( \frac{E_o E + p^2}{3 p_o} \right) \left( \frac{E_o E + p^2}{p} \right) \left( \frac{E_o E + p^2}{p} \right) \left( \frac{E_o E + p^2}{p} \right) \right]$$

where  $L = 2 \ln \left[ \frac{E_o E + p_o p - 1}{k} \right]; \quad \xi_o = \ln \left( \frac{E_o + p_o}{E_o - p_o} \right); \quad \xi = \ln \left( \frac{E + p}{E - p} \right)$

Formula 3BN(a) - Differential in photon energy.

Approximations (H), (B), (I). Reference formula 18 in ref. (c).

$$d\sigma_k = \frac{Z^2 r_o^2}{137} \frac{dk}{k} \frac{1}{3} \frac{dk}{k} \frac{1}{2} \ln \left( \frac{p_o + p}{p_o - p} \right)$$

Formula 3BN(b) - Differential in photon energy.

Approximations (H), (B), (J).

Reference Formulas: 16 in ref. (a), 21 in ref. (c), 56 in ref. (j).

$$d\sigma_k = \frac{4Z^2 r_o^2}{137} \frac{dk}{k} \left[ \left( \frac{E}{E_o} \right)^2 - \frac{2}{3} \frac{E}{E_o} \right] \left[ \ln \left( \frac{2E_o E}{k} \right) - 1/2 \right]$$

Comment: This formula results directly from Formula 3BS(e) when  $b \rightarrow 0$  and from Formula 3BS when  $\gamma \rightarrow \infty$ .

TABLE 1 (Continued)

Formula 4BS - Total Radiation Cross Section.  
 Approximations (H), (F), (J). Reference Formulas 47 in ref. (a), 34 in ref. (c), 62 in ref. (j).

$$\sigma_{\text{rad}} = \frac{4Z^2 r_0^2}{137} \left[ \ln(183Z^{-1/3}) + \frac{1}{18} \right]$$

Formula 4BN - Total Radiation Cross Section.  
 Approximations (H), (C). Reference Formulas: 29 in ref. (c), 41 in ref. (e).

$$\sigma_{\text{rad}} = \frac{Z^2 r_0^2}{137} \left\{ \frac{(12E_0^2 + 4)}{3E_0 P_0} \ln(E_0 + P_0) - \frac{(8E_0 + 6P_0)}{3E_0 P_0} \left[ \ln(E_0 + P_0) \right]^2 - \frac{4}{3} + \frac{2}{E_0 P_0} \left[ F(x) \right] \right\}$$

where  $F(x) = \int_0^x \frac{\ln(1+y)}{y} dy$  and  $x = 2P_0(E_0 + P_0)$

For small  $x$ ,  $F$  can be expanded in the power series:

$$F(x) = x - \frac{x^2}{4} + \frac{x^3}{9} - \frac{x^4}{16} + \dots$$

For large  $x$ ,  $F$  is given by

$$F(x) = \frac{1}{6} \pi + \frac{1}{2} (\ln x)^2 - F\left(\frac{1}{x}\right)$$

Formula 4BN(a) - Total Radiation Cross Section.  
 Approximations (H), (C), (I). Reference Formulas: 32 in ref. (c), 21 in ref. (d).

$$\sigma_{\text{rad}} = \frac{16}{3} \frac{Z^2 r_0^2}{137}$$

Formula 4BN(b) - Total Radiation Cross Section.  
 Approximations (H), (C), (J). Reference Formulas: 33 in ref. (c), 41 in ref. (e), 61 in ref. (j), 46 in (a), 22 in (d).

$$\sigma_{\text{rad}} = \frac{4Z^2 r_0^2}{137} \left( \ln 2E_0 - \frac{1}{3} \right)$$

TABLE 2

Bremsstrahlung Cross Section Formulas With Coulomb Correction

Formula 1CS - Differential in photon energy and in photon and electron emission angles. Approximation (J), (N). Reference Formula 7b.13 in ref. (m).

$$d\sigma_{k, \theta_0, \theta, \psi} = \frac{Z^2}{137} \left(\frac{r_0}{2\pi}\right)^2 \frac{dk}{k} \frac{p}{p_0} \frac{d\Omega_k d\Omega_p}{q_{\perp}} \left| \int_{q_z}^{\infty} dy \frac{\sqrt{y^2 - q_{\perp}^2} (1-F(y))}{y} \int_0^{\infty} d\rho \cdot \rho J_1(q_{\perp} \rho) J_1(\rho \sqrt{y^2 - q_z^2}) \exp\left\{2ia \int_0^{\infty} \frac{J_0(x\rho) [1-F(x)] dx}{x}\right\} \right|^2$$

$$\left\{ \frac{p^2 \sin^2 \theta}{(E - \cos \theta)^2} (4E_0^2 - q^2) + \frac{p_0^2 \sin^2 \theta_0}{(E_0 - p_0 \cos \theta_0)^2} (4E_0^2 - q^2) - \frac{2pp_0 \sin \theta \sin \theta_0 \cos \theta}{(E - p \cos \theta)(E_0 - p_0 \cos \theta_0)} + 2k^2 \frac{(p^2 \sin^2 \theta + p_0^2 \sin^2 \theta_0 - 2pp_0 \sin \theta \sin \theta_0 \cos \theta)}{(E - p \cos \theta)(E_0 - p_0 \cos \theta_0)} \right\}$$

where  $q^2 = p^2 + p_0^2 + k^2 - 2p_0 k \cos \theta + 2pk \cos \theta - 2p_0 p (\cos \theta \cos \theta_0 + \sin \theta \sin \theta_0 \cos \psi)$

$q_z = p_0 \cos \theta_0 + p \cos \theta - k$ ;  $q_{\perp}^2 = p_0^2 \sin^2 \theta_0 + p^2 \sin^2 \theta - 2p_0 p \sin \theta \sin \theta_0 \cos \psi$

F(x), F(y) are Atomic Form Factors discussed in Section IIE(3) and functions of the momentum variables x and y. F(x) cannot be set identically to zero as discussed in ref. (n).

Formula 2CS - Differential in photon energy and angle. Approximation (J), (N). Reference Formula 7.2 in ref. (n).

$$d\sigma_{k, \theta_0} = \frac{2Z^2 r_0^2}{137} \frac{dk}{k} \frac{d\frac{1}{\delta}}{E_0^2} \left\{ (E_0^2 + E^2) (3 + 2\Gamma) - 2E_0 E (1 + 4u^2 \frac{1}{\delta} \Gamma) \right\}$$

where  $\frac{1}{\delta} = \frac{1}{1+u^2}$ ;  $u = p_0 \theta_0$ ;  $\Gamma = \ln\left(\frac{1}{\delta}\right) - 2 - f(Z) + \mathcal{F}\left(\frac{\delta}{\delta}\right)$

$$\mathcal{F}\left(\frac{\delta}{\delta}\right) = \int_{\frac{\delta}{\delta}}^{\infty} \frac{[1-F(q)]^2 - 1}{q} dq; \delta = \frac{k}{2E_0 E}$$

Formula 2CS(a) - Complete screening ( $\frac{\gamma}{\delta} = 0$ , where  $\gamma = \frac{100k}{E_0 E Z^{1/3}}$ )

Formula 2CS with  $\mathcal{F} = \ln\left(\frac{111\gamma}{200\delta}\right)$  or  $\Gamma = \ln\left(\frac{111Z^{-1/3}}{\delta}\right) - 2 - f(Z)$ ,

where  $f(Z) = 1.2021 \left(\frac{Z}{137}\right)^2$  for low Z

$= 0.925 \left(\frac{Z}{137}\right)^2$  for high Z. See ref. (k) for further discussion.

Formula 2CS(b) - Arbitrary screening

Formula 2CS with the form factor, F(q), as an arbitrary function

Formula 2CS(c) - Intermediate screening

Formula 2CS with  $\mathcal{F}\left(\frac{\delta}{\delta}\right)$  given by:

$\frac{6Z^{1/3}}{121\delta}$	0.5	1.0	2.0	4.0	8.0	15.0	20.0	25.0	30.0	50.0	100.0
$-\mathcal{F}\left(\frac{\delta}{\delta}\right)$	0.0145	0.0490	0.1400	0.3395	0.6758	1.126	1.370	1.564	1.728	2.216	2.897

Formula 2CN - Non screened case

Formula 2CS with  $\Gamma = \ln\left(\frac{1}{\delta}\right) - 2 - f(Z)$

TABLE 2 (Continued)

Formula 3CS - Differential in photon energy.  
Approximation (J). Reference Formula 1 in ref. (l).

$$d\sigma_k = \frac{4Z^2 r_o^2}{137} \frac{dk}{k} \left\{ \left( 1 + \left( \frac{E}{E_o} \right)^2 \right) \left[ \frac{\theta_1(\gamma)}{4} - \frac{1}{3} \ln Z - f(Z) \right] - \left( \frac{2}{3} \frac{E}{E_o} \right) \left[ \frac{\theta_2(\gamma)}{4} - \frac{1}{3} \ln Z - f(Z) \right] \right\}$$

Formula 3CS(a) - Complete screening ( $\gamma=0$  or  $\theta_1(\gamma=0) = 4 \ln 183, \theta_2(\gamma=0) = \theta_1(\gamma=0) - \frac{2}{3}$ )

Formula 3CS with  $\gamma=0$ :

$$d\sigma_k = \frac{4Z^2 r_o^2}{137} \frac{dk}{k} \left\{ \left[ 1 + \left( \frac{E}{E_o} \right)^2 \right] - \frac{2}{3} \frac{E}{E_o} \left[ \ln(183Z^{-1/3}) - f(Z) \right] - \frac{1}{9} \frac{E}{E_o} \right\}$$

Formula 3CS(b) - Arbitrary screening

$$d\sigma_k = \frac{4Z^2 r_o^2}{137} \frac{dk}{k} \left\{ \left( 1 + \left( \frac{E}{E_o} \right)^2 \right) \left[ \int_{\delta}^1 (q-\delta)^2 (1-F(q))^2 \frac{dq}{q^3} + 1 - f(Z) \right] - \frac{2}{3} \frac{E}{E_o} \left[ \int_{\delta}^1 (q^3 - 6\delta^2 q \ln \frac{q}{\delta} + 3\delta^2 q - 4\delta^3) (1-F(q))^2 \frac{dq}{q^4} + \frac{5}{6} - f(Z) \right] \right\}$$

$$\text{where } \delta = \frac{k}{2E_o E}$$

Formula 3CS(c) - Intermediate screening I ( $\gamma < 2$ )

Formula 3CS with  $\theta_1(\gamma)$  and  $\theta_2(\gamma)$  given in Figure 1.

Formula 3CS(d) - Intermediate screening II ( $2 < \gamma < 15$ )

Formula 3CS with  $\theta_1(\gamma) = \theta_2(\gamma) = 19.19 - 4 \ln \gamma - 4c(\gamma)$  with  $c(\gamma)$  given in Figure 2:

$$d\sigma_k = \frac{4Z^2 r_o^2}{137} \frac{dk}{k} \left[ 1 + \left( \frac{E}{E_o} \right)^2 - \frac{2}{3} \frac{E}{E_o} \left[ \ln \frac{2E_o E}{k} - \frac{1}{2} - c(\gamma) - f(Z) \right] \right]$$

Formula 3CN - Non screened case ( $\gamma = \infty$  or  $C(\gamma) = 0$ )

Formula 3CS with  $\gamma = \infty$ :

$$d\sigma_k = \frac{4Z^2 r_o^2}{137} \frac{dk}{k} \left[ 1 + \left( \frac{E}{E_o} \right)^2 - \frac{2}{3} \frac{E}{E_o} \left[ \ln \frac{2E_o E}{k} - \frac{1}{2} - f(Z) \right] \right]$$

Formula 4CS - Total Radiation Cross Section.  
Approximation (J). Reference Formula 45 in ref. (k).

$$\sigma_{\text{rad}} = \frac{4Z^2 r_o^2}{137} \left[ \ln(183Z^{-1/3}) + \frac{1}{18} - f(Z) \right]$$

Formula 4CN - Total Radiation Cross Section.  
Approximation (J). Reference Formula 44 in ref. (k).

$$\sigma_{\text{rad}} = \frac{4Z^2 r_o^2}{137} \left[ \ln 2E_o - \frac{1}{3} - f(Z) \right]$$

TABLE 3

Approximations, Conditions of Validity and References for Bremsstrahlung Formulas of Tables 1 and 2.

<u>Approximation</u>	<u>Condition of Validity</u>
A. Nonscreened	$60Z^{-1/3} (1+p_o^2 \theta_o^2) \gg (E_o E/k)$
B. Nonscreened	$137Z^{-1/3} \gg (E_o E/k)$
C. Nonscreened	$E_o \ll 137Z^{-1/3}$
D. Complete screening	$60Z^{-1/3} (1+p_o^2 \theta_o^2) \ll (E_o E/k)$
E. Complete screening	$137Z^{-1/3} \gg (E_o E/k)$
F. Complete screening	$E_o \gg 137Z^{-1/3}$
G. Approximate screening potential:	$(Ze/r) \exp(-r/a)$
H. Born approximation	$(2\pi Z/137\beta_o), (2\pi Z/137\beta) \ll 1$
I. Nonrelativistic	$\beta_o \ll 1$
J. Extreme relativistic	$E_o, E, k \gg 1$
K. Small angles	$\sin \theta = \theta$
L. Large angles	$\theta_o \gg 0$
M. Approximation in electron angle integration. Result not accurate for	$\theta_o \lesssim (Z^{1/3}/111E_o)$
N. Small angles	$\frac{1}{5} < p_o \theta_o < 5$

Table 3 (Continued)

- (a) H. Bethe and W. Heitler, Proc. Roy. Soc. A., 146, 83 (1934).
- (b) H. Bethe, Proc. Camb. Phil. Soc., 30, 524 (1933).
- (c) W. Heitler, Quantum Theory of Radiation (Oxford Univ. Press, London, Third Edition, 1954), 244.
- (d) F. Sauter, Ann. d. Phys., 20, 404 (1934).
- (e) G. Racah, Nuovo Cimento, 11, 469 (1934).
- (f) R. L. Gluckstern and M. H. Hull, Jr., Phys. Rev., 90, 1030 (1953).
- (g) A. Sommerfeld, Wellenmechanik, (Frederick Ungar, New York, 1950), Chap. 7.
- (h) L. I. Schiff, Phys. Rev., 83, 252 (1951).
- (i) P. V. C. Hough, Phys. Rev., 74, 80 (1948).
- (j) E. Segre, Experimental Nuclear Physics, (Wiley, New York, 1953), 260.
- (k) H. Davies, H. A. Bethe, L. C. Maximon, Phys. Rev. 93, 788 (1954).
- (l) H. Olsen, Phys. Rev., 99, 1335 (1955).
- (m) H. Olsen, L. C. Maximon, H. Wergeland, Phys. Rev., 106, 27 (1957).
- (n) H. Olsen, L. C. Maximon, Phys. Rev. (To be published).

(1) Born-Approximation Cross Section Formulas

The Born-approximation calculations require the initial and final electron kinetic energies in a collision to be large enough to satisfy the conditions:  $(2\pi Z/137\beta_0)$ ,  $(2\pi Z/137\beta) \ll 1$ . At extreme-relativistic energies, the cross sections predicted by the Born-approximation formulas are larger than the true cross sections. For example, the value of the total cross section predicted for lead by the Born-approximation formula is about 10 percent larger than the value predicted by more accurate formulas<sup>7/</sup>. At very low energies, the situation is reversed and the Born-approximation cross section is smaller than the true cross section. The energy region in which the Born-approximation formulas require only small corrections is approximately between 4 and 10 Mev for the initial electron kinetic energy. As a rough guide, it is estimated that Born-approximation formulas for the total radiation cross section,  $\sigma_{\text{rad}}$ , are correct to within 10 percent for initial electron kinetic energies above 2 Mev and within a factor of two below 2 Mev.

(2) Extreme-Relativistic Cross Section Formulas with the Coulomb Correction

The formulas in Table 2 are valid for arbitrary Z and have been developed in a series of papers by Bethe and Maximon<sup>10/</sup>, Olsen<sup>11/</sup>, Olsen, Maximon and Wergeland<sup>7/</sup>, Olsen and Maximon<sup>8/, 12/</sup>, and Davies, Bethe, and Maximon<sup>13/</sup>. Their calculations were carried out (a) with Sommerfeld-Maue wave functions, and (b) with the extreme relativistic approximations:  $E_0, E, k \gg 1$  and  $p_0 \theta_0 \sim 1$ . These formulas are estimated<sup>10/</sup> to have an accuracy of the order of  $(Z/137)^2 (\ln E/E)$  which is better than 2 percent for electron kinetic energies above 50 Mev and for Z equal to 80.

#### D. Graphical Representations of the Formulas

A general picture of the dependence of the cross section formulas in Section IIC on the electron and photon energies, the photon emission angle, and screening corrections is presented in Figures 3 - 10. These graphs provide various types of theoretical intercomparisons primarily for energies above 1 Mev. Such a detailed examination of the predictions is useful only for the high energy region where the theories are reasonably accurate and require much smaller corrections than in the low energy region. It should be noted that the high energy intercomparisons rely heavily on the extreme-relativistic predictions of Schiff<sup>14/</sup> which depend on the validity of the complete screening approximation (See Section IIE(3)). The reason for this emphasis is that the Schiff formulas are given in a relatively simple analytical form, and have been used extensively for estimating the spectrum shape from a high energy accelerator even though other more complicated formulas with intermediate-screening approximations are believed to be more accurate (See Table 5).

##### (1) Dependence of the Bremsstrahlung Spectrum on Electron Energy

Figure 3 shows the dependence of the bremsstrahlung spectrum (integrated over the photon directions) on various initial electron kinetic energies for a platinum target ( $Z = 78$ ). The spectra for 0.05 and 0.5 Mev electrons were calculated from Formula 3BN. The spectra for 5, 50, and 500 Mev electrons were calculated from Formula 3BS(e). Figure 4 compares spectrum shapes predicted by Formula 3BS(e) for various electron energies.

##### (2) Dependence of the Bremsstrahlung Spectrum on Photon Angle

Figures 5(a) - (e) show the dependence of the spectrum shape on the reduced photon angle,  $E_0 \theta_0$ , as obtained from Formula 2BS. The figures show that as the emission angle increases, the relative number of high frequency photons increases until the trend reverses at the larger angles. For comparison, the spectrum shape integrated over the emission angle is evaluated from Formula 3BS(e) and is shown by the dashed line. In Figures 6(a) - (e), the dependence of the cross section (Formula 2BS) on the photon emission angle,  $\theta_0$ , is plotted for various photon and electron energies.

The spectrum shape integrated<sup>15/</sup> over the photon directions with the limits from zero to a maximum value of  $\theta_0$  equal to  $\pi$  is of practical interest to experimentalists. Figures 7(a) - (e) show the spectra obtained for different values of  $E_0$  by integrating Formula 2BS within the above limits of  $\theta_0$ . These curves facilitate estimates of the change in thin-target spectra for different experimental arrangements that subtend various angles. In Figures 8(a) - (c), the curves give estimates of the fraction of the total number of photons at any given energy that are included within the angular limits from zero to  $E_0$ ; these curves are obtained by graphical integration from Figures 6(a), (c), and (e) for initial electron kinetic energies of 10, 40, and 300 Mev.

Figures 5 - 8 present some predictions of the Born-approximation formulas given in Table 1. For comparison, the spectrum shapes as a function of the photon emission angle that are predicted by the more accurate extreme-relativistic Formula 2CS(c) in Table 2, are shown in Figures 9(a) through (e) with a normalization of unity for zero photon energy. The spectra for electron kinetic energies of 10, 20, and 40 Mev, Figures 9(a), (b), and (c), are predicted with a zero Coulomb correction factor,  $f(Z) = 0$ , in Formula 2CS(c), and the spectra for electron kinetic energies of 90 and 300 Mev, Figures 9(d) and (e), include the Coulomb correction factor for  $Z = 78$ . A comparison of the spectral shapes with and without the Coulomb correction factor shows only small differences compared to the larger effects that occur with different types of screening approximations.

### (3) Screening Effects and Coulomb Corrections

Figures 10(a) - (e) intercompare Formula 2BS ( $0^\circ$  Schiff), Formula 3BS(c) (Schiff's formula integrated over the photon angle), Formula 3BS (Bethe-Heitler's formula integrated over the photon angle), and the latter formula including the Davies, Bethe, Maximon correction (Formula 3CS and Section IIE(1)). It should be noted that the three curves that are integrated over photon angle are appreciably different in shape.

For example, the curves labelled "Schiff" and "Davies, Bethe, Maximon" are 10 percent different for an electron kinetic energy of 10 Mev at a fractional photon energy of 0.7 with the normalization used in this figure. For the sake of completeness, the spectra corrected for multiple scattering are also plotted in these figures. The multiple scattering correction as calculated by Hisdal<sup>16/</sup> will be discussed in Section IV.

#### E. Corrections for the Cross Section Formulas

Various corrections have been obtained for the formulas given in Section IIC. These corrections may be classified according to three types: (1) Coulomb corrections, (2) high-frequency-limit corrections, and (3) screening corrections. In each case, the correction is restricted to a particular energy region, and is intended to apply only to the formula for a particular differential form of cross section as specified below.

##### (1) Coulomb Corrections

(a) Non-Relativistic Energies. In the non-relativistic region where  $T_0 \ll 1$ , Elwert<sup>17/</sup> has estimated a multiplicative Coulomb correction factor for the cross section Formula 3BN(a). The Elwert factor,  $f_E$ , can be written as

$$f_E = \frac{\beta_0 \left\{ 1 - \exp \left[ - (2\pi Z / 137 \beta_0) \right] \right\}}{\beta \left\{ 1 - \exp \left[ - (2\pi Z / 137 \beta) \right] \right\}} \quad (\text{II-6})$$

This factor is valid only if  $(Z/137)(\beta^{-1} - \beta_0^{-1}) \ll 1$ . This requirement forbids the use of the Elwert factor near the high frequency limit. In addition, it should be emphasized that the Elwert correction was derived on the basis of a comparison between the non-relativistic Born-approximation and the non-relativistic Sommerfeld calculations. Therefore the factor is restricted to non-relativistic electron energies. For higher electron energies (of the order of the electron rest energy), the experimental results in Section II-F show that the Elwert factor breaks down. As a rough guide, the Elwert factor may be expected to give results that are accurate to about 10 percent for electron energies below about 0.1 Mev.

(b) Intermediate Energies. In the energy region from roughly 0.1 to 2.0 Mev, Coulomb corrections to the Born-approximation formulas are not available in analytical form. Therefore these corrections must be estimated empirically from experimental results (Section IIF). For the cross section formulas differential in photon energy,  $d\sigma_k$ , such empirical corrections cannot be determined in enough detail from the available data to cover the whole energy region. However corrected estimates of the integrated cross section,  $\sigma_{rad}$ , are given in Section IIF, from which empirical correction factors can be obtained. The results indicate that the corrections to the Born-approximation formulas for  $\sigma_{rad}$  are as large as a factor of two in the energy region close to the electron rest energy, and less than 10 percent in the energy region from about 4 to 20 Mev.

(c) Extreme-Relativistic Energies. In this energy region, formulas that include the Coulomb correction for the differential cross sections,  $d\sigma_{k,\theta}, \sigma_{\theta}$  and  $d\sigma_k$  are given in Table 2. A comparison of the formulas in Tables 1 and 2 shows that the Coulomb correction can be applied to the Born-approximation formulas for  $d\sigma_k$  by the addition of

$$\Delta = - \frac{4Z^2 r_o^2}{137} \frac{dk}{k} \left[ 1 + \left( \frac{E}{E_o} \right)^2 - \frac{2}{3} \frac{E}{E_o} \right] f(Z) \quad (II-7)$$

where  $f(Z)$  is approximately equal  $\frac{13}{137}$  to  $1.20 \left( \frac{Z}{137} \right)^2$  for low  $Z$  and  $0.925 \left( \frac{Z}{137} \right)^2$  for high  $Z$ . This additive term is independent of the type of screening approximation that is used and is similar to the correction derived for the pair production process  $\frac{11}{137}$ . For lead and energies above 50 Mev, the correction decreases the Born-approximation  $\sigma_{rad}$  with intermediate screening by about 10%. The corrected cross section should be accurate to about 2%.

Accurate experimental data corroborating the cross section values predicted by these formulas are not yet available. However, confirmation is available in the results of absolute pair cross sections. The ratios of the experimental pair-production cross sections to the Born-approximation cross sections are found to agree with the Davies, Bethe, Maximon  $\frac{13}{137}$  values, as shown in Figure 11.

(2) High-Frequency-Limit Corrections

The formulas in Tables 1 and 2 are derived on the basis of certain approximations which do not permit an evaluation of the cross section at the high frequency limit. This shortcoming has been emphasized by various experimental studies<sup>18/</sup> which indicate that the cross section has a finite value at this limit.

Recent calculations made in the Sauter approximation (expansion in powers of  $Z/137\beta_0$  and  $Z/137$ ) by Fano<sup>19/</sup> predict a finite value for the cross section at the high frequency limit. In contrast, the cross section with the Born-approximation (expansion in powers of  $Z/137\beta_0$  and  $Z/137\beta$ ) becomes zero at the limit. The cross section formulas for the high frequency limit obtained by Fano are<sup>20/</sup>

$$\left[ d\sigma_{k,\theta_0} \right]_{k=T_0} = \frac{Z^3 r_0^2}{137^2} \frac{\beta_0}{k^2 E_0^3} \frac{dk}{k} \frac{4\pi \sin^3 \theta_0 d\theta_0}{(1-\beta_0 \cos \theta_0)^4} \left\{ 1 + \frac{1}{2} E_0 (E_0 - 1) (E_0 - 2) (1 - \beta_0 \cos \theta_0) \right\} \quad (\text{II-8})$$

and after integration over  $\theta_0$ ,

$$\left[ d\sigma_k \right]_{k=T_0} = 4\pi \frac{Z^3}{137^2} r_0^2 \frac{dk}{k} \frac{E_0 \beta_0}{(E_0 - 1)^2} \left\{ \frac{4}{3} + \frac{E_0 (E_0 - 2)}{(E_0 + 1)} \left[ 1 - \frac{1}{2\beta_0 E_0^2} \ln \left( \frac{1+\beta_0}{1-\beta_0} \right) \right] \right\} \quad (\text{II-9})$$

Fano, Koch, and Motz<sup>21/</sup> have shown that Formula (II-9) overestimates the cross section at the high frequency limit and that a more accurate estimate is obtained for a given electron kinetic energy if this formula is multiplied by the ratio of the "exact" to the Sauter photoelectric cross sections<sup>22/</sup>. A summary of their results is given in Figure 12 which shows the dependence of the bremsstrahlung cross section (integrated over photon direction) at the high frequency limit on the incident electron energy for aluminum and gold targets. The solid lines (Sauter-Fano) are predicted by Formula (II-9) and the dashed lines (corrected Sauter-Fano) are estimated to be the corrected cross section values. A comparison of the theoretical and experimental values indicates that the true cross sections at the high frequency limit are predicted by the dashed curves with an accuracy of approximately 20 percent.

### (3) Screening Corrections

Screening effects are most important for extreme-relativistic and for non-relativistic electron kinetic energies. Corrections for screening have been adequately included only in the extreme relativistic calculations, where  $E_0, E, k \gg 1$ . The screening corrections for both the Born-approximation and Coulomb-corrected formulas in Tables 1 and 2 have been given by the Born-approximation procedure. In these screening calculations, the cross section is proportional to the square of the matrix element

$$M = \int V(r) \exp (i \mathbf{q} \cdot \mathbf{r}) d\tau \quad (\text{II-10})$$

where  $V(r)$  is the potential that determines the interaction for the bremsstrahlung process and  $r$  is the radius vector in units of the Compton wave length,  $\lambda_0$ . This potential for an atom is represented by the sum,  $V_n + V_e$ , where  $V_n$  is the potential arising from the nuclear charge and  $V_e$  is the potential arising from the charge of the atomic electrons. If the atomic electron form factor is defined as

$$F_e(q, Z) = \frac{4\pi}{Ze} \int \rho(r) \left( \frac{\sin qr}{qr} \right) r^2 dr \quad (\text{II-11})$$

where  $\rho(r)$  is the electron charge distribution, then the matrix element,  $M$ , can be written as proportional to the quantity  $(Z/q^2)(F_n - F_e)$ .

$F_n$  is the nuclear form factor which is roughly equal to unity<sup>23/</sup>. Therefore, the unscreened differential cross section formulas may be corrected for screening effects by including the multiplicative factor,  $[1-F_e]^2$ .

For a Thomas-Fermi model,  $F_e$  depends on the quantity,  $qZ^{-1/3}$ , where  $q$  has a minimum value of  $(p_0 - p - k)$ . At high energies,  $q_{\min}$  becomes equal to  $(k/2E_0)$  and screening calculations are expressed in terms of  $\gamma = 100k (E_0 E Z^{1/3})^{-1}$ .  $\gamma$  is approximately equal to the radius of the Thomas-Fermi atom ( $r_{TF} = 137Z^{-1/3}$ ) divided by  $r_{\max}$ , where  $r_{\max}$  is the maximum impact parameter discussed by Heitler<sup>9/</sup> and is equal to  $q_{\min}^{-1}$ . If  $r_{\max}$  is large compared to the nuclear radius but small compared to the atomic radius,  $r_{TF}$ , then  $\gamma$  is large and  $F_e(q, Z) = 0$ . If  $r_{\max}$  is of the order of  $r_{TF}$ , then  $\gamma \sim 1$  and screening must be taken into account. If the impact parameter is of the order of the nuclear radius, then the distribution of the nuclear charge must be included by a nuclear form factor<sup>23/</sup> although the influence of the distribution of the atomic electrons can be neglected.

The dependence of  $r_{\max}$  on the initial electron kinetic energy at all energies can be obtained by setting  $r_{\max}$  equal to  $(p_0 - p - k)^{-1}$ . The results are shown in Figure 13 for  $k$  equal to  $0.1 T_0$ ,  $0.5 T_0$ , and  $0.9 T_0$ . Also the dashed lines give the Thomas-Fermi atomic radii for beryllium and gold. A comparison of  $r_{\max}$  with  $r_{TF}$  shows that  $r_{\max}$  is larger than  $r_{TF}$  at low and high energies. To be specific, screening effects can be expected to become important over a large part of the spectrum for electron kinetic energies above approximately 5 Mev and below approximately 10 kev. For low fractional photon energies where  $k \leq 0.1 T_0$ , screening effects are important for all values of  $T_0$ . It is interesting to observe that for the high photon energies the screening effects are the least important for values of  $T_0$  approximately equal to the electron rest energy.

The accuracy obtainable with a bremsstrahlung formula corrected for screening depends on the validity of the extreme-relativistic approximations and on the adequacy of the atomic model used to provide the form factor. Only the latter will be commented on here. The most extensive calculations and applications have been based on the Thomas-Fermi atomic model. However, the Hartree self-consistent field model is more accurate<sup>24/</sup> but more difficult to apply. The atomic form factors predicted by the two models have been compared by Nelms and Oppenheim<sup>24/</sup> and are given in Figure 14. The curves in this figure show that the accuracy of the Thomas-Fermi model decreases as the atomic number decreases.

Information concerning the influence of the form factor differences on the bremsstrahlung cross section can be obtained by referring to pair production calculations. The nuclear momentum distribution in the pair production process at extreme-relativistic energies as calculated by Jost, Luttinger, and Slotnik<sup>25/</sup>, is given in Figure 15. Their results show that the most probable  $q$  values are of the order of 0.1. Table 4 gives the ratio of the Thomas-Fermi to the Hartree form factors for representative  $q$  values, as obtained by Nelms and Oppenheim<sup>24/</sup> for carbon and mercury. These differences produce different estimates for the pair production cross section: for example at 60 Mev, the cross section for carbon with the Hartree form factor is increased by 1/2 percent above the cross section calculated with the Thomas-Fermi form factor<sup>26/</sup>. Comparable detailed information is not available for the bremsstrahlung process. However, general conclusions are possible on the basis of a comparison of the maximum impact parameters for bremsstrahlung and pair production. The maximum impact parameter for bremsstrahlung is  $(2E_0 E/k)$  and the similar expression for pair production is  $(2E_+ E_-/k)$  where  $E_+$  and  $E_-$  are the total energies of the positron and electron. By varying the values of  $E$  and  $k$  for fixed  $E_0$  in bremsstrahlung and the values of  $E_+$  and  $E_-$  for fixed  $k$  in pair production, we find that the important impact parameters in bremsstrahlung are larger on the average than those in pair production. This fact explains why the screening effect is much larger on  $\emptyset_{\text{rad}}$  than on  $\emptyset_{\text{pair}}$  for equal values of  $E_0$  and  $k$  (see, for example, the total cross sections for the two processes in reference 9, pages 252 and 262). The larger screening effect indicates that the use of

the Hartree form factor in place of the Thomas-Fermi factor will have a greater effect on  $\emptyset_{\text{rad}}$  than on  $\emptyset_{\text{pair}}$ .

TABLE 4

Ratios of Thomas-Fermi to Hartree Atomic Form Factors

q	$\left(\frac{\text{Thomas-Fermi}}{\text{Hartree}}\right)$ carbon	$\left(\frac{\text{Thomas-Fermi}}{\text{Hartree}}\right)$ mercury
0.1	1.11	0.802
0.2	2.50	1.00
0.3	3.67	1.07
0.4	4.10	1.15
0.5	4.63	1.26

The first detailed study of the influence of form factors on screened bremsstrahlung cross sections was made by Bethe<sup>27/</sup>. Bethe's calculations, which are summarized in the formulas of Tables 1 and 2, consider four types of screening:

1. Complete screening condition:  $\gamma \approx 0$
2. Intermediate screening condition I:  $\gamma < 2$
3. Intermediate screening condition II:  $2 < \gamma < 15$
4. No screening condition:  $\gamma \gg 1$ .

The Bethe<sup>27/</sup> and Bethe-Heitler<sup>28/</sup> screening calculations with intermediate conditions I and II were performed numerically using the tabulations of the atomic form factor for the Thomas-Fermi model given by Bethe<sup>29/</sup>.

In the work of Schiff<sup>14/</sup> analytical calculations were made possible by the use of the complete screening condition ( $\gamma \approx 0$ ) and an approximate screened atom potential,  $V$ , given by  $(Ze/r)\exp(-r/a)$ , where  $a = (111/Z^{1/3})$ .

The atomic form factor,  $F_e(q,Z)$ , corresponding to this potential is given by the quantity  $\left[1 + (aq)^2\right]^{-1}$ . For many purposes the Schiff Formula 2BS and 3BS(c) are sufficiently accurate. Schiff<sup>14/</sup> notes that compared to the intermediate screening Formula 3BS, the complete-screening Formula 3BS(e), "is larger than it should be by less than 2 percent for moderate values of Z and is never more than 4 percent high in the worst case of large Z and energies such that screening is incomplete".

A third procedure for including form factor effects was developed by Moliere<sup>30/</sup>. By approximating the Thomas-Fermi potential with a simple analytical expression, he obtained the following relation:

$$\frac{\left[1 - F_e(q,Z)\right]}{q^2} = \sum_{i=1}^3 \frac{\alpha_i}{\beta_i^2 + q^2} \quad (\text{II-12})$$

where  $\alpha_1 = 0.10$ ,  $\alpha_2 = 0.55$ ,  $\alpha_3 = 0.35$ ,

$$\beta_i = \frac{Z^{1/3} b_i}{121} \quad ; \quad b_1 = 6.0, \quad b_2 = 1.20, \quad b_3 = 0.30 .$$

The Molière function has been applied by Olsen and Maximon<sup>8/</sup> to obtain intermediate screening formulas that include Coulomb corrections.

The most accurate predictions of screening corrections to bremsstrahlung cross sections for specific target elements can be obtained by the use of the Hartree form factors in the formulas that permit the use of arbitrary form factors, e.g., Formulas 3BS(b) and 2CS(b). Unfortunately, the screening corrections for these formulas must be evaluated numerically and are not as convenient to use as the complete screening formulas just discussed.

## F. Comparison of Theory and Experiment

Very few experimental determinations of the bremsstrahlung cross section are available for comparison with the estimates given in Section IIC, D, and E. At present, experimental data on cross sections have been obtained for electron kinetic energies of 34 kev<sup>31/</sup> by Amrehn<sup>32/</sup> and Röss<sup>32/</sup>, 50 kev by Motz and Placious<sup>33/</sup>, 90 to 180 kev by Mausbeck<sup>34/</sup> and Zeh<sup>34/</sup>, 0.5 and 1.0 Mev by Motz<sup>35/</sup>, and 2.72, 4.54, and 9.66 Mev by Starfelt and Koch<sup>36/</sup>. The important results of these studies are combined and summarized below.

### (1) Cross Section Differential in Photon Energy and Angle

For electron kinetic energies that are small compared with the electron rest energy, the experimental results<sup>31/,32/,33/</sup> show general agreement with the Sommerfeld theory<sup>5/</sup> except for certain minor discrepancies which probably occur because the theory does not account for relativistic and screening effects. On the other hand, the Born-approximation theory (Formula 2BN) is seriously inadequate in this energy region and no analytical correction factors for the Born-approximation formula are available in this differential form. Furthermore, no quantitative studies are available on the importance of screening.

For electron kinetic energies that are of the same order of magnitude as the electron rest energy, the Born-approximation theory (Formula 2BN) underestimates the experimental cross section<sup>34/,35/</sup> as shown by the comparison in Figure 16. These data also show that the differences between the theory and experiment increase with (a) the photon energy, (b) the photon angle, and (c) the atomic number of the target.

For electron kinetic energies that are large compared with the electron rest energy, the experimental results<sup>36/</sup> agree within 10 percent with the Born-approximation theory. For example, in Figure 17, the experimental cross sections for gold at 4.54 Mev<sup>36/</sup> show general agreement with the predictions of the screened, extreme-relativistic Schiff Formula 2BS and of the unscreened Sauter Formula 2BN. There are differences in detail (generally less than 10 percent in this energy region):

(a) Near the high frequency limit, the experimental cross sections are greater than the Schiff cross sections which in turn are greater than the Sauter cross sections; (b) In the low frequency region, the experimental cross sections show good agreement with the Schiff cross sections, but are less than the unscreened Sauter cross sections. For low  $Z$  targets, there is better agreement with the Sauter formula.

## (2) Cross Section Differential in Photon Energy

A comparison<sup>21/</sup> of experimental and theoretical values for the cross section differential in photon energy,  $d\sigma_k$ , is given in Figures 18 - 21 for electron energies of 0.05, 0.5, 1.0, and 4.5 Mev. Each of these figures gives the estimates of (a) the Born-approximation cross sections (Formulas 3BN or 3BN(a)), (b) the Corrected Sauter-Fano cross sections at the high frequency limit (Section IIE(2)), (c) the Elwert-Born approximation cross sections (Section IIE(1)), and (d) the experimental results. The solid lines show the cross sections computed from Formula 3BN(a) for 0.05 Mev, and Formula 3BN for 0.5, 1, and 4.5 Mev. The dashed lines give the Born-approximation cross sections corrected by the Elwert factor defined in Formula (II-4). The comparison with the experimental results shows that the Elwert correction gives the most accurate results at very low energies (below 0.1 Mev). For electron kinetic energies of the order of the electron rest energy, the cross sections obtained with the Elwert correction factor are still less than the experimental values (by as much as a factor of two in the worst case). For very high energies, the Born-approximation theory overestimates the actual cross sections, and the Elwert factor is no longer valid, although it gives good agreement with experiment in the 5-Mev cross-over region. (See Section IIF(3)). The corrected Sauter-Fano cross sections at the high frequency limit show good agreement with the experimental results as noted previously in Figure 12.

### (3) Total Cross Section

The experimental values for the total cross section,  $\sigma_{\text{rad}}$  (defined in Section IIC), are shown in Figure 22 by the closed and open circles for initial electron kinetic energies of  $0.05 \text{ Mev}^{33/}$ ,  $0.5 \text{ Mev}^{35/}$ , and  $1.0 \text{ Mev}^{35/}$ . The theoretical values are shown by the solid lines, which are predicted by Formulas 4BN(a) in the region where  $T_0 \leq 0.5$  and by Formula 4BN for no screening. The curves that include screening corrections for  $Z = 13$  and  $79$  are obtained by numerical integration of the intermediate screening Formulas 3BS(c) and 3BS(d). For extreme-relativistic energies, the triangles give the most accurate theoretical cross section values for  $Z = 79^{37/}$ , which are estimated by numerical integration of the Coulomb-corrected Formula 3CS. The most accurate values for  $\sigma_{\text{rad}}$ , which are estimated from the above combined data, are shown by the dashed curve for  $Z = 13$  and the dot-dashed curve for  $Z = 79$ .

Approximate correction factors for the Born-approximation  $\sigma_{\text{rad}}$  values with screening have been estimated as a function of the initial electron kinetic energy from the ratios of the cross section values shown in Figure 22 by the empirical (dashed and dot-dashed) curves and by the Born-approximation curves with screening. These estimated factors are given in Figure 23, and show that the ratios are equal to unity at the energy of approximately 10 Mev for aluminum and 6 Mev for gold. For energies larger than these cross-over energies, the Born-approximation formula overestimates the cross section; for smaller energies, the reverse is true. It should be noted that even though the correction factor for  $\sigma_{\text{rad}}$  may be close to unity for a given electron energy, much larger (or smaller) correction factors may be required for the differential cross section,  $d\sigma_k$ , in the high or low frequency region because of a cross over effect (see Figure 39 in Bethe and Salpeter, reference 1), which is masked by the integration of  $d\sigma_k$ . It is interesting to observe in Figure 23, that the maximum correction factor for the Born-approximation calculations occurs at electron kinetic energies approximately equal to the electron rest energy.

### G. Summary

A survey of the above data leads to some general conclusions about the accuracy of the cross section values predicted by the various formulas and correction factors. Also, suggestions can be made for selecting formulas that give the best estimates for the cross section or that can be easily evaluated to give reasonably accurate results. These judgments are summarized below.

In Table 1, the screened formulas depend on the extreme-relativistic approximation and therefore are valid only in the energy region  $T_0 \gg 1$ . For  $T_0 \ll 1$ , only the nonscreened formulas are applicable<sup>38/</sup>. The nonscreened formulas require relatively large correction factors except in the region near the crossover energy (see Figure 22). At the extreme relativistic energies the nonscreened formulas are less accurate than the screened formulas.

In Table 2, the extreme-relativistic cross section formulas for  $d\sigma_{k, \theta_0, \phi}$  and  $d\sigma_k$  are estimated to have an accuracy that is given approximately by the factor  $(Z/137)^2 (h\nu/E)$ . For  $f(Z) = 0$ , the formulas in Table 2 are the same as the Born-approximation formulas in Table 1 except for differences in the screening corrections which are reviewed in Section IIE(3).

An estimate of the general accuracy with which the formulas in Tables 1 and 2 predict the cross section values over the whole range of electron energies can be obtained from a comparison of the theoretical and experimental predictions for  $\phi_{\text{rad}}$  in Figures 22 and 23.

For the cross section differential in photon energy,  $d\sigma_k$ , a summary of the corrected formulas for specified energy ranges of the incident electron is given in Table 5. Conservative estimates of the accuracies of these formulas have been made on the basis of the experimental data assembled in this report. It will be noted that the greatest uncertainties are in the energy range from 0.10 to 2.0 Mev. Because of the uncertainties of screening effects, no corrected formulas are given for the energy region below 0.01 Mev. These corrected formulas are tentative and it can be expected that some will be replaced by more accurate expressions as more data becomes available.

For the cross section formulas differential in photon energy and angle,  $d\sigma_{k, \theta_0, \phi}$ , no quantitative corrections are available for low and intermediate energies because of insufficient data. For extreme relativistic energies, the most accurate estimates (3 percent) for  $d\sigma_{k, \theta_0, \phi}$  are given by Formula 2CS.

TABLE 5

Corrected Cross Section Formulas for  $d\sigma_k$

Kinetic Energy Range for Incident Electron, Mev	Corrected Cross Section Formula <sup>+</sup>	Restrictions	Estimated Accuracy*
0.01 - 0.10	$d\sigma_k = f_E d\sigma_k^{3BN(a)}$	$k > .01T_o$	±5%
0.10 - 2.0	$d\sigma_k = Af_E d\sigma_k^{3BN}$	$k > .01T_o$	±20%
2.0 - 15	$d\sigma_k = A d\sigma_k^{3BN}$	$\gamma > 15$	*
	$= A d\sigma_k^{3BS(d)}$	$2 < \gamma < 15$	±5%
	$= A d\sigma_k^{3BS(c)}$	$\gamma < 2$	±5%
15 - 50	$d\sigma_k = d\sigma_k^{3BN}$	$\gamma > 15$	*
	$= A d\sigma_k^{3BS(d)}$	$2 < \gamma < 15$	±3%
	$= A d\sigma_k^{3BS(c)}$	$\gamma < 2$	±3%
50 - 500	$d\sigma_k = d\sigma_k^{3BN}$	$\gamma > 15$	*
	$= d\sigma_k^{3CS(a)}$	$2 < \gamma < 15$	±3%
	$= d\sigma_k^{3CS(b)}$	$\gamma < 2$	±3%

where  $f_E$  is defined in Formula (II-6),

A is the correction factor given in Figure 23,

$\gamma$  is equal to the quantity  $100k(E_o/EZ)^{1/3} - 1$ .

<sup>+</sup>The superscripts for  $d\sigma_k$  give the formula numbers defined in Section IIC.

\*No estimated accuracy is given at photon energies near the high frequency limit of the spectrum. If better accuracy is desired in this region, the cross section at the high frequency limit can be obtained from the dashed curves in Figure 12, and the spectrum shape may be adjusted by fitting this end to the curves given by the formulas in column 2 above.

### III. Electron-Electron Bremsstrahlung

The bremsstrahlung cross section formulas for electron-nuclear interactions in Section IIC vary as  $Z^2$ . For targets with high atomic numbers, the additional influence of electron-electron bremsstrahlung can be included approximately by replacing  $Z^2$  by  $Z(Z+1)$ . However for very low  $Z$  elements such as hydrogen or beryllium, the electron-electron bremsstrahlung contributions must be included more accurately. Cross section calculations for this process are complicated because of the exchange character of the interaction in which there is a large energy and momentum transfer to the recoil electron, in contrast to the electron-nuclear bremsstrahlung process in which the nucleus is assumed to be infinitely heavy. No complete calculations are available for predicting the detailed features of electron-electron bremsstrahlung<sup>39/</sup>. A summary of pertinent results that have been obtained is given below.

#### A. Maximum Photon Energy

In the electron-electron bremsstrahlung process, the maximum photon energy that is available in the laboratory system at the laboratory angle  $\theta_0$  is

$$k_{\max} = F / (1 - \sqrt{F} \cos\theta_0) \quad \text{(III-1)}$$

where  $F$  is equal to  $(E_0 - 1)/(E_0 + 1)$ . Table 6 gives some values of  $k_{\max}$  at zero and 90 degrees obtained from Formula (III-1) for various incident electron kinetic energies. From the very sparse experimental information<sup>35/,36/</sup> available on electron-electron bremsstrahlung, some results<sup>35/</sup> have shown reasonably good agreement with the values of  $k_{\max}$  predicted by Formula (III-1).

TABLE 6  
Maximum Photon Energy for Electron-Electron Bremsstrahlung

$T_0$	$k_{\max}$	
	$\theta_0 = 0^\circ$	$\theta_0 = 90^\circ$
100	99.	0.98
10	9.7	0.83
1.0	0.79	0.33
0.1	0.069	0.048
0.01	0.0054	0.0050

B. Cross Section Formulas for Free Electrons.

(1) ~~Non-relativistic~~ Energies

In contrast to the electron-nucleus and electron-positron systems, the electron-electron system has no dipole moment. Therefore the electron-electron bremsstrahlung cross section becomes zero for calculations based only on the non-relativistic dipole approximation. Garibyan<sup>40/</sup> has made calculations beyond the dipole approximation and has obtained the following non-vanishing result for the cross section differential in photon energy:

$$d\sigma_k' = \frac{r_o^2 Z}{137} \left( \frac{8}{15} \frac{\beta}{\beta_o^3} \frac{dk}{k} \right) \left[ 17 - \frac{3(\beta_o^2 - \beta^2)^2}{(\beta_o^2 + \beta^2)^2} + \left( \frac{\beta_o^2 + \beta^2}{\beta_o \beta} + 26 \frac{\beta_o \beta}{\beta_o^2 + \beta^2} - \frac{24\beta_o^3 \beta^3}{(\beta_o^2 + \beta^2)^3} \right) \ln \left( \frac{\beta_o + \beta}{\beta_o - \beta} \right) \right], \quad (III-2)$$

which for  $k \rightarrow 0$  becomes<sup>39/</sup>

$$d\sigma_{k \rightarrow 0}' = \frac{r_o^2 Z}{137} \left[ \frac{32}{5} \frac{dk}{k} \frac{1}{\beta_o^2} \left( \ln \frac{4\beta_o^2}{k} + \frac{17}{12} \right) \right] \quad (III-3)$$

These results are only valid for  $T_o \ll 1$ .

(2) ~~Extreme-relativistic~~ Energies

Several calculations<sup>39/</sup> based on the extreme-relativistic approximations give the following approximate formula for the cross section differential in photon energy:

$$d\sigma_k' = \frac{4r_o^2 Z}{137} \frac{dk}{k} \left[ \left( 1 + \left( \frac{E}{E_o} \right)^2 - \frac{2}{3} \frac{E}{E_o} \right) \left( \ln \frac{2E_o E}{k} - \frac{3}{2} \right) - \frac{E_o E}{9} \right], \quad (III-4)$$

which is similar in form to the electron-nuclear cross section Formula 3BN(b).

The total radiation cross section obtained from Formula (III-4), is given as

$$\sigma_{\text{rad}}' = \frac{4r_0^2 Z}{137} \left( \ln 2E_0 - \frac{4}{3} \right) \quad (\text{III-5})$$

C. Cross Section Formulas with Binding Corrections.

The influence of atomic binding on the electron-electron bremsstrahlung cross section has been calculated only in the extreme-relativistic approximation. With the Thomas-Fermi model, the corrected formula for the cross section differential in photon energy is<sup>39/</sup>

$$\begin{aligned} d\sigma_k' = \frac{4Z}{137} \frac{dk}{k} & \left[ \left( 1 + \left( \frac{E}{E_0} \right)^2 \right) \left( \frac{1}{4} \Psi_1(\epsilon) - 1 - \ln z^{2/3} \right) \right. \\ & \left. - \frac{2}{3} \frac{E}{E_0} \left( \frac{1}{4} \Psi_2(\epsilon) - \frac{5}{6} - \ln z^{2/3} \right) \right] \end{aligned} \quad (\text{III-6})$$

where  $\epsilon$  is equal to  $100k(E_0 E z^{2/3})^{-1}$ , and  $\Psi_1$  and  $\Psi_2$  are given<sup>41/</sup> by the data in Figure 24. For complete screening where  $\epsilon \sim 0$ , the cross section becomes

$$d\sigma_k' = \frac{4Z}{137} \frac{dk}{k} \left( 1 + \left( \frac{E}{E_0} \right)^2 - \frac{2}{3} \frac{E}{E_0} \right) \ln \frac{530}{z^{2/3}} \quad (\text{III-7})$$

The total radiation cross section which is obtained for the complete screening case from (III-7) is given by

$$\sigma_{\text{rad}}' = \frac{4r_0^2 Z}{137} \ln \frac{530}{z^{2/3}} \quad (\text{III-8})$$

A comparison of this Formula (III-8) with the electron-nuclear bremsstrahlung cross section Formula 4BS shows that the Z electrons in an atom increase the electron-nuclear cross section by the factor  $\eta$  so that the total cross section becomes

$$\sigma_{\text{rad}}^{\text{Total}} = Z(Z + \eta) \left( \frac{\sigma_{\text{rad}}^{4BS}}{Z^2} \right) \quad (\text{III-9})$$

For complete screening,  $\eta$  is given by

$$\eta = \ln \frac{530}{z^{2/3}} \left( \ln \frac{183}{z^{1/3}} + \frac{1}{18} \right) \quad (\text{III-10})$$

which varies from 1.04 for magnesium to 0.88 for lead.

For most cases, a value of  $M$  equal to unity is sufficiently accurate.

#### IV. Thick-Target Bremsstrahlung Production

Bremsstrahlung is produced in thick targets for most practical cases. In this discussion, a target is defined to be thick if the scattering and energy loss processes that occur as the electrons traverse the target have an appreciable influence on the bremsstrahlung production. In principle, a complete description of the bremsstrahlung emitted from a given target can be obtained from the cross sections for the pertinent elementary processes. For example, the angular distribution of the total bremsstrahlung power, the shape of the bremsstrahlung spectrum from an X-ray tube, or the efficiency of bremsstrahlung production can be calculated if detailed data are available with regard to the bremsstrahlung and electron scattering (elastic and inelastic) processes. However, any such analysis is necessarily a complicated procedure, since the calculations for the energy loss and scattering of the primary electrons and the absorption of the X-rays in the target must be included with the cross section information of Section II. Also, the analysis depends on the characteristics of a given experimental situation. For these reasons, this paper does not give a complete, systematic treatment of thick-target bremsstrahlung production; instead it is confined to the presentation of pertinent experimental data as well as useful analytical results and procedures. Also, emphasis is placed on thick-target results that give absolute data on photon intensities and bremsstrahlung production efficiencies.

Some of the analytical results for thick-target bremsstrahlung are most conveniently expressed in terms of certain quantities which are defined in the following discussion. When an electron traverses a target, the average energy lost in the path length element  $dx$  by radiation can be written as

$$- dE_0 = NE_0 (K\phi_{rad}^*) dx = KE_0 dt \quad (IV-1)$$

where  $N$  is the number of target atoms per  $cm^3$  and  $K\phi_{rad}^*$  is equal to the cross section  $\phi_{rad}$  defined in Section IIC.  $\phi_{rad}^*$  is equal to  $(4Z^2 r_0^2 / 137) \ln(183Z^{-1/3}) cm^2$ , which is approximately the same as the expression for  $\phi_{rad}$  at extreme-relativistic energies (see Formula 4BS).

K is defined as the radiation probability correction factor and is plotted in Figure 25 for various values of the target atomic number and the electron kinetic energy. The length  $t$  is given in units of the radiation length,  $t_0$ , which is defined as

$$t_0 = \frac{1}{N\sigma_{\text{rad}}^*} \text{ cm} \quad (\text{IV-2})$$

Values for  $t_0$  in units of  $\text{gm/cm}^2$  as a function of the target atomic number are plotted in Figure 26.

#### A. Thick-Target Bremsstrahlung Angular Distributions

##### (1) Non-relativistic and Intermediate Energies<sup>42/</sup>

For electron energies that are small or comparable to the electron rest energy, no analytical or empirical formulas have been derived for estimating the bremsstrahlung angular distribution from thick targets, and only a few experimental results are available.

In contrast to the extreme-relativistic region, the radiation intensity produced at these low energies is important at large angles, and is about the same order of magnitude at both zero and ninety degrees. However, because the absorption of the bremsstrahlung photons in the target is large, the angular distribution of the bremsstrahlung is largely dependent on the target geometry in specific experimental situations. One of the few examples in which angular distribution data are presented in a more general way with corrections for the geometry and the target absorption is to be found in the measurements of Buechner, Van de Graaff, Burrill, and Sperduto<sup>43/</sup> for initial electron kinetic energies in the region from 1.25 to 2.35 Mev. Their results for beryllium and gold targets are given in Figure 27. The curves show the angular dependence of the radiation intensity integrated over photon energy for specified electron energies. These data indicate that the intensity ratio at zero and ninety degrees is approximately 10 for beryllium and 3 for gold at 1.5 Mev, and approximately 40 for beryllium and 4 for gold at 2.35 Mev. Also from these data, we can obtain the following empirical expressions for the power radiated at zero degrees

$$I_{(\alpha=0)}(\text{Au}) = 9.4 (\mathcal{T}_0)^{2.9} \text{ roentgens per minute per ma at } 1 \text{ meter for gold} \quad (\text{IV-3})$$

$$I_{(\alpha=0)}(\text{Be}) = 0.92 (\mathcal{T}_0)^{3.4} \text{ roentgens per minute per ma at } 1 \text{ meter for beryllium}$$

where  $\mathcal{T}_0$  is the electron kinetic energy in  $m_0 c^2$  units for the electrons incident on the target, and  $\alpha$  is the angle between the photon direction and the direction of the incident electron beam. Then with the approximate conversion factor of one roentgen equal to  $3000 \pm 500 \text{ ergs/cm}^2$  for photons with energies in the range from 0.1 to 2 Mev<sup>44/</sup>, we have

$$I_{(\alpha=0)}(\text{Au}) = 0.5 (\mathcal{T}_0)^{2.9} \text{ watts/ma-steradian} \quad (\text{IV-4})$$

$$I_{(\alpha=0)}(\text{Be}) = 0.05 (\mathcal{T}_0)^{3.4} \text{ watts/ma-steradian.}$$

From these equations, the fraction, R, of the total incident electron kinetic energy that is radiated per steradian at zero degrees is

$$R_{(\alpha=0)}(\text{Au}) = 10^{-3} (\mathcal{T}_0)^{1.9} \text{ for gold}$$

and

$$R_{(\alpha=0)}(\text{Be}) = 10^{-4} (\mathcal{T}_0)^{2.4} \text{ for beryllium.} \quad (\text{IV-5})$$

## (2) Relativistic Energies

At high energies, estimates of the bremsstrahlung angular distribution from thick targets have been made on the basis of the following simplifying approximations. First, the thin target spectrum integrated over photon angle (Formula 3BS) is assumed to represent the spectrum shape for any angle. Second, the intrinsic (thin target) angular spread of the bremsstrahlung (Formula 2BS) is neglected at large angles where  $\alpha \gg E_0^{-1}$  but not at small angles where  $\alpha \leq E_0^{-1}$ ; therefore at large angles the photon is assumed to have the same direction as the electron that is multiply scattered before it radiates.

With these approximations, the following analytical results have been obtained. For large angles where  $\alpha \gg E_o^{-1}$ , the fraction, R, of the total incident electron kinetic energy that is radiated per steradian at the angle,  $\alpha$ , is given<sup>45/</sup> as

$$R_{(\alpha \gg E_o^{-1})} = \frac{K \mathcal{E}_o^2}{1760 \pi} \text{Ei} \left[ \frac{-\mathcal{E}_o^2 \alpha^2}{1760 t} \right], \quad (\text{IV-6})$$

where  $\mathcal{E}_o$  is the total energy in  $m_o c^2$  units of the electron incident on the target, and Ei is the exponential integral<sup>46/</sup>

$$-\text{Ei}(-y) = \int_y^\infty \frac{e^{-z}}{z} dz, \quad y > 0 \quad (\text{IV-7})$$

For small angles where  $\alpha \lesssim E_o^{-1}$ , Muirhead, Spicer and Lichtblau<sup>47/</sup> have obtained the following expression for the bremsstrahlung angular distribution

$$R_{(\alpha \lesssim E_o^{-1})} = \frac{K \mathcal{E}_o^2}{1760 \pi} \left\{ -\text{Ei} \left[ \frac{-\mathcal{E}_o^2 \alpha^2}{1760 t} \right] + \text{Ei} \left[ \frac{-\mathcal{E}_o^2 \alpha^2}{7.15} \right] \right\} \quad (\text{IV-8})$$

This formula gives good agreement with experimental data<sup>47/</sup> and can readily be evaluated at small angles by keeping the first term in the expansion of the exponential integrals which is

$$\text{Ei}(-z_1) - \text{Ei}(-z_2) \rightarrow \ln(z_1/z_2) \quad \text{for } z_1, z_2 \rightarrow 0. \quad (\text{IV-9})$$

$$\text{Thus } R_{(\alpha=0)} = \frac{K \mathcal{E}_o^2}{1760 \pi} \ln 246t, \quad \text{for } t \gg 2 \times 10^{-3}. \quad (\text{IV-10})$$

It is interesting to note that for  $t = 0.1$  and  $\mathcal{E}_o = 3$ , this formula agrees reasonably well with the result predicted by the low energy Formula (IV-5). For thin-targets, this "on-axis" intensity becomes<sup>45/</sup>

$$R_{(\alpha=0)} = \frac{Kt \mathcal{E}_o^2}{4\pi}, \quad \text{for } t \ll 2 \times 10^{-3}. \quad (\text{IV-11})$$

Estimates of the ratio  $R_{\alpha} / R_{(\alpha=0)}$  for tungsten ( $Z=74$ ) are given in Figure 28 for three target thicknesses.

Several conclusions for high-energy angular distributions can be drawn from the form of the Formulas (IV-8), (IV-10), and (IV-11). The logarithmic form of Formula (IV-10) shows that most of the radiation comes from the front part of the target. Also, since the fractional energy radiated depends on  $\mathcal{E}_0^2$ , the total energy radiated at zero degrees will depend on  $\mathcal{E}_0^3$ . Two additional effects influence the dependence on  $\mathcal{E}_0$  of the total radiated energy. The factor  $K$ , according to Figure 25, increases slightly with  $\mathcal{E}_0$ , and for very thick targets the effective  $t$  in Formula (IV-10) will increase logarithmically with  $\mathcal{E}_0$ . Therefore, the total energy radiated on the axis of the bremsstrahlung beam will depend on at least a 3.2 exponent for a thin-target and on a slightly higher exponent for a thick-target. The specific exponent to be used will obviously depend on the energy range of interest, the effective target thickness, and the experimental geometry.

#### B. Thick-Target Bremsstrahlung Spectra

##### (1) Non-relativistic and Intermediate Energies<sup>42/</sup>

In this low energy region the radiation has a broad angular distribution (see IVA), and the dependence of the spectrum shape on photon angle is important<sup>48/</sup>. No general analytical expressions which accurately predict the spectrum as a function of angle for any experimental situation are available at these energies. Part of the difficulty has been the inadequacy of the Born-approximation cross section differential in photon energy and angle (Formula 2BN). Nevertheless it has been possible to obtain reasonable agreement between theoretical and experimental thick target spectrum shapes shown in Figure 29 for a particular application<sup>49/</sup> with an initial electron kinetic energy of 1.4 Mev, photon angles of zero and ninety degrees, and a tungsten target. In this example, the experimental results confirm the theoretical dependence of the spectrum shape on photon angle after distortions due to photon absorption in the target and surrounding materials are eliminated. The results also show that the relative number of photons in the high frequency region increases as the emission angle becomes smaller. This trend is just opposite to the behavior observed for thin target spectra<sup>35/</sup>.

With regard to estimates of the shape of the spectrum integrated over the photon direction, Kramers<sup>50/</sup> obtained the following simple, analytical expression:

$$I_k = AZ (k_0 - k) , \quad (IV-12)$$

where  $I_k$  is the energy radiated in all directions in the energy interval,  $(k, k + dk)$ ,  $A$  is a proportionality constant, and  $k_0$  is the photon energy at the high frequency limit. This result was derived on the basis of a non-relativistic, semi-classical calculation, in which electron scattering effects (including backscattering) were neglected and only the electron energy loss was considered. In spite of these limitations and because of its simplicity, the Kramers Formula (IV-12) has been used extensively to estimate the thick target spectrum (not including the characteristic radiation<sup>51/</sup>) at a given angle for various experimental cases, with corrections included for the photon absorption in the target and surrounding materials. Results obtained for various electron energies in this low energy region have shown general qualitative agreement between the theoretical (Kramers) and experimental spectrum shapes<sup>52/</sup>, and indicate that Formula (IV-12) is satisfactory at least for order of magnitude estimates.

## (2) Relativistic Energies<sup>42/</sup>

Two complementary procedures for calculating thick target spectra at high energies which include effects of electron scattering in the target are given by Penfold<sup>53/</sup> and Hisdal<sup>54/</sup>. The Penfold calculations estimate the thick target effects primarily in the high frequency region and give the spectrum integrated over photon directions up to a maximum angle,  $\Gamma$ , with respect to the direction of the incident electron beam. The Hisdal calculations estimate the thick target effects on the over-all spectrum shape in the forward direction and should not be applied to the high frequency region.

The Penfold method<sup>53/</sup> assumes that (a) the Schiff Formula 3BS(e) describes the intrinsic spectrum at all angles, (b) the electron energy loss rather than electron scattering in the target produces the predominant effect on the shape of the spectrum for large values of  $\Gamma$ , (c) no electron radiates more than one photon, and (d) the photon absorption in the target is negligible. With these approximations, Penfold obtained the following

formula for the thick target spectrum integrated over photon direction to a maximum angle,  $\Gamma$ , determined by the detector:

$$P_k = n N_o \int_{k+1}^{\mathcal{E}_o} S(\mathcal{E}_o, E_o, \Gamma, x_o) d\sigma_k dE_o \quad (\text{IV-13})$$

where  $P_k$  is the number of photons in the energy interval  $k$  to  $k + dk$ ,  $N_o$  is the number of target atoms per  $\text{cm}^3$ ,  $n$  is the number of electrons incident on the target,  $\mathcal{E}_o$  is the total energy of the incident electron in  $m_o c^2$  units,  $x_o$  is the target thickness in  $\text{gm}/\text{cm}^2$ , and  $d\sigma_k$  is given by Formula 3BS(e) for electrons with energy  $E_o$ . The function  $S$  represents the probability that radiation produced by the electrons reaches the detector, and can be written as

$$S(\mathcal{E}_o, E_o, \Gamma, x_o) = \int_0^{x_o} B_3(\mathcal{E}_o, E_o, \Gamma, x) B_4(\Gamma, E_o, x) B_5(x_o, x) dx \quad (\text{IV-14})$$

where the function  $B_3$  gives the fraction of the radiation emitted by electrons with energy  $E_o$  at the target depth  $x$ ,  $B_4$  is the fraction of electrons that penetrate beyond the thickness  $x$ , and  $B_5$  accounts for path length straggling. These B functions require involved numerical evaluations, and the results are described in detail in the Penfold report<sup>53/</sup>. Motz, Miller, and Wyckoff<sup>56/</sup> have estimated the thick target spectrum for a particular experimental situation in which the bremsstrahlung is produced with an 11.3 Mev (kinetic energy) electron beam incident on a tungsten target (approximately .010 inch thick), and is measured on the beam axis with a small detector ( $\Gamma \approx 0$ ). They have used the following simplified, analytical form for the thick-target generating function:

$$S = 1 - \exp \left\{ - \frac{1}{51(\mathcal{E}_o - E_o)} \left( \frac{\mathcal{E}_o}{E_o} \right)^2 \right\} \quad (\text{IV-15})$$

and, as shown in Figure 30, have obtained good agreement with experimental results. For the more general calculations, Penfold has used Formulas (IV-13) and (IV-14) to estimate the thick target spectrum shapes for an

incident electron kinetic energy of 15 Mev, a 0.020-inch platinum target, and for two detectors which subtend different angles on the electron beam axis, ( $\Gamma = 10$  degrees,  $\Gamma \gg 10$  degrees). A comparison is made in Figure 31 of these two Penfold results (curves C and D) with the spectrum shape predicted by Formula 3BS(e) (curve A) and with the shape resulting from the application of the S function in Formula (IV-15) (curve B). The curves show that Formulas 3BS(e) and (IV-15) give a greater number of photons in the high frequency region relative to the total number in the spectrum compared with the more accurate spectral shape predicted by the Penfold procedure. For certain cases, the spectrum shape predicted by the simplified Formula (IV-15) may be sufficiently accurate.

The Hisdal method<sup>51/</sup> assumes that (a) the spectrum variation with angle as given by the Schiff Formula 2BS has the dominant effect on the thick target spectrum shape, (b) the energy loss of electrons in the target is negligible, (c) no electron radiates more than one photon, and (d) the photon absorption in the target is negligible. With these approximations, Hisdal has calculated tables for estimating the spectrum shape to be expected in a small detector placed on the electron beam-target axis. Hisdal's results are given in terms of a correction factor which is multiplied by Formula 3BS(e) for a given value of  $k$ , to obtain the corrected spectrum for a particular target thickness. Examples of spectra calculated by Hisdal's method are given in Figures 32(a) - (e) for 10, 20, 40, 90, and 300 Mev electrons, and are compared with the Schiff spectra integrated over photon direction, (Formula 3BS(e)). Obviously when the detector subtends a large solid angle at the target, the measured spectrum shape is given by the cross section integrated over the photon direction. Figures 7 and 8 give data for the spectrum shape included within a given detector angle. If this shape for a given experimental arrangement is estimated to be similar to the zero degree spectrum, then the Hisdal correction will be important; if this shape is estimated to be more similar to the spectrum integrated over all angles, then Hisdal's correction will be unimportant.

### C. Efficiency for Bremsstrahlung Production

The bremsstrahlung production efficiency for a given electron kinetic energy and target material is defined as the ratio of the total bremsstrahlung power radiated when an electron current is incident on a target to the total power in the incident electron beam. The results of various theoretical and experimental determinations of the efficiency are given below.

#### (1) Non-relativistic and Intermediate Energies

The efficiency results presented for this energy region apply only to the cases in which the electrons expend all of their kinetic energy in the target. Experimental determinations are complicated by (a) the large photon absorption in the target and (b) the large electron backscattering from the target<sup>49/</sup>. In the available measurements of the efficiency, corrections have been made for effect (a) but not for effect (b). Therefore, these experimental efficiencies are less than the values that would be obtained if all of the electrons were completely stopped in the target.

In this low energy region, most experimental and theoretical results<sup>58/</sup> are in agreement within a factor of two with an efficiency,  $\epsilon$ , given by the following formula:

$$\epsilon = 5 \times 10^{-4} Z^2 J_0 \quad (IV-16)$$

#### (2) Relativistic Energies

##### (a) Intermediate Thickness Targets

A target is defined to have an intermediate thickness if the incident electrons do not expend all of their energy as they traverse the target. This condition usually exists in high energy electron accelerators.

The efficiency of bremsstrahlung production for targets having an intermediate or small ( $\ll t_0$ ) thickness can be estimated from the expression

$$\epsilon = \left[ \frac{(dE_0)_R}{J_0} \right] \sim K t \quad (IV-17)$$

where  $(dE_0)_R$  is the energy loss by radiation,  $t$  is the target thickness in units of the radiation length,  $t_0$ , (Formula (IV-2)), and  $K$  is the radiation probability correction factor given in Figure 25.

(b) Thick Targets

For thick targets, the incident electrons lose all of their energy in the target. Formula (IV-16) obviously does not apply at high energies for which the efficiency must remain less than one. An approximate relation for the efficiency in this high energy region has been derived<sup>59</sup> by assuming that the total electron energy loss per unit path length can be written as

$$-\frac{d\epsilon_0}{dx} = -\left(\frac{\rho Z}{A}\right) \left\{ 6 + 3.5 \times 10^{-3} \epsilon_0 Z \right\} \quad (\text{IV-18})$$

where  $\rho$  is the density and  $A$  the atomic weight of the target material, and where the first term is the collision loss and the second term is the radiation loss. Integration from the initial energy  $\epsilon_0$  to 1 gives the following distance,  $x_0$ , travelled by an electron in losing all of its energy:

$$x_0 = \frac{A}{3.6 \times 10^{-3} \rho Z^2} \ln(1 + 6 \times 10^{-4} Z \epsilon_0) \quad (\text{IV-19})$$

Then the efficiency becomes

$$\epsilon = 1 - \frac{\text{collision loss}}{\epsilon_0} = 1 - \frac{6\rho Z}{A} \frac{x_0}{\epsilon_0} = \frac{3 \times 10^{-4} Z \mathcal{T}_0}{1 + 3 \times 10^{-4} Z \mathcal{T}_0} \quad (\text{IV-20})$$

This procedure does not account for the large fluctuations in the radiation loss process and, therefore, provides only a rough estimate of the efficiency. At low energies, Formula (IV-20) reduces to  $3 \times 10^{-4} Z \mathcal{T}_0$ , which agrees roughly with Formula (IV-16). Some representative values of the efficiency obtained from Formula (IV-20) are given in Table 7. These values do not include corrections for the X-ray absorption in the target, which cannot be neglected for most situations.

TABLE 7

Approximate Percentage Efficiencies for X-ray Production

Electron kinetic energy:	2	4	10	20	50	600
Carbon	0.36	0.72	1.77	3.47	8.3	52
Aluminum	0.77	1.54	3.75	7.2	16.3	70
Iron	1.54	3.0	7.2	13.5	28.1	82
Lead	4.7	9.0	19.7	33	55	94

V. Acknowledgments

This report has benefitted considerably from discussions with Drs. U. Fano, M. Danos, J. Leiss, and H. O. Wyckoff. We are grateful to them for their helpful comments and criticisms. We express our special thanks to Dr. L. Maximon who critically reviewed the manuscript and made available a paper by Olsen and Maximon prior to publication. We are also indebted to Mr. John Hubbell for the comparison of the Hisdal and Sirlin results and for most of the computations and detailed plotting in the figures.

References

1. H. Bethe and E. Salpeter, Encyclopedia of Physics, 35(Springer, Berlin, 1957) 425; S. T. Stephenson, Encyclopedia of Physics 30 (Springer, Berlin, 1957), 337.
2. Except for electron-electron bremsstrahlung which is briefly considered in Section III, no results are presented for other bremsstrahlung processes involving for example the acceleration of positrons or protons.
3. A target is defined to be thin if both the electron scattering and energy loss processes have a negligible influence on the energy and angular distributions of the bremsstrahlung. Order of magnitude estimates of such thin targets for particular energy regions, can be found in in the references listed in Section IIG.
4. A detailed discussion of this problem is given by H. A. Bethe and L. C. Maximon, Phys. Rev. 93, 768 (1954).
5. A. Sommerfeld, Wellenmechanik (Frederick Ungar, New York, 1950), Chap. 7.
6. P. Kirkpatrick and L. Wiedmann, Phys. Rev. 67, 321 (1945).
7. H. Olsen, L. C. Maximon, and H. Wergeland, Phys. Rev. 106, 27 (1957).
8. H. Olsen and L. C. Maximon, Phys. Rev. (To be published).
9. W. Heitler, The Quantum Theory of Radiation (Oxford University Press, London, 1954) Third Edition, p. 242.
10. H. Bethe and L. C. Maximon, Phys. Rev. 93, 768 (1954).
11. H. Olsen, Phys. Rev., 99, 1335 (1955).
12. H. Olsen, and L. C. Maximon, Phys. Rev. 110, 589 (1958).
13. H. Davies, H. Bethe, and L. C. Maximon, Phys. Rev. 93, 788 (1954).
14. L. I. Schiff, Phys. Rev., 83, 252 (1951).
15. J. H. Hubbell, J. Applied Phys. (To be published).
16. E. Hisdal, Phys. Rev. 105, 1821 (1957).
17. G. Elwert, Ann. Phys. 34, 178 (1939).
18. W. C. Miller and B. Waldman, Phys. Rev. 75, 425 (1949);  
E. G. Fuller, E. Hayward, and H. W. Koch, Phys. Rev. 109, 630 (1958);  
D. Jamnik, Private communication.

19. U. Fano, Phys. Rev., (To be published).
20. Note that the cross section differential in  $\theta_0$  is proportional to  $\sin^3 \theta_0$ . Therefore, both the Sauter-approximation and the Born-approximation calculations predict that the cross section at the high frequency limit is zero for  $\theta_0$  equal to zero.
21. U. Fano, H. W. Koch, and J. Motz, Phys. Rev., 112, 1679 (1958).
22. Detailed formulas for the Sauter photoelectric cross section and for the "exact" cross sections of Sauter-Stobbe and Nagasaka are given by Heitler<sup>9/</sup> and by G. White Grodstein, NBS Circular No. 583 (1957). The "exact" photoelectric cross section formula for energies above 5-Mev has been recently given by Nagasaka and Guth (private communication) as

$$\sigma = \frac{4\pi r_0^2 Z^5}{137^4} \frac{G}{k} \left[ \sigma_0 - \sqrt{\frac{E}{k}} \left( \frac{E-2}{E-1} \right) 0.832 \left( \frac{Z}{137} \right) + 0.3 \left( \frac{Z}{137} \right)^2 \right].$$

Where E is the total energy of the ejected electron

$$(E = 1 + k - I), \quad I = 1/2 \left( \frac{Z - 0.3}{137} \right)^2,$$

$$\sigma_0 = \frac{(E^2 - 1)^{3/2}}{(E-1)^4} \left[ \frac{4}{3} + \frac{E(E-2)}{E+1} \left( 1 - \frac{1}{2E\sqrt{E^2-1}} \ln \left[ \frac{E + \sqrt{E^2-1}}{E - \sqrt{E^2-1}} \right] \right) \right], \text{ and}$$

$$G = \exp \left[ \frac{-\pi Z}{137} + Z \left( \frac{Z}{137} \right)^2 - \left( \frac{Z}{137} \right)^2 \ln \left( \frac{Z}{137} \right) \right] \quad \text{for } \frac{1}{E^2} \ll 1.$$

23. S. J. Biel and E. H. S. Burhop, Proc. Phys. Soc. (London), A68, p. 165 (1955).
24. A. T. Nelms and I. Oppenheim, J. Res. NBS, 55, p. 53 (1955).
25. R. Jost, J. M. Luttinger, and M. Slotnik, Phys. Rev. 80, 189 (1950).
26. R. McGinnies, Private communication.
27. H. Bethe, Proc. Camb. Phil. Soc., 30, 524 (1934).
28. H. Bethe and W. Heitler, Proc. Roy. Soc., A146, p. 83 (1934).
29. H. Bethe, Ann. d. Physik, 5, p. 385 (1930).
30. G. Molière, Z. Naturforsch., 2a, 133 (1947).

31. Most of the experimental data that is available in this low energy region has been produced by the pioneering work of Kulenkampff and his co-workers. Their measurements give extensive information about relative angular distributions and spectra from thin targets, and show general agreement with the non-relativistic Sommerfeld theory<sup>5/</sup>. However, the details of their various results are not included in this report which is primarily concerned with absolute cross section measurements and comparisons with the Born-approximation theory.
32. H. Amrehn, Zeit. f. Physik 144, 529 (1956);  
D. Röss, Thesis, University of Würzburg, Dec. (1957).
33. J. W. Motz and R. C. Placious, Phys. Rev. 109, 235 (1958).
34. H. Mausbeck, Thesis, University of Würzburg (1957);  
H. Zeh, Thesis, University of Würzburg (1957).
35. J. W. Motz, Phys. Rev. 100, 1560 (1955).
36. N. Starfelt and H. W. Koch, Phys. Rev., 102, 1598 (1956).
37. For  $Z = 13$ , the corrected values for energies above 50 Mev have only small differences (less than one percent) with the values shown by the solid line for  $Z = 13$ .
38. A Born-approximation formula that includes screening effects without the extreme-relativistic approximation, has been given by Gluckstern and Hull, Phys. Rev. 90, 1030 (1953). However, this formula applies mainly to the low frequency region and has been found to be inadequate<sup>36/</sup> in the high frequency region.
39. For a general review of the available theories on electron-electron bremsstrahlung, see J. Joseph and F. Rohrlich, Rev. Mod. Phys. 30, 354 (1958).
40. G. M. Garibyan, Zh. Eksptl. i. Teoret. Fiz. 24, 617 (1953).
41. J. A. Wheeler and W. E. Lamb, Phys. Rev. 55, 858 (1939), and 101, 1836 (1956).
42. The results that are presented for the non-relativistic and intermediate energy region where  $T_0 \leq 1$  apply only to targets that are thick enough to stop the electrons. For the relativistic region where  $T_0 \gg 1$ , there is no such restriction on the target thickness.

43. Buechner, Van de Graaff, Burrill, and Sperduto, Phys. Rev., 74, 1348 (1948).
44. W. V. Mayneord, Brit. J. of Radiology, Supplement No. 2, 136, (1950).  
For photons outside this energy range, the conversion factor has a significant energy dependence and the factor must be weighted by the bremsstrahlung spectrum shape.
45. J. D. Lawson, Nucleonics 10, No. 11, 61 (1952).
46. Exponential integral functions are tabulated in National Bureau of Standards Tables of Sine, Cosine, and Exponential Integrals, Vols. 1 and 2 (MT5 and MT6) (Government Printing Office).
47. Muirhead, Spicer and Lichtblau, Proc. Phys. Soc. (London), A65, 59 (1952).
48. One of the earliest experimental indications of this dependence was found by C. E. Wagner, Phys. Zeitschrift 21, 621 (1920).
49. Miller, Motz, and Ciafella, Phys. Rev., 96, 1344 (1954).
50. H. A. Kramers, Phil. Mag., 46, 836 (1923).
51. For estimates of the thick-target characteristic radiation intensities that are superimposed on the continuous spectrum, see Compton and Allison, X-rays in Theory and Practice (Van Nostrand 1949), p. 69-89.
52. A detailed summary of such comparisons is given in National Bureau of Standards Handbook 62, p. 20-24 (1957).
53. A. Penfold, University of Illinois Report (unpublished).
54. E. Hisdal, Phys. Rev., 105, 1821 (1957); E. Hisdal, Archiv for Mathematic of Naturvidenskab, 54, No. 3, 1 (1957).
55. A similar but less general method has been used by R. Wilson, Proc. Phys. Soc., A66, 638 (1953). Wilson's calculations did not include electron scattering effects in the target and his results give a spectrum shape averaged over the photon directions.
56. Motz, Miller, and Wyckoff, Phys. Rev., 89, 968 (1953).
57. Similar calculations that apply only to a specific target material and electron energy have been made by A. Sirlin, Phys. Rev. 106, 637 (1957). While the Hisdal calculations include only the Schiff complete screening approximations, Sirlin examined the effects of both the intermediate and complete screening approximations on the spectrum shape.

58. These results are summarized by H. Kulenkampff, Physics of the Electron Shells-Fiat Review of German Science. 1939-1946 (H. Kopfermann, Editor) p. 95; R. D. Evans, The Atomic Nucleus, McGraw Hill, p. 616 (1955), and by S. T. Stephenson (reference 1).
59. H. W. Koch and J. <sup>M</sup>~~W~~. Wyckoff, IRE Trans. of the Professional Group on Nuclear Science, Vol. NS-5, No. 3, (1958).



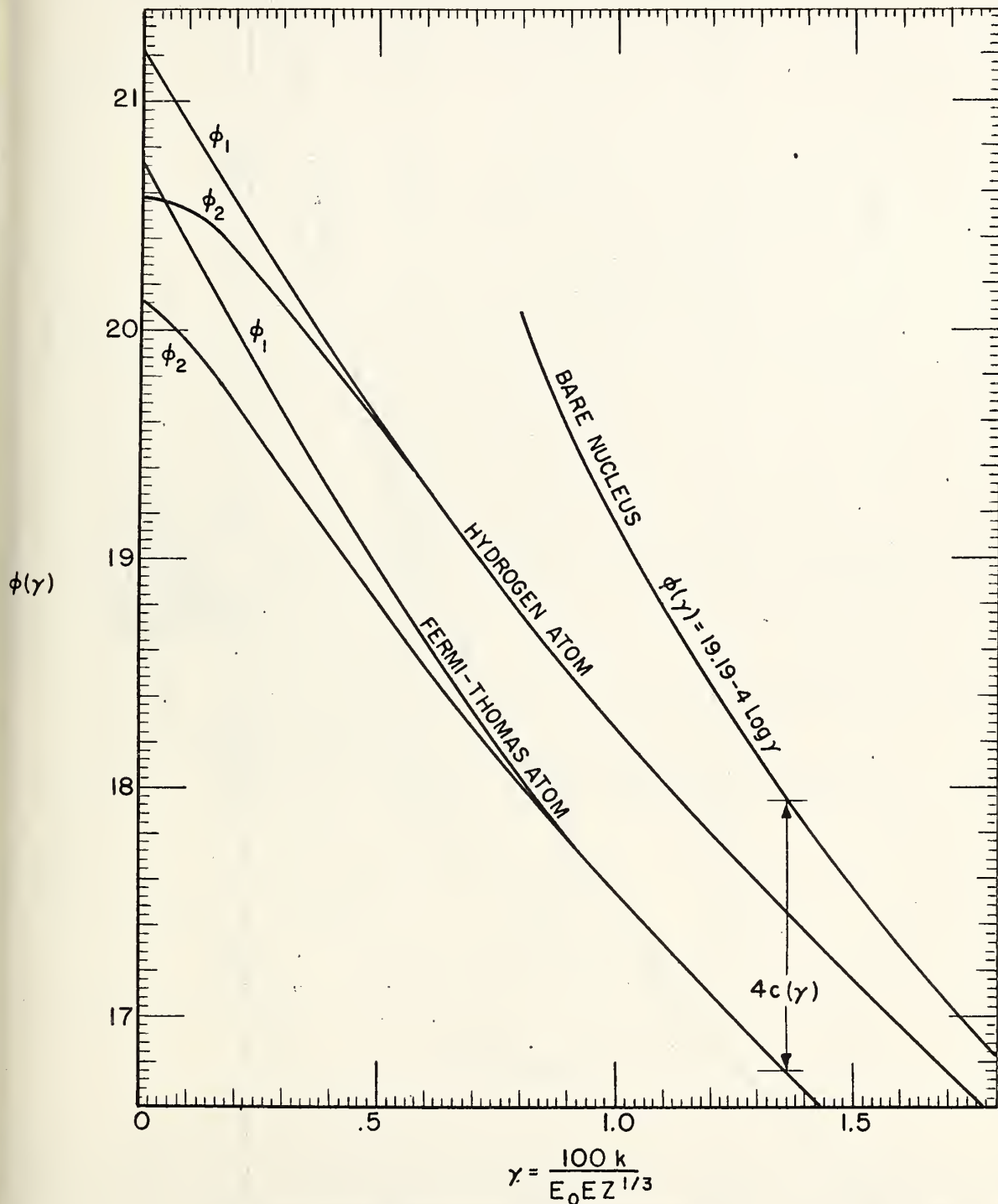


Fig. 1. Screening factors  $\frac{28}{41}$ ,  $\phi_1(\gamma)$  and  $\phi_2(\gamma)$ , for electron-nuclear bremsstrahlung, plotted as a function of  $\gamma = 100k/E_0 E Z^{1/3}$ . The curve marked "Hydrogen atom" was calculated  $\frac{41}{41}$  with exact wave functions. The curves for the Thomas-Fermi atom and a bare nucleus differ by the quantity  $4c(\gamma)$ , where the function  $c(\gamma)$  is plotted in Fig. 2.

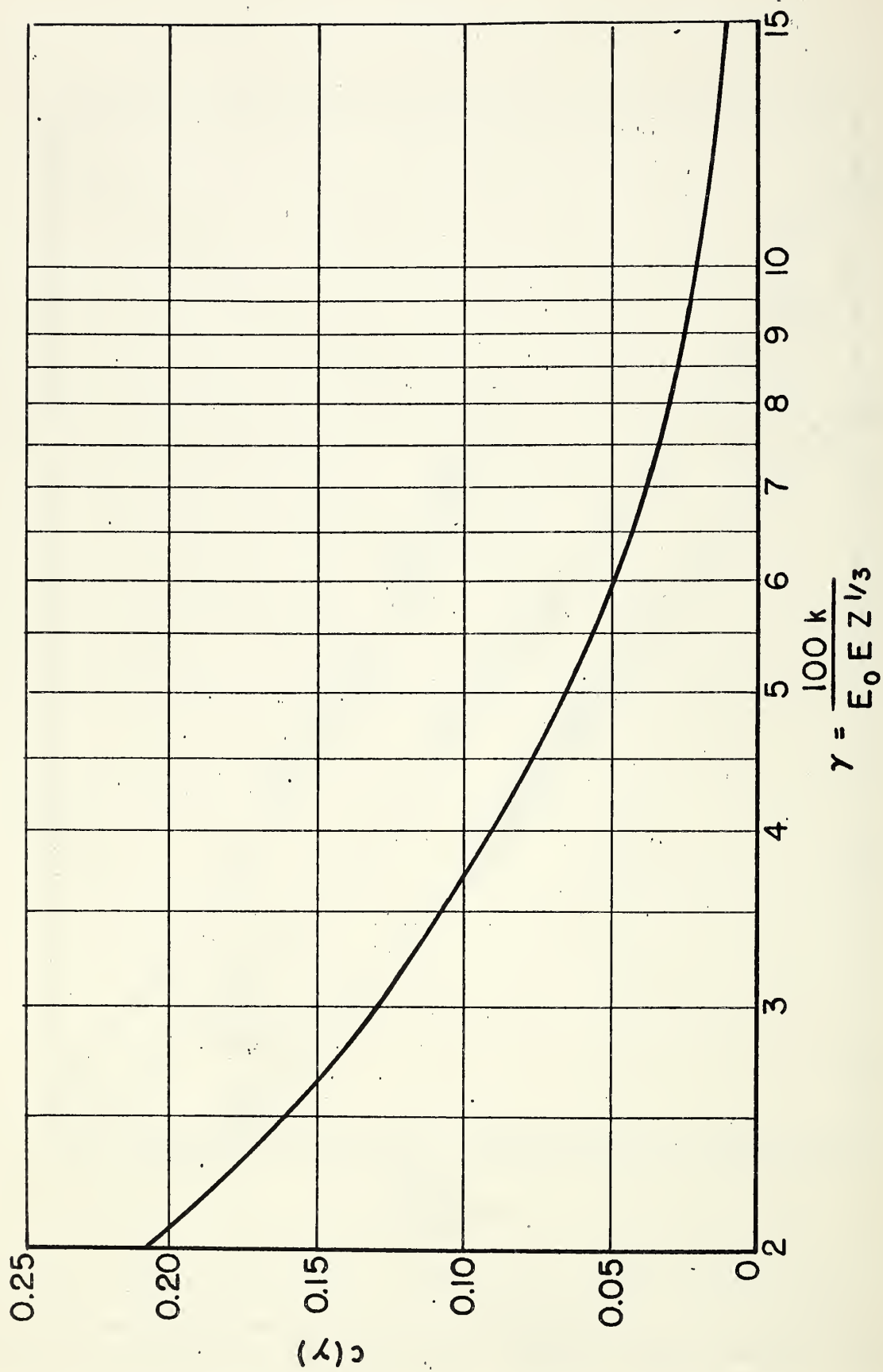


Fig. 2. Screening factor  $\frac{28}{c(\gamma)}$ ,  $c(\gamma)$ , for electron-nuclear bremsstrahlung plotted as a function of  $\gamma = 100k/E_0 E Z^{1/3}$ .

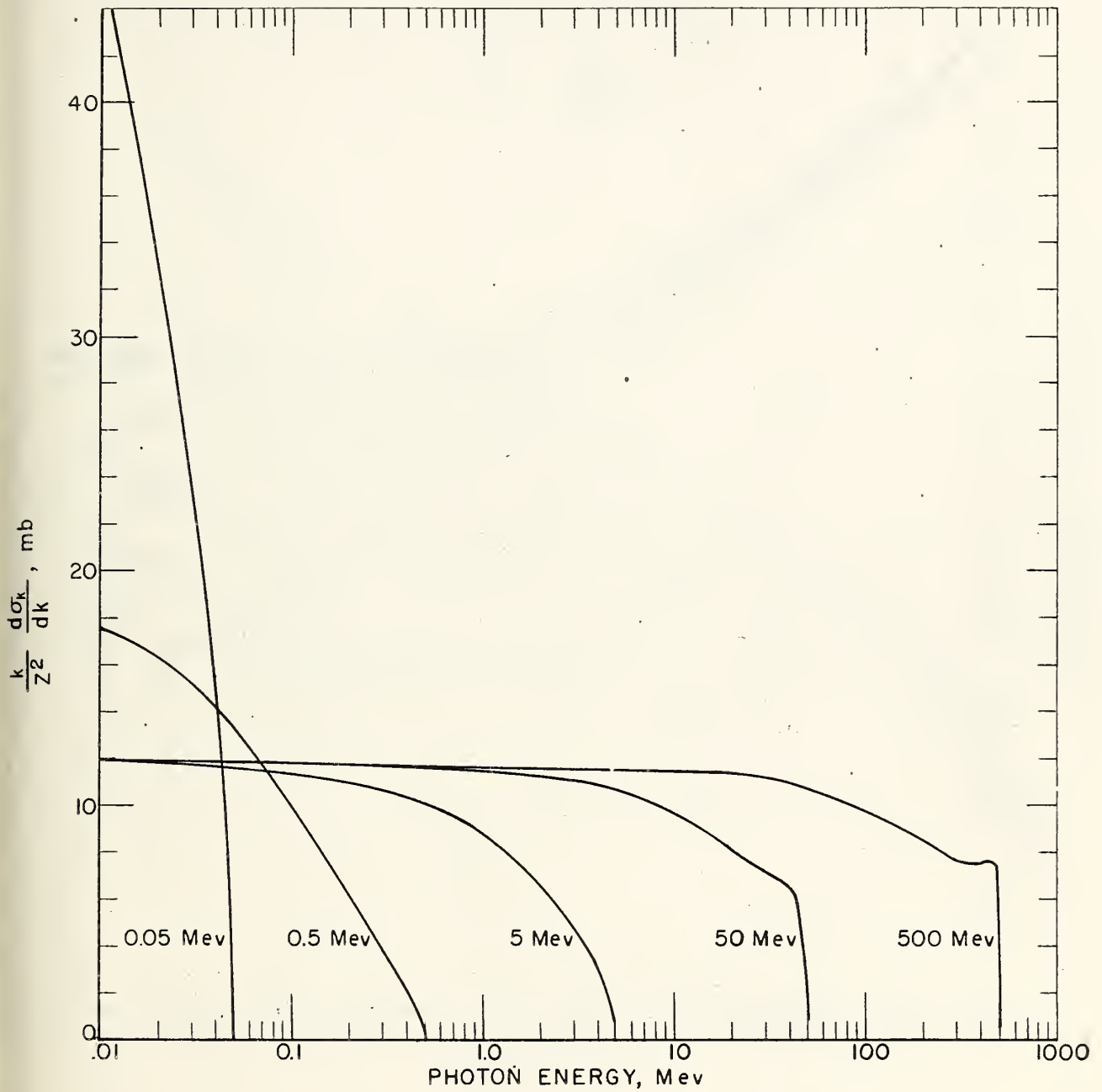


Fig. 3. Dependence of the Born-approximation cross section integrated over the photon directions on the photon and electron energy. The ordinate values for these curves are obtained from Formula 3BN for 0.05 and 0.50 Mev electrons, and from Formula 3BS (e) for 5, 50, and 500 Mev electrons.

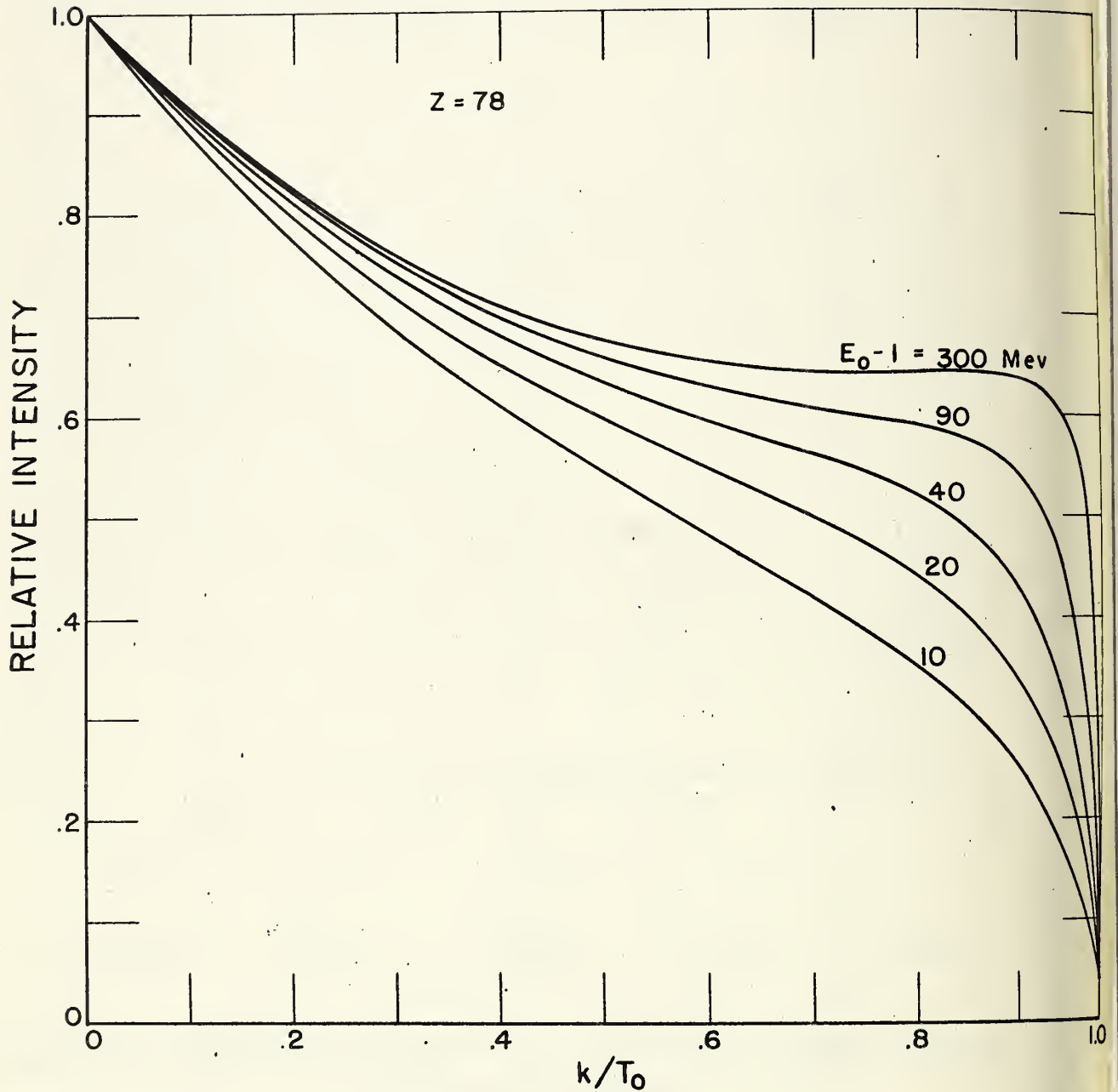


Fig. 4. Dependence of the bremsstrahlung spectrum shape on the electron kinetic energy for a platinum target ( $Z = 78$ ). The relative intensity (defined as proportional to the product of the photon energy and number per unit time) is integrated over the photon direction and is normalized to unity for zero photon energies. The intensity values were computed from Formula 3BS(e).

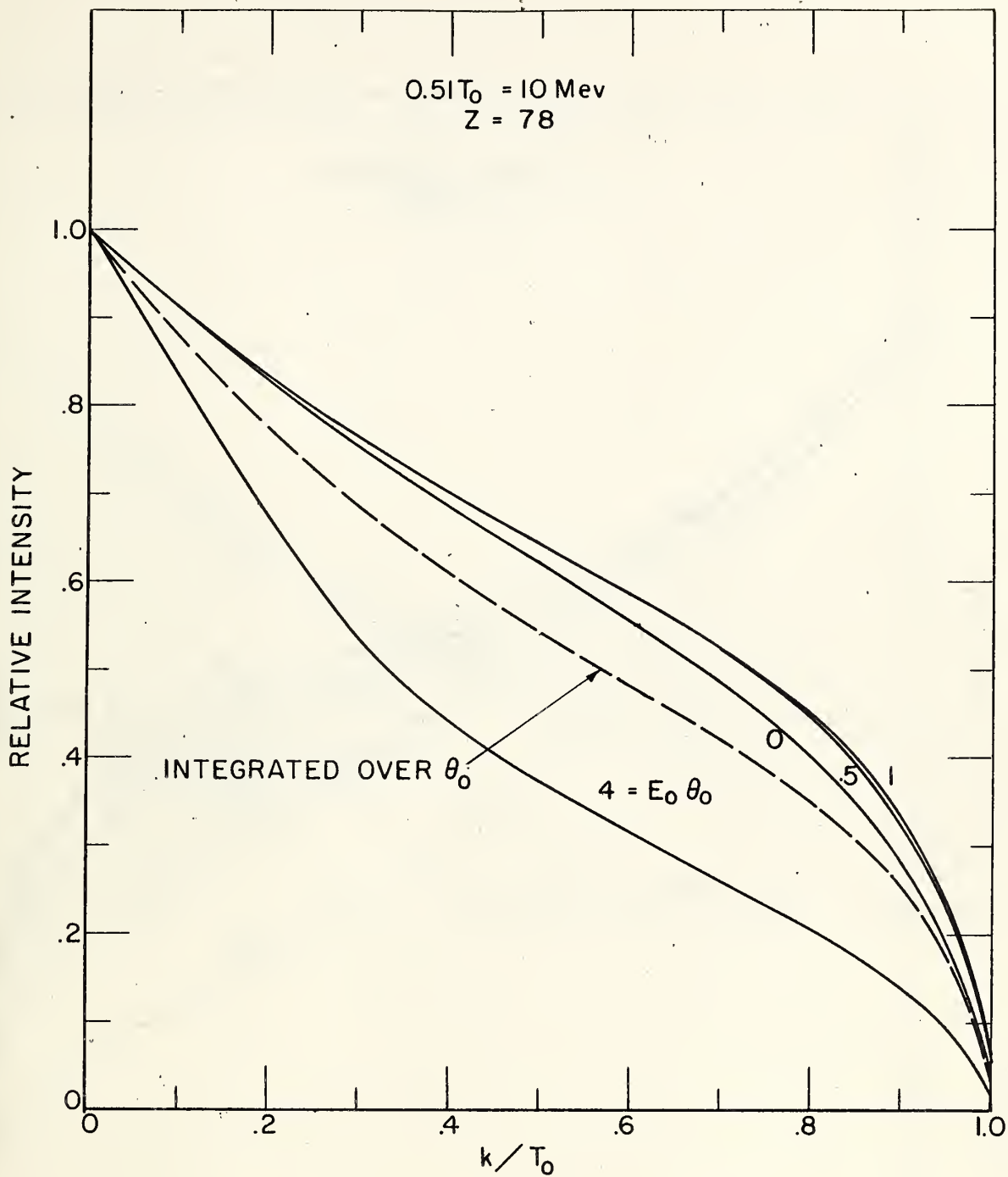


Fig. 5(a). Dependence of the Schiff spectrum shape on the photon emission angle,  $\theta_0$ , for 10 Mev electrons and for  $Z = 78$ . The data are obtained from Formula 2BS (solid lines) and from Formula 3BS(e) (dashed line). The values for the intensities (defined as proportional to the product of the photon energy and number per unit time) are normalized to unity at the zero photon energy.

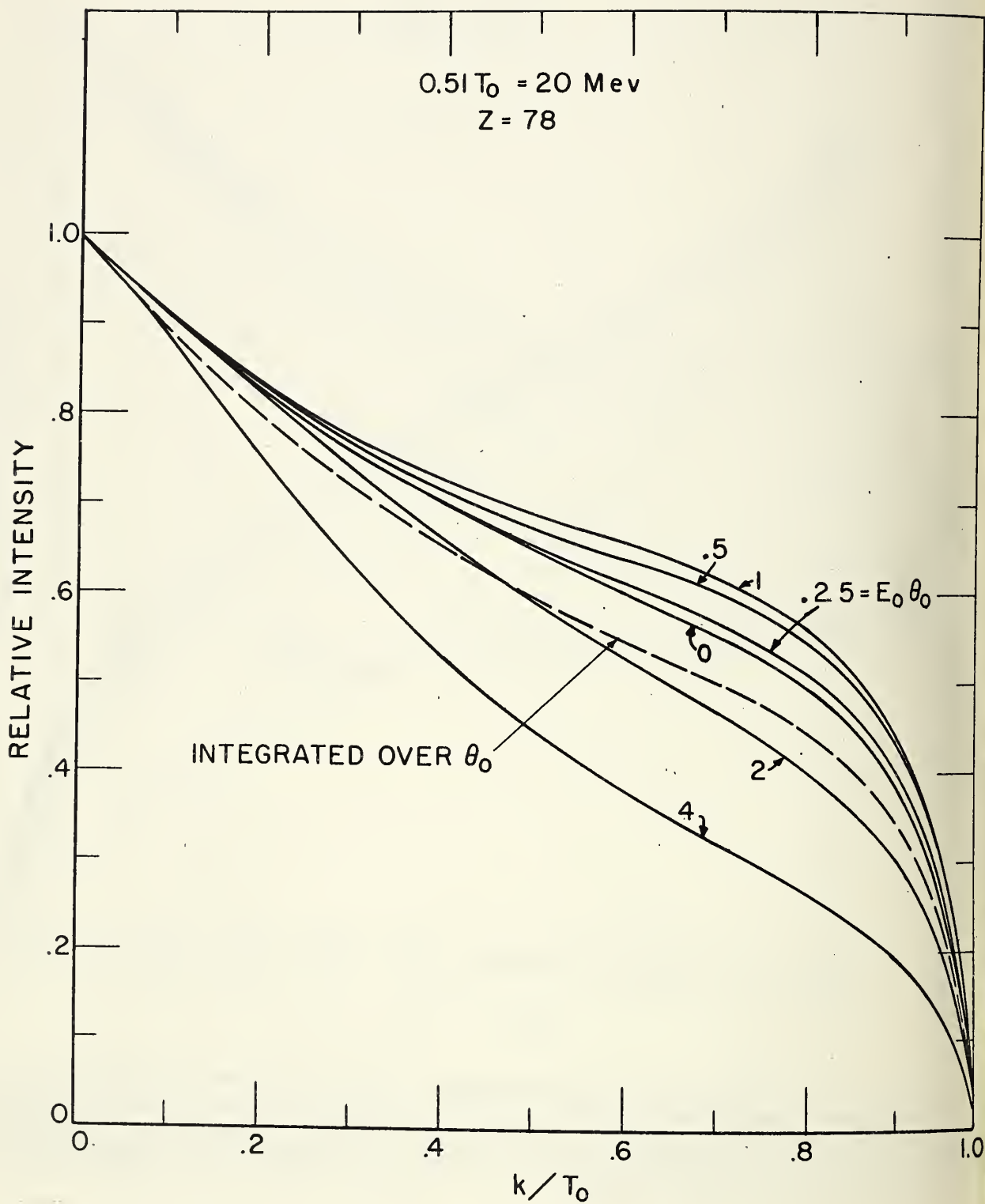


Fig. 5(b). Dependence of the Schiff spectrum shape on the photon emission angle  $\theta_0$ , for 20 Mev electrons and for  $Z = 78$ . See 5(a).

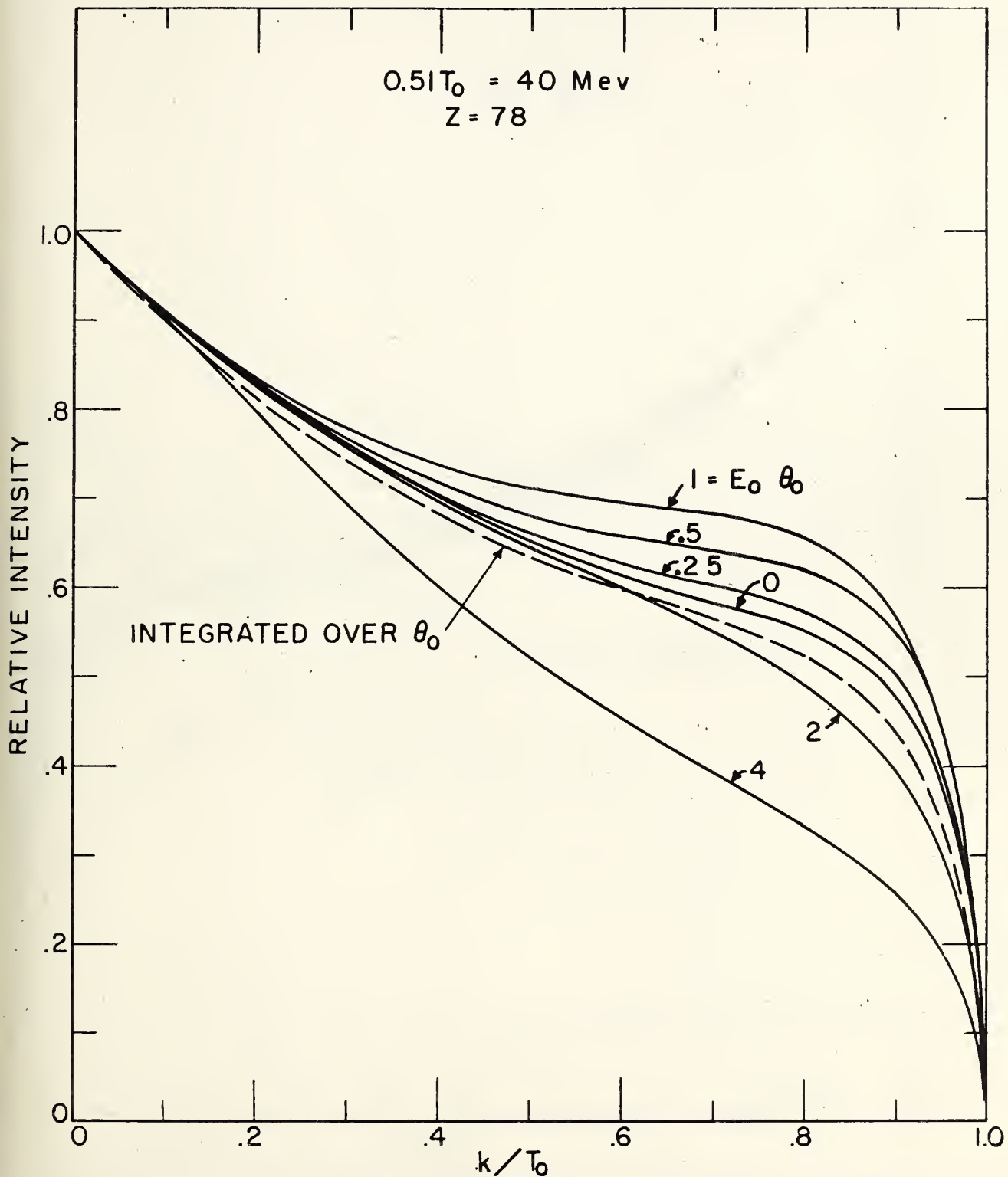


Fig. 5(c). Dependence of the Schiff spectrum shape on the photon emission angle,  $\theta_0$ , for 40 Mev electrons and for  $Z = 78$ . See 5(a).

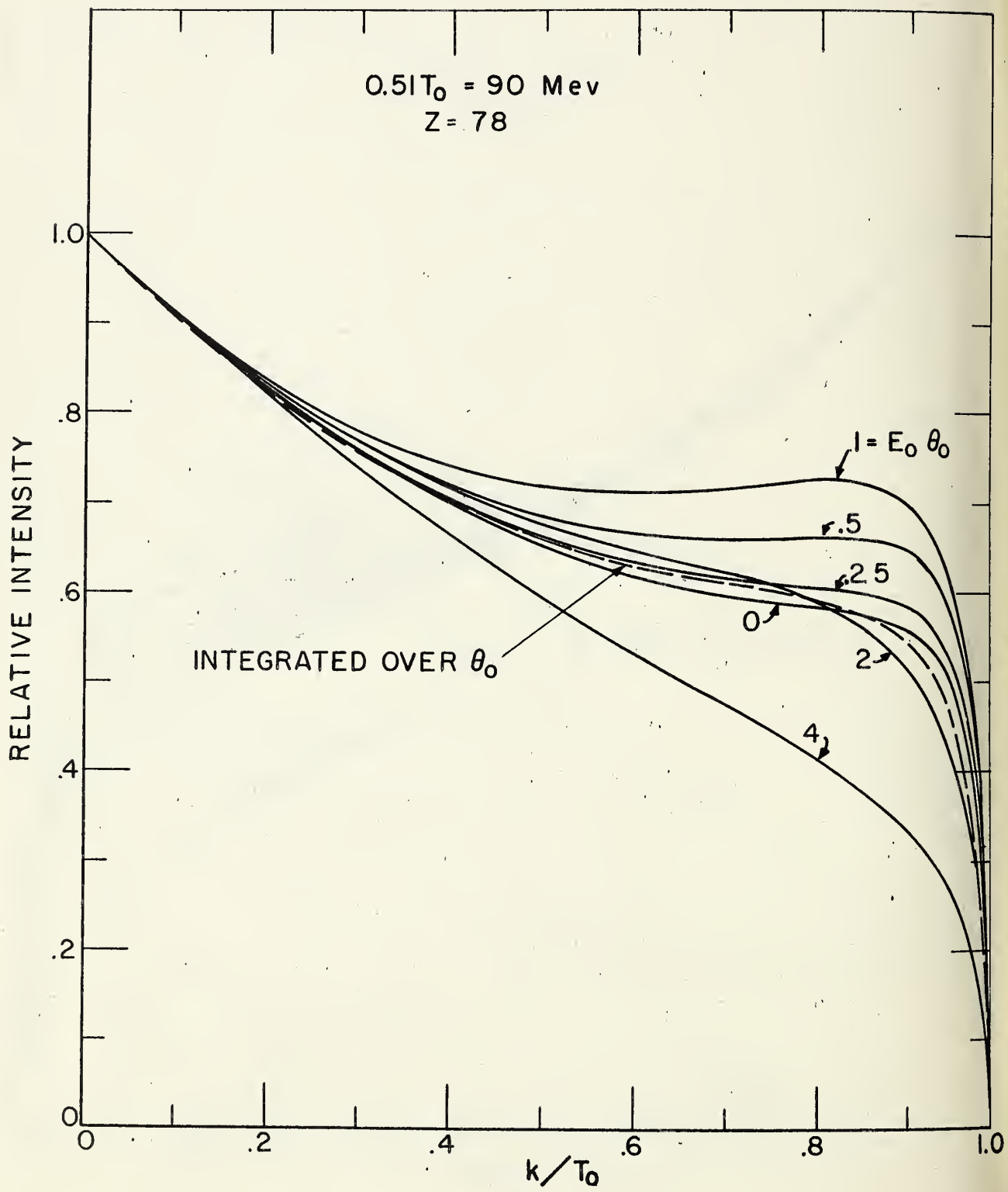


Fig. 5(d). Dependence of the Schiff spectrum shape on the photon emission angle,  $\theta_0$ , for 90 Mev electrons and for  $Z = 78$ . See 5(a).

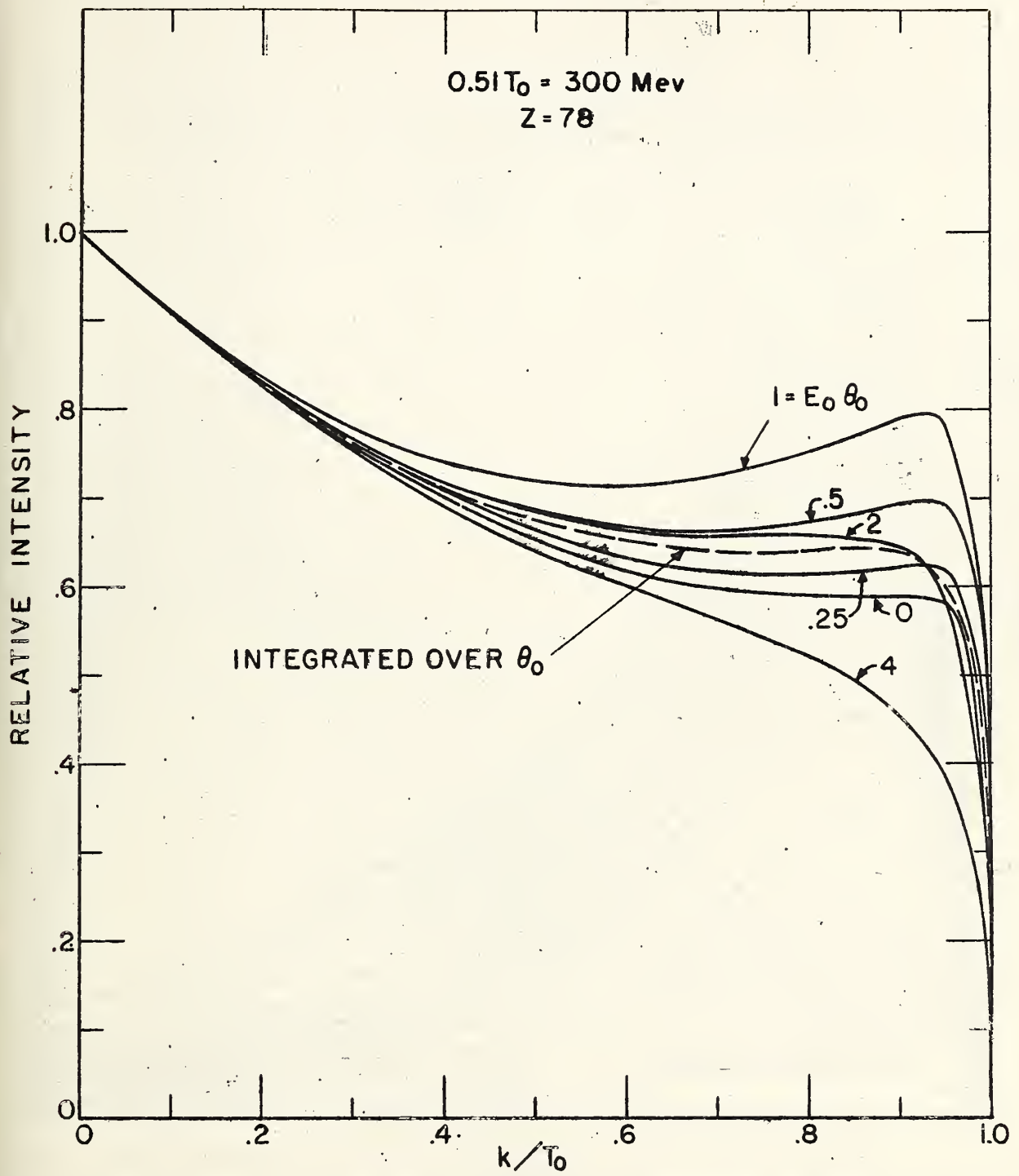


Fig. 5(e). Dependence of the Schiff spectrum shape on the photon emission angle,  $\theta_0$ , for 300 Mev electrons. See 5(a).

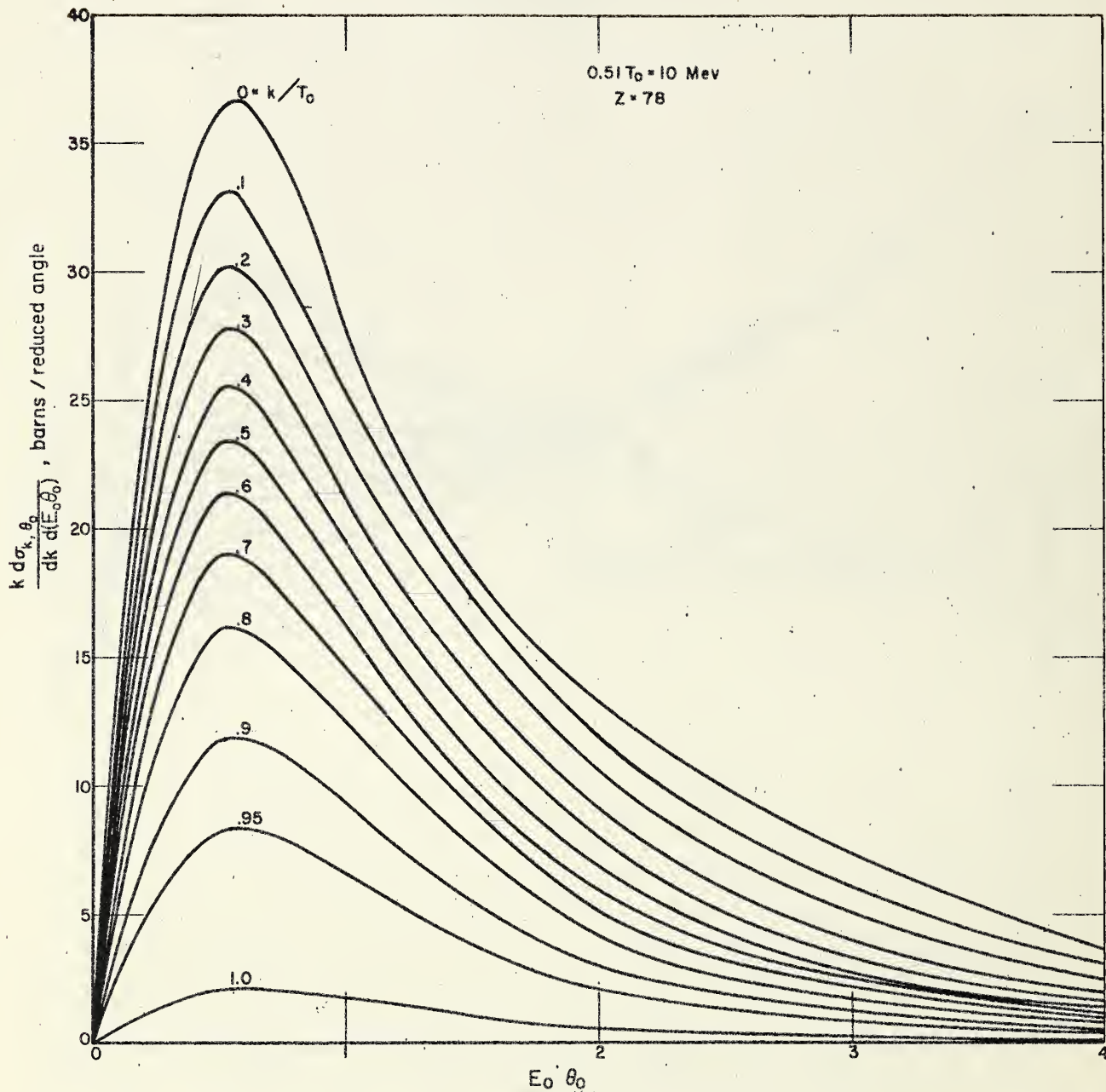


Fig. 6(a). Angular dependence of the Schiff cross section (Formula 2BS,  $Z = 78$ ) at various photon energies for 10 Mev electrons.

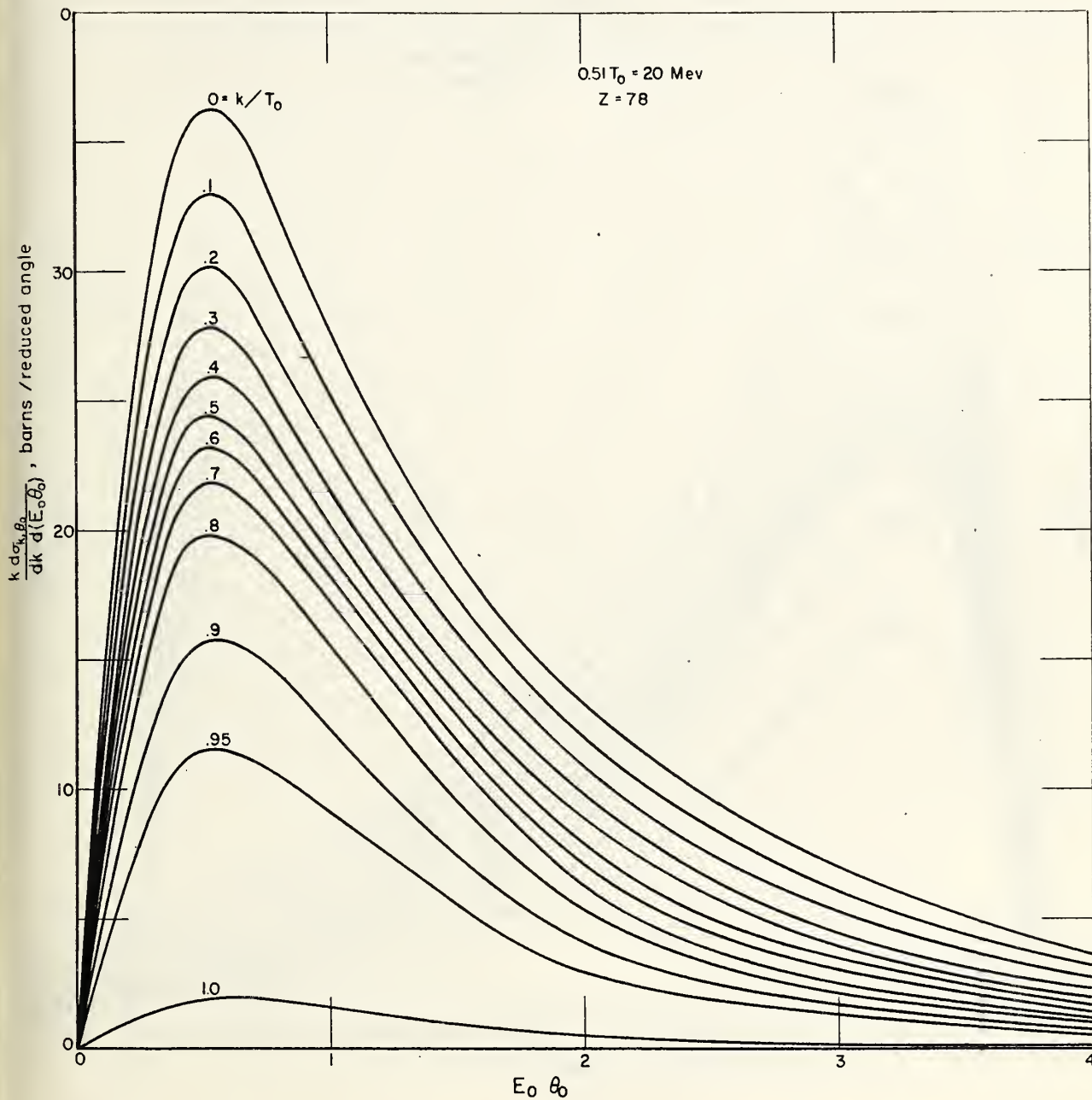


Fig. 6(b). Angular dependence of the Schiff cross section (Formula 2BS,  $Z = 78$ ) at various photon energies, for 20 Mev electrons.

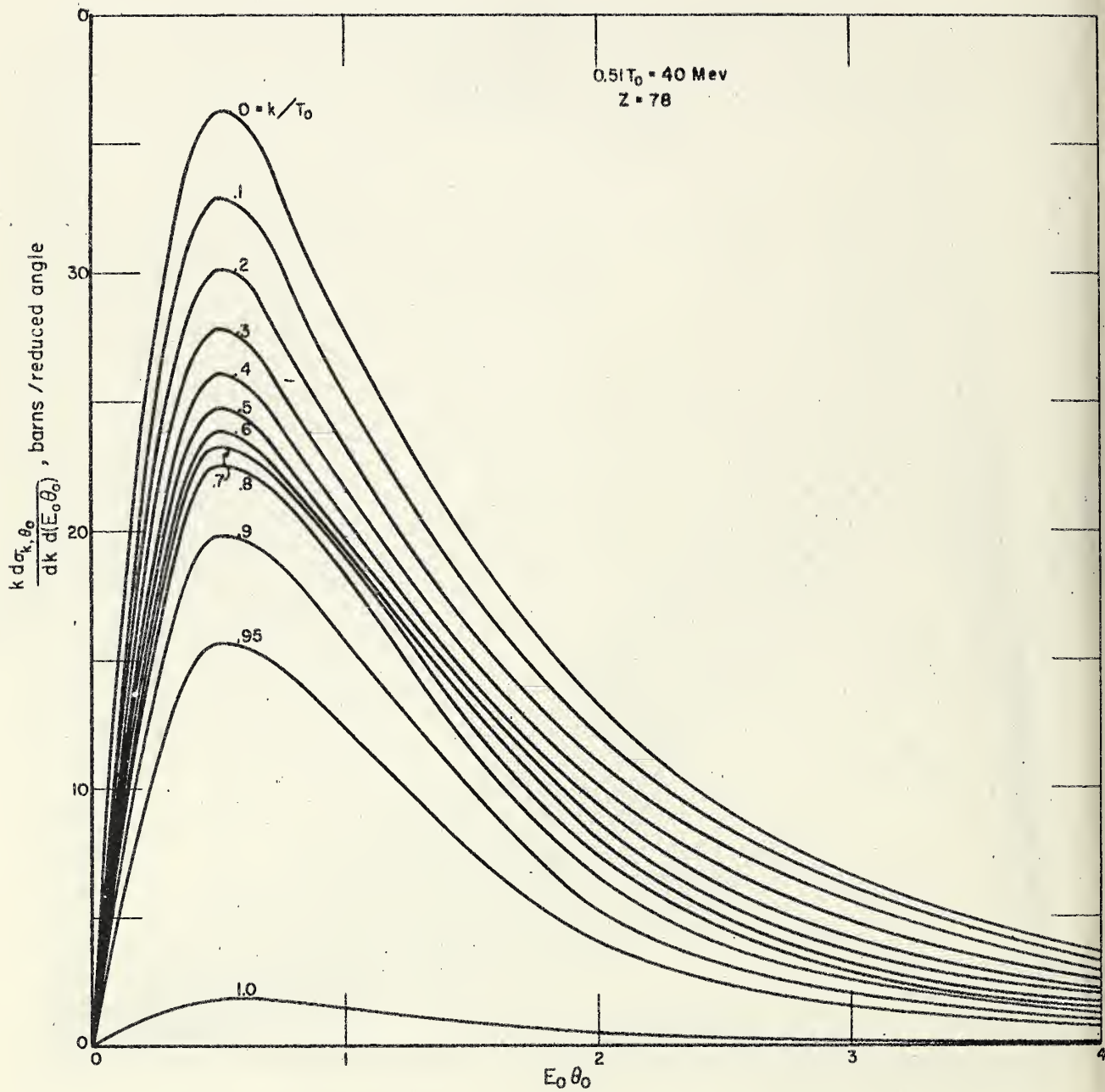


Fig. 6(c). Angular dependence of the Schiff cross section (Formula 2BS,  $Z = 78$ ) at various photon energies for 40 Mev electrons.

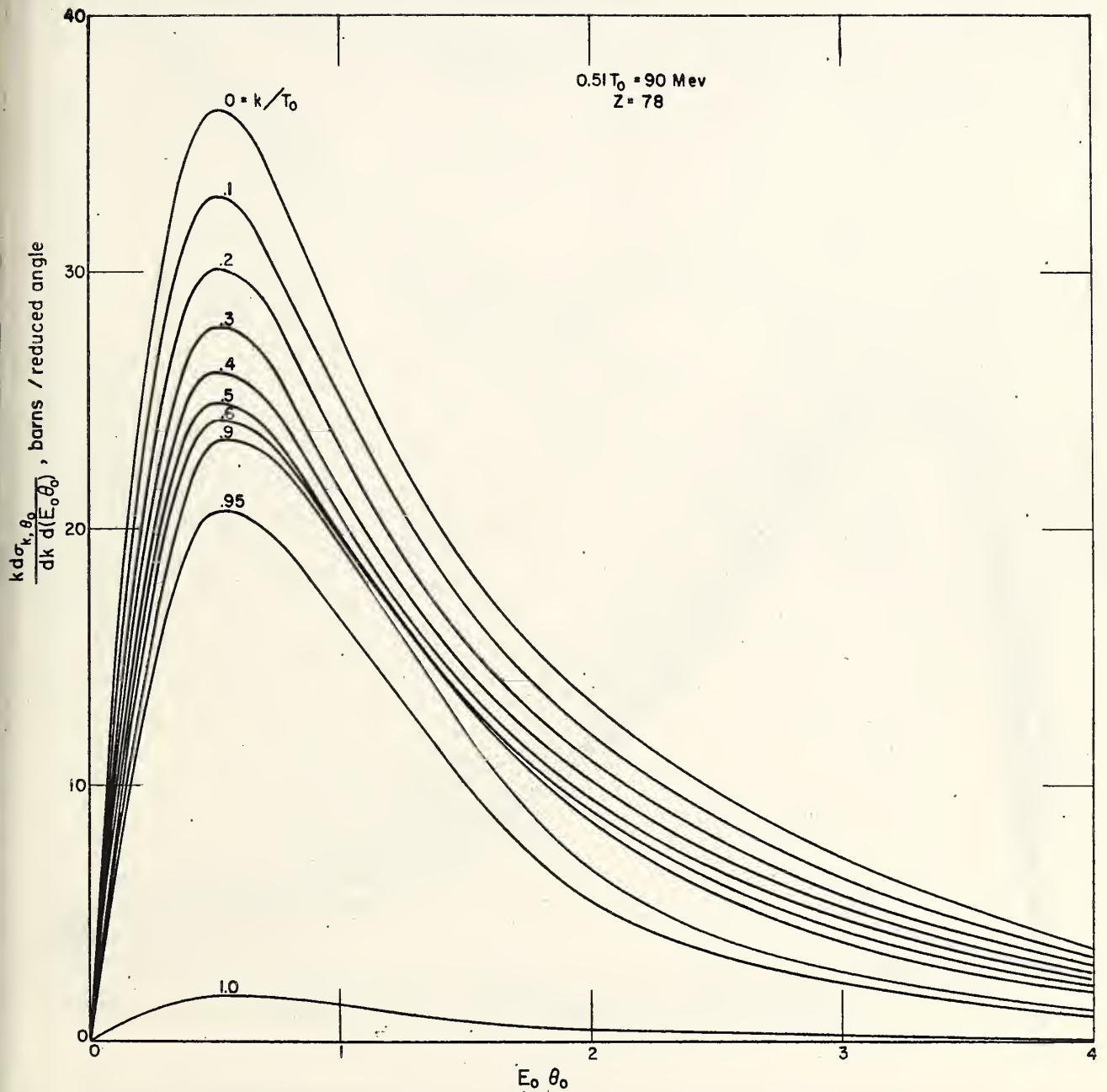


Fig. 6(d). Angular dependence of the Schiff cross section (Formula 2BS,  $Z = 78$ ) at various photon energies for 90 Mev electrons.

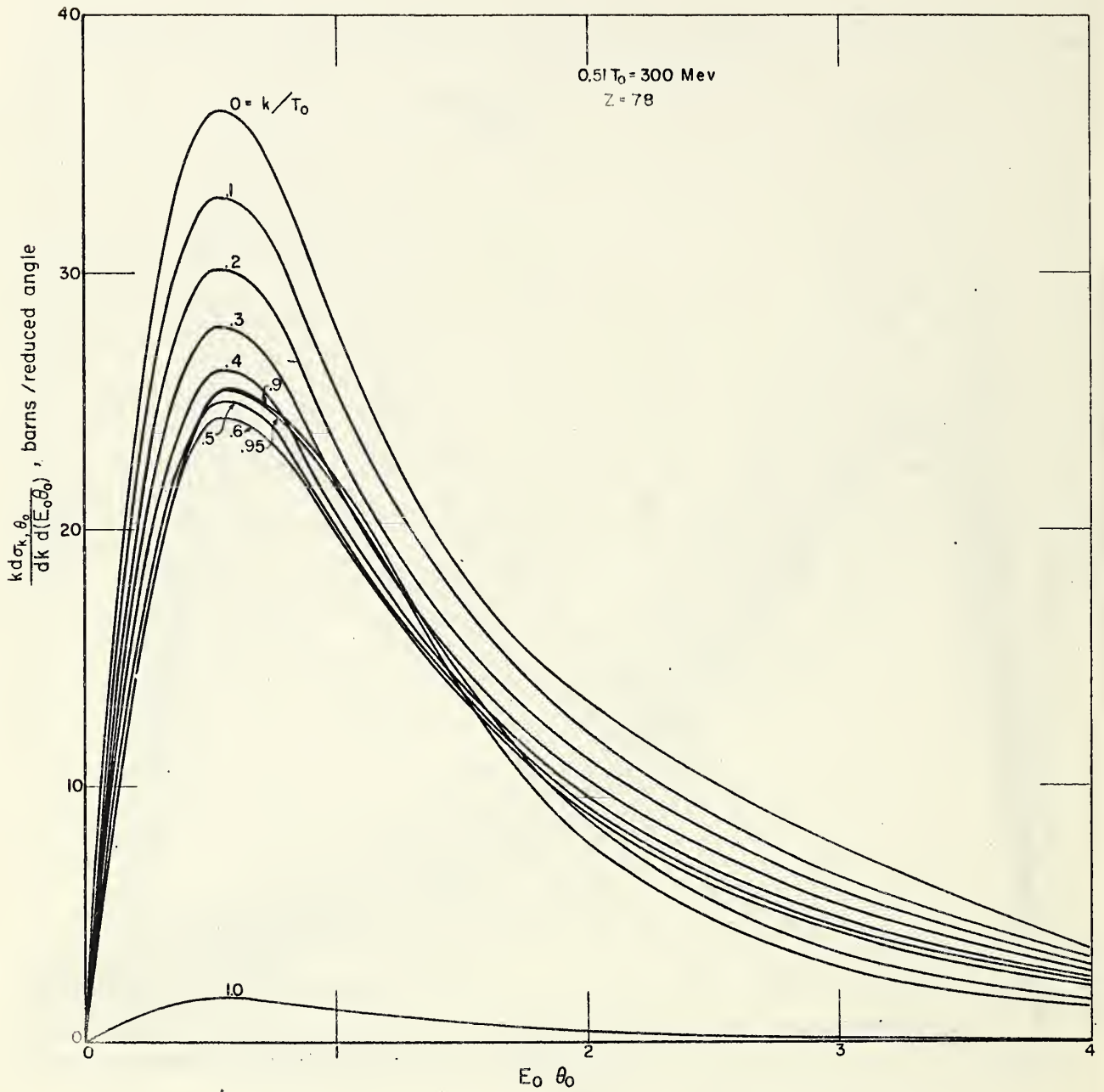


Fig. 6(e). Angular dependence of the Schiff cross section (Formula 2BS, Z = 78) at various photon energies for 300 Mev electrons.

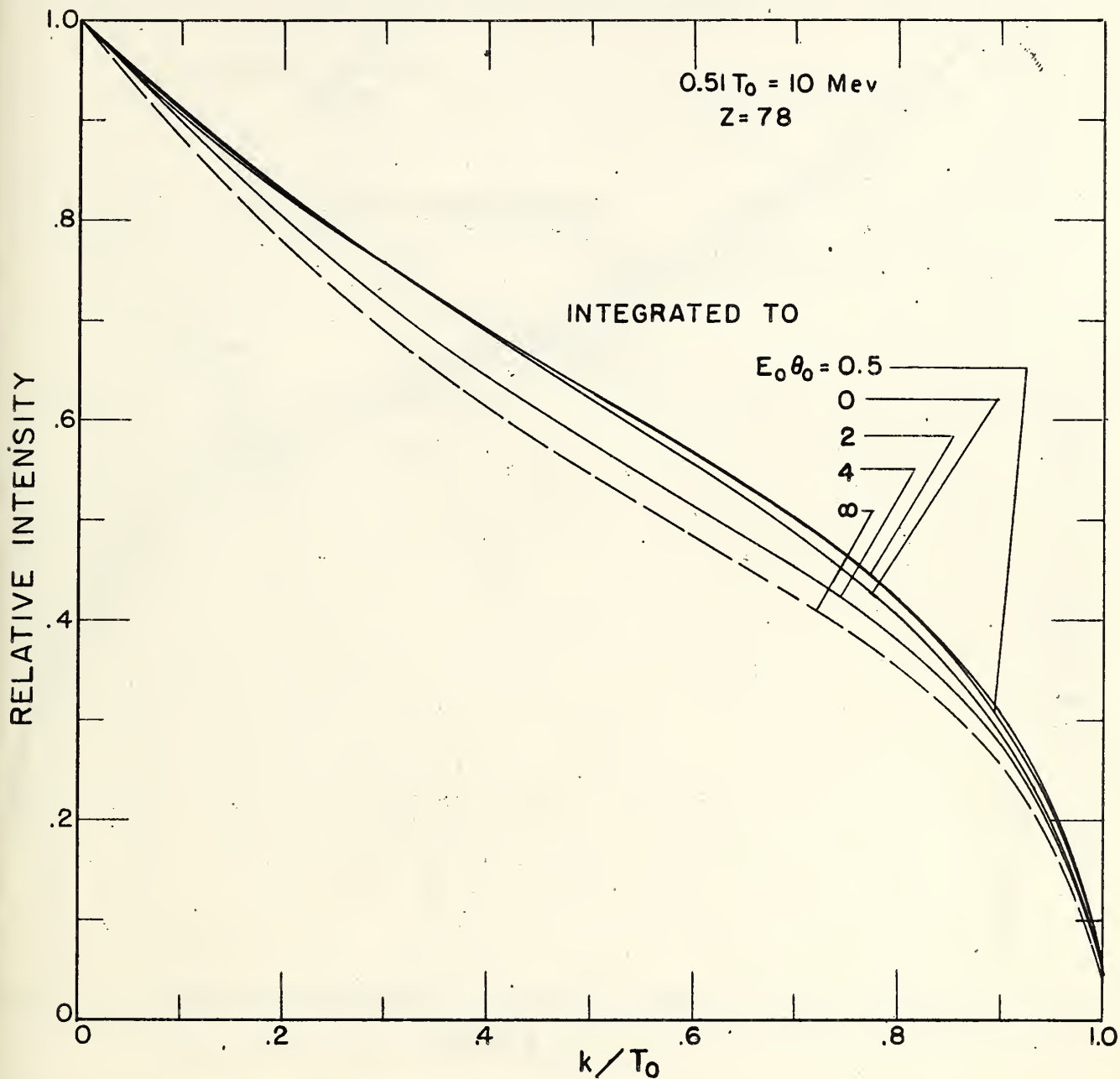


Fig. 7(a). Comparison of Schiff spectra integrated up to various photon emission angles for 10 Mev electrons and for  $Z = 78$ . The curves were derived by graphical integration of the cross section curves given in Fig. 6, and may also be derived analytically by the integration of Formula 2BS. The curve labeled  $\infty$  represents the spectrum integrated over all angles. The values of the intensity (defined as proportional to the product of the photon energy and number per unit time) are normalized to unity at the zero photon energy.

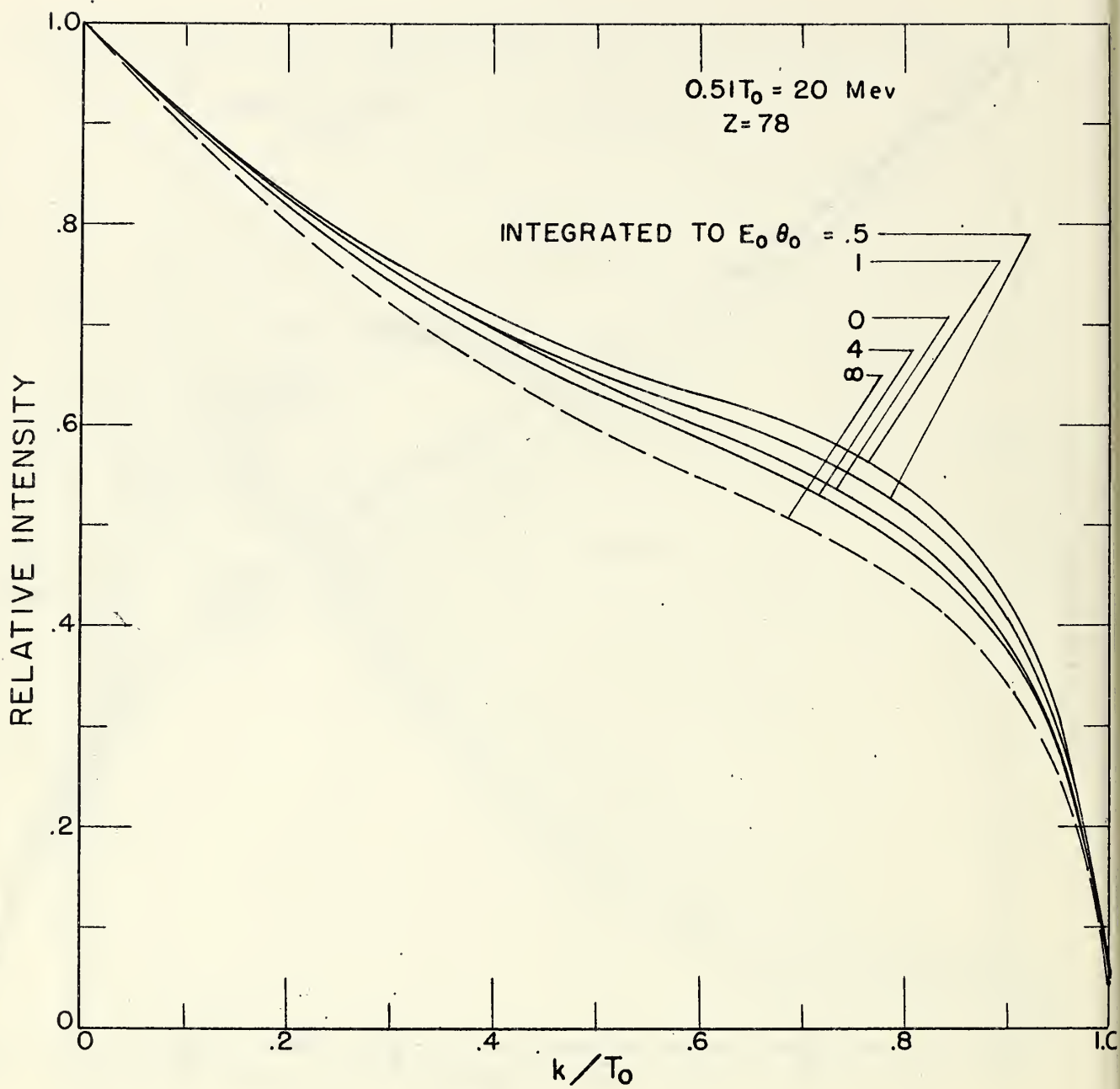


Fig. 7(b). Comparison of Schiff spectra integrated up to various photon emission angles for 20 Mev electrons. See 7(a).

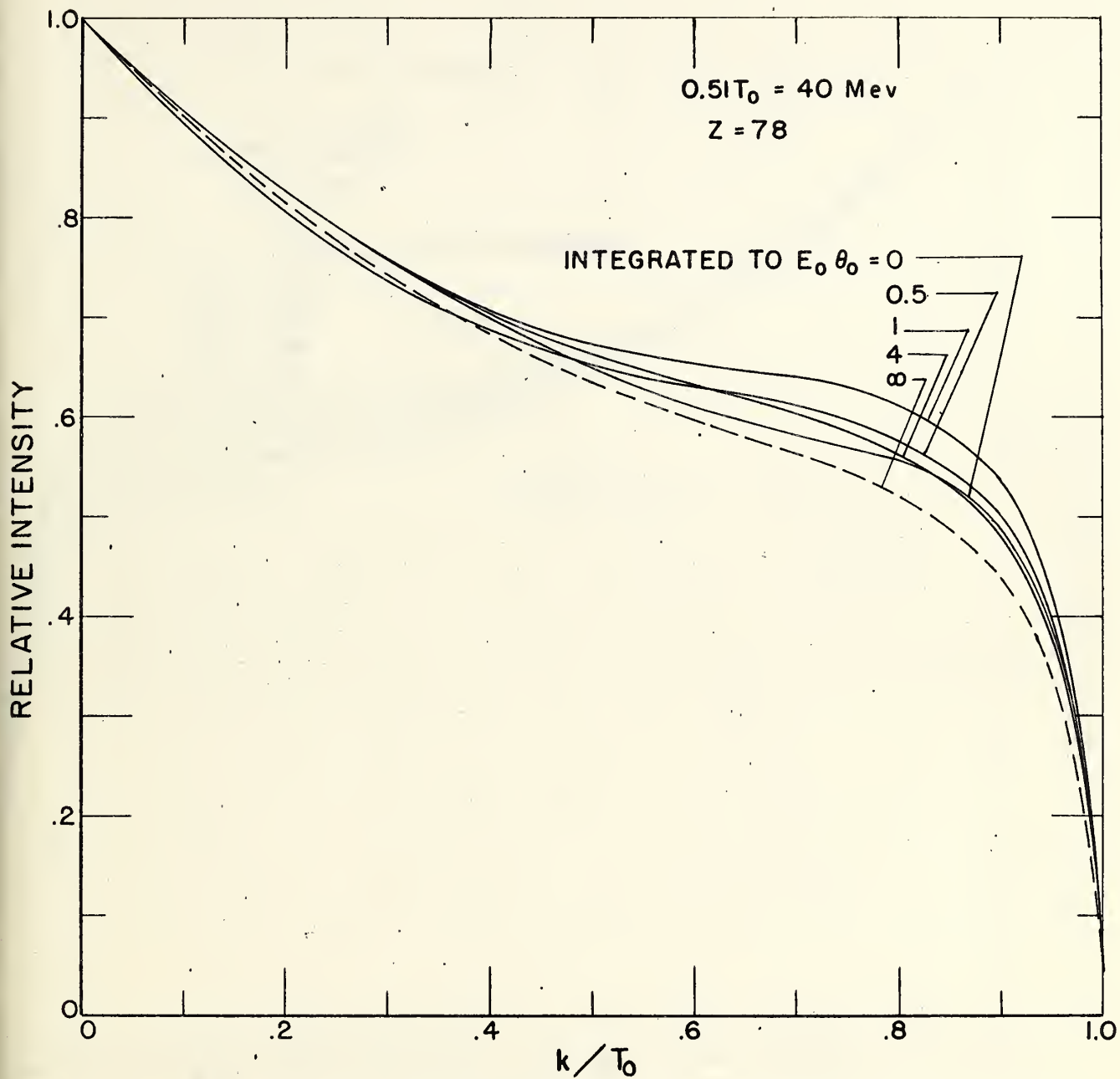


Fig. 7(c). Comparison of Schiff spectra integrated up to various photon emission angles for 40 Mev electrons. See 7(a).

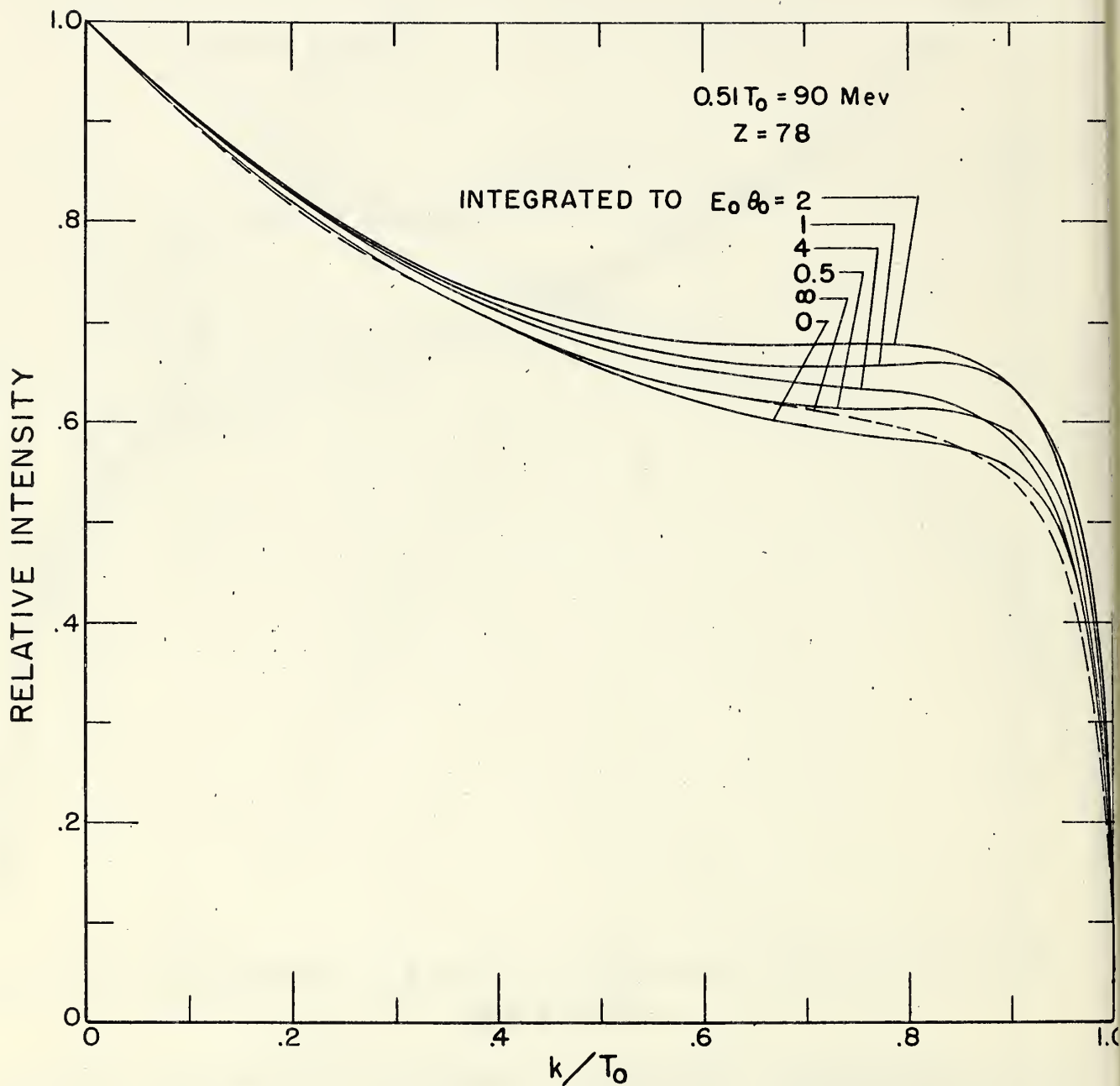


Fig. 7(d). Comparison of Schiff spectra integrated up to various photon emission angles for 90 Mev electrons. See 7(a).

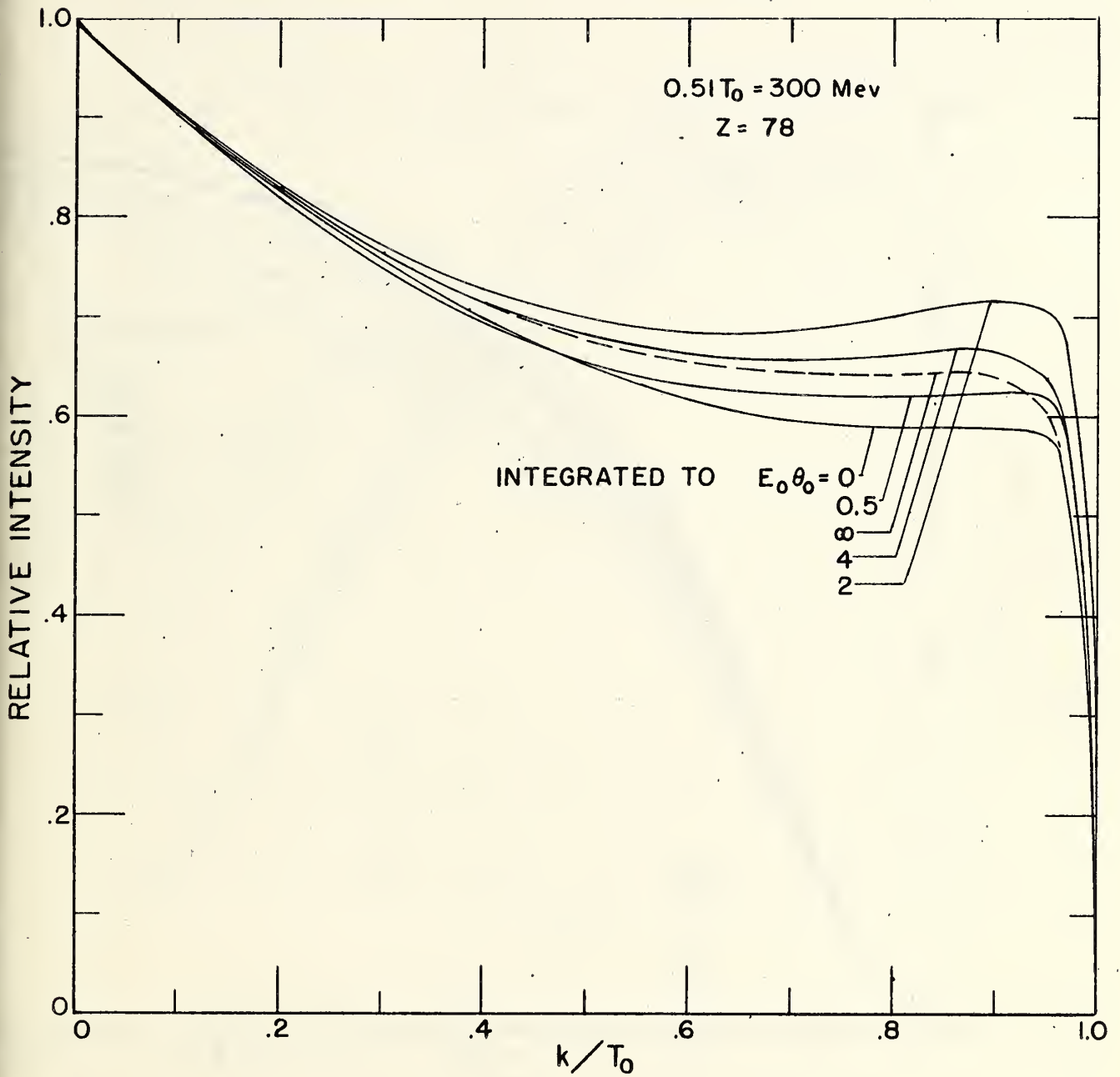


Fig. 7(e). Comparison of Schiff spectra integrated up to various photon emission angles for 300 Mev electrons. See 7(a).

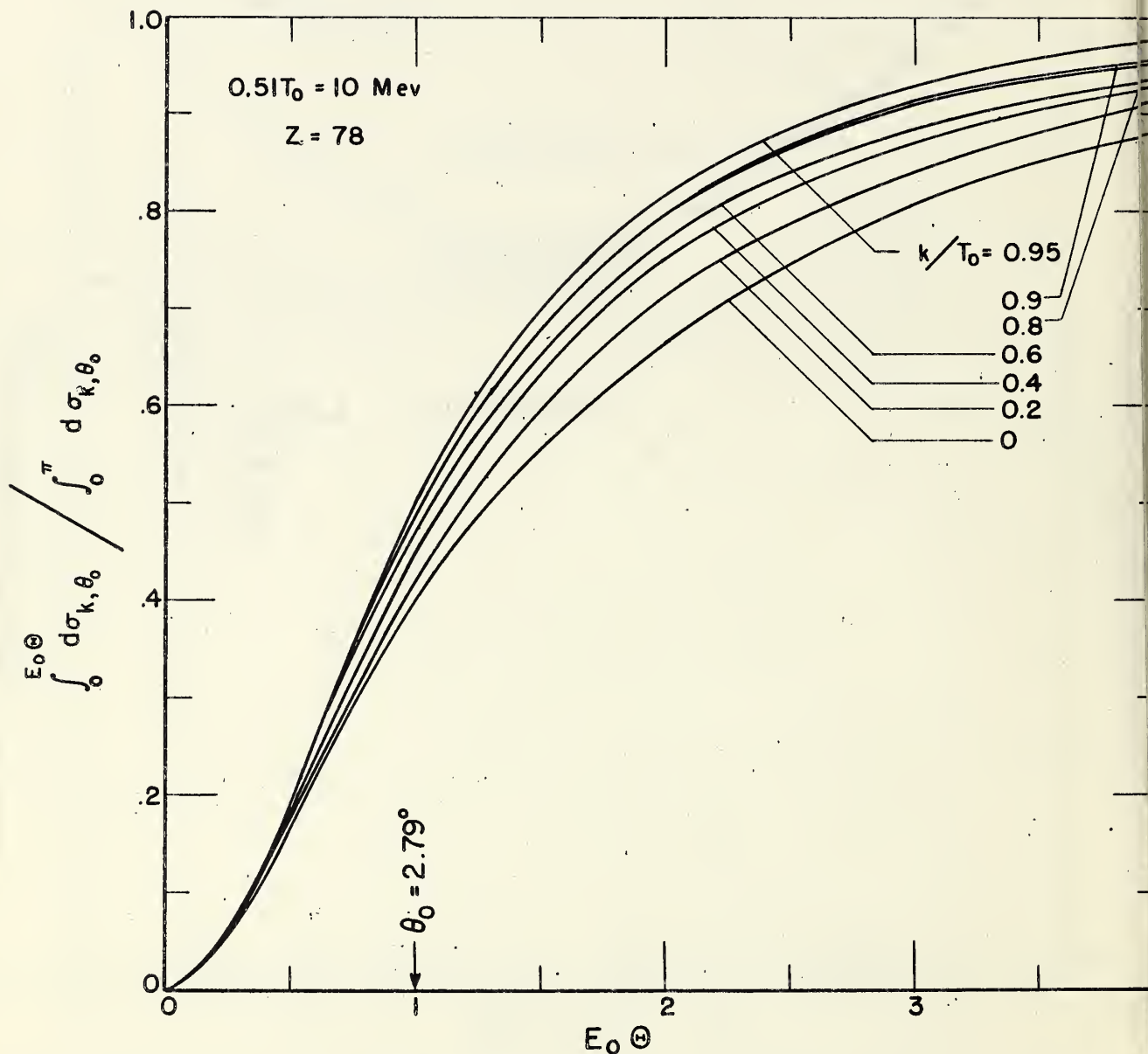


Fig. 8(a). Dependence of the Schiff cross section on the angular integration limit,  $E_0 \oplus$ , for various photon energies with 10 Mev electrons. The curves are derived by graphical integration of the curves in Fig. 6(a), (c), and (e), and may also be derived analytically by the integration of Formula 2BS.

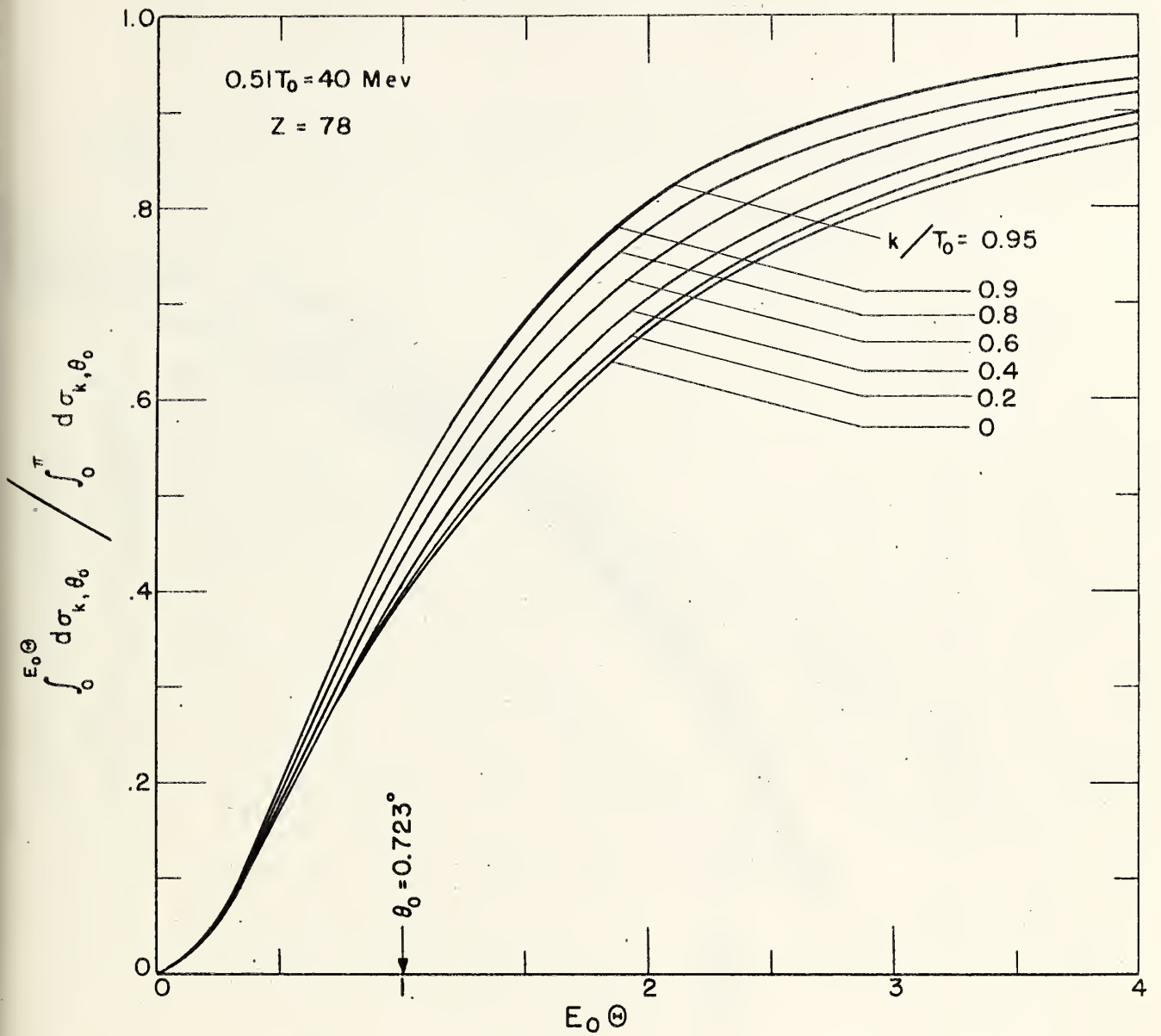


Fig. 8(b). Dependence of the Schiff cross section on the angular integration limit,  $E_0 \odot$ , for various photon energies with 40 Mev electrons. See 8(a).

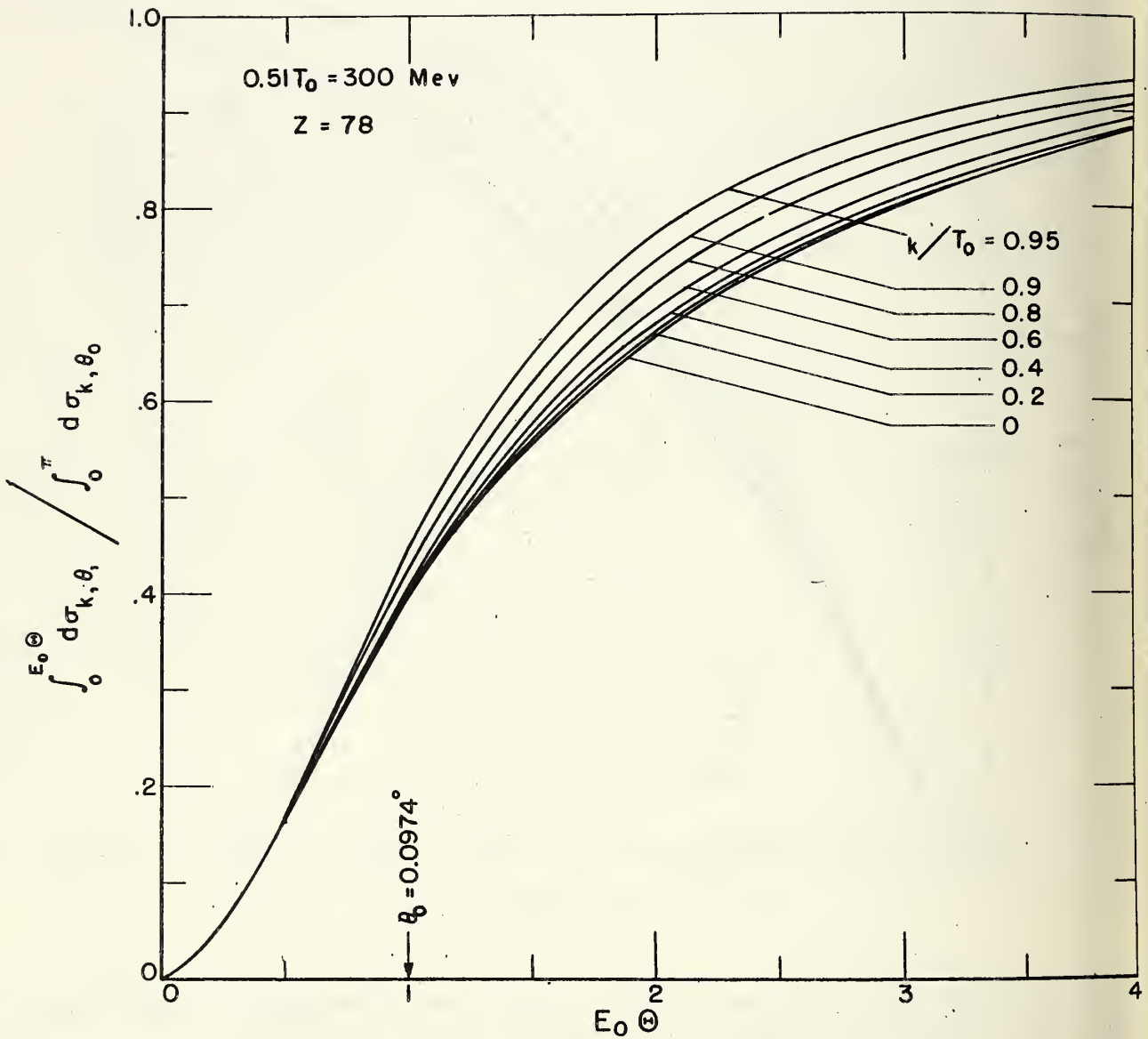


Fig. 8(c). Dependence of the Schiff cross section on the angular integration limit,  $E_0 \Theta$ , for various photon energies with 300 Mev electrons. See 8(a).

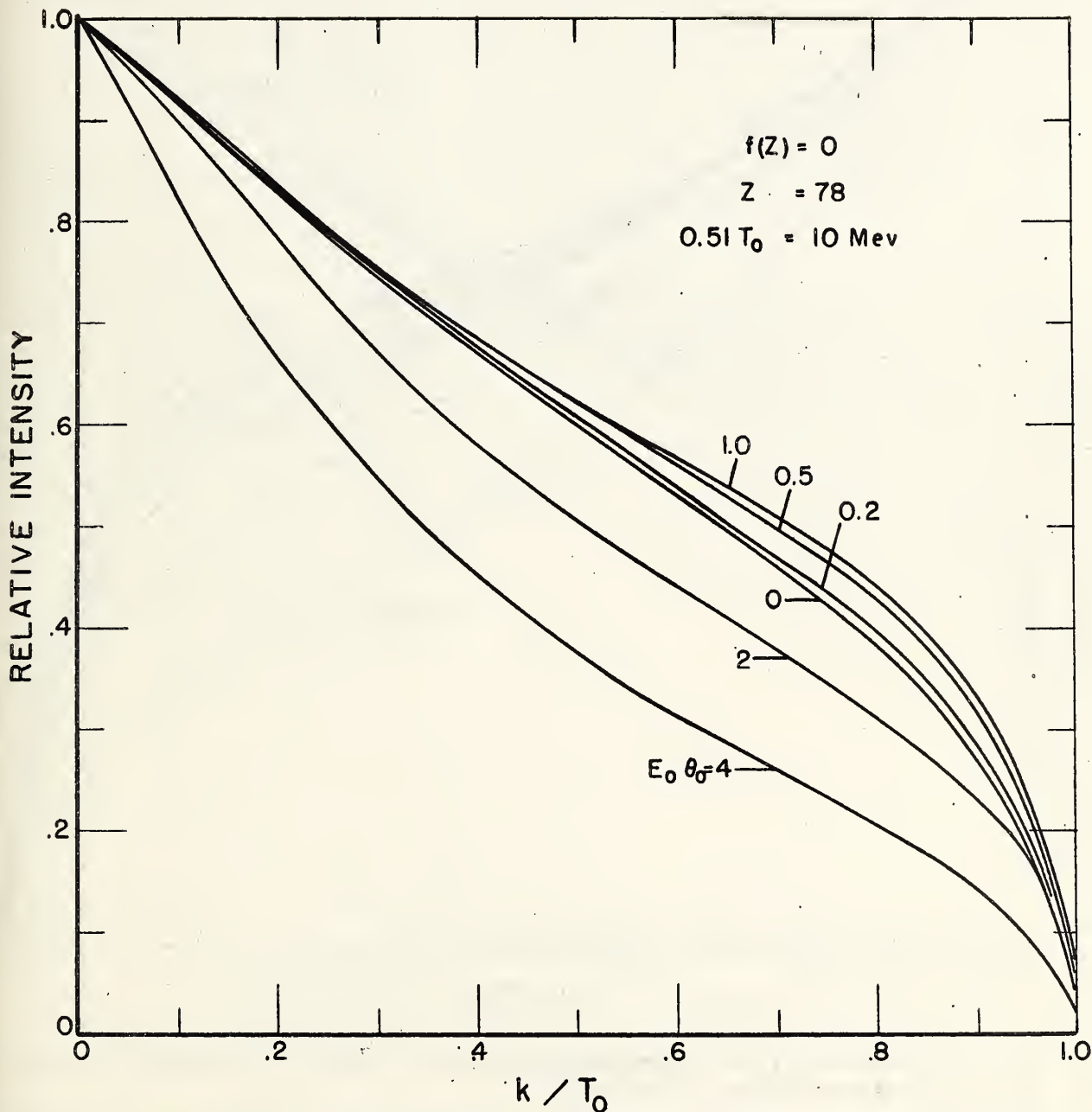


Fig. 9(a). Dependence of the Olsen-Maximon spectrum shape on the photon emission angle,  $\theta_0$ , for 10 Mev electrons. The values for the intensities (defined as proportional to the product of the photon energy and number per unit time) are obtained from Formula 2CS(c) with  $f(Z) = 0$  and are normalized to unity at the zero photon energy.

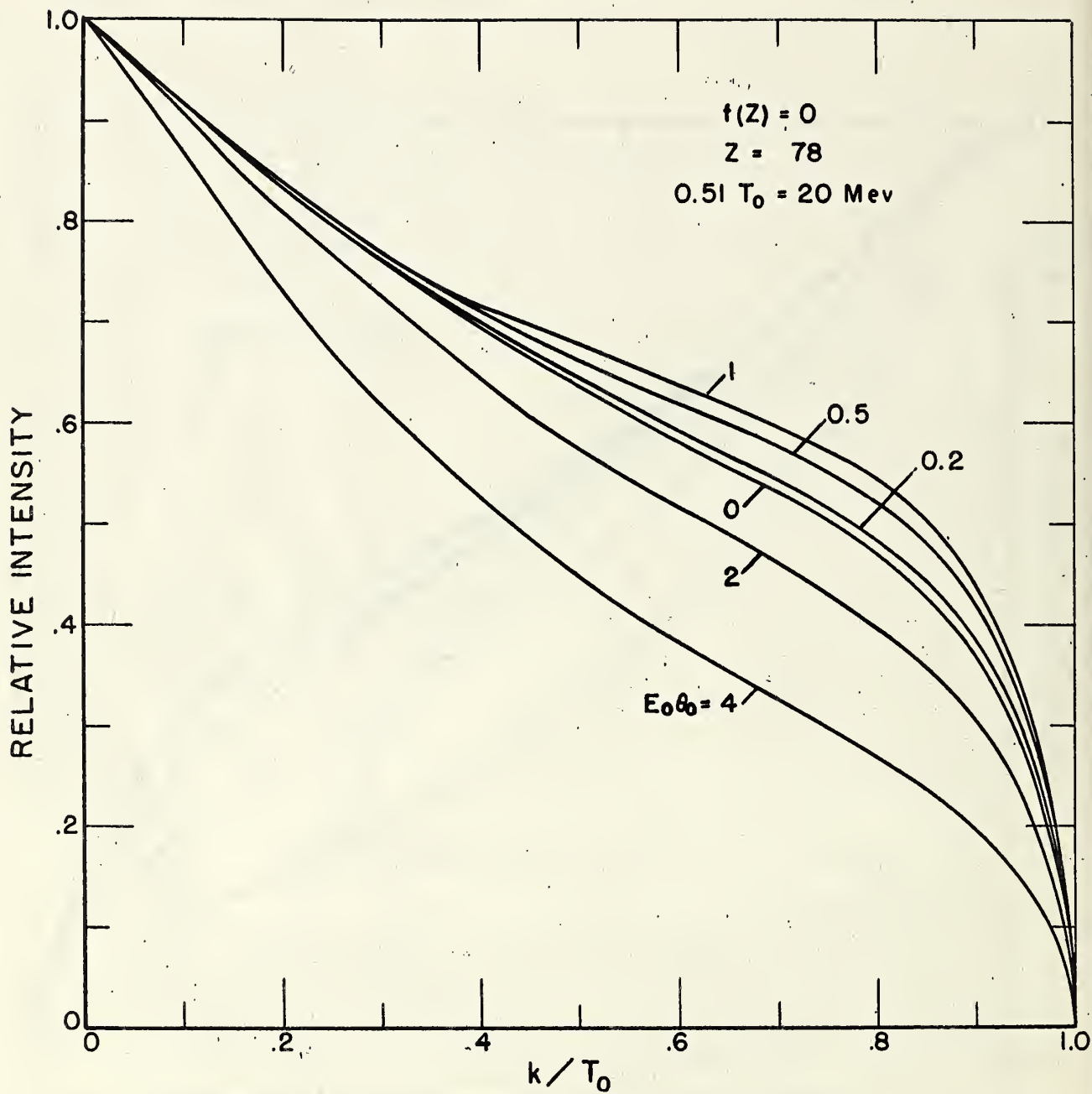


Fig. 9(b). Dependence of the Olsen-Maximon spectrum shape on the photon emission angle,  $\theta_0$ , for 20 Mev electrons. See 9(a).

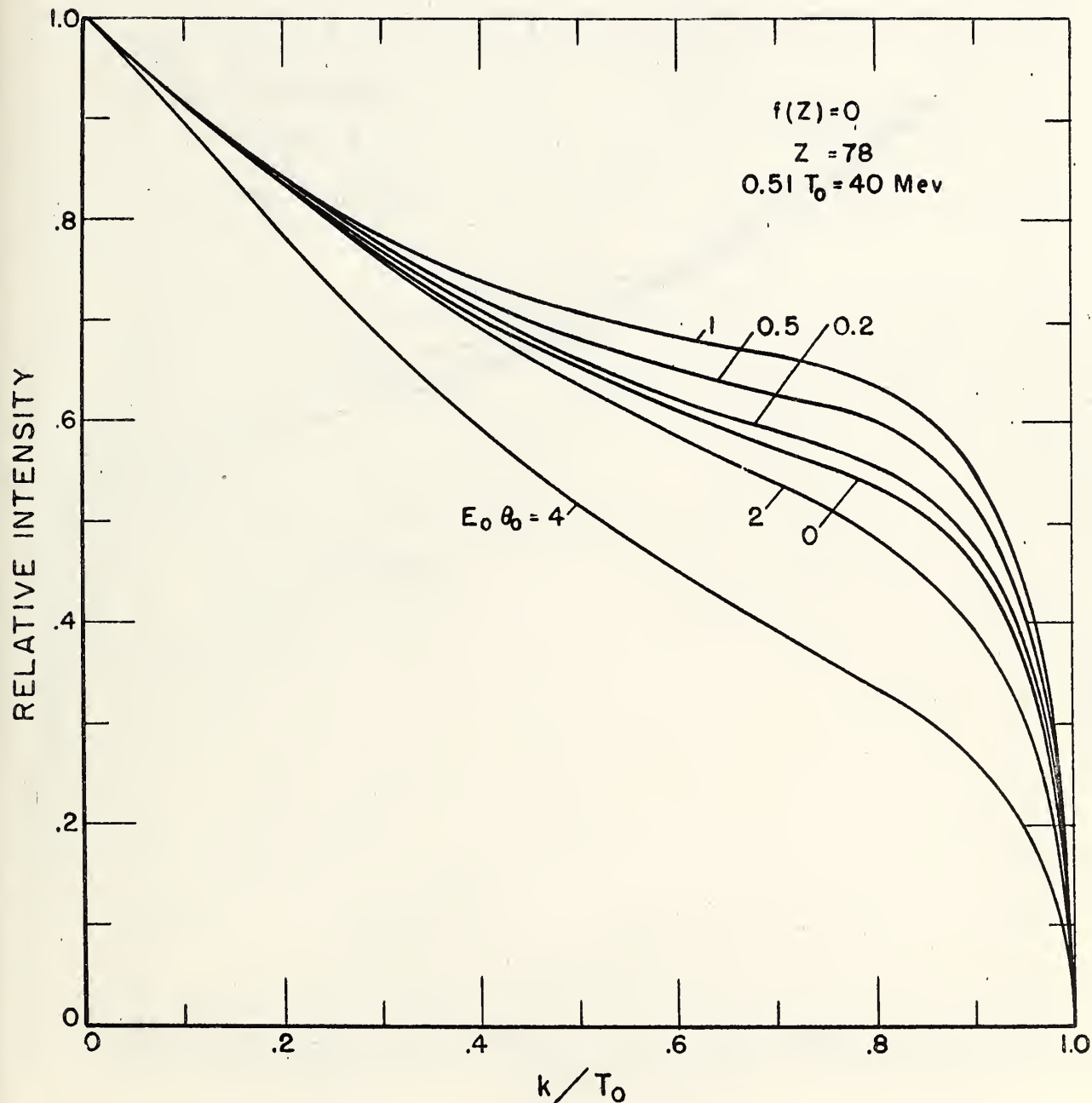


Fig. 9(c). Dependence of the Olsen-Maximon spectrum shape on the photon emission angle,  $\theta_0$ , for 40 Mev electrons. See 9(a).

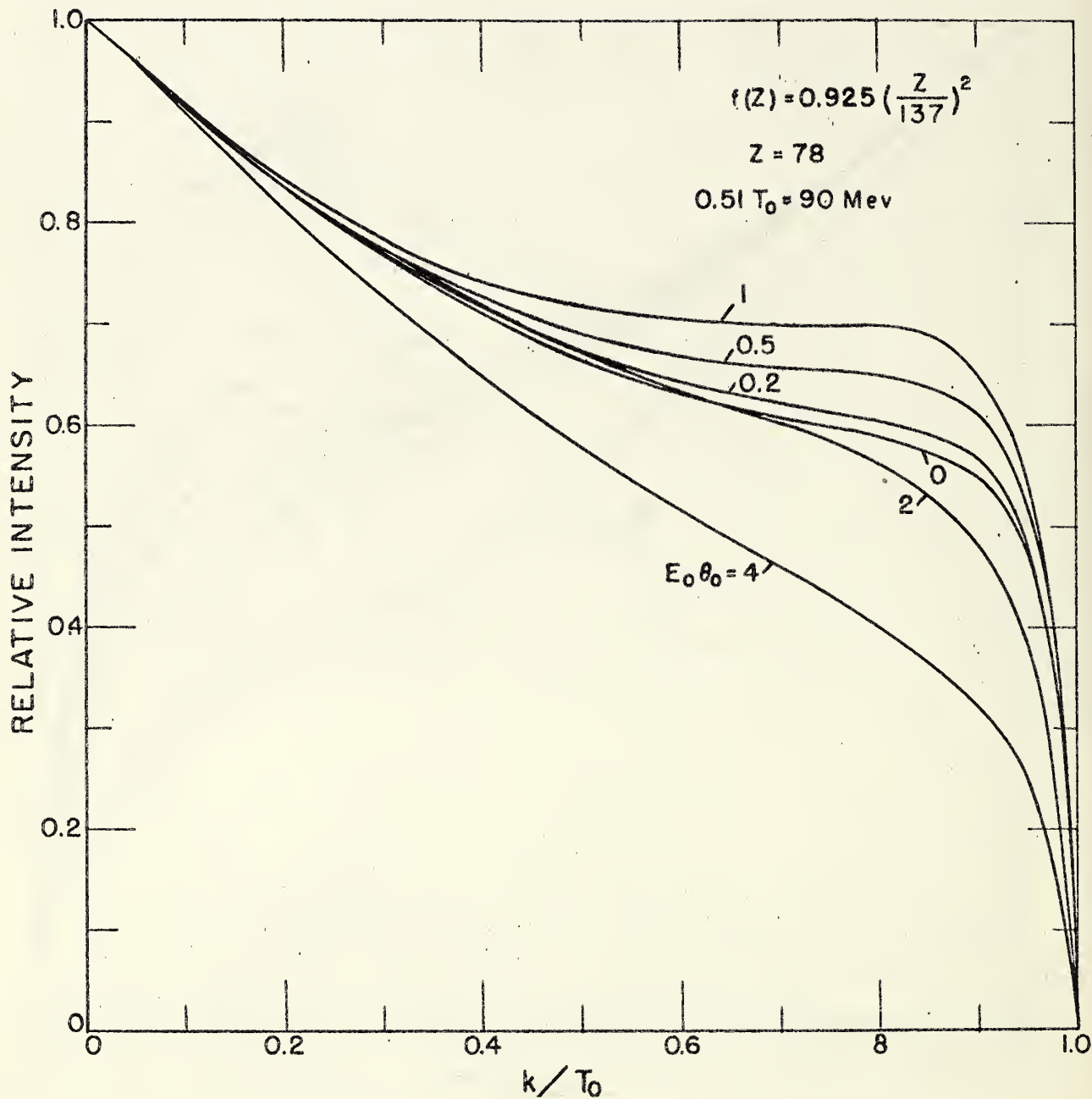


Fig. 9(d). Dependence of the Olsen-Maximon spectrum shape on the photon emission angle,  $\theta_0$ , for 90 Mev electrons and  $f(Z) = 0.925 (Z/137)^2$ . See 9(a).

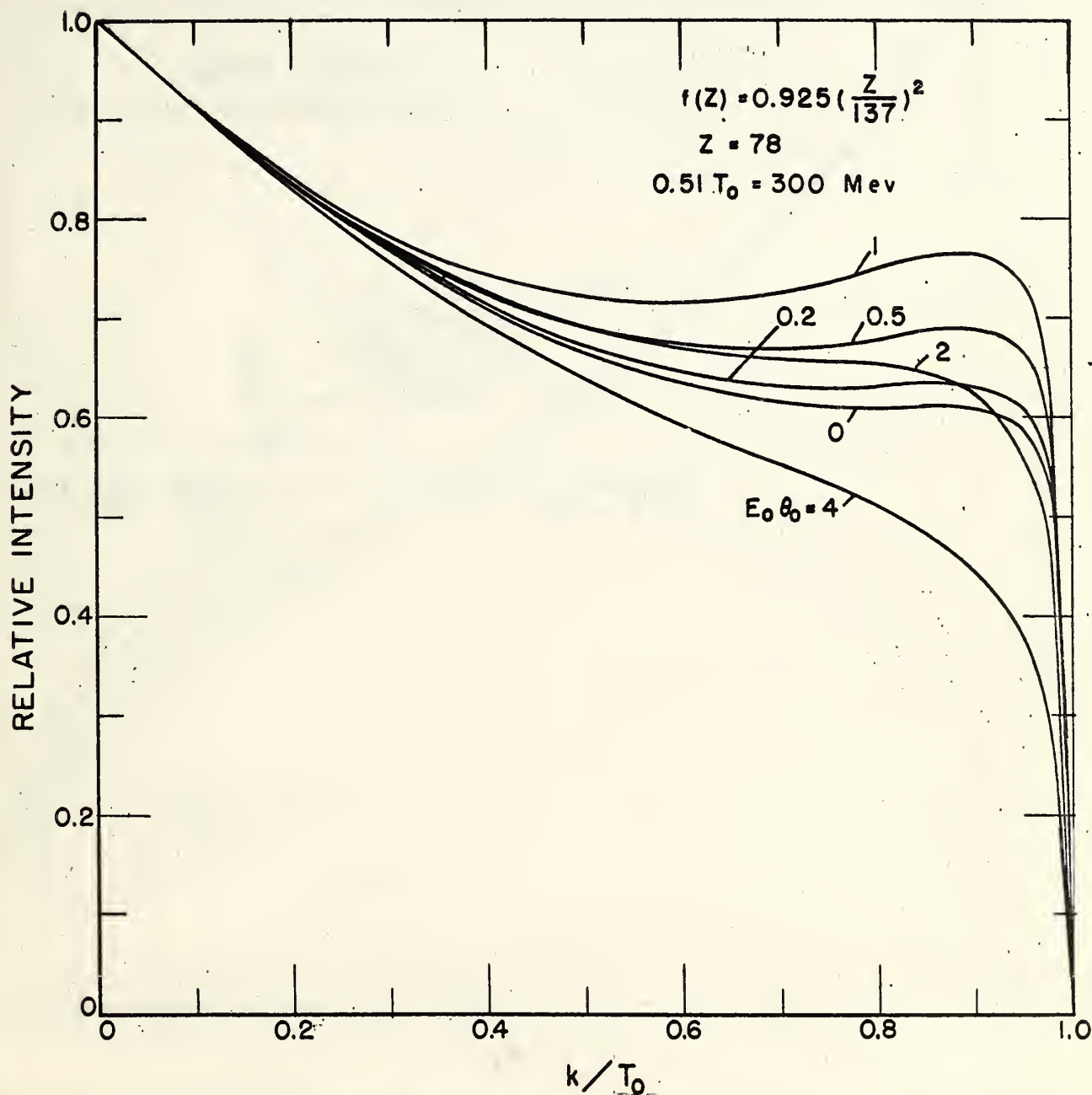


Fig. 9(e). Dependence of the Olsen-Maximon spectrum shape on the photon emission angle,  $\theta_0$ , for 300 Mev electrons and  $f(Z) = 0.925 (Z/137)^2$ . See 9(a).

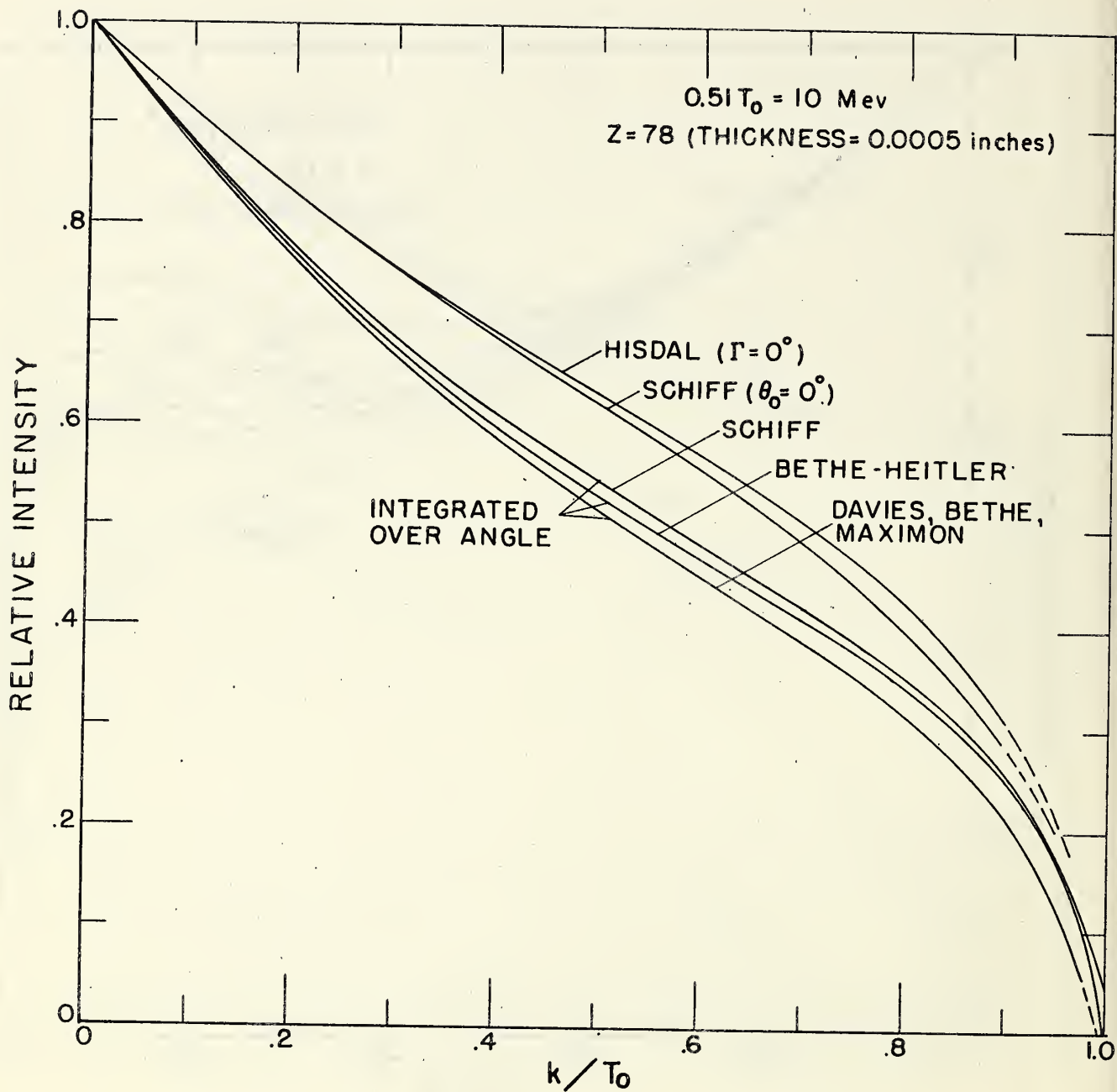


Fig. 10(a). Comparison of 10 Mev spectrum shapes predicted by Formula 2BS for  $\theta_0 = 0^\circ$  (Schiff), Formula 3BS(c) (Schiff integrated over photon angle), Formula 3BS (Bethe-Heitler integrated over photon angle), Formula 3CS (Davies, Bethe, Maximon integrated over photon angle), and the Hisdal calculations with multiple scattering corrections for  $\Gamma = 0^\circ$  (see Section IVB).

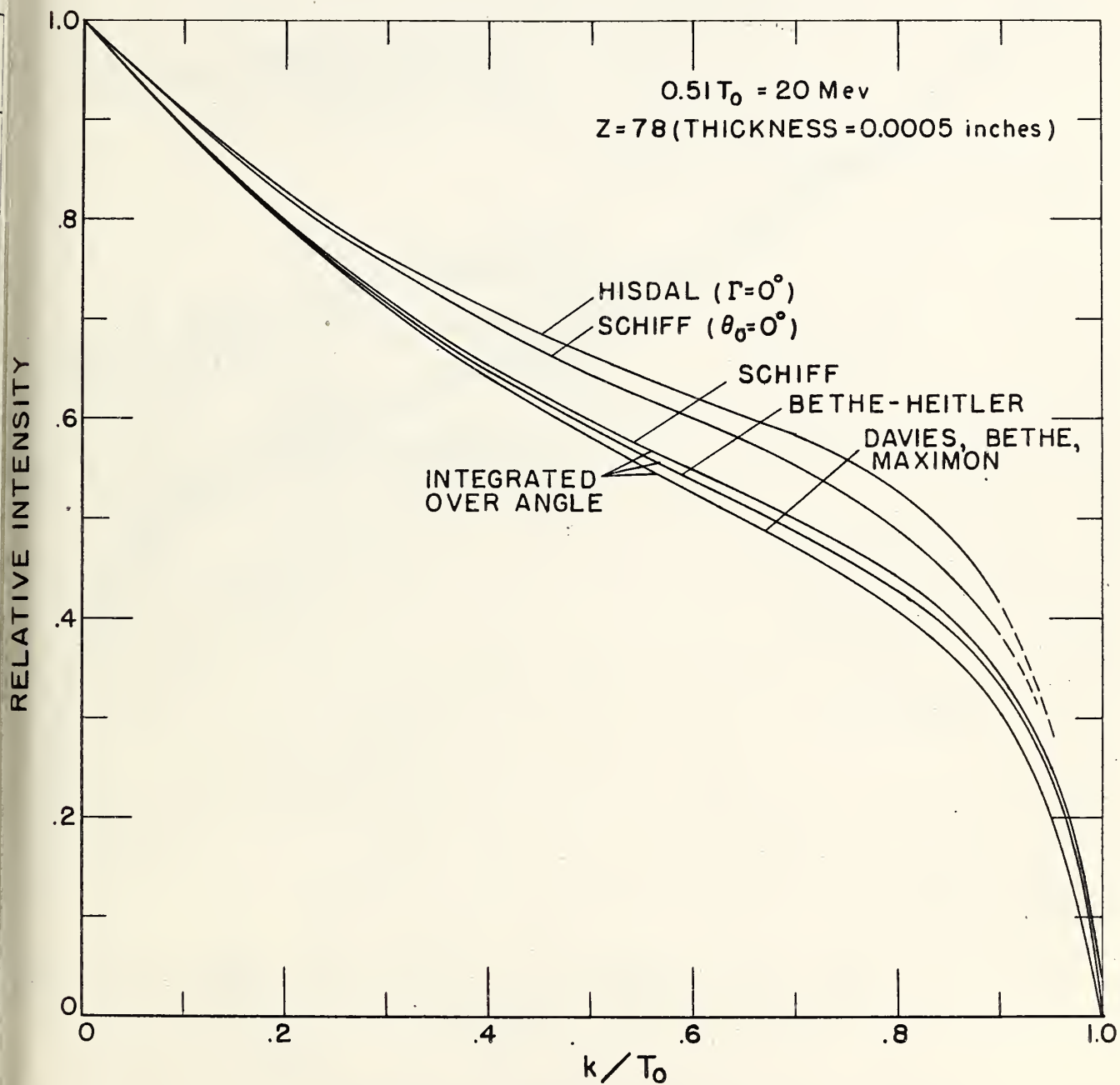


Fig. 10(b). Comparison of 20 Mev spectrum shapes. See 10(a).

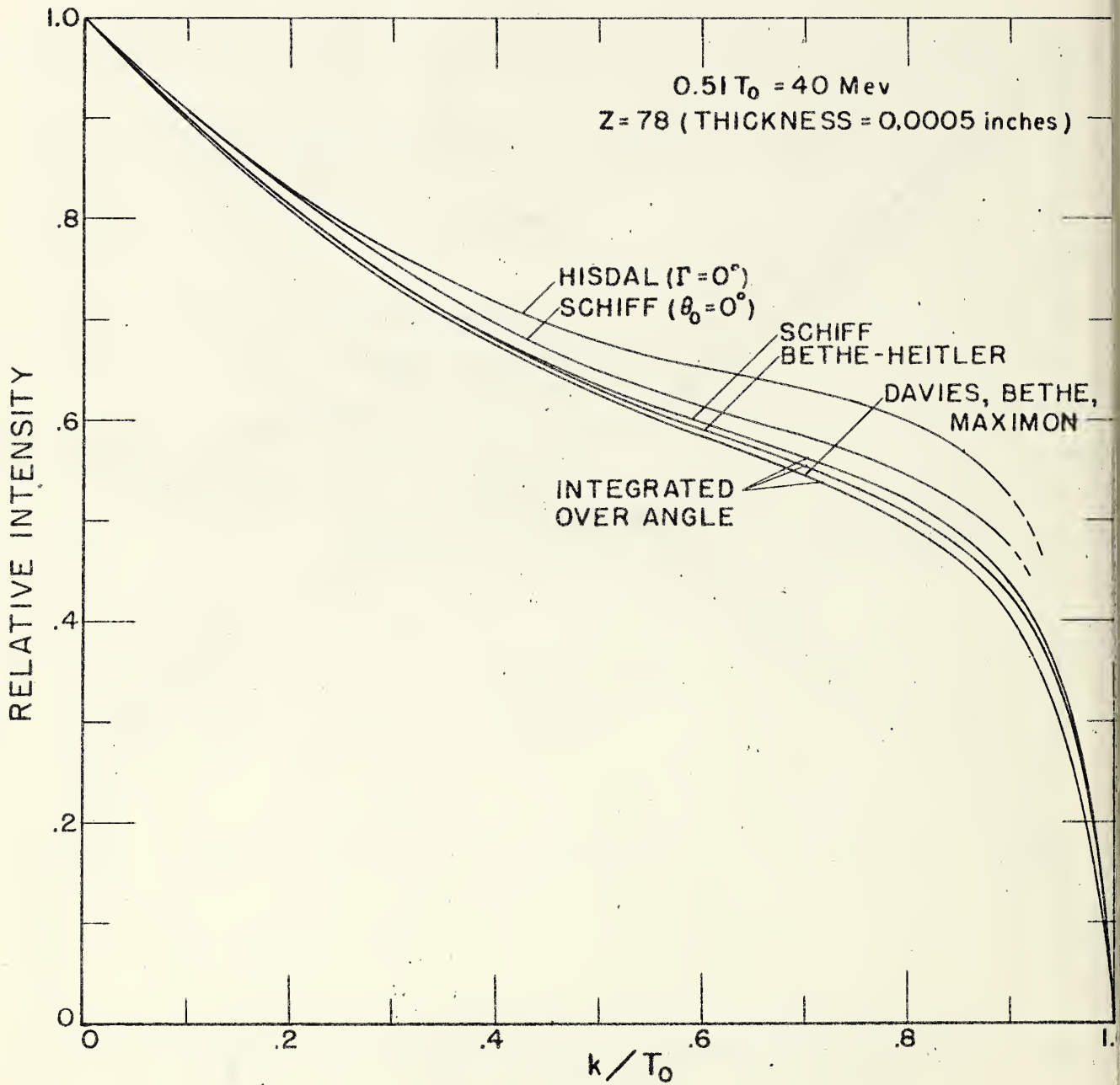


Fig. 10(c). Comparison of 40 Mev spectrum shapes. See 10(a).

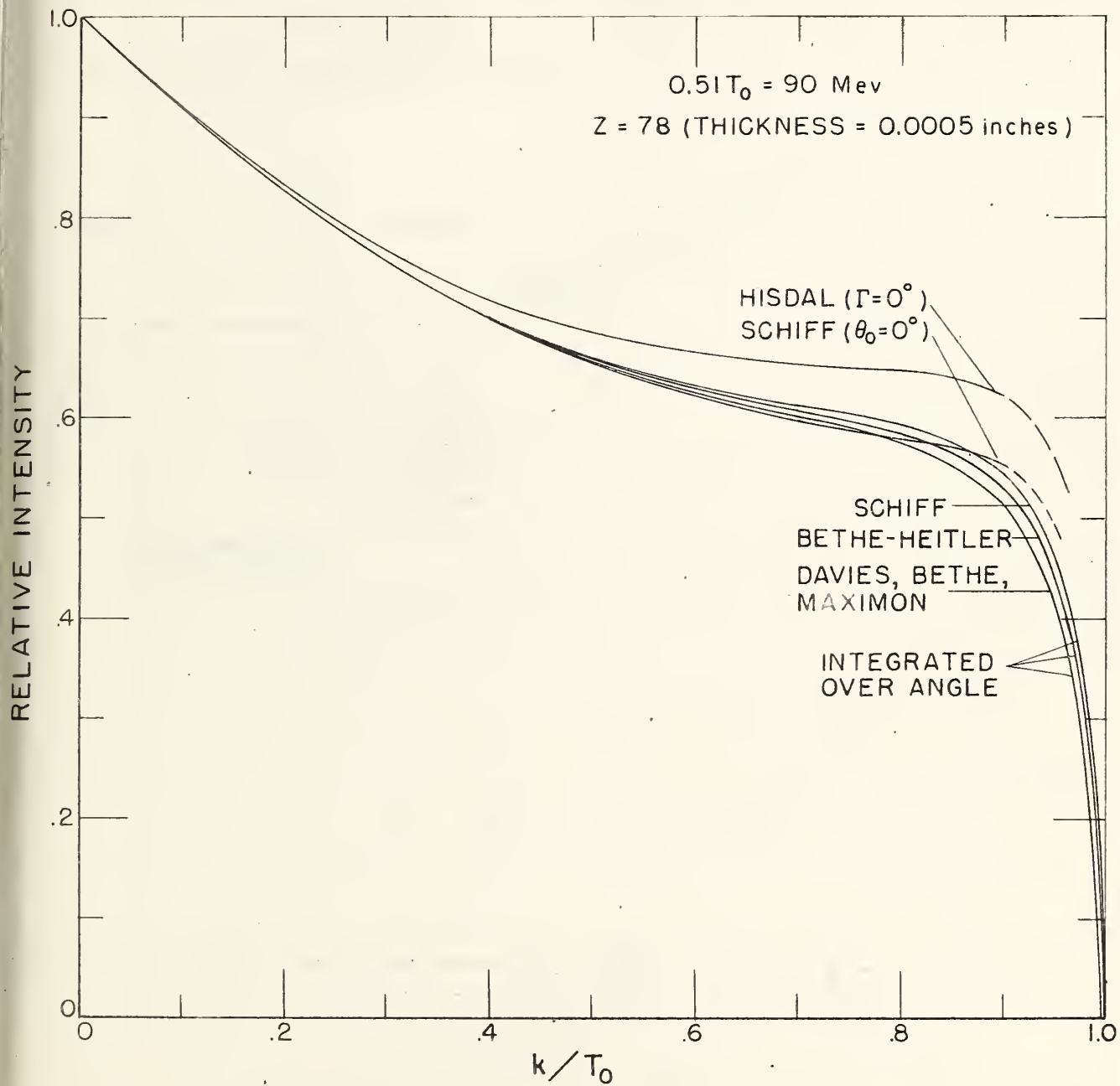


Fig. 10(d). Comparison of 90 Mev spectrum shapes. See 10(a).

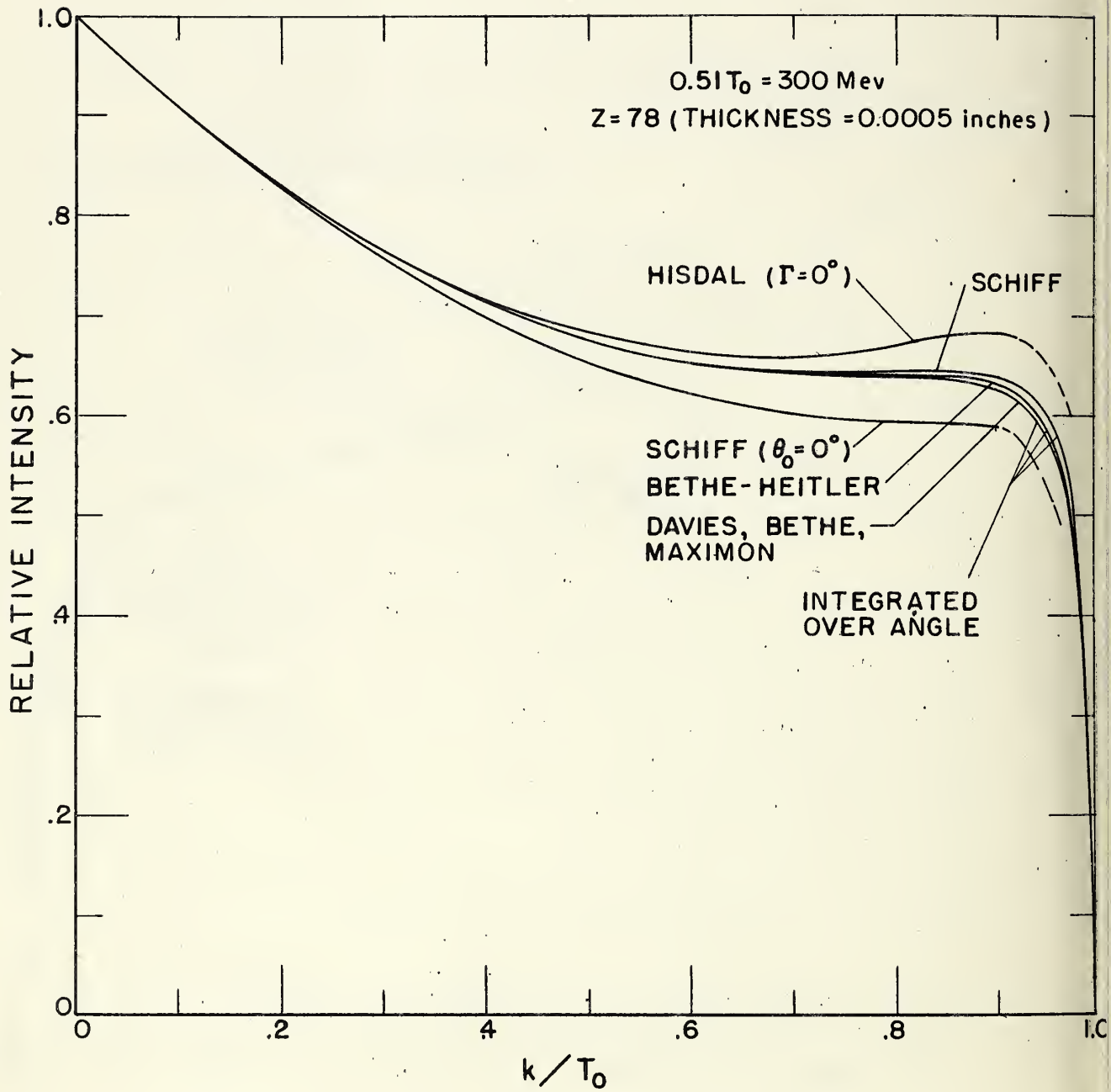


Fig. 10(e). Comparison of 300 Mev spectrum shapes. See 10(a).

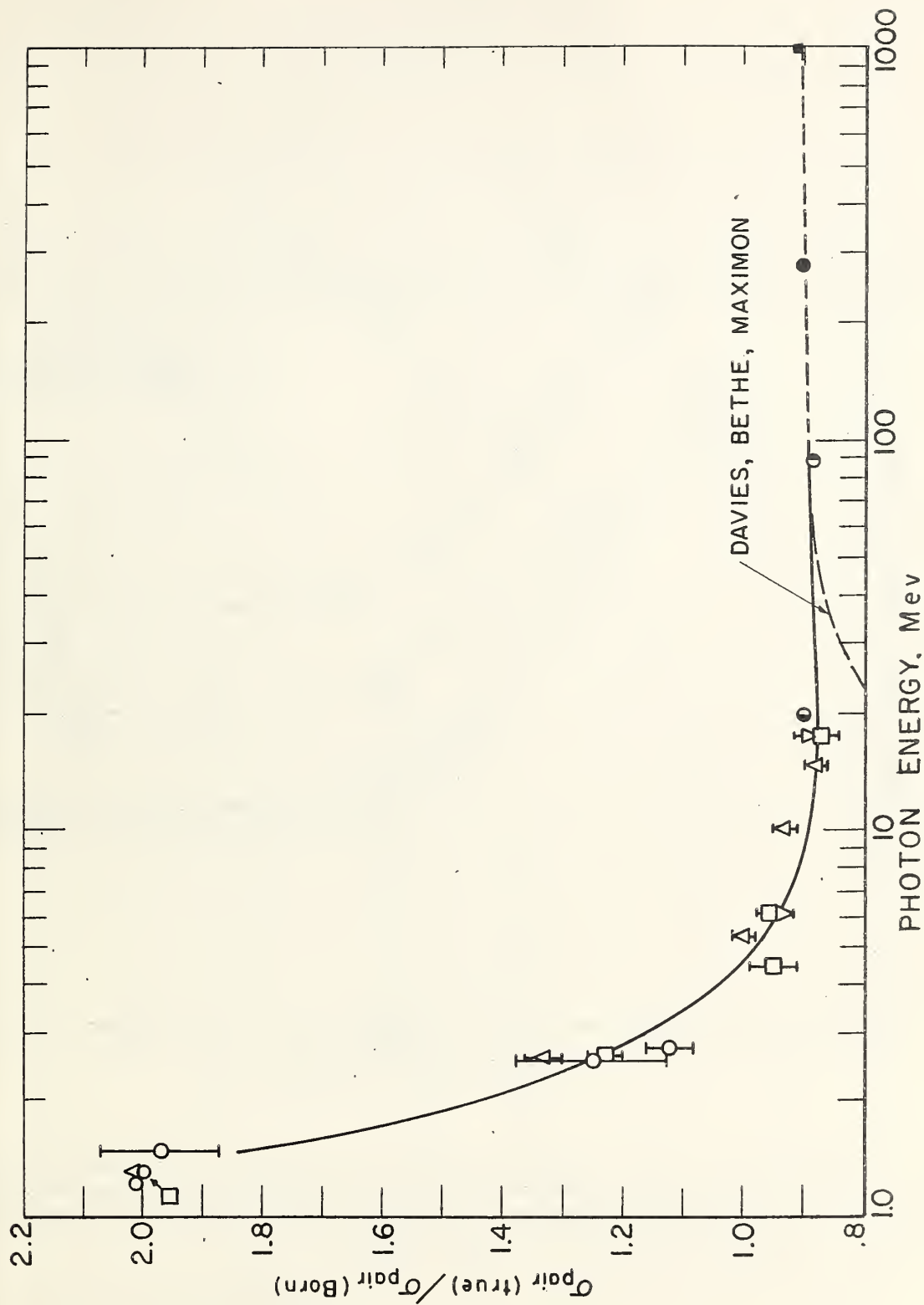


Fig. 11. Dependence of the pair cross section ratio,  $d\sigma_{\text{pair}}(\text{true})/d\sigma_{\text{pair}}(\text{Born})$ , on the photon energy. The solid curve is taken from Grodstein<sup>22</sup> and the dashed curve is taken from Reference 13.

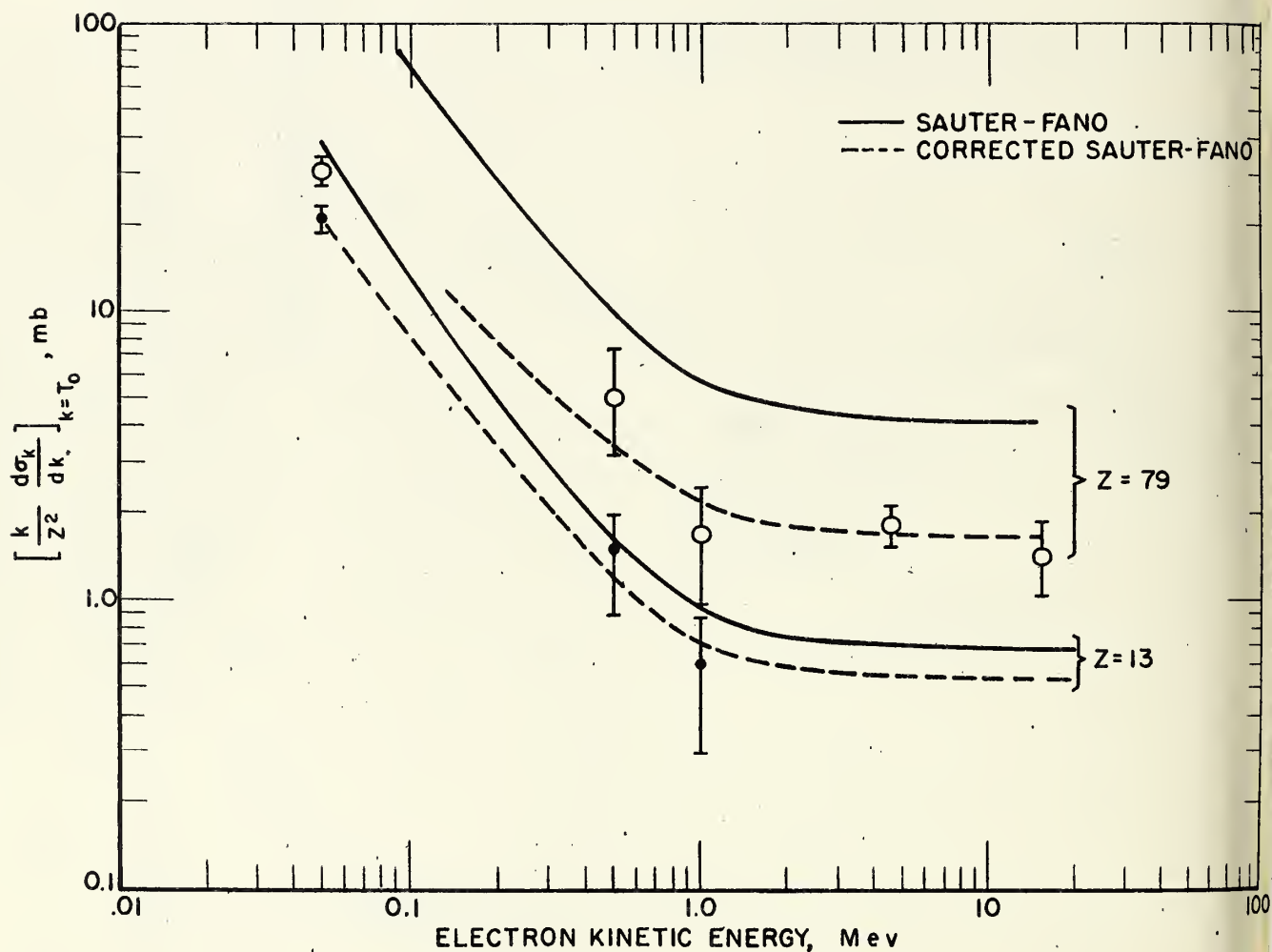


Fig. 12. Dependence of the bremsstrahlung cross section at the high frequency limit, integrated over photon direction, on the incident electron kinetic energy. These data are obtained from Reference 21, and the dashed curves are estimated to give the most accurate values for the cross section.

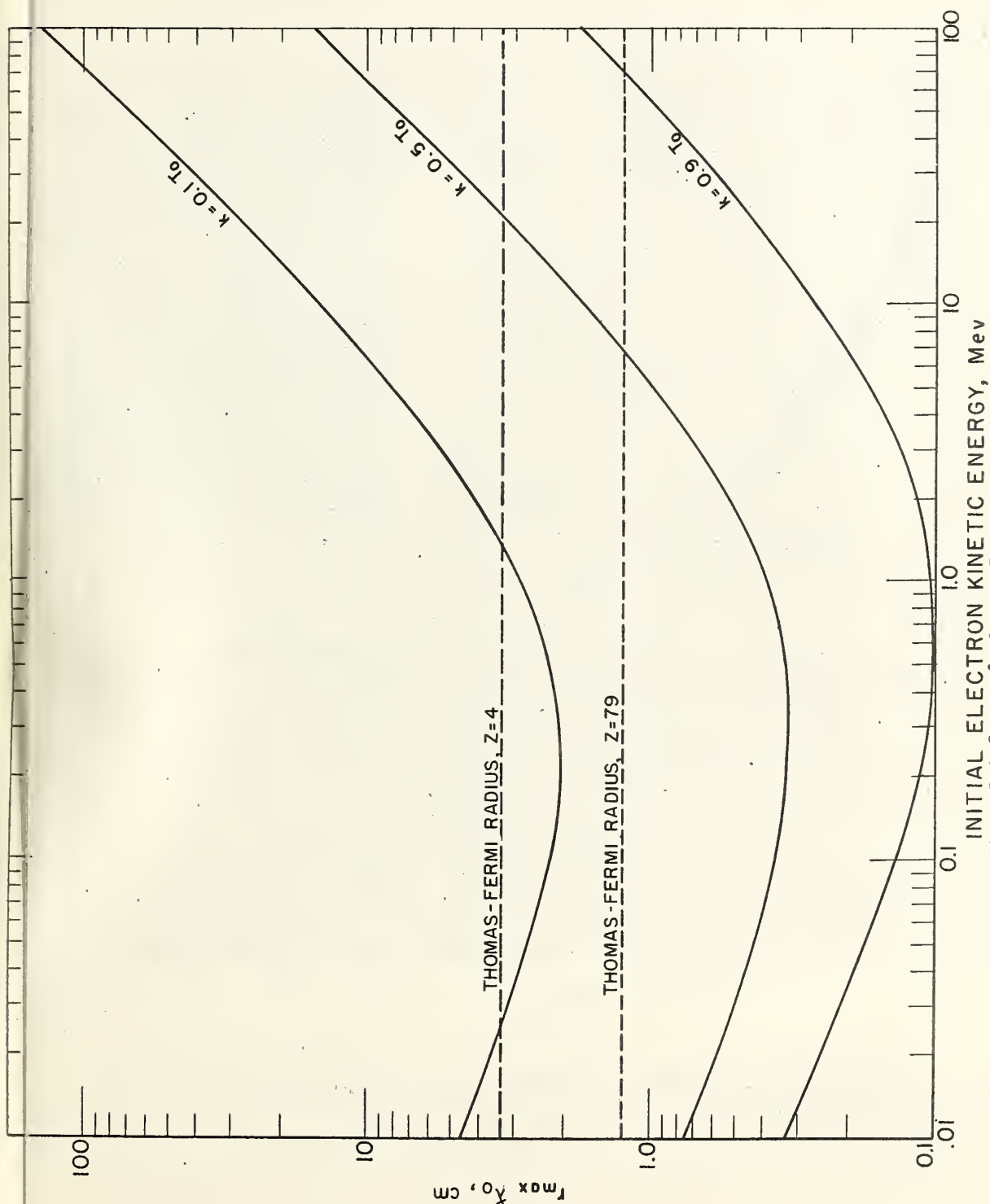


Fig. 13. Dependence of  $r_{\max}$  on the initial electron kinetic energy for  $k$  equal to  $0.1 T_0$ ,  $0.5 T_0$ , and  $0.9 T_0$ .  $r_{\max}$  is the reciprocal of the minimum momentum transferred to the nucleus ( $= p_0 - p - k$ ), and is given in units of the Compton wave length,  $\lambda_0$ . The dashed lines give the values of the Thomas-Fermi radius ( $= 137Z^{-1/3}$ ) for beryllium and gold.

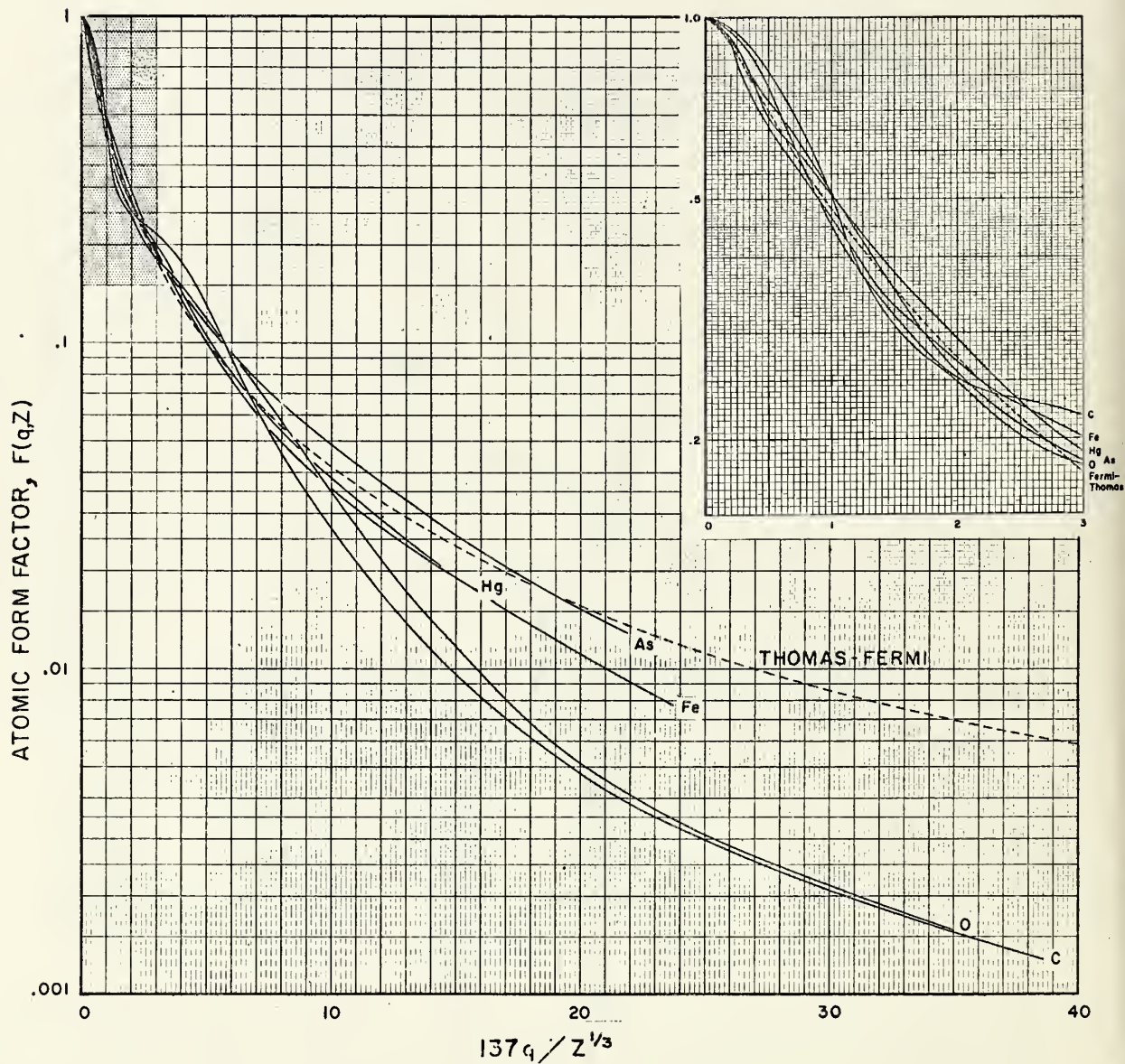


Fig. 14. Evaluation<sup>24/</sup> of the atomic form factor,  $F(q, Z)$ , for the Hartree self-consistent field model (solid lines) and for the Thomas-Fermi model (dashed line), as a function of the nuclear momentum transfer,  $q$ .

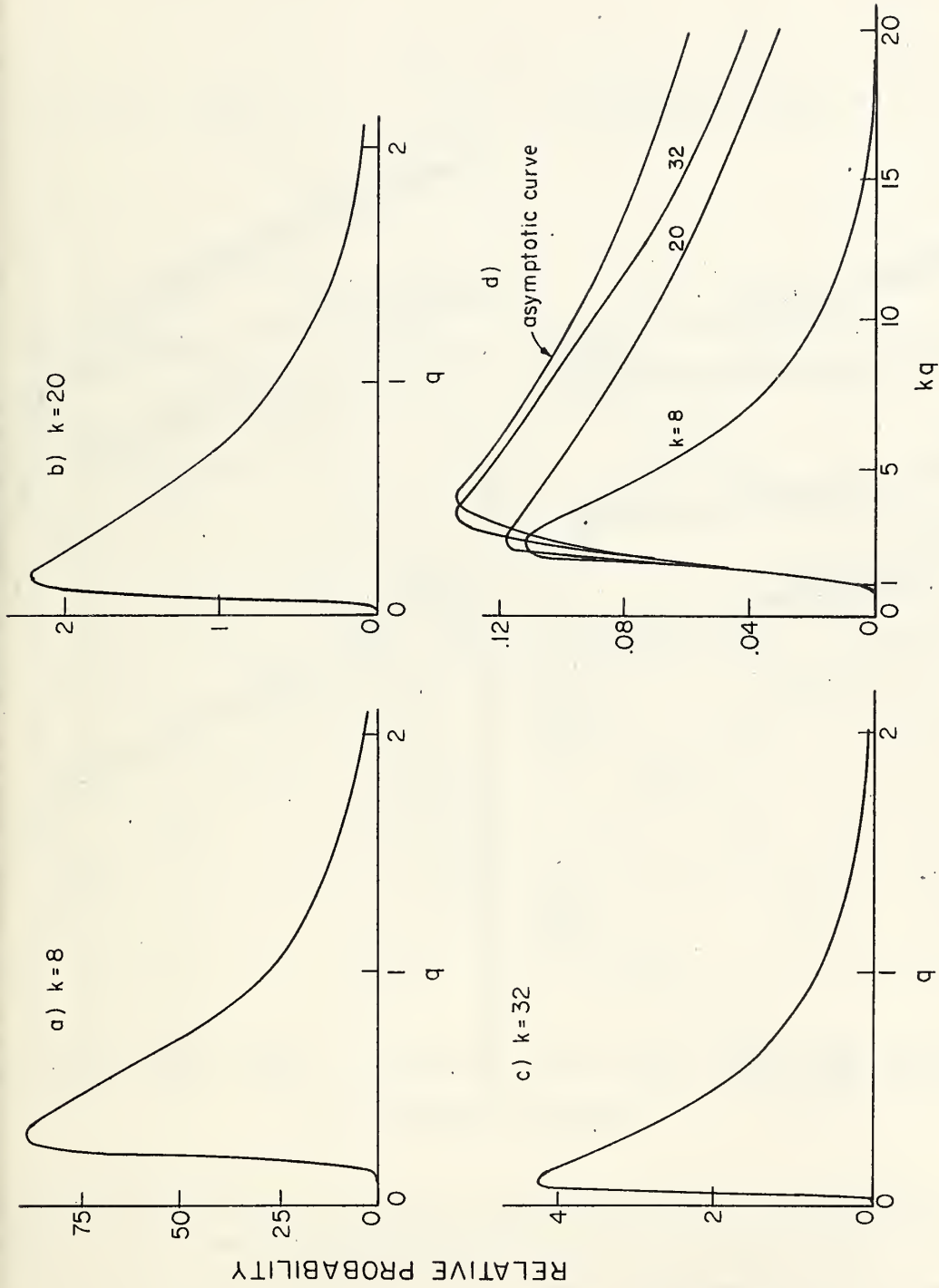


Fig. 15. Momentum distributions  $\frac{25}{}$  for the recoil nucleus in nuclear pair production for several photon energies. The relative number of recoils versus the momentum,  $q$ , are plotted in Figures (a), (b), and (c). These curves are summarized in (d) and are compared with the asymptotic curve.

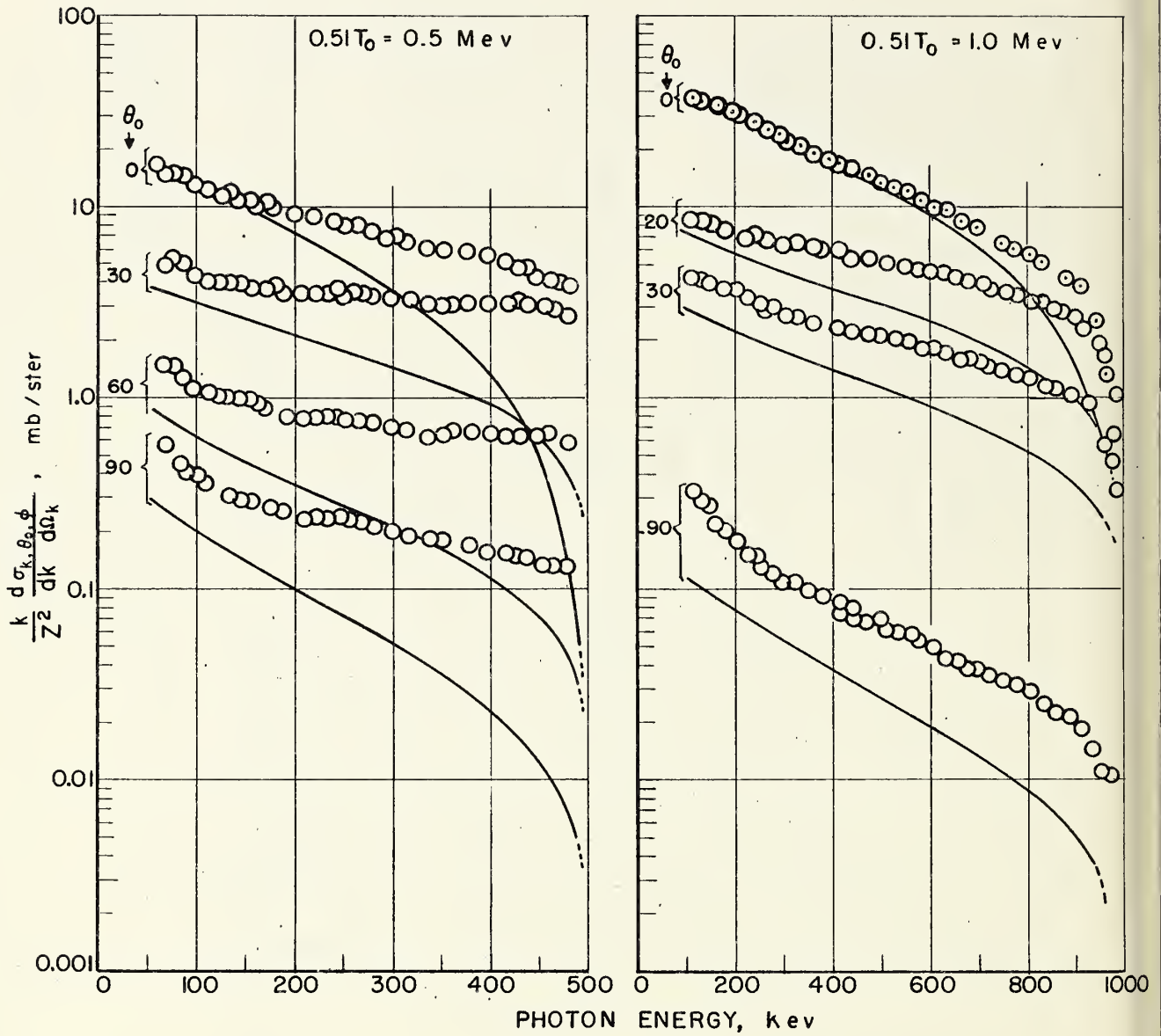


Fig. 16. Dependence of the bremsstrahlung cross section  $d\sigma_{k,\theta_0,\phi}$  on photon energy and angle,  $\theta_0$ , for 0.5 and 1.0 Mev electrons. The theoretical cross sections shown by the solid curves are calculated from Formula 2BN, and the experimental values<sup>35/</sup> for gold are given by the open circles.

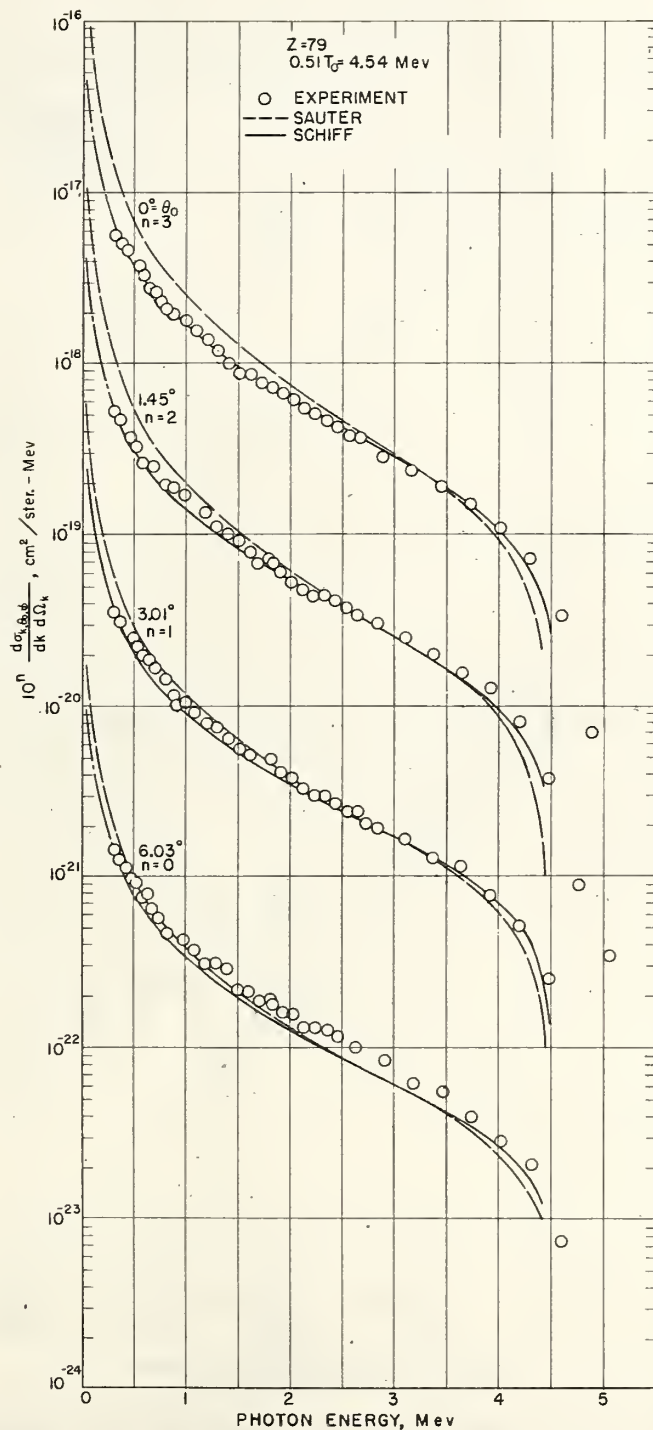


Fig. 17. Dependence of the bremsstrahlung cross section  $d\sigma_{k,\theta_0,\phi}$  for gold, on the photon energy and angle,  $\theta_0$ , for 4.54 Mev electrons. The theoretical cross sections are given by the solid curve (Schiff, Formula 2BS), and by the dashed curve (Sauter, Formula 2BN). The experimental values<sup>36/</sup> for gold are given by the open circles.

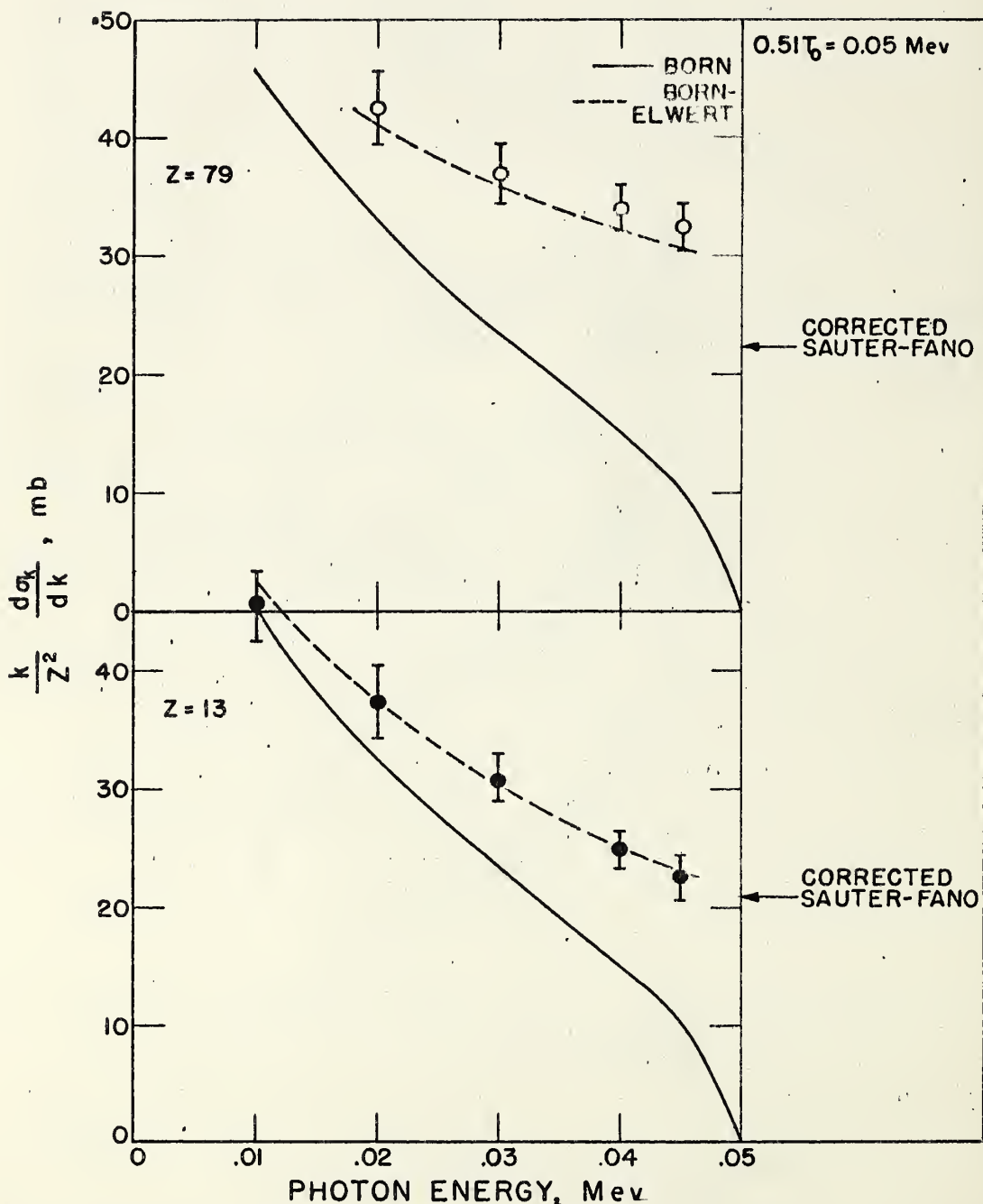


Fig. 18. Dependence of the bremsstrahlung cross section integrated over photon angle on the photon energy for 0.05 Mev electrons. The Born-approximation cross sections shown by the solid curves are calculated from Formula 3BN(a), and the Born-Elwert cross sections shown by the dashed curves are obtained from the product of Formula 3BN(a), and the Elwert factor, Formula (II-4). The experimental values<sup>33/</sup> are shown by the open and closed circles for gold and aluminum respectively. The corrected Sauter-Fano values at the high frequency limit are estimated in Reference 21.

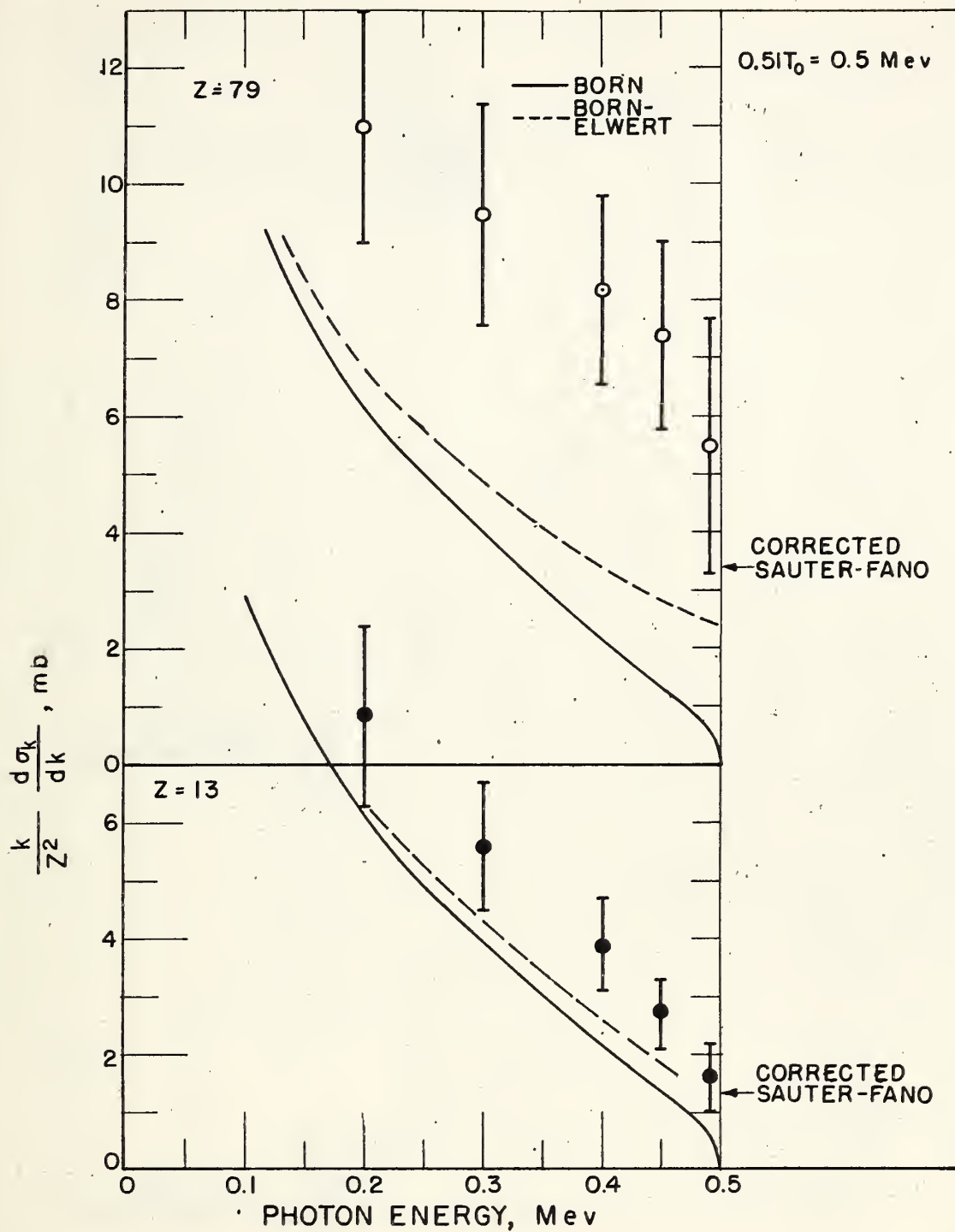


Fig. 19. Dependence of the bremsstrahlung cross section integrated over photon angle on the photon energy for 0.5 Mev electrons. The Born-approximation cross sections shown by the solid curves are calculated from Formula 3BN, and the Born-Elwert cross sections shown by the dashed curves are obtained from the product of Formula 3BN and the Elwert factor, Formula (II-4). The experimental values<sup>35/</sup> are shown by the open and closed circles for gold and aluminum respectively. The corrected Sauter-Fano values at the high frequency limit are estimated in Reference 21.

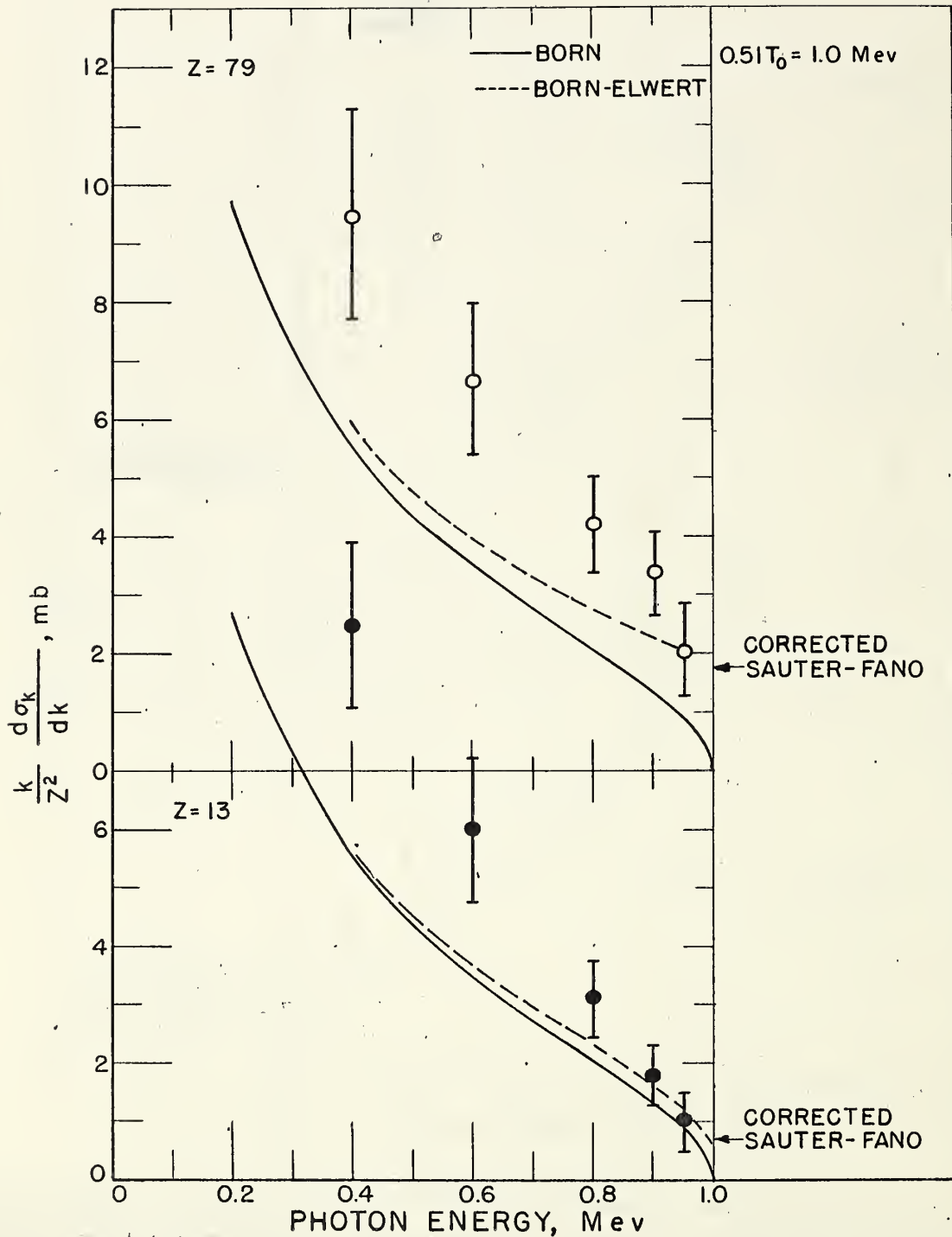


Fig. 20. Dependence of the bremsstrahlung cross section integrated over photon angle on the photon energy for 1.0 Mev electrons. The Born-approximation cross sections shown by the solid curves are calculated from Formula 3BN, and the Born-Elwert cross sections shown by the dashed curves are obtained from the product of Formula 3BN and the Elwert factor, Formula (II-4). The experimental values<sup>35/</sup> are shown by the open and closed circles for gold and aluminum respectively. The corrected Sauter-Fano values at the high frequency limit are estimated in Reference 21.

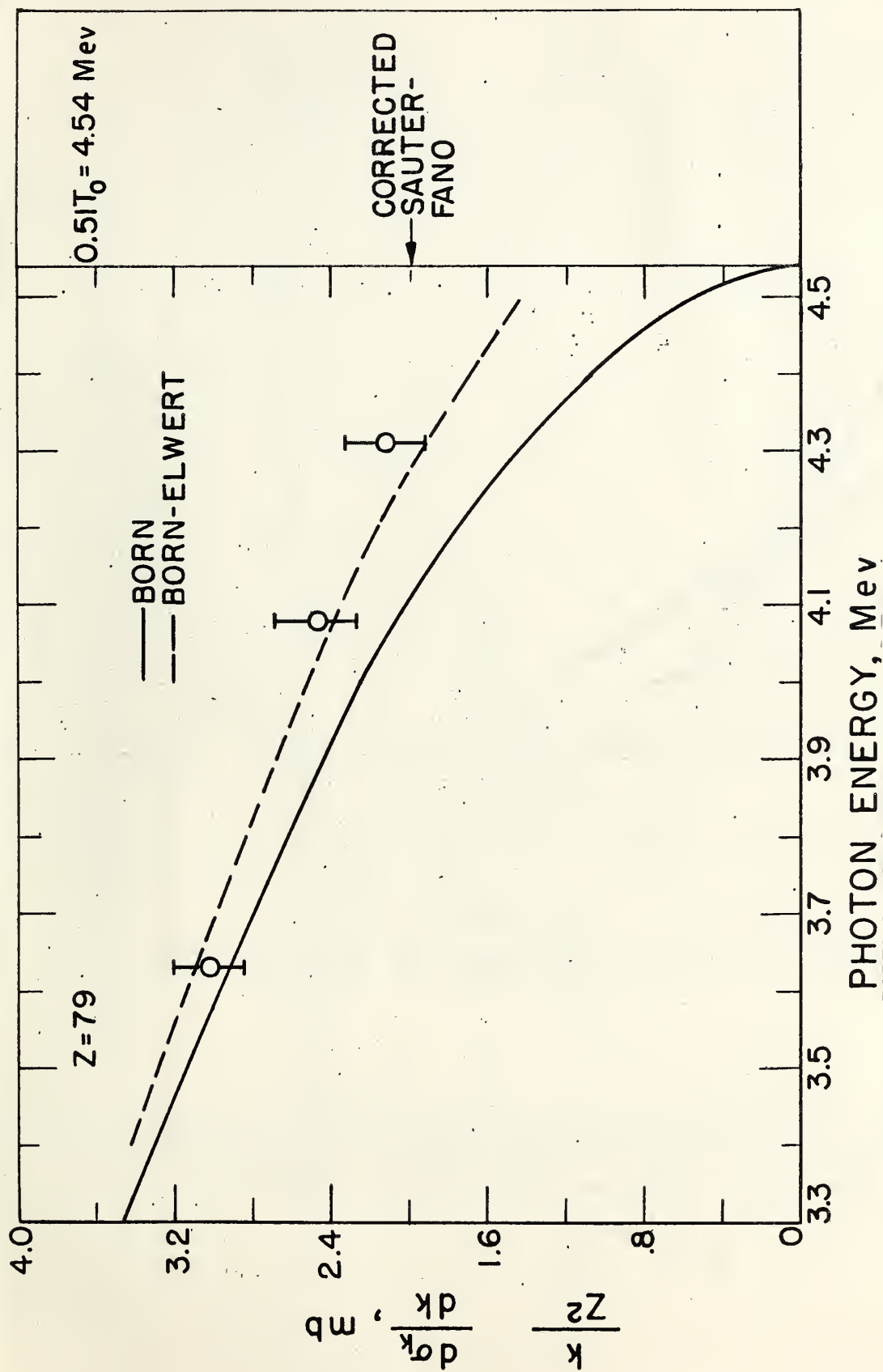


Fig. 21. Dependence of the bremsstrahlung cross section integrated over photon angle on the photon energy for 4.54 Mev electrons. The Born-approximation cross sections shown by the solid curve are calculated from Formula 3BN, and the Born-Elwert cross sections shown by the dashed curve are obtained from the product of Formula 3BN and the Elwert factor, Formula (II-4). The experimental values<sup>36/</sup> are shown by the open circles for gold. The corrected Sauter-Fano values at the high frequency limit are estimated in reference 21.

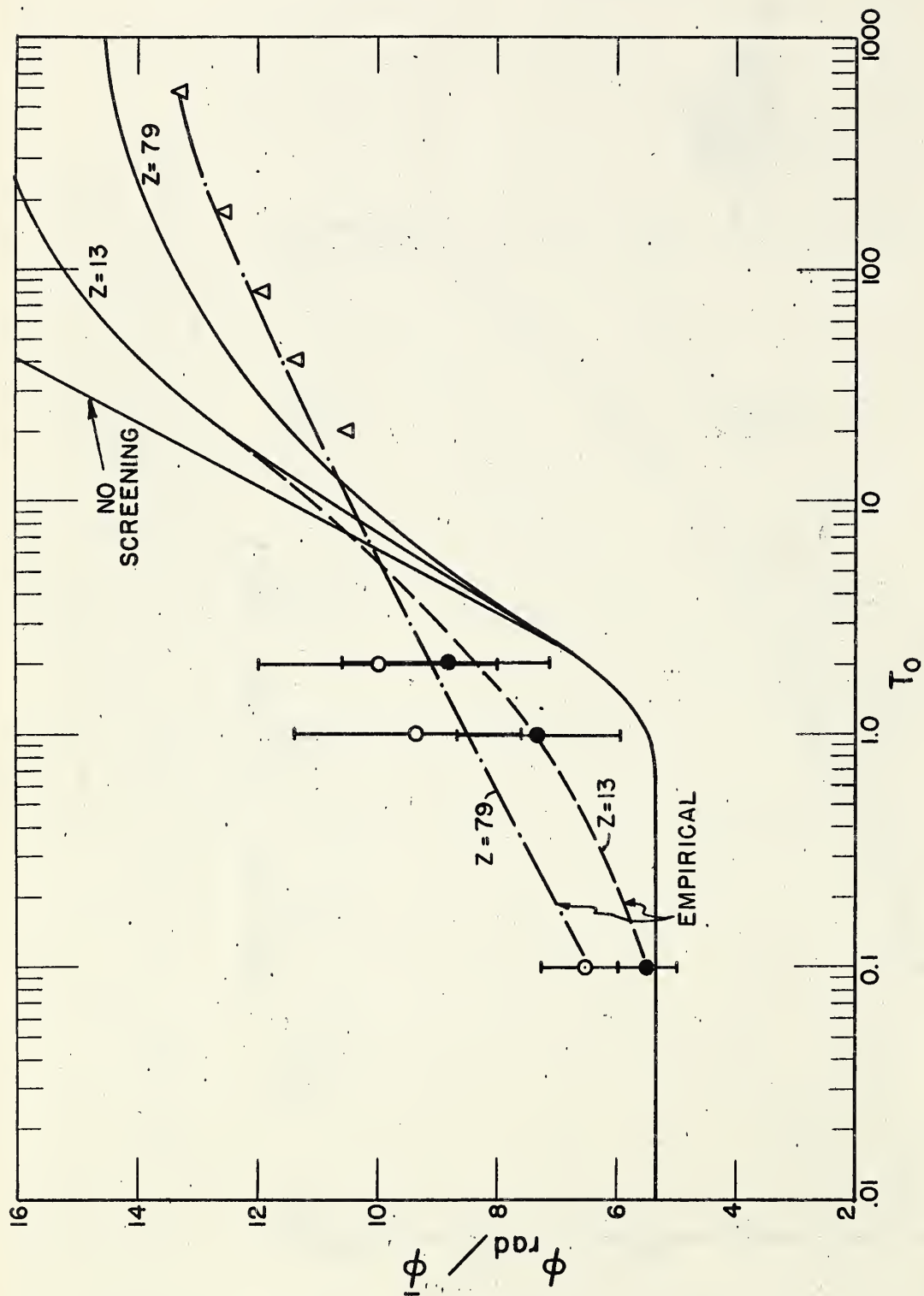


Fig. 22. Dependence of the total radiation cross section,  $\phi_{rad} (= \int_0^{T_0} k d\sigma_k)$ , on the initial electron kinetic energy,  $T_0$ . The solid lines are obtained from Formula 4BN for no screening, and from the numerical integration of Formulas 3BS(c) and 3BS(d) with screening corrections for  $Z$  equal to 13 and 79. The experimental points 33,35/ are shown by the open and closed circles for a gold and aluminum target respectively. The values shown by the triangles are estimated by numerical integration of Formula 3CS for  $Z = 79$ . On the basis of the experimental data at the low energies and the theoretical values (triangles) predicted by the exact theory at the extreme relativistic energies, the dashed curves have been drawn as an estimate of the most accurate  $\phi_{rad}$  values for  $Z$  equal to 13 and 79.

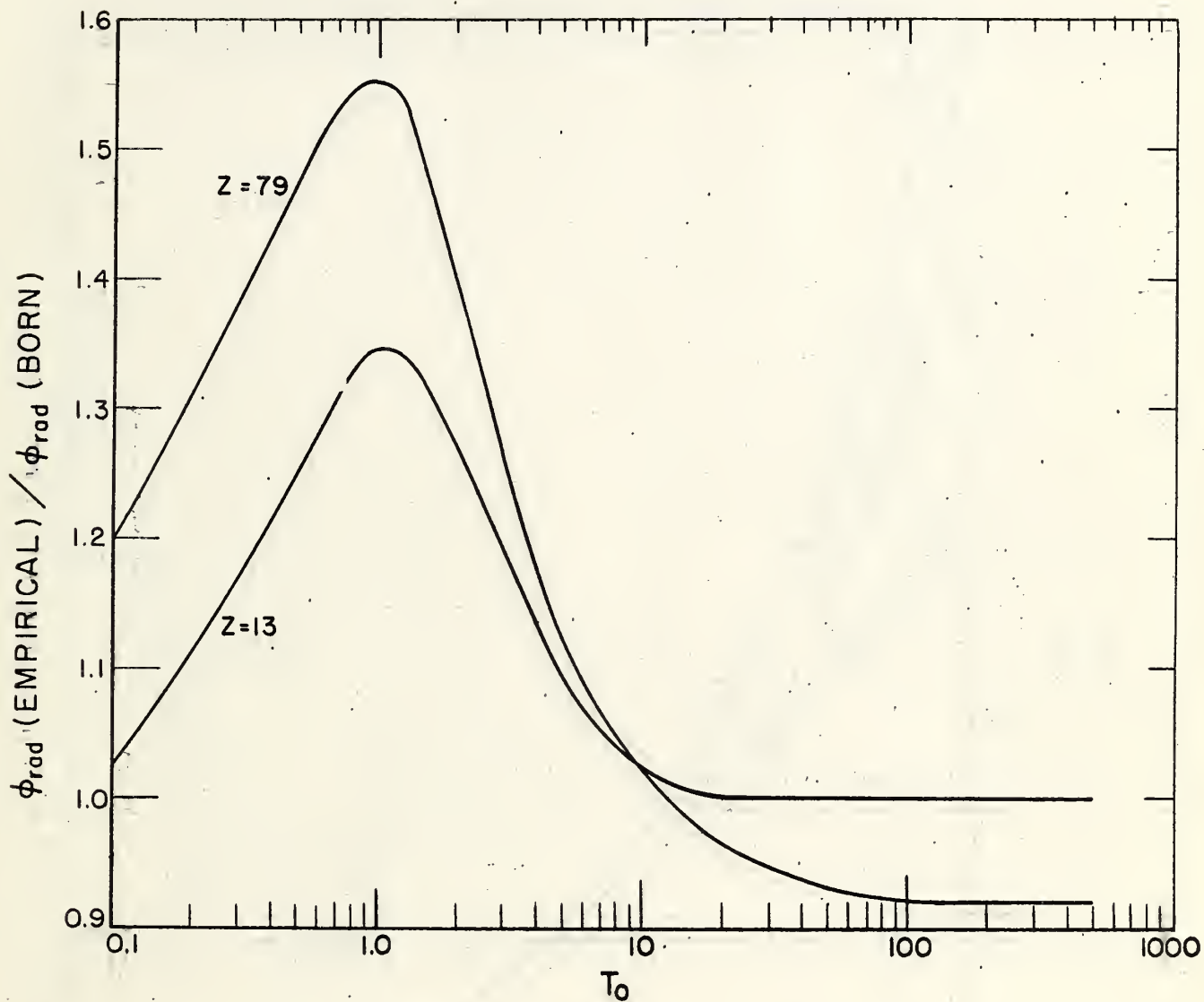


Fig. 23. Approximate correction factors for the Born-approximation  $\phi_{rad}$  values with screening shown in Fig. 22. These factors have been estimated from the ratios of the empirical (dashed and dot-dashed) curves to the Born-approximation curves with screening in Fig. 22.

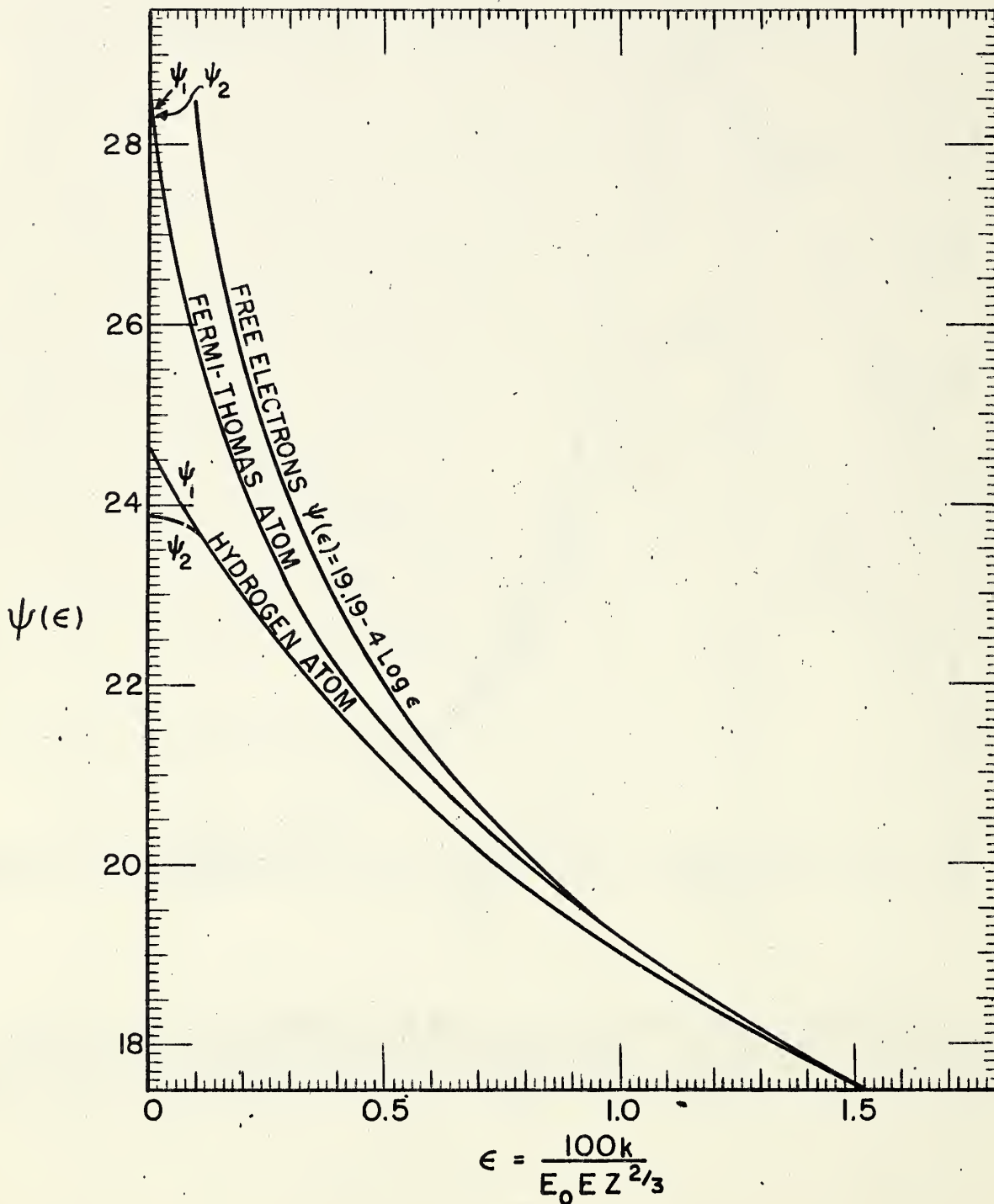


Fig. 24. Screening factors  $\psi_1$  and  $\psi_2$ , for electron-electron bremsstrahlung. The curve marked "Hydrogen atom" was calculated with exact wave functions. For free electrons,  $\psi_1 = \psi_2 = \psi$ .

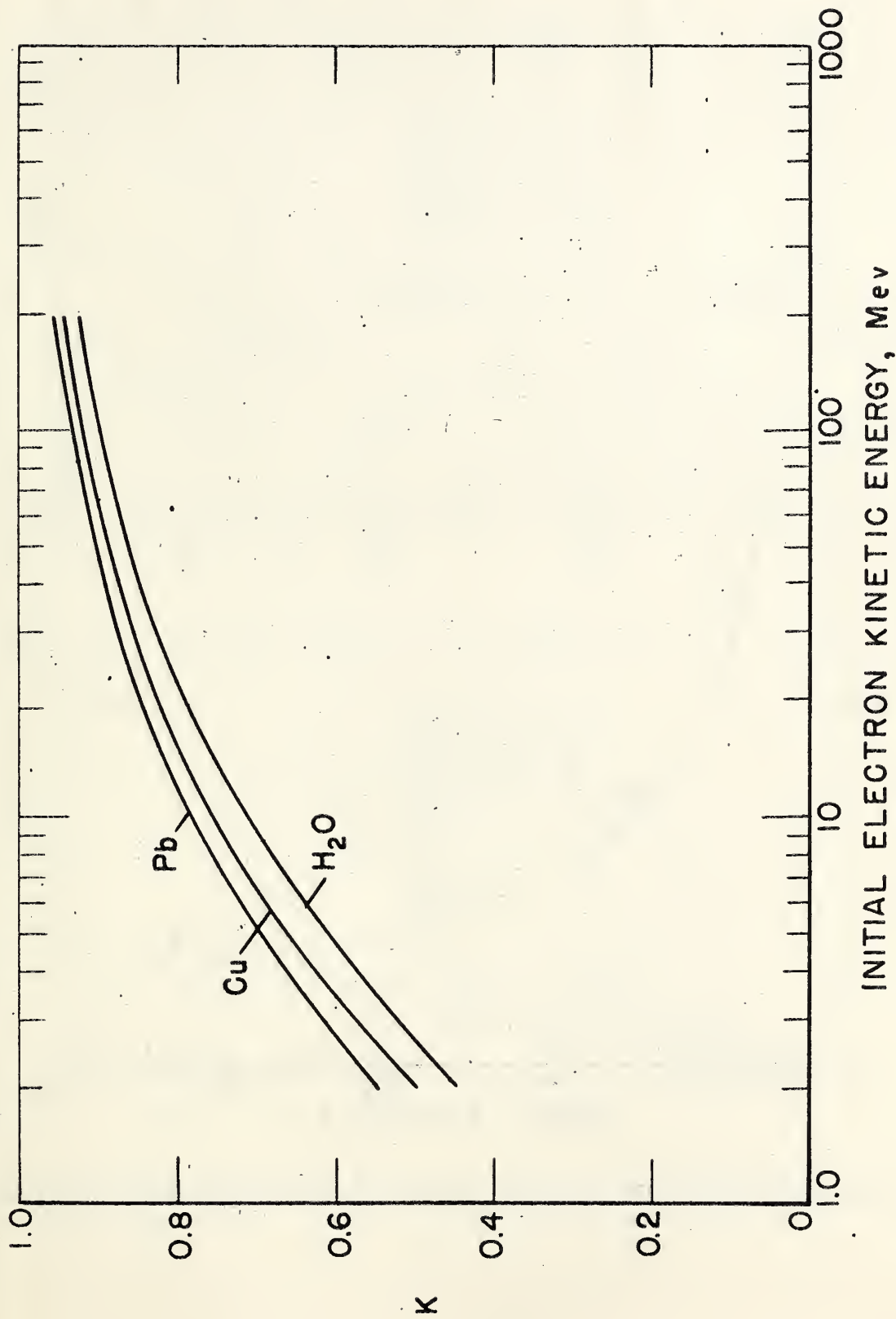


Fig. 25. Dependence of the radiation probability correction factor,  $K \left( = \frac{\phi_{\text{rad}}}{\phi_{\text{K}}^{\text{rad}}} \right)$ , on the initial electron kinetic energy and the target atomic number.

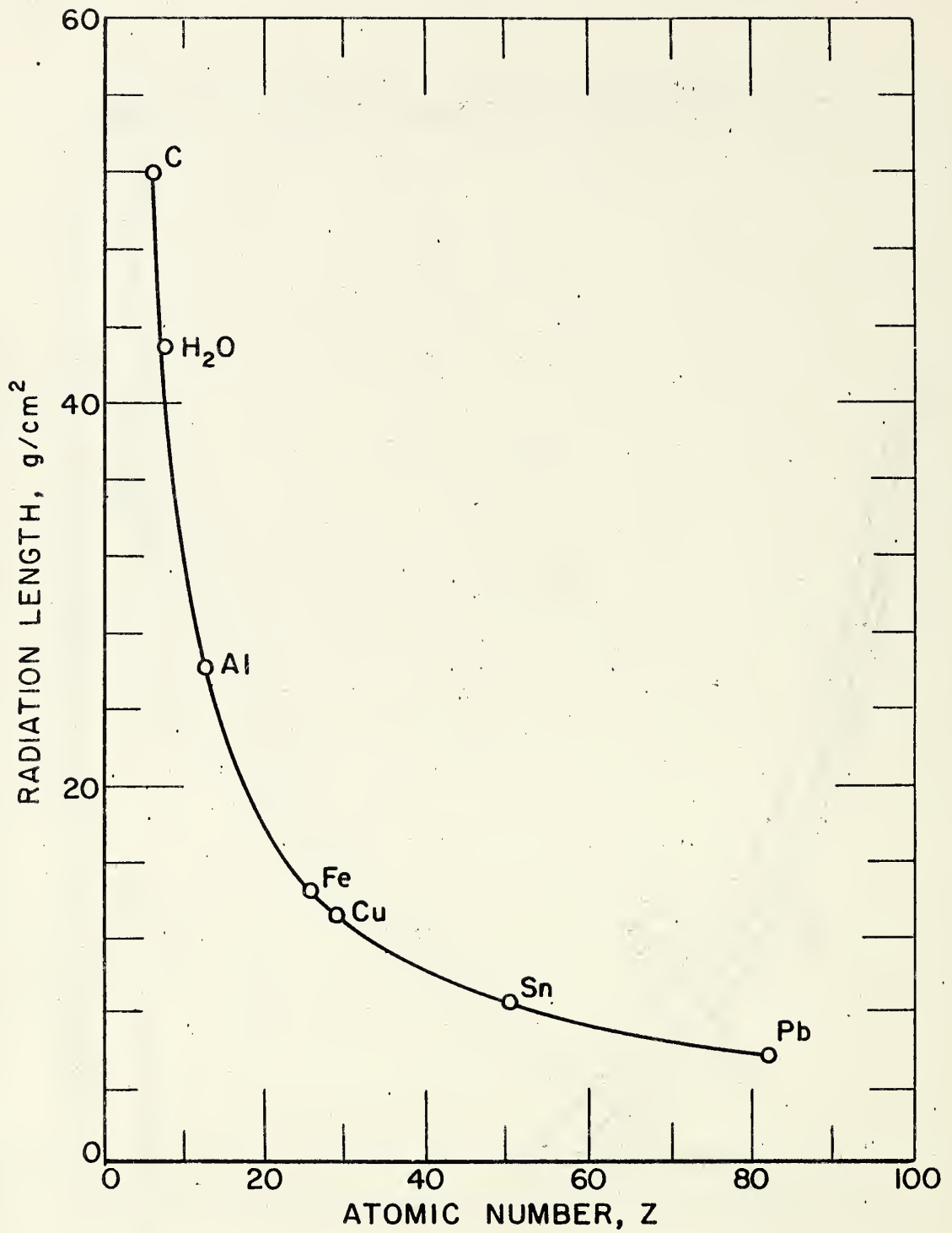


Fig. 26. Radiation lengths in grams per square centimeter for various materials.

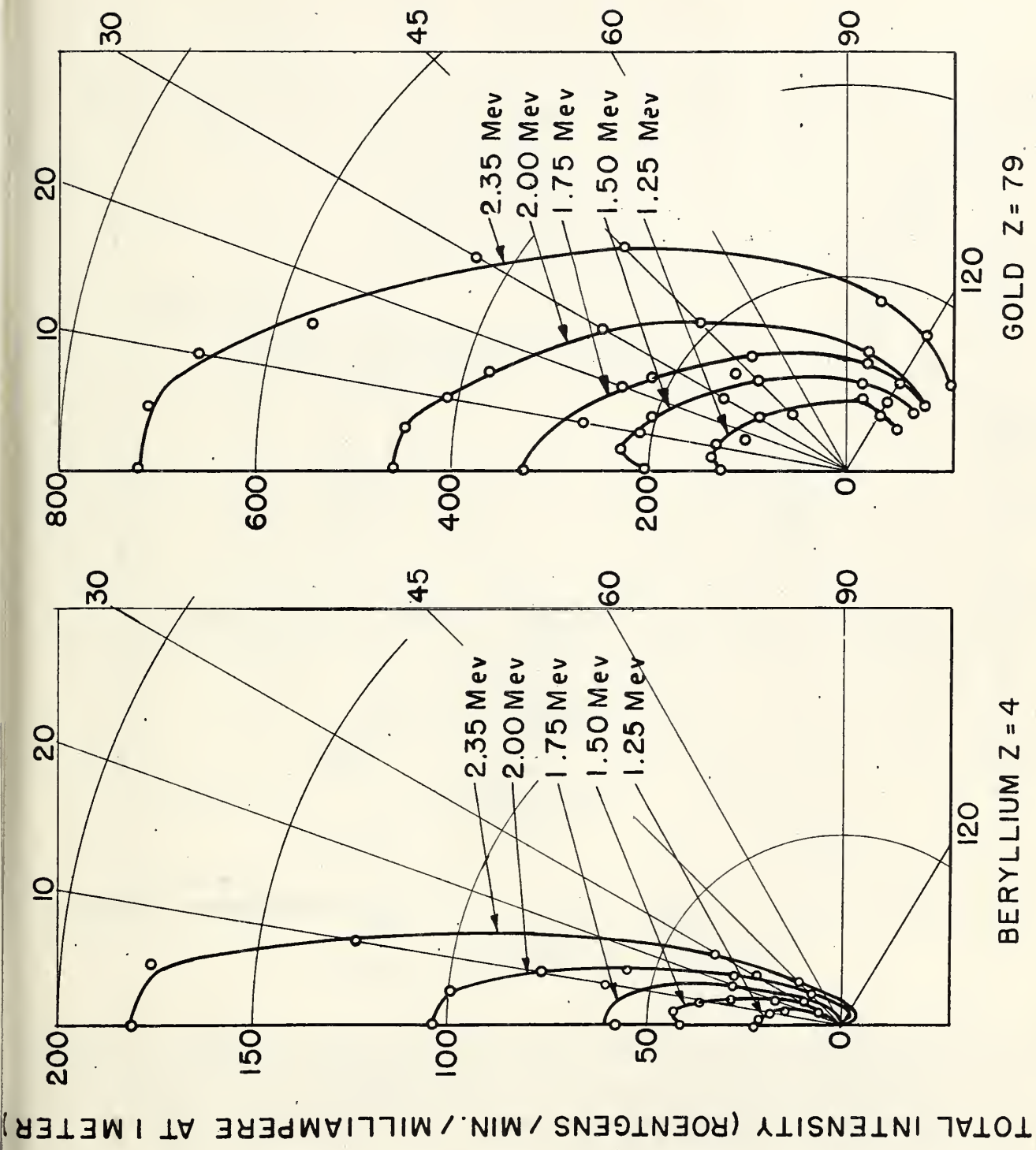


Fig. 27. Angular dependence of the thick target bremsstrahlung intensity integrated over photon energy for 1.25 to 2.35 Mev electrons. These results were obtained by Buechner, Van de Graaff, Burrill, and Spurduto<sup>43/</sup> and include corrections for the target

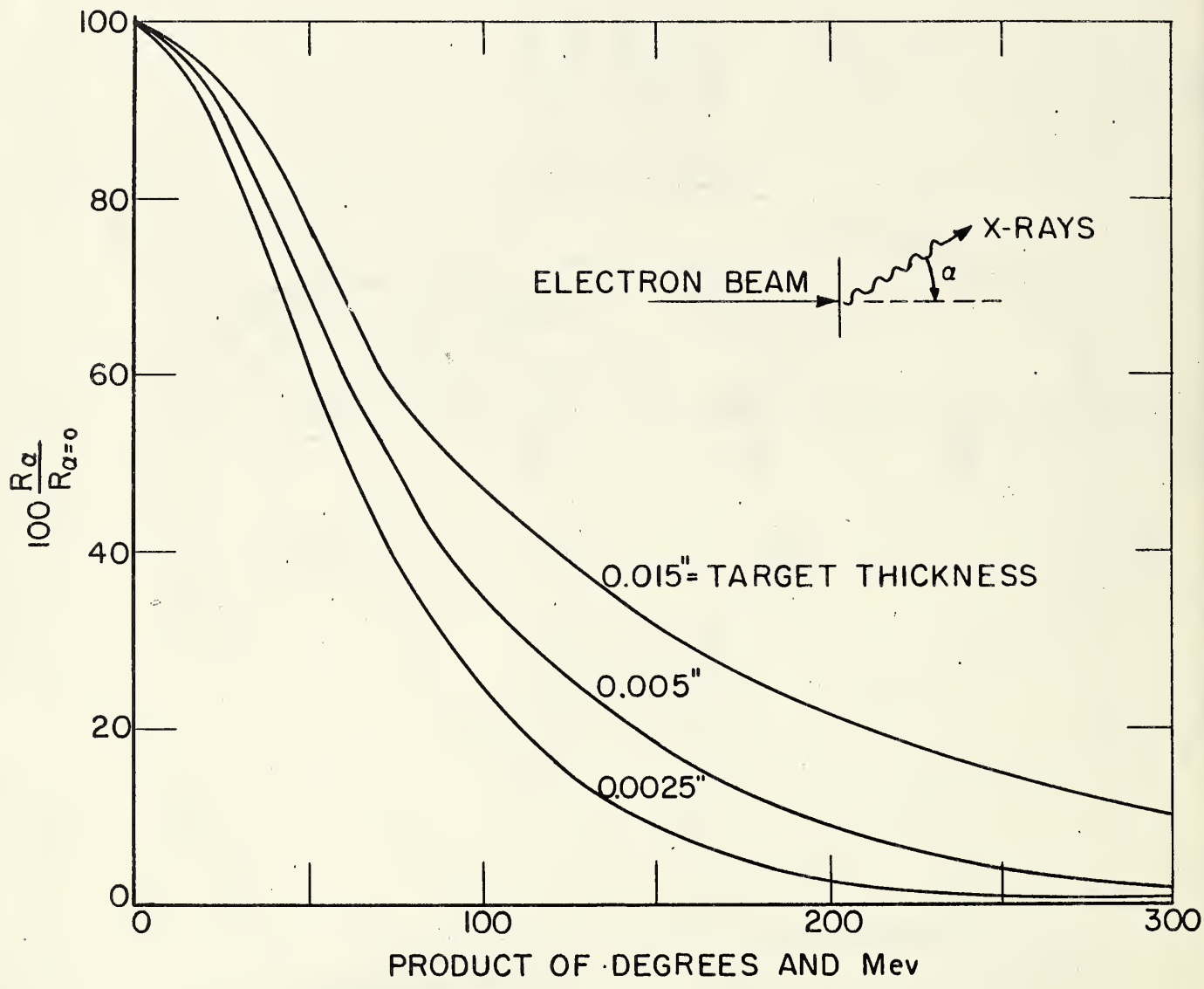


Fig. 28. Theoretical bremsstrahlung angular distributions from thick tungsten targets for relativistic energies. These data are obtained from the National Bureau of Standards Handbook 55.  $R_\alpha$  is defined as the fraction of the total incident electron kinetic energy that is radiated per steradian at the angle  $\alpha$ .

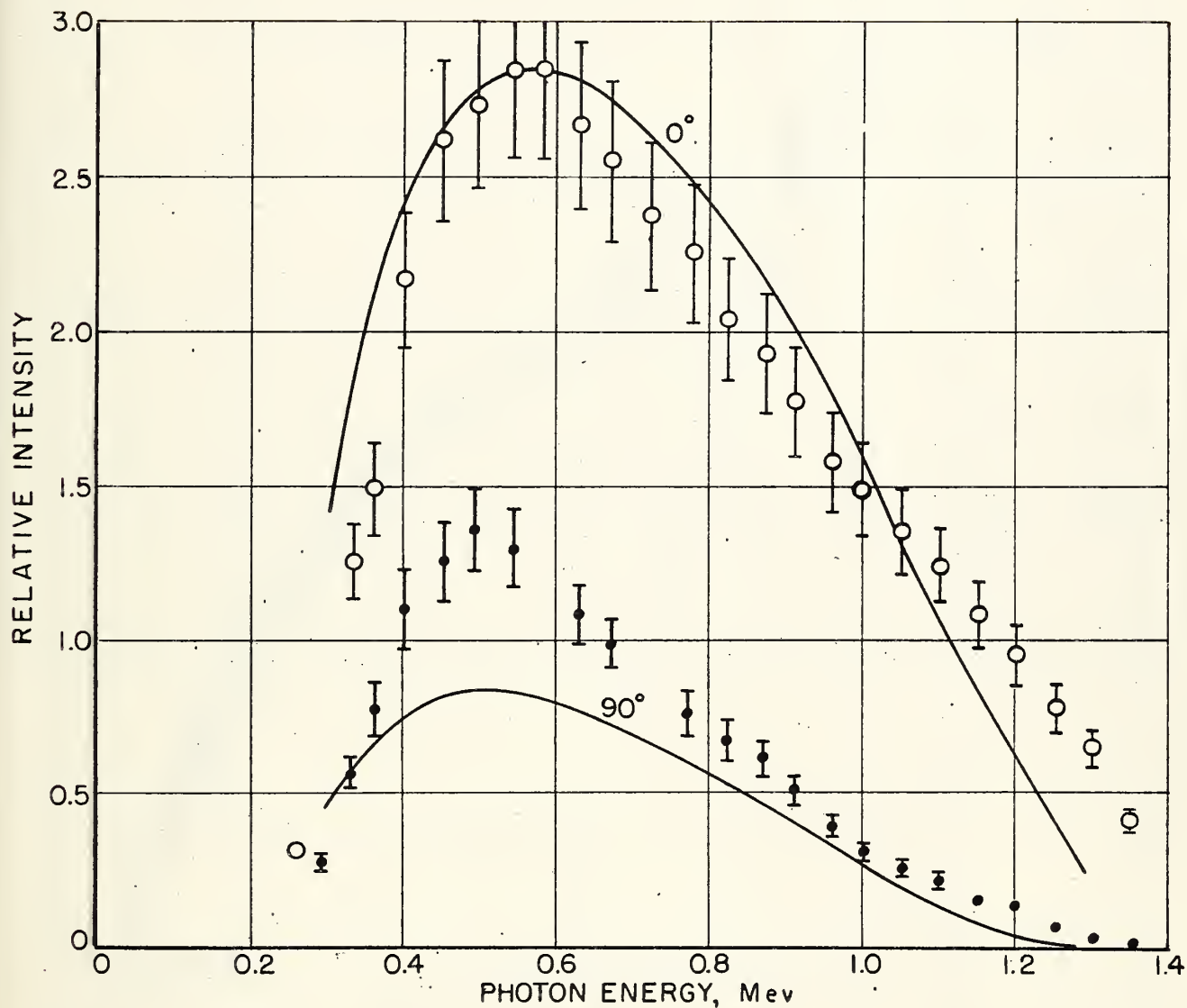


Fig. 29. Relative spectral intensities at  $0^\circ$  and  $90^\circ$  for 1.4 Mev electrons incident on a thick tungsten target<sup>49/</sup>. The solid curves are obtained from theoretical estimates that include electron scattering effects and photon absorption in the materials surrounding the target. The experimental values have been normalized and are shown by the open (zero degrees) and closed (90 degrees) circles. To obtain absolute spectral intensities in Mev per steradian per Mev per incident electron, the ordinate should be multiplied by  $10^{-3}$  for the theoretical curves and by  $2.1 \times 10^{-3}$  for the experimental points.

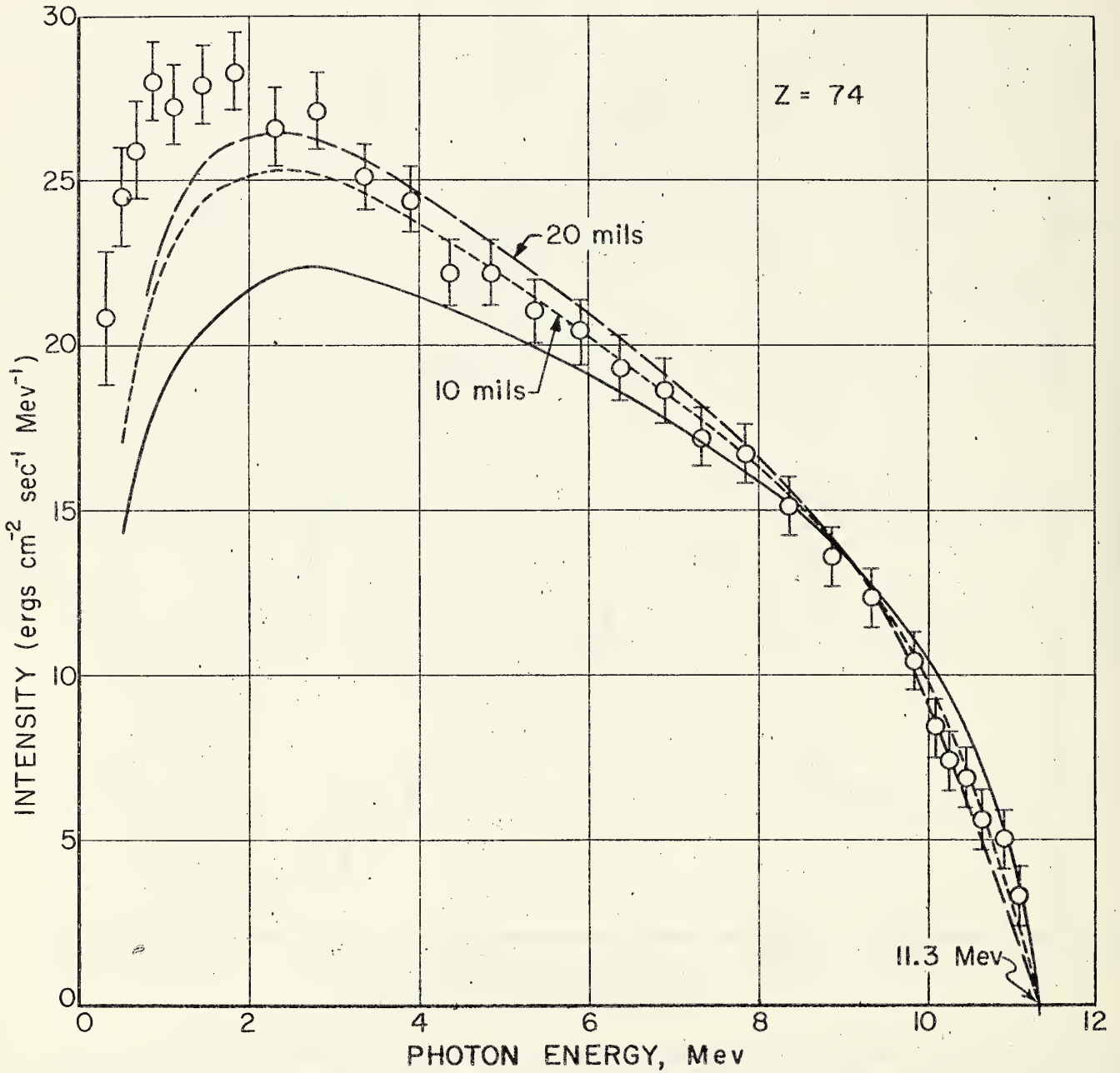


Fig. 30. Bremsstrahlung intensity spectrum in the forward direction for 11 Mev electrons incident on a thick-tungsten target<sup>56/</sup>. The thin-target Born spectrum, modified by the photon absorption in the materials surrounding the target, is shown by the solid curve. The dashed curves show the spectra expected for a 10 mil and a 20 mil target, and the experimental values are given by the open circles.

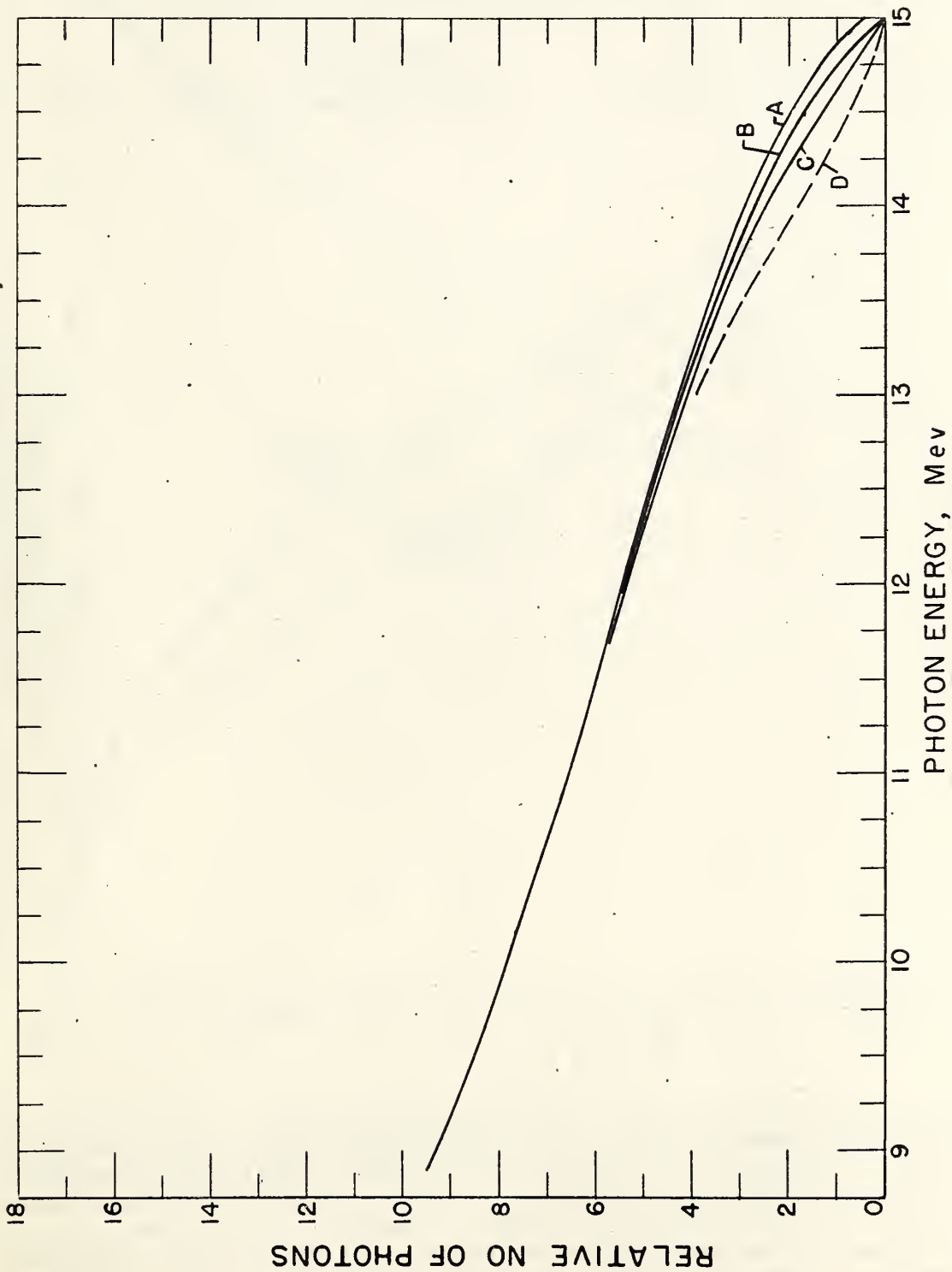


Fig. 31. Comparison of the spectrum shapes predicted by the thick target Penfold calculations<sup>53/</sup> and by Schiff's thin target Formula 3BS(e) for 15 Mev electrons. The Schiff curve A shows the spectrum integrated over photon angle. Curve B is the spectrum shape predicted by Formula (IV-13) with the simplified S function given by Formula (IV-15). Curve C is the spectrum shape predicted by the Penfold calculations (Formulas (IV-13) and (IV-14)) for a 0.020 inch platinum target and a detector which subtends an angle,  $\Gamma$ , of 10 degrees. Curve D gives the Penfold spectrum for  $\Gamma \gg 10$  degrees.

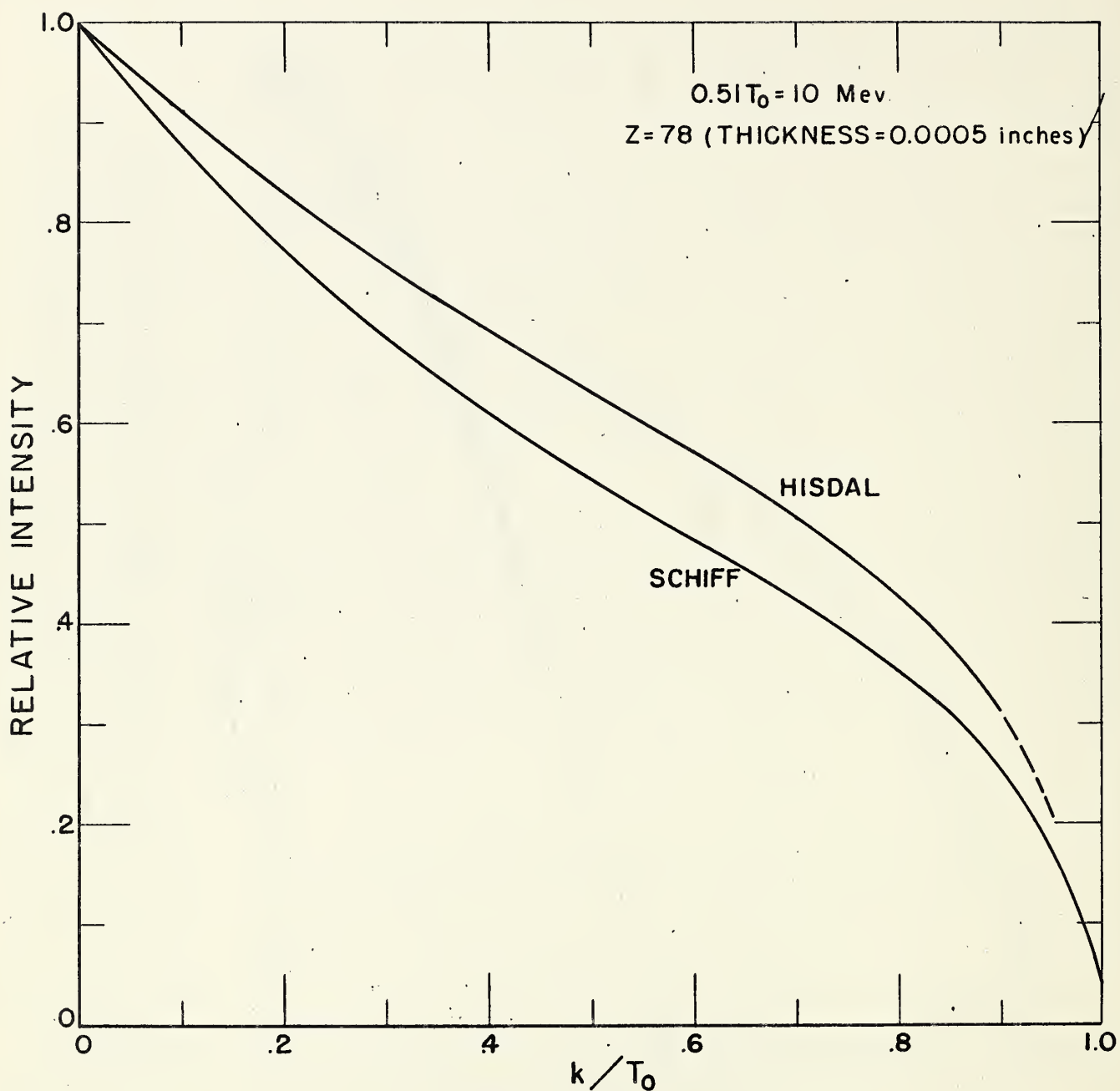


Fig. 32(a). Comparison of bremsstrahlung spectrum shapes predicted by the thick target calculations of Hisdal<sup>51/</sup> and by the thin target calculations of Schiff<sup>14/</sup> for 10 Mev electrons. The Schiff spectrum is integrated over the photon direction, Formula 3BS(e), and the Hisdal curve gives the spectrum in the forward direction,  $\Gamma = 0$ , after corrections have been made for multiple scattering in the target (See IVB). The values of the intensity (defined as proportional to the product of the photon energy and number per unit time) are normalized to unity for zero photon energies.

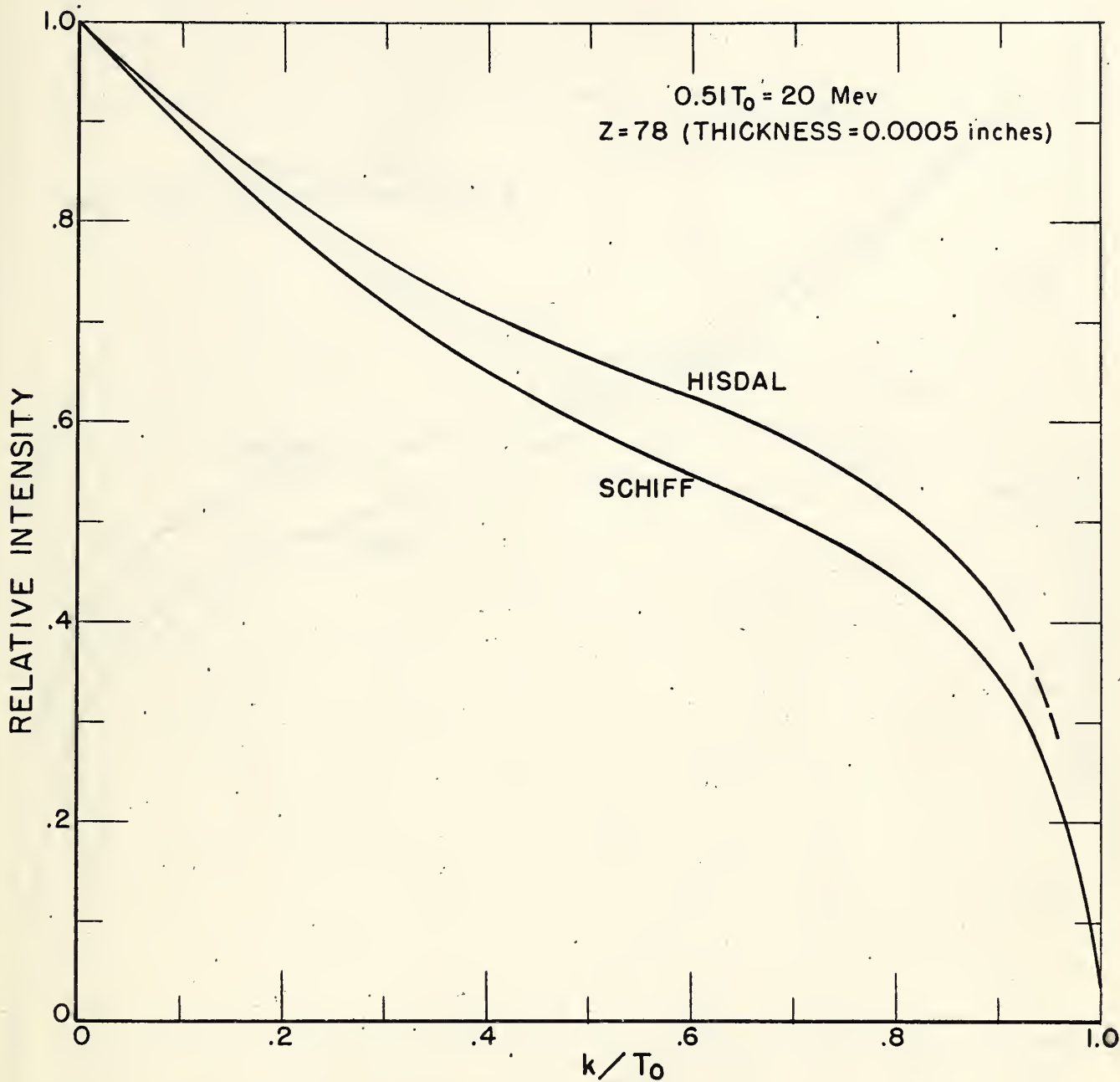


Fig. 32(b). Comparison of bremsstrahlung spectrum shapes predicted by the thick target calculations of Hisdal<sup>51/</sup> and by the thin target calculations of Schiff<sup>14/</sup> for 20 Mev electrons. See 32(a).

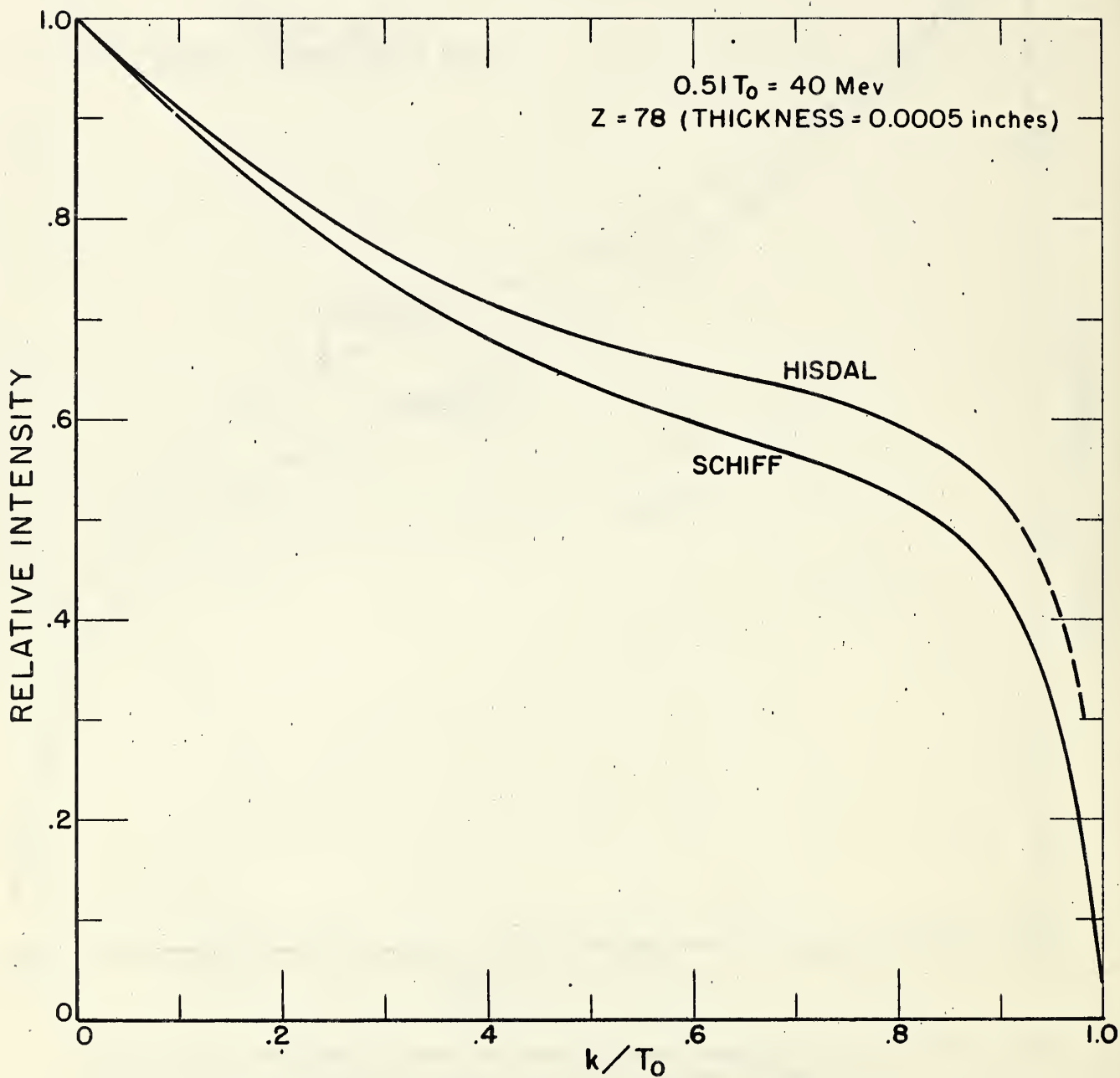


Fig. 32(c). Comparison of bremsstrahlung spectrum shapes predicted by the thick target calculations of Hisdal<sup>51/</sup> and by the thin target calculations of Schiff<sup>14/</sup> for 40 Mev electrons. See 32(a).

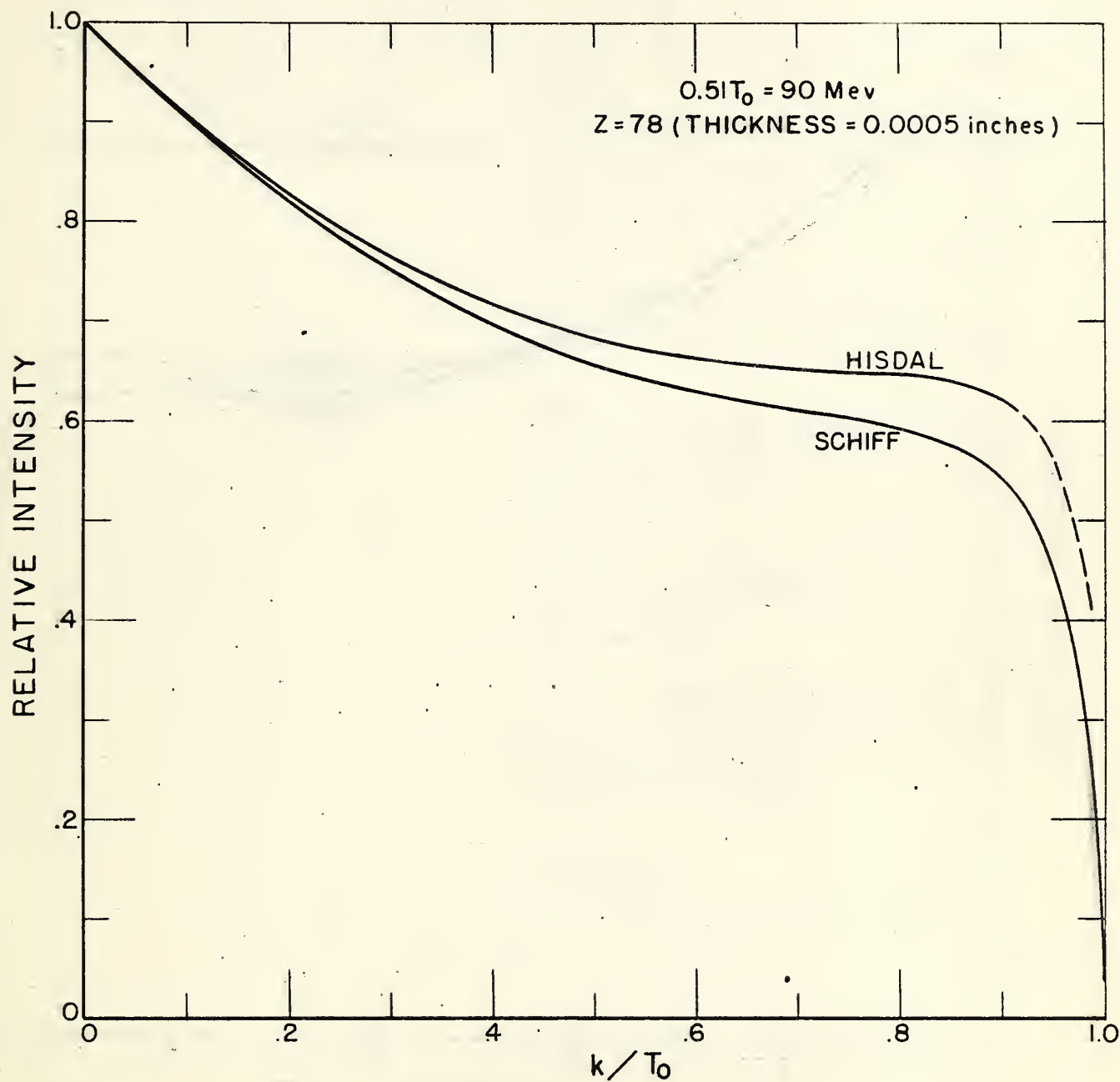


Fig. 32(d). Comparison of bremsstrahlung spectrum shapes predicted by the thick target calculations of Hisdal<sup>51/</sup> and by the thin target calculations of Schiff<sup>14/</sup> for 90 Mev electrons. See 32(a).

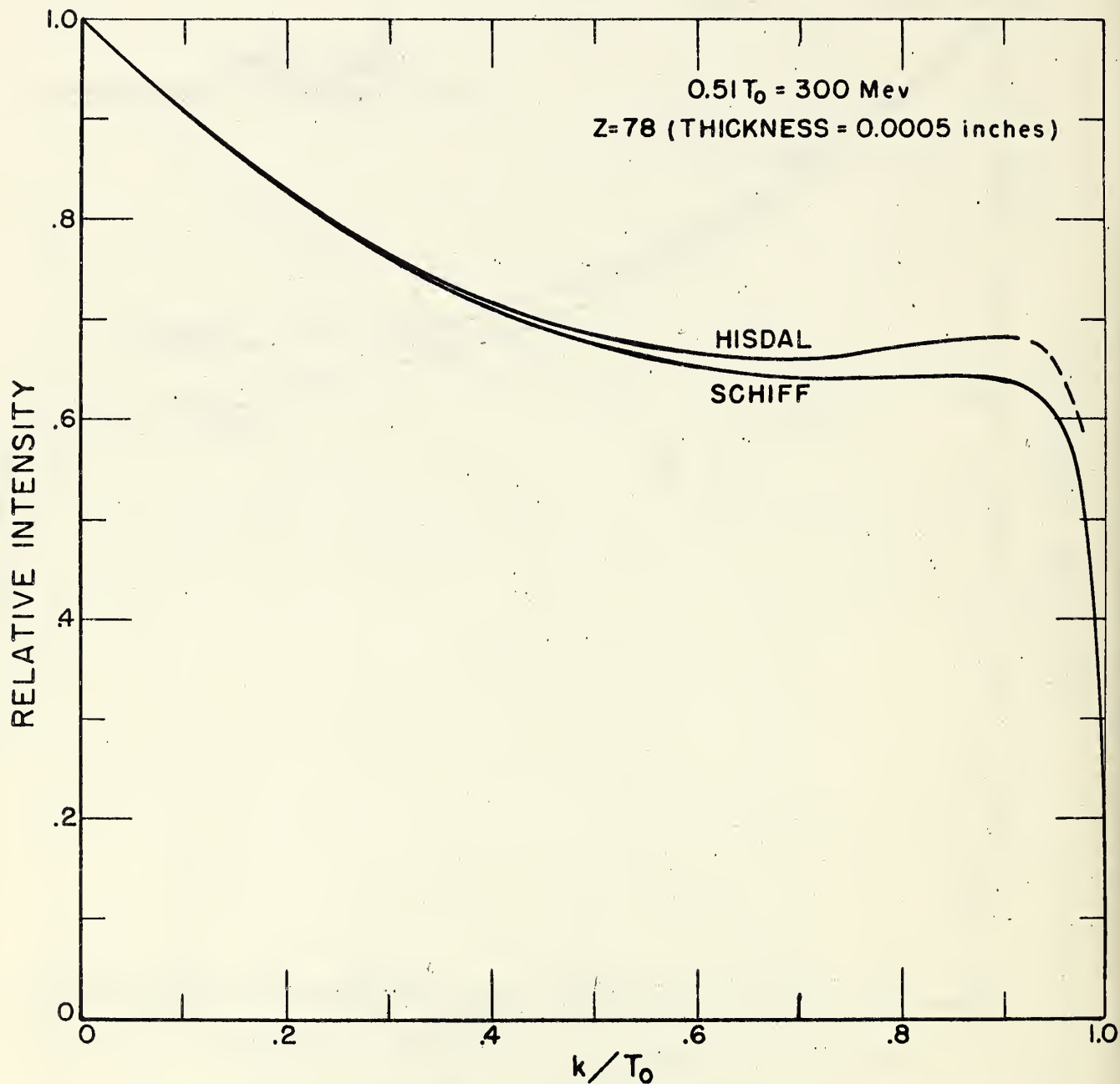


Fig. 32(e). Comparison of bremsstrahlung spectrum shapes predicted by the thick target calculations of Hisdal<sup>51/</sup> and by the thin target calculations of Schiff<sup>14/</sup> for 300 Mev electrons. See 32(a).

DISTRIBUTION LIST

GOVERNMENTAL

<u>No. of Copies</u>	<u>Agency</u>
5	Commander Air Force Office of Scientific Research Air Research and Development Command ATTN: SRY Washington 25, D C
4	Commander Wright Air Development Center ATTN: WCOSI-3 Wright-Patterson Air Force Base, Ohio
1	Commander Air Force Cambridge Research Center ATTN: Technical Library L. G. Hanscom Field Bedford, Mass.
1	Commander Rome Air Development Center ATTN: RCSST-4 Rome, New York
1	Director, Office for Advanced Studies Air Force Office of Scientific Research Air Research & Development Command Post Office Box 2035 Pasadena 2, California
2	Commander European Office Air Research & Development Command 47 rue Cantersteen Brussels, Belgium (Air Mail)
10	Commander ASTIA ATTN: TIPDR Arlington Hall Station Arlington 12, Virginia
1	Director of Research & Development Headquarters USAF ATTN: AFDRD Washington 25, D. C.

Distribution List (Continued)

<u>No. of Copies</u>	<u>Agency</u>
1	Chief of Naval Research Department of the Navy ATTN: Code 420 Washington 25, D. C.
1	Director, Naval Research Laboratory ATTN: Technical Information Officer Washington 25, D. C.
1	Director, Research & Development Division General Staff Department of the Army Washington 25, D. C.
1	Chief, Physics Branch, Division of Research U. S. Atomic Energy Commission Washington 25, D. C.
1	U. S. Atomic Energy Commission Technical Information Extension Post Office Box 62 Oak Ridge, Tenn.
1	National Bureau of Standards Library Room 301, Northwest Building Washington 25, D. C.
1	National Science Foundation 1520 H Street, N. W. Washington 25, D. C.
1	Director, Office of Ordnance Research Box CM, Duke Station Durham, North Carolina
1	Office of Technical Services Department of Commerce Washington 25, D. C.
1	Commander Arnold Engineering Development Center ATTN: Technical Library Tullohoma, Tenn.
1	Commander Air Force Armament Center ATTN: Technical Library Eglin Air Force Base, Florida

Distribution List (Continued)

No. of Copies

Agency

1

Commander  
Air Force Flight Test Center  
ATTN: Technical Library  
Edwards Air Force Base, Calif.

1

Commander  
Air Force Missile Test Center  
ATTN: Technical Library  
Patrick Air Force Base  
Cocoa, Florida

1

Commander  
Air Force Speical Weapons Center  
ATTN: Technical Library  
Kirtland Air Force Base, New Mexico

1

Commander  
Air Force Missile Development Center  
ATTN: Technical Library  
Holloman Air Force Base, New Mexico

1

Commander  
AF Cambridge Research Center  
ATTN: CROTR  
L. G. Hanscom Field  
Bedford, Mass.

1

Commander  
Army Rocket & Guided Missile Agency  
Redstone Arsenal  
ATTN: ORDXR-OTL  
Alabama

1

Commandant  
Air Force Institute of Technology  
ATTN: MCLI, Technical Library  
Wright-Patterson Air Force Base, Ohio

1

Commander  
Air Force Ballistic Missile Division  
Headquarters ARDC  
ATTN: WDSOT  
Post Office Box 262  
Inglewood, Calif.

1

Distribution Lis (Continued)

No. of Copies

Agency

1

Applied Mechanics Reviews  
Southwest Research Institute  
8500 Culebra Road  
San Antonio 6, Texas

1

Institute of the Aeronautical Sciences  
ATTN: Librarian  
2 East 64th Street  
New York 16, New York

U. S. DEPARTMENT OF COMMERCE

Lewis L. Strauss, *Secretary*

NATIONAL BUREAU OF STANDARDS

A. V. Astin, *Director*



## THE NATIONAL BUREAU OF STANDARDS

The scope of activities of the National Bureau of Standards at its headquarters in Washington, D. C., and its major laboratories in Boulder, Colo., is suggested in the following listing of the divisions and sections engaged in technical work. In general, each section carries out specialized research, development, and engineering in the field indicated by its title. A brief description of the activities, and of the resultant publications, appears on the inside front cover.

### WASHINGTON, D. C.

**Electricity and Electronics.** Resistance and Reactance. Electron Devices. Electrical Instruments. Magnetic Measurements. Dielectrics. Engineering Electronics. Electronic Instrumentation. Electrochemistry.

**Optics and Metrology.** Photometry and Colorimetry. Optical Instruments. Photographic Technology. Length. Engineering Metrology.

**Heat.** Temperature Physics. Thermodynamics. Cryogenic Physics. Rheology. Engine Fuels. Free Radicals Research.

**Atomic and Radiation Physics.** Spectroscopy. Radiometry. Mass Spectrometry. Solid State Physics. Electron Physics. Atomic Physics. Neutron Physics. Radiation Theory. Radioactivity. X-rays. High Energy Radiation. Nucleonic Instrumentation. Radiological Equipment.

**Chemistry.** Organic Coatings. Surface Chemistry. Organic Chemistry. Analytical Chemistry. Inorganic Chemistry. Electrodeposition. Molecular Structure and Properties of Gases. Physical Chemistry. Thermochemistry. Spectrochemistry. Pure Substances.

**Mechanics.** Sound. Mechanical Instruments. Fluid Mechanics. Engineering Mechanics. Mass and Scale. Capacity, Density, and Fluid Meters. Combustion Controls.

**Organic and Fibrous Materials.** Rubber. Textiles. Paper. Leather. Testing and Specifications. Polymer Structure. Plastics. Dental Research.

**Metallurgy.** Thermal Metallurgy. Chemical Metallurgy. Mechanical Metallurgy. Corrosion. Metal Physics.

**Mineral Products.** Engineering Ceramics. Glass. Refractories. Enameled Metals. Concreting Materials. Constitution and Microstructure.

**Building Technology.** Structural Engineering. Fire Protection. Air Conditioning, Heating, and Refrigeration. Floor, Roof, and Wall Coverings. Codes and Safety Standards. Heat Transfer.

**Applied Mathematics.** Numerical Analysis. Computation. Statistical Engineering. Mathematical Physics.

**Data Processing Systems.** SEAC Engineering Group. Components and Techniques. Digital Circuitry. Digital Systems. Analog Systems. Application Engineering.

• Office of Basic Instrumentation.

• Office of Weights and Measures.

### BOULDER, COLORADO

**Cryogenic Engineering.** Cryogenic Equipment. Cryogenic Processes. Properties of Materials. Gas Liquefaction.

**Radio Propagation Physics.** Upper Atmosphere Research. Ionospheric Research. Regular Propagation Services. Sun-Earth Relationships. VHF Research. Ionospheric Communication Systems.

**Radio Propagation Engineering.** Data Reduction Instrumentation. Modulation Systems. Navigation Systems. Radio Noise. Tropospheric Measurements. Tropospheric Analysis. Radio Systems Application Engineering. Radio-Meteorology.

**Radio Standards.** High Frequency Electrical Standards. Radio Broadcast Service. High Frequency Impedance Standards. Electronic Calibration Center. Microwave Physics. Microwave Circuit Standards.

